

Appendix B

Estimation of Net Infiltration at the Idaho Nuclear Technology and Engineering Center Tank Farm

Peter Martian, Idaho National Laboratory

Estimation of Net Infiltration at the Idaho Nuclear Technology and Engineering Center Tank Farm

B-1 OBJECTIVES

The contaminated soil beneath the Idaho Nuclear Technology and Engineering Center (INTEC) tank farm is currently undergoing a remedial investigation and baseline risk assessment (RI/BRA). Infiltrating water, resulting from precipitation, may move down through the contaminated soil to mobilize contaminants and eventually transport them to the aquifer. This infiltration study simulated the vadose zone water balance at several locations within the tank farm soil and provided estimates of the net infiltration rate through the tank farm soil.

The main objective of this study was to quantify the net infiltration rate through the tank farm soil from observations of soil moisture. This was accomplished by simulating infiltration patterns with a one-dimensional vadose zone model and calibrating the model to transient observed soil moisture. The model calibration consisted of estimating soil hydraulic properties and infiltration from precipitation events by matching the simulated soil moisture to the observed soil moisture during winter 1993 and spring 1994. The model used a daily meteorological record as the upper model boundary condition and the precipitation amount was modified to account for snowpack accumulation, snowpack melting, and water redistribution over a synthetic membrane covering the tank farm soil. The results of the calibration were then used to simulate infiltration during the entire operational period of the INTEC (1954-2003). The final simulation results will be used as a surface recharge boundary condition in further subsurface pathway modeling efforts for the Waste Area Group 3, Operable Unit 3-14, RI/BRA and evaluation of proposed INTEC remedial actions.

B-2 INTEC TANK FARM SOIL MOISTURE MONITORING

B-2.1 Geologic and Climatic Conditions

The INTEC is located on an alluvial plain near the Big Lost River. The INTEC subsurface is a complex sequence of surficial sediments underlain by basalt flows and occasional interbeds. The surficial sediments are gravelly medium-to-coarse textured alluvium deposited from past meandering of the ancestral Big Lost River. The alluvium ranges from 2 to 73 ft in thickness and is underlain by fractured basalt. Sedimentary interbeds occur infrequently in the sequence of basalt flows and range in thickness from a few feet to tens of feet. The basalt flows continue down to, and through the top of, the aquifer, which is located approximately 460 ft below the land surface.

The climate at the Idaho National Laboratory (INL) Site is that of a semiarid, high desert region and is characterized by large daily and seasonal temperature variations. During the summer, low humidity, clear skies, and high temperatures result in high potential evaporation rates while average winter temperatures remain below freezing for 2 to 3 months, essentially preventing soil water evaporation during the winter. The average annual temperature is approximately 42° F, and the average annual precipitation is 8.7 in./yr with 30% falling as snow (Clawson, Start, and Ricks 1989).

Much of the precipitation occurs between the fall and late spring, with an occasional thunderstorm occurring during the summer. The highest annual precipitation recorded was 14.4 in./yr and the lowest recorded precipitation was 4.5 in./yr. Precipitation usually exceeds evaporation from October through May, and evaporation exceeds precipitation during June through September (Clawson, Start, and Ricks 1989). The highest daily precipitation rate recorded at the INL Site was 1.64 in./day, and the highest hourly precipitation rate was 1.37 in./hour (DOE-ID 2003a).

The average annual potential evaporation from open water is approximately 43 in./yr and exceeds the average precipitation by several times. The highest relative humidity occurs in the winter and the average

midday value is approximately 55%. The lowest relative humidity occurs in the summer and the average midday value is approximately 18%. The prevailing wind direction at the INTEC is southwesterly with a diurnal shift to northeasterly. The average wind speed at 6 m ranges from 5.1 mph in December to 9.3 mph in March and April. Calm conditions exist approximately 11% of the time (DOE-ID 2003a).

B-2.2 Tank Farm Description

The INTEC tank farm was used to store liquid radioactive waste generated from reprocessing spent nuclear fuel until the liquid radioactive waste was converted to a solid granular form. The reprocessing used concentrated nitric acid (1 to 2 mol/L) to dissolve the fuel rods. The waste generated from this process was a very acidic liquid containing fission products, transuranic elements, and various metals. Two types of liquid waste have been stored at the Tank Farm Facility. The first was high-level nonsodium-bearing waste, which was generated from first-cycle reprocessing of spent nuclear fuel. The second is sodium-bearing waste generated from second- and third-cycle reprocessing and other INTEC operations such as decontamination activities.

Construction of the INTEC facility began in 1950 and the tank farm began operation in 1953. The Tank Farm Facility includes 11 belowground 300,000-gal tanks and four belowground 30,000-gal tanks. The last tank was installed in 1962. The tank farm tanks rest on basalt and construction of the tank farm was performed by excavating the alluvium down to basalt at approximately 42 ft, installing the stainless-steel storage tanks into concrete vaults, and backfilling the alluvium to the original land surface. In 1977 the tank farm surface was graded, to promote drainage, and covered with a synthetic membrane designed to inhibit water infiltration. The membrane is covered by approximately 6 in. of gravel. Most of the leaks and spills associated with the contaminated soil at the tank farm occurred several years prior to installation of the membrane, and many of the mobile contaminants have already moved deep into the subsurface below the tank farm.

B-2.3 Moisture Monitoring Data

An investigation of tank farm soil contamination performed in 1993 included measurements of soil moisture content using a neutron moisture probe at 20 locations near and within the tank farm. The measurements were recorded at 1-ft intervals on each monitoring date during the months of December 1993 through May 1994. The neutron probe used the manufacturer's standard calibration curve for Schedule 80 stainless-steel casing and a "standard block" to calibrate the probe response. The calibration was verified by comparing neutron-probe measurements at two locations to laboratory-measured soil moisture from the same locations. The overall ratio between probe and laboratory-measured moisture content was 1:0.92, and the calibration was thought to be adequate for tank farm soil (LITCO 1995). The monitoring dates for each location are summarized in Table B-1 and the monitoring locations are illustrated in Figure B-1. The soil moisture data are illustrated with the simulated soil moisture in Sections 4.3.1 and 4.3.2.

The tank farm soil moisture investigation also included two small-scale infiltration tests, which were performed to determine the extent of lateral migration versus vertical infiltration and speed of wetting front movement. The first test consisted of a 120-degree arc-shaped infiltration basin around neutron access tube (NAT) A-67, which is located approximately 400 ft north of the tank farm. The basin inner radius was 7 ft from the NAT and the outer radius was 15.8 ft from the NAT. The basin was filled to a 3.8-in. depth and the well was monitored for 72 hours. The wetting front was never observed in the NAT, and it was concluded that water moves vertically through the alluvium with very little lateral movement.

The second test consisted of a 10-ft-radius infiltration pond around NAT A-68. The basin was filled to a 3.8-in. depth and monitored for 72 hours. The wetting front reached a 10-ft depth after 2 hours and the basalt interface within 20 hours. The rapid movement of the wetting front through the alluvium indicated that monitoring of at least twice daily would be needed to observe wetting front movement after a period of significant precipitation. The data presented in Table B-1 were collected approximately monthly and most

likely do not contain each infiltration event that occurred over the monitoring period. This makes a calibration less reliable than if the monitoring was performed more frequently.

Inspection of the NAT A-68 infiltration test data suggests the data may not be adequate to provide a reliable means of estimating in situ soil properties or the speed of a wetting front. Soil moisture was measured after 2, 20, 40, and 70 hours. The wetting front was seen at 10 ft after 2 hours. After 20 hours, the soil moisture was near pretest conditions, indicating that the water had already drained from the alluvium and entered the underlying fractured basalt. The data are suspect for two reasons. The first reason is that integrating the change in moisture content with depth after 2 hours indicates that 4.8 in. of water had entered the soil, assuming that the water movement is effectively one-dimensional. This is 125% of the 3.8-in. applied water, and moisture content at the surface was much higher than at the wetting front, indicating that water may have been still entering the soil after 2 hours. The second reason is that unsaturated hydraulic conductivity values measured for INTEC alluvial soil cores would not allow a wetting front to move at the observed speed at the observed moisture content. The very fast wetting front movement and the larger-than-applied amount of water measured in the soil suggest that water flowed down and around the borehole wall.

The tank farm construction may be responsible for two infiltration regimes present in the soil. The first is an ambient regime in the disturbed, gravelly, and alluvial soil that is exposed to atmospheric conditions. These locations are outside of the area covered by the synthetic membrane, where soil moisture can evaporate. The second regime is infiltration occurring through holes in the membrane and soil moisture cannot readily evaporate above or below the membrane. This is based on the following observations: (1) the membrane has been breached many times by maintenance activities and may not have been adequately resealed in places, (2) the gravel covering the liner will not readily allow evaporation of any water ponded on the liner surface, and (3) the tank farm tank vault sumps need pumping to remove infiltrate.

Richards (1993) estimated that 12,170 gal/yr enter the tank vaults and the total tank vault footprint is approximately 40,000 ft². These values indicate a hypothetical recharge rate of approximately 1.2 cm/year, assuming all infiltration accumulates in the tank vaults. During September 2001 through July 2003, a total of 26,502 gal was pumped from the tank vaults (DOE-ID 2003b). This value indicates a hypothetical recharge rate of 1.4 cm/year. Considering the vaults have concrete roofs and some of the concrete roofs have moisture barrier material applied to the concrete's outer surface, the average net infiltration rate through the tank farm soil would presumably be many times higher in the vicinity of those vaults that accumulate standing water because the concrete vault roofs should only allow a fraction of the total infiltration to enter the vaults.

Table B-1. Tank farm infiltration monitoring data summary.

Neutron Access Tube	Total Monitored Depth (ft)	Monitoring Dates	Within Tank Farm
A-60	32	12/8/93, 1/28/94, 2/28/94, 4/11/94, 5/11/94	Yes
A-61	34	12/8/93	Yes
A-62	36	12/8/93, 1/28/94, 3/1/94, 4/11/94, 5/11/94	Yes
A-63	36	3/1/94, 4/11/94, 5/11/94	Yes
A-64	35	12/8/93, 1/28/94, 3/1/94, 4/11/94, 5/11/94	Yes
A-65	30	12/7/93, 1/28/94, 3/1/94, 4/11/94, 5/11/94	Yes
A-66	35	12/7/93	Yes
A-67	37	12/7/93, 1/28/94, 3/1/94, 3/31/94, 5/11/94	No
A-68	30	12/7/93, 1/28/94, 3/1/94, 3/31/94, 5/11/94	No

Neutron Access Tube	Total Monitored Depth (ft)	Monitoring Dates	Within Tank Farm
81-02	28	12/8/93, 1/28/94, 2/28/94, 4/11/94	Yes
81-04	15	2/28/94, 4/11/94, 5/11/94	Yes
81-05	13	2/28/94, 4/11/94, 5/11/94	Yes
81-06	27	4/11/94, 5/11/94	Yes
81-09	22	4/11/94, 5/11/94	Yes
81-10	28	12/8/93, 1/28/94, 2/28/94, 4/11/94, 5/11/94	Yes
81-15	11	12/8/93, 1/28/94, 2/28/94, 4/11/94	Yes
81-17	17	12/8/93, 1/28/94, 2/28/94, 4/11/94, 5/11/94	Yes
81-19	23	4/11/94, 5/11/94	Yes
81-20	28	4/11/94, 5/11/94	Yes
81-21	11	12/8/93, 1/28/94, 4/11/94, 5/11/94	Yes

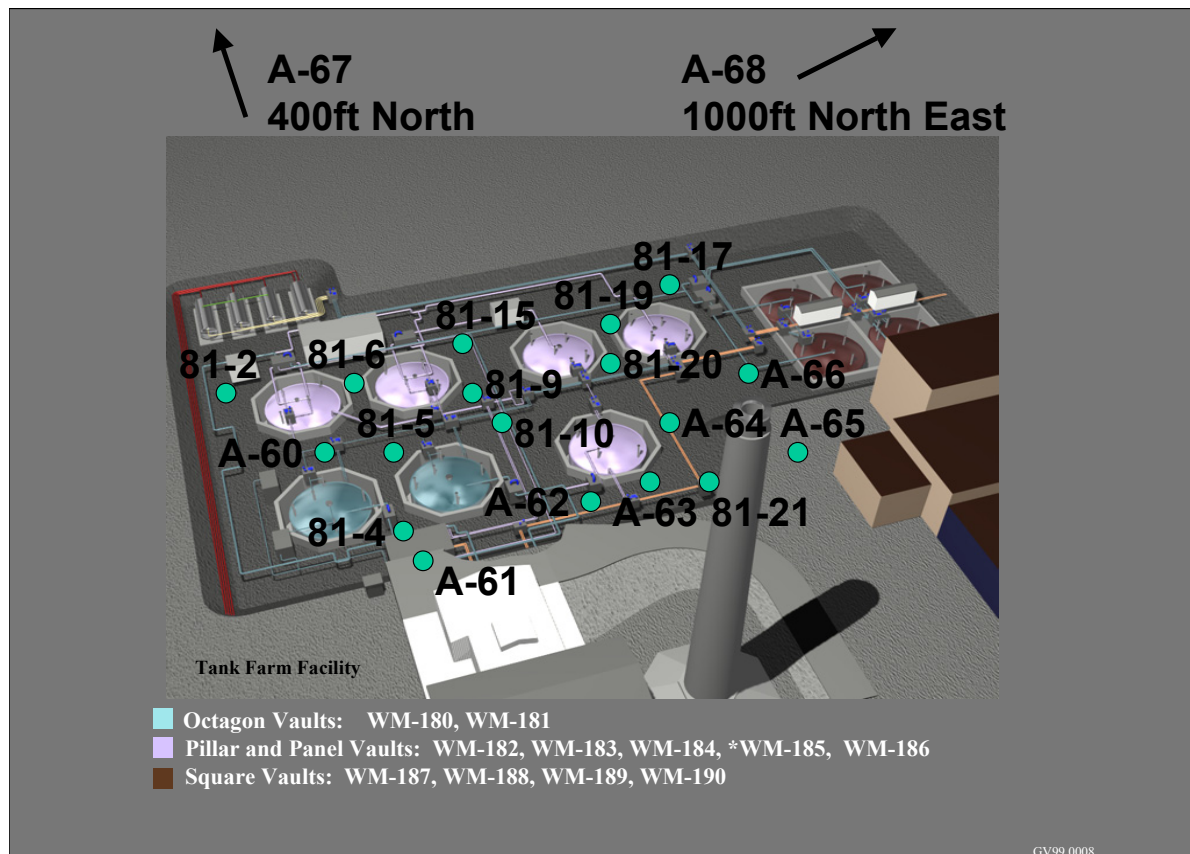


Figure B-1. Soil moisture monitoring locations.

B-3 NUMERICAL MODEL

B-3.1 Infiltration Mechanisms

Infiltration is the process by which surface water enters the soil. Redistribution is the process through which water from infiltration redistributes itself in response to gravity and capillary forces. The redistribution process will ultimately partition the infiltrated water into a three-part water balance. These parts consist of (a) surface losses that are due to evaporation and transpiration, (b) drainage that becomes aquifer recharge, and (c) storage that remains in the vadose zone.

When water is applied in relatively small amounts (i.e., at rates less than the soil's infiltration capacity), the water infiltrates as fast as it is applied, and the application rate controls the infiltration. However, as often is the case during spring snowmelt, application rates may exceed the soil's infiltration capacity, and the soil's hydraulic conductivity controls the infiltration rate after the initial soil wetting. During the initial wetting, the infiltration rate can be very large and may even exceed the saturated hydraulic conductivity. This large initial infiltration rate is due to the extremely large matric potential gradients between the dry soil ahead of the wetting front and the moist soil behind the wetting front. Eventually, the infiltration rate will decrease with time because of pore filling and eventually reach a steady-state rate near the soil's saturated hydraulic conductivity.

The partial differential equation governing unsaturated flow, including infiltration and redistribution, can be derived from the general mass conservation equation as originally performed by Richards (1931).

B-3.2 Selected Model

The UNSAT-H Version 3.01 computer code (Fayer 2000) was chosen for the simulations in this study because of its ability to model infiltration from meteorological conditions at semiarid locations. Specifically, the code has the ability to account for (a) liquid and vapor water movement, (b) heat transfer by conduction and convection, (c) evaporation at the soil surface, and (d) transpiration by plants. The UNSAT-H Version 1.0 code was verified and benchmarked by Baca and Magnuson (1990) and was successfully applied to simulate moisture transport at several semiarid locations (Baca et al. 1992, Magnuson 1993, Martian and Magnuson 1993, Martian 1995).

B-3.2.1 General Description

The UNSAT-H model is designed to simulate the dynamics of water movement through the vadose zone as a function of meteorologic conditions and soil hydraulic properties. UNSAT-H Version 3.0 is an enhanced version of UNSAT-H 1.0 and 2.0. Version 1.0 simulates the processes of infiltration, redistribution, drainage, and evapotranspiration and uses the potential evapotranspiration (PET) concept. Version 2.0 additionally includes options to calculate soil heat transfer coupled with water flow, surface-energy balance, and actual evaporation. Version 3.0 includes the following enhanced capabilities: hysteresis, the modified Picard solution technique, additional hydraulic functions, and multiple-year simulation capability.

The model is written in FORTRAN 77 and consists of three main programs: (1) DATAINH, a preprocessor; (2) UNSAT-H, the flow simulator; and (3) DATAOUT, a post-processor. For most problems, the model runs efficiently on a personal computer.

B-3.2.2 Theoretical Background

The UNSAT-H model solves an extended, one-dimensional form of Richards' equation, which includes both liquid- and vapor-phase water movement. The extended form of Richards' equation, as implemented in the model, is

$$C(h)\frac{\partial h}{\partial t} = \frac{\partial}{\partial z}\left[K_T(h)\frac{\partial h}{\partial z} + K_L(h)\right] - S(z, t) \quad (1)$$

where

- z = depth
- h = total head
- S(z,t) = evapotranspiration sink term
- K_T = total hydraulic conductivity; K_T=K_L+K_{vh}
- K_L = liquid conductivity
- K_{vh} = isothermal vapor conductivity
- C(h) = slope of soil moisture retention curve; $\partial\theta/\partial h$, where θ is volumetric moisture content.

The governing equations are solved using an iterative finite difference approximation with a Crank-Nicholson method for the time derivative or the modified Picard iteration scheme. The finite difference technique replaces the partial derivatives with a quotient of two finite differences. The end result of using finite differences is that the partial differential equation is approximated by a series of algebraic equations.

UNSAT-H permits the user to select several boundary conditions, including unit gradient, constant head, or specified flux. When the flux option is selected as the upper boundary condition, it is a function of meteorologic conditions that alternates between a flux and a constant head. Initially, during periods of infiltration or evaporation, the boundary is a flux. However, if the value at the surface node becomes less than a minimum suction head (saturated conditions) during infiltration, it becomes a constant (zero head); or, if the surface node exceeds a maximum value (unnaturally dry conditions) during evaporation, the upper boundary becomes a constant head, which is calculated internally from atmospheric relative humidity. The tank farm infiltration simulations used the atmospheric flux upper and unit gradient lower boundary conditions.

The surface evaporation rate can be calculated with an energy balance at the soil surface, if the heat transfer option is selected or by the PET concept. The PET is calculated from the daily weather parameter using the Penman equation. If the PET concept is used, the actual evaporation is restricted by the soil's unsaturated hydraulic conductivity and available soil moisture. The tank farm simulations were isothermal and used the PET concept. The Penman equation implemented in UNSAT-H is

$$PET = \frac{sR_{ni}}{s + \gamma} + \frac{\gamma}{s + \gamma} 0.27 \left(1 + \frac{U}{100}\right) (e_a - e_d) \quad (2)$$

where

- s = slope of the saturation vapor pressure-temperature curve, mb 1/K
- R_{ni} = isothermal net radiation, mm 1/d
- γ = psychometric constant, mb 1/K
- U = 24-hr wind run, km 1/d
- e_a = saturation vapor pressure at the mean air temperature, mb
- e_d = actual vapor pressure, mb.

The UNSAT-H model does not directly calculate runoff. However, if the flux of meteoric water into the surface exceeds the infiltration capacity, the upper boundary condition becomes a constant zero head value, and excess water is assumed to be lost to runoff.

To solve Richards' equation, the UNSAT-H code must be supplied with the following four basic components: soil hydraulic properties, computational grid, initial conditions, and boundary conditions. Each of these components is discussed in Sections 3.2.3 through 3.2.6, respectively.

B-3.2.3 Hydraulic Properties

Characterizing unsaturated flow requires three basic hydraulic properties for each material type identified in the simulation profile. These three properties are (a) the moisture characteristic curve, which is the relationship between the matric potential and moisture content; (b) the hydraulic conductivity curve, which is the relationship between the matric potential and the unsaturated hydraulic conductivity; and (c) the saturated hydraulic conductivity. The van Genuchten equations were used to represent these constitutive relationships. The equation for the moisture characteristic curve is

$$\theta = \theta_r + \frac{(\theta_s - \theta_r)}{[1 + (\alpha h)^n]^{1 - \frac{1}{n}}} \quad (3)$$

where

- h = suction head
- θ = volumetric moisture content
- θ_r = residual volumetric moisture content
- θ_s = porosity
- n = pore-size distribution index
- α = inverse air-entry potential.

The equation for the hydraulic conductivity curve is

$$K(h) = K_s \frac{\{1 - (\alpha h)^{n-1} [1 + (\alpha h)^n]^{1 - 1/n}\}^2}{[1 + (\alpha h)^n]^{l(1 - 1/n)}} \quad (4)$$

where

- K(h) = unsaturated hydraulic conductivity
- K_s = saturated hydraulic conductivity
- l = pore interaction term.

Although obtaining soil hydraulic properties is one of the final objectives of this study, initial estimates of these properties were needed before beginning the calibration process. Initial values for the surficial sediment hydrological properties were taken from the OU 3-13 Group 4 remedial work (DOE-ID 2003c). This work collected and performed laboratory testing of sediment samples during the Phase I drilling. The geometric average of the van Genuchten parameters determined from the laboratory testing was used for the initial sediment hydraulic properties. Although this is a simplistic method for estimating the average hydraulic properties because it does not consider correlation between each parameter, it was thought sufficient for providing a starting point for the calibration.

The hydraulic properties from DOE-ID (2003c) are summarized in Table B-2. The fractured basalt hydraulic properties were not adjusted during the model calibration and were taken from inverse modeling of an observed arrival of a wetting front in fractured basalt beneath the INL Site's Subsurface Disposal Area (Magnuson 2004). The basalt properties are presented in Table B-3.

Table B-2. INTEC alluvium unsaturated hydraulic properties from DOE-ID (2003c).

Well Name (ICPP-SCI-P-)	Depth (ft)	Unified Soil Class	In Situ Volumetric Moisture Content	Dry Bulk Density (g/cm ³)	Saturated Hydraulic Conductivity (cm/sec)	van Genutchen Alpha Parameter (1/cm)	van Genutchen N Parameter	Residual Volumetric Moisture Content	Saturated Moisture Content
216	33-34	GW-GM	0.066	1.8	4.80E-02	1.9868	1.2407	0.026	0.2555
216	34-35	GM	0.21	1.3	1.10E-01	1.2729	1.1024	1.00E-04	0.4198
226	10-10.5	GW-GM	0.117	2.01	6.90E-02	0.3126	1.2521	0.0256	0.2864
226	19-20	GP	0.097	2.16	7.40E-03	0.1123	1.5444	0.0516	0.2247
226	45-46	SM-SC	0.223	1.79	6.60E-07	0.0163	1.1881	1.00E-04	0.401
226	51-52	ML-CL	0.379	1.95	6.70E-08	0.0002	1.3428	1.00E-04	0.3851
248	10-10.5	GP	0.048	1.78	3.80E-02	0.1723	1.4687	0.0326	0.3321
248	18-18.5	GP-GM	0.053	1.68	4.70E-02	0.0467	2.0252	0.0602	0.3696
250	15-15.5	GW	0.062	1.7	8.00E-02	0.0124	2.3011	0.0316	0.2354
250	26-26.5	GP	0.095	1.67	1.00E-01	0.2086	1.3291	0.0144	0.3745
250	31-31.5	GP-GM	0.11	1.61	1.60E-02	0.3134	1.2618	0.0192	0.3923
251	19-19.5	GP	0.081	2	3.00E-02	0.0197	4.2289	0.0622	0.3142
251	19-19.5	GW	0.102	1.9	2.70E-02	0.123	1.327	0.0265	0.3477
251	30.5-31	GP-GM	0.103	1.82	1.70E-02	1.5208	1.1435	1.00E-04	0.2677
252	20-23	GP	0.087	1.89	5.60E-02	0.7955	1.2084	1.00E-04	0.321
252	26-27	GW	0.085	1.99	4.40E-02	0.0861	1.914	0.0642	0.2518
252	41-42.5	GP-GM	0.087	1.88	6.10E-02	0.159	1.5421	0.0432	0.2939
Geometric mean			0.101	1.81	0.00967	0.113	1.51	0.00617	0.316

Table B-3. Initial basalt hydraulic properties.

Parameter	Value
Saturated hydraulic cond. (cm/sec)	0.00029
Residual volumetric moisture content	0.00005
Saturated volumetric moisture content	0.05
van Genuchten Alpha parameter (1/cm)	0.1
van Genuchten N parameter	2.5

B-3.2.4 Computational Grid

The general model domain is a one-dimensional vertical column. Soil layer profiles were constructed from the observed December 1993 soil moisture profiles. The December 1993 observed soil moisture should represent near steady-state field capacity because the ground surface was frozen and moisture should not have entered the profile for approximately 6 weeks. The differences in the winter soil moisture should identify the different soil horizons, which have different hydraulic properties.

The computational grids were assigned to the simulation profiles using exponentially decreasing and increasing spacing moving towards and away from soil type boundaries, respectively. Exponential spacing at material interfaces places more nodes in areas where they are needed (i.e., at high-gradient areas at the surface due to evaporation or infiltration and high-gradient areas across interfaces due to different material types). The end result is to reduce pressure gradients across adjacent nodes and provide a more accurate solution.

B-3.2.5 Initial Conditions

For calibrating the tank farm soil hydraulic properties, initial matric potentials in the layers were directly estimated from the neutron probe measurements of moisture content using the moisture characteristics from the initial estimate of soil hydraulic properties. As the soil properties were adjusted during the calibration process, a new estimate of initial matric potential was calculated.

The method used to obtain initial conditions for the final 1954-2003 simulations was to select a time far enough in advance of the simulation period of interest so that the water profile in the surficial sediments would be in quasi-equilibrium with meteorologic conditions at the start of the simulation period. The starting time that was chosen for this purpose was January 1, 1950. This starting time allowed 3 years for this equilibrium to occur. The simulated moisture content did not significantly change after the third year, which indicated quasi-equilibrium condition was reached.

B-3.2.6 Boundary Conditions

The lower boundary condition was specified as a unit gradient (water movement across the bottom boundary layer is only influenced by gravity). The upper boundary, as implemented in the UNSAT-H code, can be either a specified flux or constant head as discussed in Section 3.2.2.

The UNSAT-H code requires daily records of meteorologic data in order to compute the upper boundary condition. These parameters are maximum and minimum air temperature, dewpoint temperature, solar radiation, average wind speed, average cloud cover, and daily precipitation. However, the cloud cover information is used only to calculate radiative heat losses at the soil surface when the heat transfer option has been selected and the tank farm infiltration simulations were isothermal.

The meteorologic data used in the infiltration simulations represented the period January 1, 1950, through December 31, 2003. The data were obtained from the National Oceanographic and Atmospheric

Administration (NOAA) weather stations located near or at the INL Site. The NOAA weather station located at the Central Facilities Area (CFA) provided most of the data until the INTEC weather station became operational in April 1993. However, solar radiation, cloud cover, and dewpoint information were not available from CFA from 1950 to 1993. There were also missing periods of average wind speed in the CFA weather data.

The average wind speed for the periods 1950-1954 and 1971-1981 were obtained from the NOAA weather station located at the Pocatello airport. The average dewpoint temperature for the period 1950-1986 was also from the Pocatello airport. Magnuson (1993) found a good correlation between weather parameters measured at the Pocatello airport and at the CFA. The missing solar radiation data were synthetically generated using the WGEN computer program (Richardson and Wright 1984). WGEN allows the synthetic data to be conditioned on observed precipitation and temperatures. Magnuson (1993) showed a high correlation between synthetic values generated with WGEN and measured values at a United States Geological Survey weather station adjacent to the SDA. The missing cloud cover information was not necessary because the UNSAT-H heat transfer option was not used.

The NOAA weather station near the INTEC collected most of the needed data after April 1993. However, a small amount of data was missing in INTEC weather data due to random equipment failure. Those missing data were extracted from the CFA weather station. If the data were missing in both the INTEC and CFA data sets, it was interpolated from previous and following values.

The precipitation amounts were modified during the winter months to account for snow accumulation and melting following the degree day method (Mockus 1972). This was necessary because the daily precipitation records collected at the NOAA weather station included all forms of precipitation including both rain and snow. The snowpack accumulated when the average temperature was below freezing and melted at the rate provided by the equation:

$$M = CD \quad (5)$$

where

- M = snowmelt rate (in./day)
- C = climatic condition constant (0.06)
- D = degree days (average temperature-32° F).

The results of this modification were to concentrate winter precipitation into a short period of snowmelt each spring. The observed and modified annual precipitation totals for the 1950-2003 calendar years are provided in Table B-4.

Table B-4. Annual INTEC precipitation totals for 1950 through 2003

Year	Precipitation Total (in.)	Precipitation Total Adjusted for Snowpack Accumulation and Melt (in.)
1950	4.9	4.4
1951	7.4	7.4
1952	5.6	5.7
1953	5.3	5.5
1954	7.4	7.4
1955	6.8	6.9
1956	5.8	5.8

Year	Precipitation Total (in.)	Precipitation Total Adjusted for Snowpack Accumulation and Melt (in.)
1957	12.3	12.3
1958	7.3	7.3
1959	8.0	7.1
1960	8.2	9.2
1961	10.0	9.7
1962	10.3	10.7
1963	14.4	13.4
1964	12.4	12.6
1965	9.0	9.6
1966	4.5	4.1
1967	8.4	8.0
1968	13.3	12.7
1969	8.1	9.4
1970	9.4	7.9
1971	10.9	10.6
1972	7.4	8.3
1973	10.2	10.0
1974	7.7	8.1
1975	9.4	10.0
1976	7.8	7.9
1977	6.1	5.9
1978	7.8	7.1
1979	8.1	8.7
1980	9.9	10.2
1981	9.5	8.5
1982	9.9	8.7
1983	11.0	12.0
1984	11.3	11.3
1985	9.6	8.9
1986	11.3	13.0
1987	8.0	7.7
1988	5.4	3.7
1989	6.9	8.4
1990	6.5	6.7
1991	8.6	8.7
1992	5.3	4.0
1993	9.8	10.9
1994	6.3	6.4
1995	12.1	12.1
1996	8.1	8.2

Year	Precipitation Total (in.)	Precipitation Total Adjusted for Snowpack Accumulation and Melt (in.)
1997	7.5	7.0
1998	9.8	10.1
1999	6.4	6.5
2000	6.3	6.0
2001	4.3	3.9
2002	4.3	4.8
2003	5.8	5.8
Average	8.3	8.3

When the ground surface is covered with snow, the snow prevents most evaporation from occurring by insulating the ground from wind and solar radiation. Additionally, as the ground freezes, the effective porosity and hydraulic conductivity can be reduced by any remaining moisture freezing in the soil pores. This further reduces evaporation by limiting the amount of soil moisture that can move toward the soil surface. The combination of the above processes effectively stops evapotranspiration during the winter season. To accurately simulate winter soil processes, the potential evapotranspiration was set to zero during the winter period.

The criteria for selecting the start of the winter period was the beginning of the first extended period in which the previous 5-day moving average temperature fell below freezing. The average temperature was calculated as the average of the maximum and minimum values. Conversely, the criteria for selecting the last day of the winter period was the day preceding the first period in which the 5-day moving average was above freezing. Table B-5 lists the periods when the potential was not set to zero for each simulation year.

Table B-5. Period of nonzero evapotranspiration by calendar year.

Year	First Day	Last Day	Year	First Day	Last Day
1950	77	335	1977	84	314
1951	82	337	1978	82	315
1952	98	309	1979	79	316
1953	69	322	1980	51	321
1954	83	332	1981	49	329
1955	97	305	1982	49	315
1956	80	318	1983	60	324
1957	55	313	1984	90	321
1958	50	318	1985	94	312
1959	78	316	1986	50	327
1960	83	310	1987	63	320
1961	73	307	1988	78	317
1962	84	321	1989	69	329
1963	51	322	1990	62	330
1964	93	317	1991	45	321
1965	67	329	1992	43	309

Year	First Day	Last Day	Year	First Day	Last Day
1966	84	338	1993	85	309
1967	77	325	1994	59	305
1968	60	318	1995	69	338
1969	89	321	1996	67	331
1970	82	317	1997	77	315
1971	83	301	1998	73	338
1972	66	321	1999	75	336
1973	94	325	2000	85	309
1974	73	328	2001	77	328
1975	97	315	2002	83	301
1976	78	318	2003	67	304

B-4 MODEL CALIBRATION

Model calibration is the trial-and-error process of adjusting input data until computed data match the field observations. The model calibration was evaluated by plotting simulated and observed data on a single plot, visually inspecting agreement, and calculating calibration statistics to ensure the visual inspections provided the best calibration achieved during the manual parameter adjustment process.

B-4.1 Evaluation Statistics

The moisture contents from the neutron probe measurements were used to evaluate how well the numerical model approximated the conditions in the field for each well simulated. Two statistics were chosen to measure the agreement between field data and simulation results. The first statistic was the root mean square (RMS) error; the second was the correlation coefficient.

The RMS error provides a good estimation of the average error throughout the two data sets and is defined by the equation

$$RMS = \frac{\sqrt{\sum_{i=1}^k (s_i - f_i)^2}}{k} \quad (6)$$

where

- f_i = field data point
- s_i = simulation data point
- k = number of comparison points.

The correlation coefficient measures the degree to which there is a linear correlation between corresponding field data and simulation results. It provides an estimate of how well the trends between the data sets agree (i.e., the shape of the data curve). The correlation coefficient is defined by the quantity

$$r = \frac{k \sum_{i=1}^k s_i f_i - \sum_{i=1}^k s_i \sum_{i=1}^k f_i}{\sqrt{\left[k \sum_{i=1}^k s_i^2 - \left(\sum_{i=1}^k s_i \right)^2 \right] \left[k \sum_{i=1}^k f_i^2 - \left(\sum_{i=1}^k f_i \right)^2 \right]}} \quad (7)$$

A perfectly linear relationship between data sets would result in a correlation coefficient of 1. At the other end of the scale, a correlation coefficient of 0 indicates that no correlation exists and the data sets are completely independent.

B-4.2 Calibration Parameters and Assumptions

The Well A-68 infiltration test suggests recharge events can quickly move through the alluvial soil and increased soil moisture does not persist for extended periods in the INTEC alluvium after infiltration events. For this reason, only the monitoring locations with monitoring dates including the early 1994 spring were simulated. Wells that were monitored only during the 1994 winter or 1994 summer were excluded from the simulations and calibration because they do not provide any information on the response in soil moisture to transient infiltration events resulting from snowmelt. The wells that were simulated included the two locations outside the tank farm: Wells A-67 and A-68, and the following wells within the tank farm: A-65, A-64, A-63, A-62, A-60, 81-02, 81-04, 81-05, 81-10, 81-15, 81-17, and 81-21. Most wells were monitored on five dates during the 1993-1994 monitoring season and included December 1993, January 1994, February or March 1994, April 1994, and May 1994. The model soil profiles were calibrated to all monitoring dates at each location.

The model calibration locations were divided into two infiltration regime areas. The first is for the area outside of the synthetic membrane cover. Evaporation was assumed to occur in this infiltration regime and the calibration parameters were limited to the soil hydraulic properties and modifying the snowpack to account for snow drifting or winter maintenance activities such as road plowing. Wells A-67 and A-68 were assumed to represent this infiltration regime. Well A-68 is located approximately 1,000 ft northeast of the tank farm and Well A-67 is located approximately 400 ft north of the tank farm. The second infiltration regime represented the area within the tank farm and under the synthetic membrane cover. This regime included the remaining A-series wells. Evaporation was assumed to not occur after the cover was installed. The model calibration parameters included the soil hydraulic properties, snowpack adjustment to account for drifting snow and winter maintenance, and precipitation adjustment to account for water redistribution over the membrane. The snowpack and precipitation were only adjusted if model agreement with the observed soil moisture could not be obtained from reasonable adjustment of soil hydraulic parameters alone.

The UNSAT-H model soil hydraulic parameters that were adjusted in the calibration process were the van Genuchten model parameters: saturated volumetric moisture content (θ_s), residual volumetric moisture content (θ_r), inverse air-entry potential (α), pore size distribution index (n), and saturated hydraulic conductivity (K_s). The amount of water available for infiltration through the tank farm soil was adjusted by multiplying the snowpack calculated by the degree day method and the nonfreezing precipitation events by different values if needed. This allowed sufficient flexibility in matching the infiltration pattern from snowmelt and precipitation not related to snowfall at locations under the membrane. The membrane is most likely redistributing infiltrate by focusing recharge through membrane cover breaches. Winter maintenance activities such as snow removal from roads and walkways and snow drifting around the tank farm structures may have redistributed the snowpack.

The precipitation adjustment for the two locations outside the tank farm only included adjustment of the snowpack because winter maintenance operations, such as road plowing and snow drifting, may have affected the snowpack at these two locations but should not have affected infiltration from nonsnowfall-related precipitation events. The nonsnowfall-related precipitation events almost never exceed the soil's infiltration capacity, but rapid spring snowmelt often results in overland flow and surface water redistribution at the INL Site. This is because the soil is often frozen when the snowpack melts and does not allow the water to infiltrate.

B-4.3 Calibration Results

The soil moisture content during the 1993-1994 monitoring period did not vary dramatically with time. This may be due to several reasons, including (1) the precipitation events at the semiarid INL are relatively rare, (2) the monitoring was infrequent (approximately 1/month), and (3) the alluvium is comprised of very permeable sandy gravel that can rapidly transmit water at a relatively low moisture content. However, increasing soil moisture resulting from snowmelt occurring near the end of February can be seen at most locations (see Figures B-2 through B-15).

The moisture content profiles obtained from the final calibration simulations generally showed good agreement with the field moisture content measurements. The average correlation coefficient between the simulated volumetric moisture contents and the field measurements varied between a high of 0.92 for Well 81-04 and a low of 0.35 for Well A-62. The average correlation coefficient for all wells was 0.65. The RMS error varied between 0.014 for Well A-60 and 0.006 for Well A-63. The average RMS error for all wells was 0.010. The calibration results for areas inside and outside the tank farm are presented next.

B-4.3.1 Inside Tank Farm Area

The calibration results for the wells located under the tank farm cover are summarized in Table B-6 and the simulated with observed volumetric moisture content for each monitoring date are illustrated in Figures B-2 through B-13. Appendix B-A provides the final hydraulic properties and soil layering. There were some significant differences between the observed and simulated moisture content at several wells. The problems and possible reasons for the differences are

- The observed moisture at Well 81-02 (see Figure B-2) indicates a significant spring snowmelt event occurred during January 28, 1994. The March 1, 1994, spring snowmelt calculated by the degree day method was not seen. It was not possible to match the observed early snowmelt event without adjusting the snowpack melt rate timing. Adjusting the snowmelt timing was not a calibration parameter and the magnitude of the March 1, 1994, snowmelt infiltration event was adjusted to match the observed January 28, 1994 event.
- It was not possible to match the transient behavior in the lower half of Well 81-10 (see Figure B-5). The observed soil moisture between the 500- to 700-cm depth decreased and the soil moisture from 700 to 800 cm increased during the month of May. The increase in soil moisture below 700 cm may be explained by a recharge event that was not seen higher in the profile because of the infrequent monitoring period or because of lateral flow not considered in the one-dimensional modeling. However, the decrease in soil moisture below that seen in December 1993 cannot be explained because the December 1993 measurement should represent steady-state field capacity soil moisture.
- An earlier-than-observed snowmelt event occurred in Well 81-21 (see Figure B-8). The moisture monitoring indicates an infiltration event occurred on January 28, 1994, which was much earlier than the snowmelt predicted by the degree day method on approximately March 1, 1994. Soil moisture for March 1, 1994, was not available for this location and it was uncertain whether the observed January 28, 1994, snowmelt event may have replaced the March 1, 1994, event. The snowmelt infiltration at this location was not adjusted because of the absent March data.

- Well A-60 appears to have evaporation occurring, which was not included in the tank farm cover infiltration regime assumption (see Figure B-9). Very little rainfall occurred during the period from early March through early April 1994 and the soil moisture near the surface continued to decrease below the winter moisture content. This suggests evaporation was drying the surface at this location.
- An earlier-than-observed snowmelt event was seen in Well A-65 on January 28, 1994 (see Figure B-13). The very moist conditions near the surface resulting from the March 1, 1994, snowmelt infiltration event could not be matched without losing good agreement lower in the profile at later dates. The calibration was judged complete with increasing the snowpack by a factor of five.

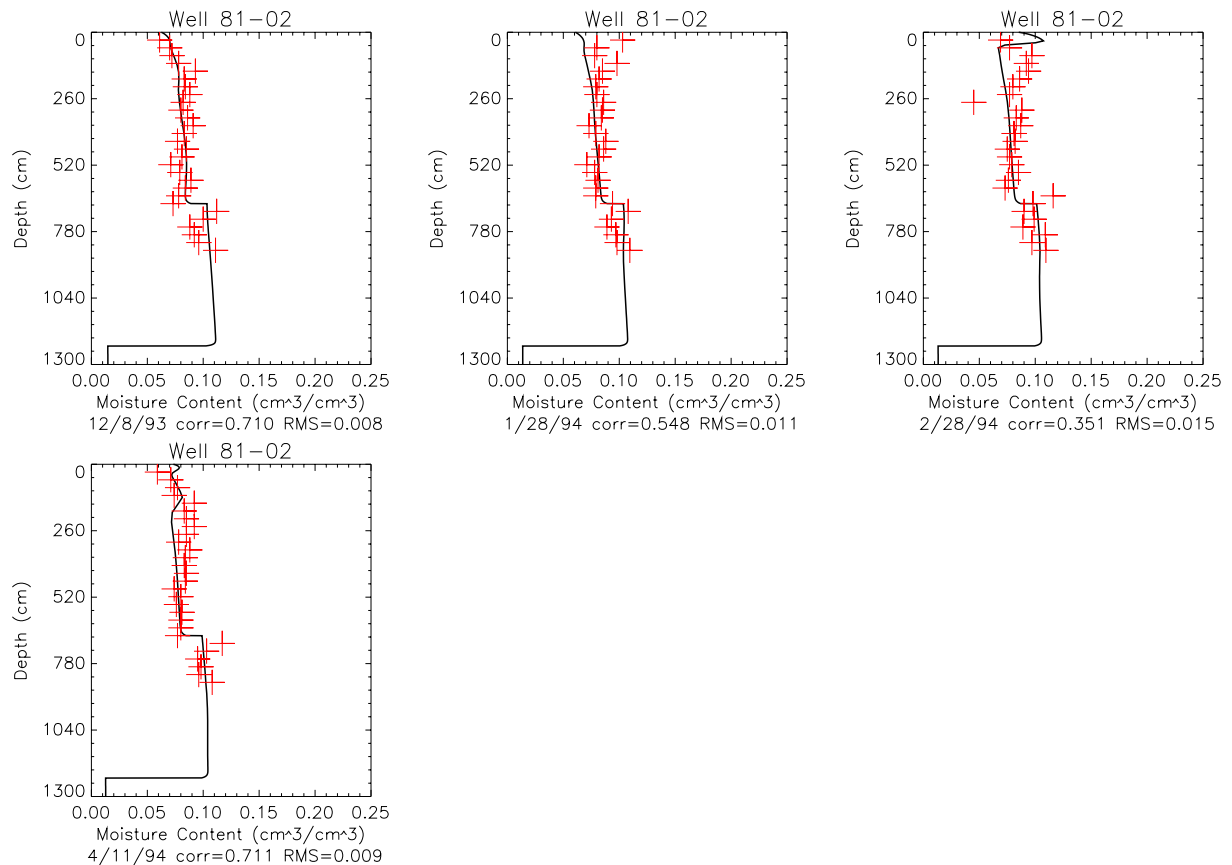


Figure B-2. Calibration results for Well 81-02. (Simulated volumetric moisture contents are solid lines and field volumetric moisture contents are crosses.)

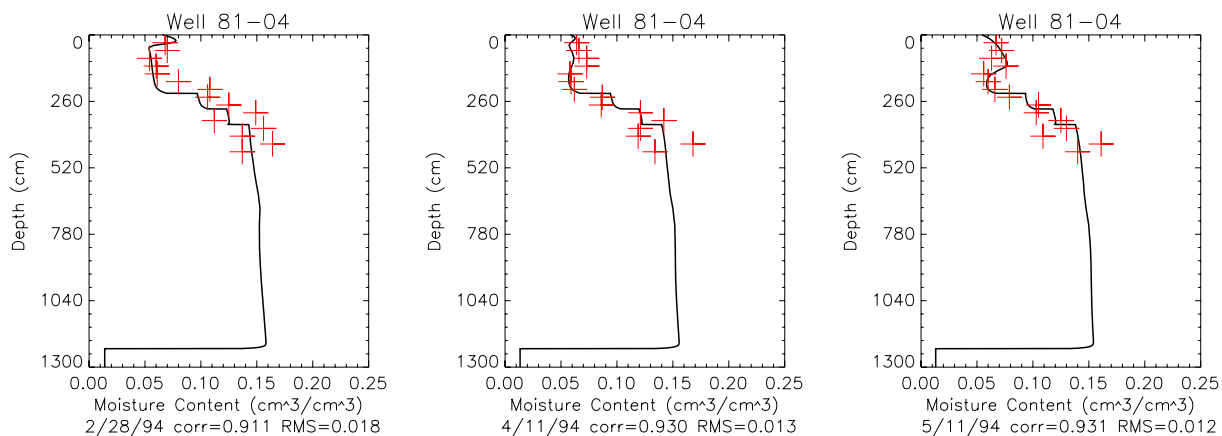


Figure B-3. Calibration results for Well 81-04. (Simulated volumetric moisture contents are solid lines and field volumetric moisture contents are crosses.)

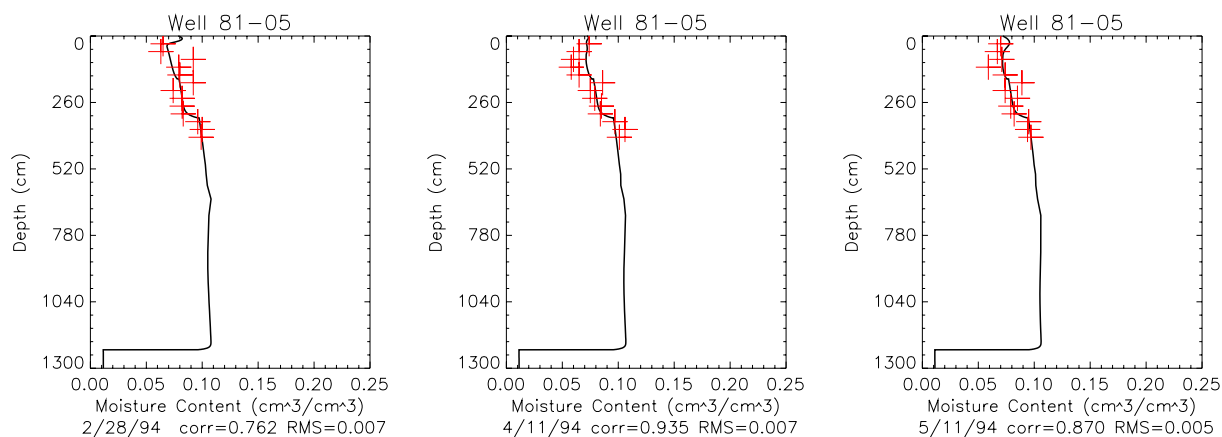


Figure B-4. Calibration results for Well 81-05. (Simulated volumetric moisture contents are solid lines and field volumetric moisture contents are crosses.)

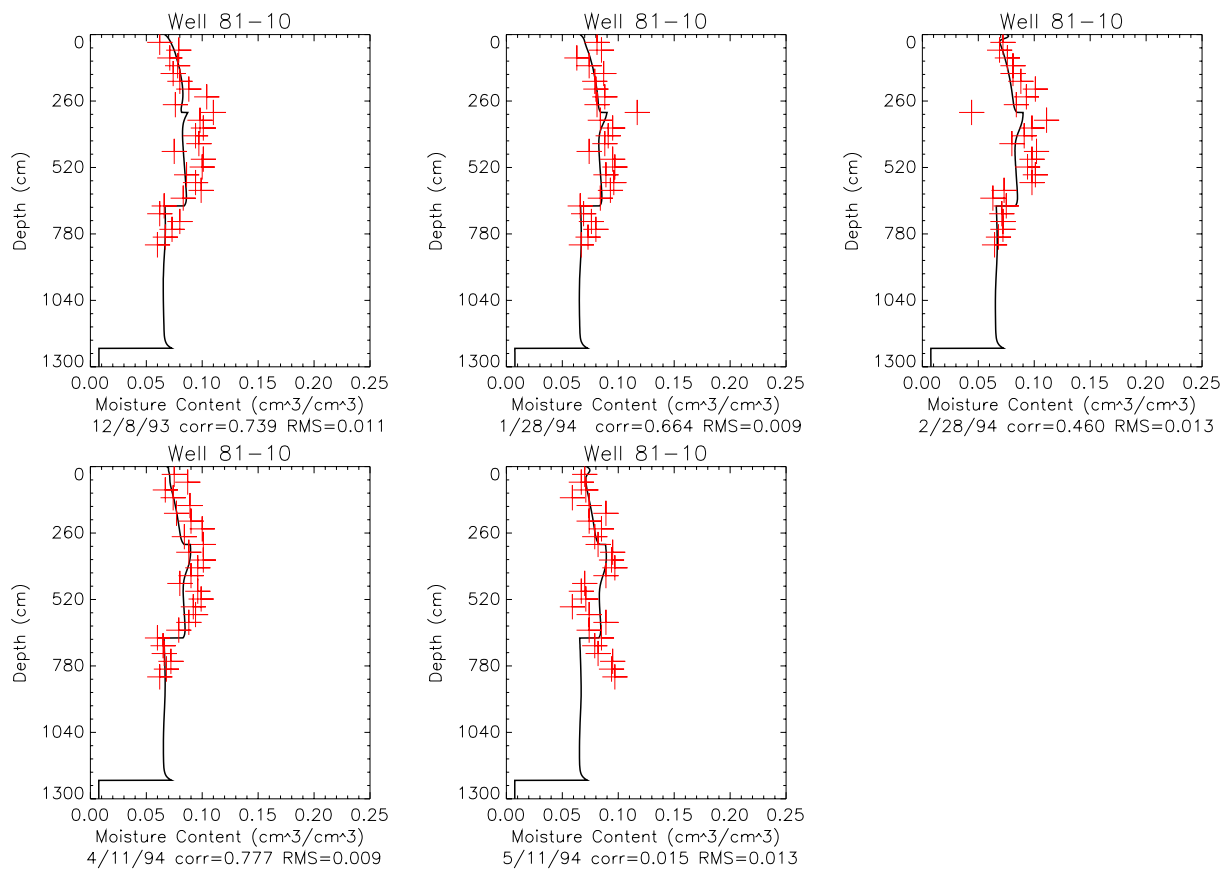


Figure B-5. Calibration results for Well 81-10. (Simulated volumetric moisture contents are solid lines and field volumetric moisture contents are crosses.)

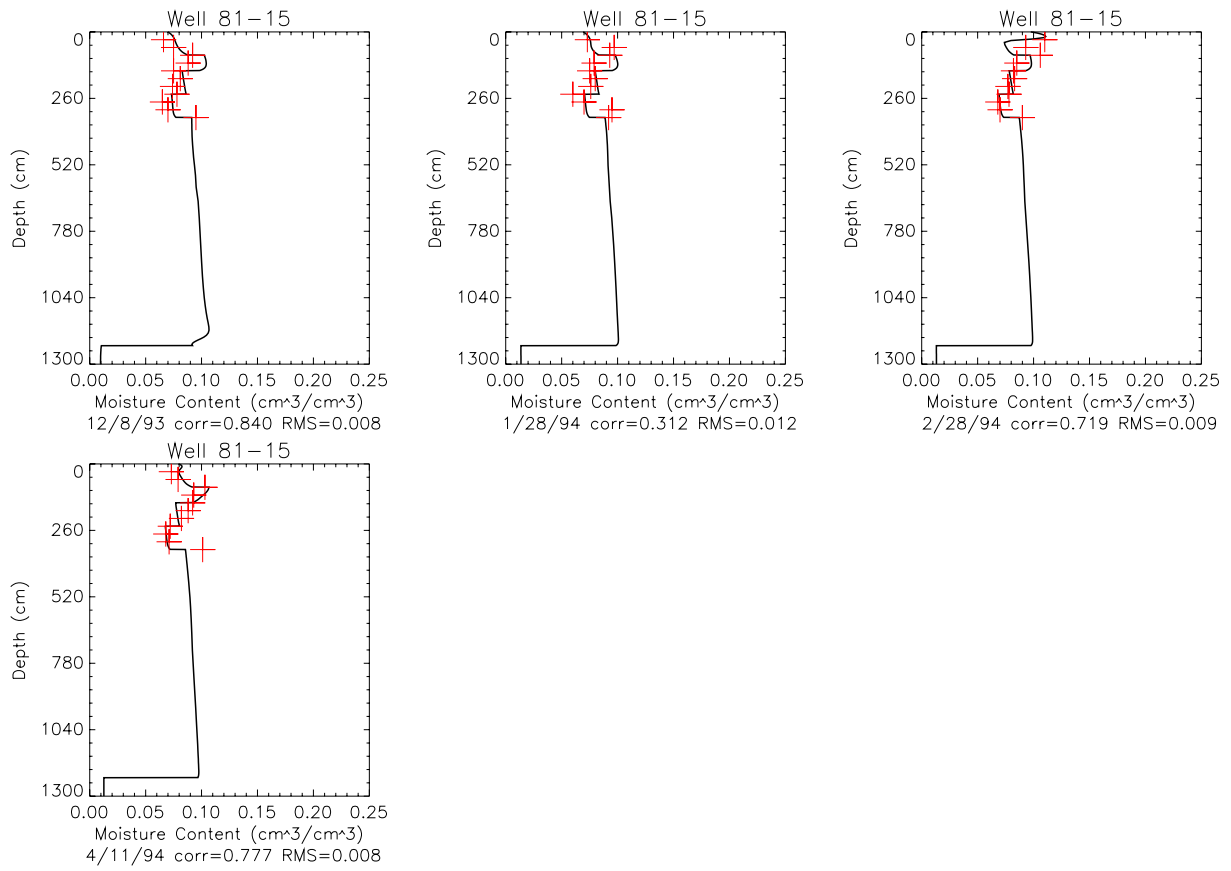


Figure B-6. Calibration results for Well 81-15. (Simulated volumetric moisture contents are solid lines and field volumetric moisture contents are crosses.)

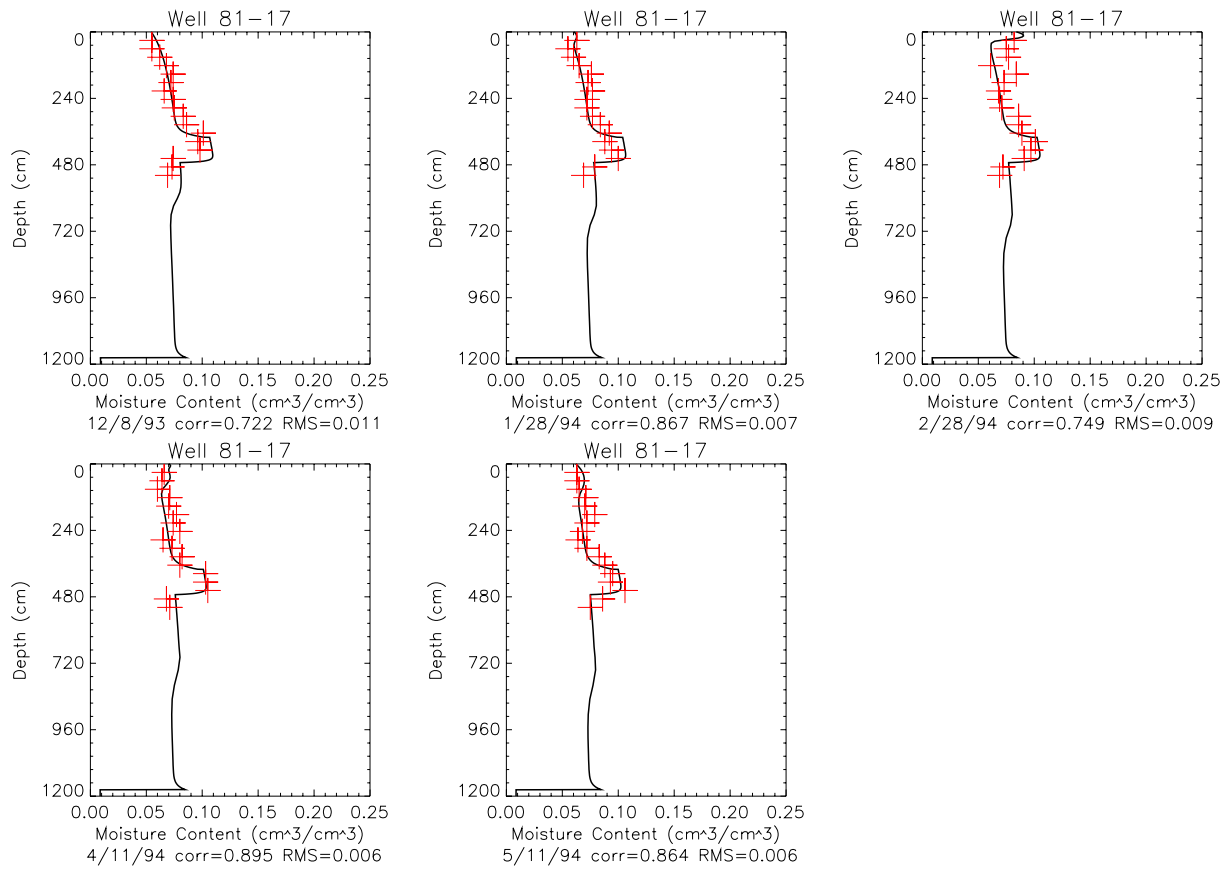


Figure B-7. Calibration results for Well 81-17. (Simulated volumetric moisture contents are solid lines and field volumetric moisture contents are crosses.)

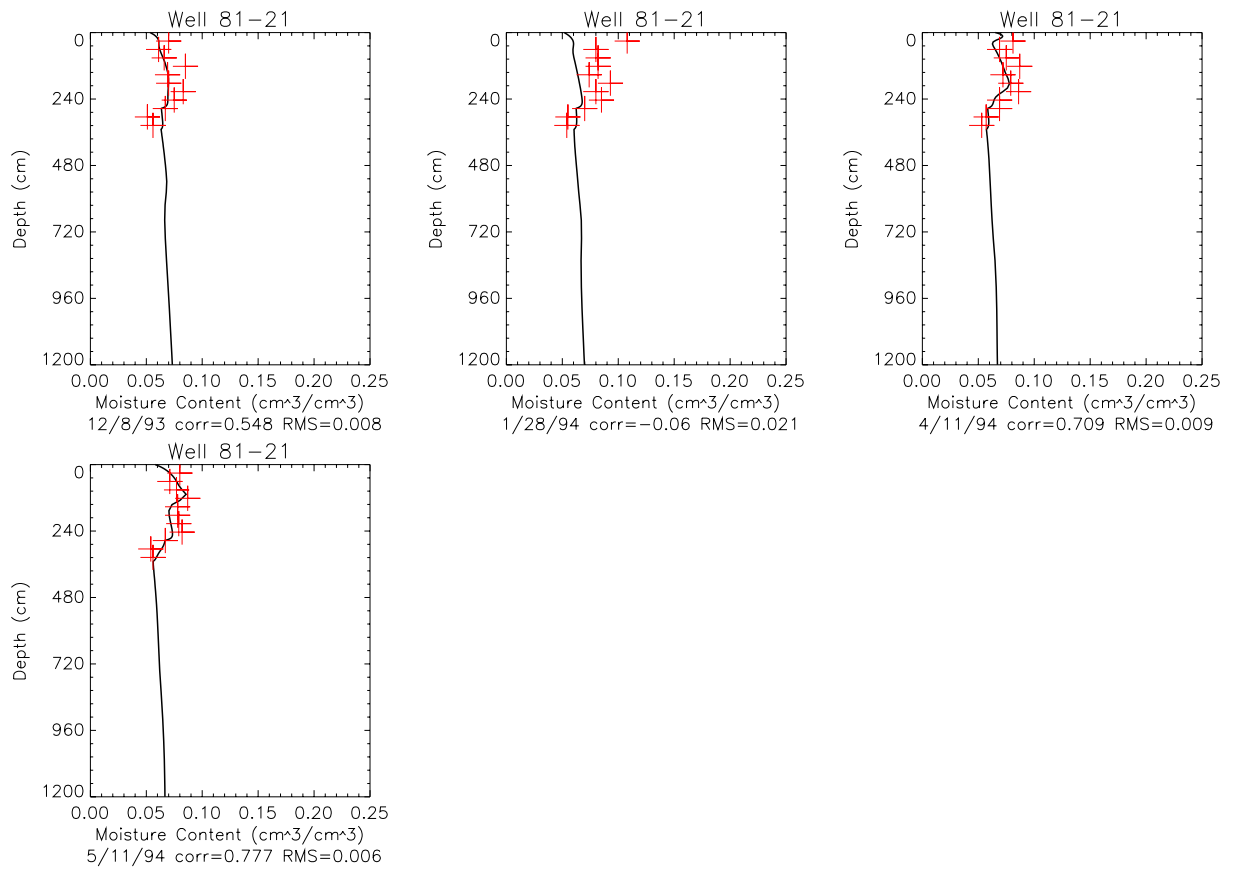


Figure B-8. Calibration results for Well 81-21. (Simulated volumetric moisture contents are solid lines and field volumetric moisture contents are crosses.)

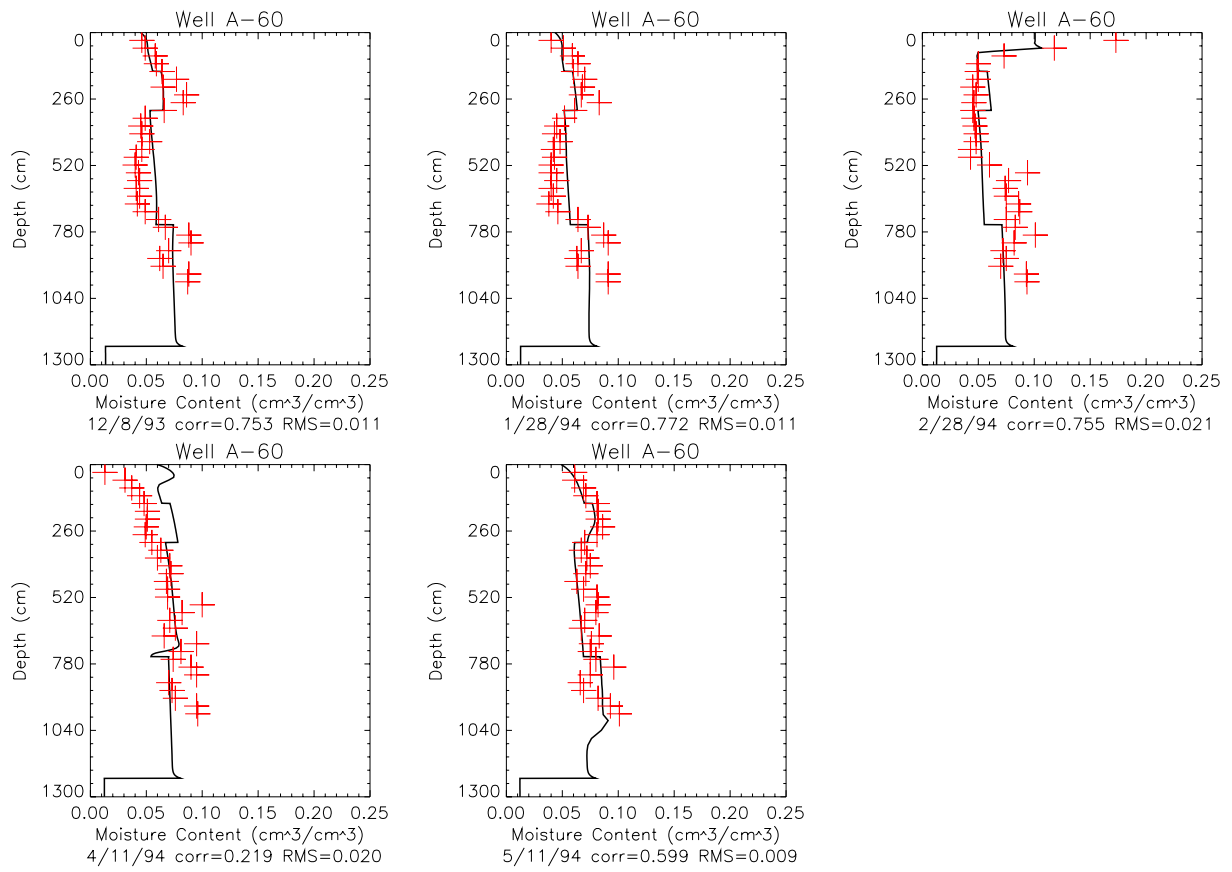


Figure B-9. Calibration results for Well A-60. (Simulated volumetric moisture contents are solid lines and field volumetric moisture contents are crosses.)

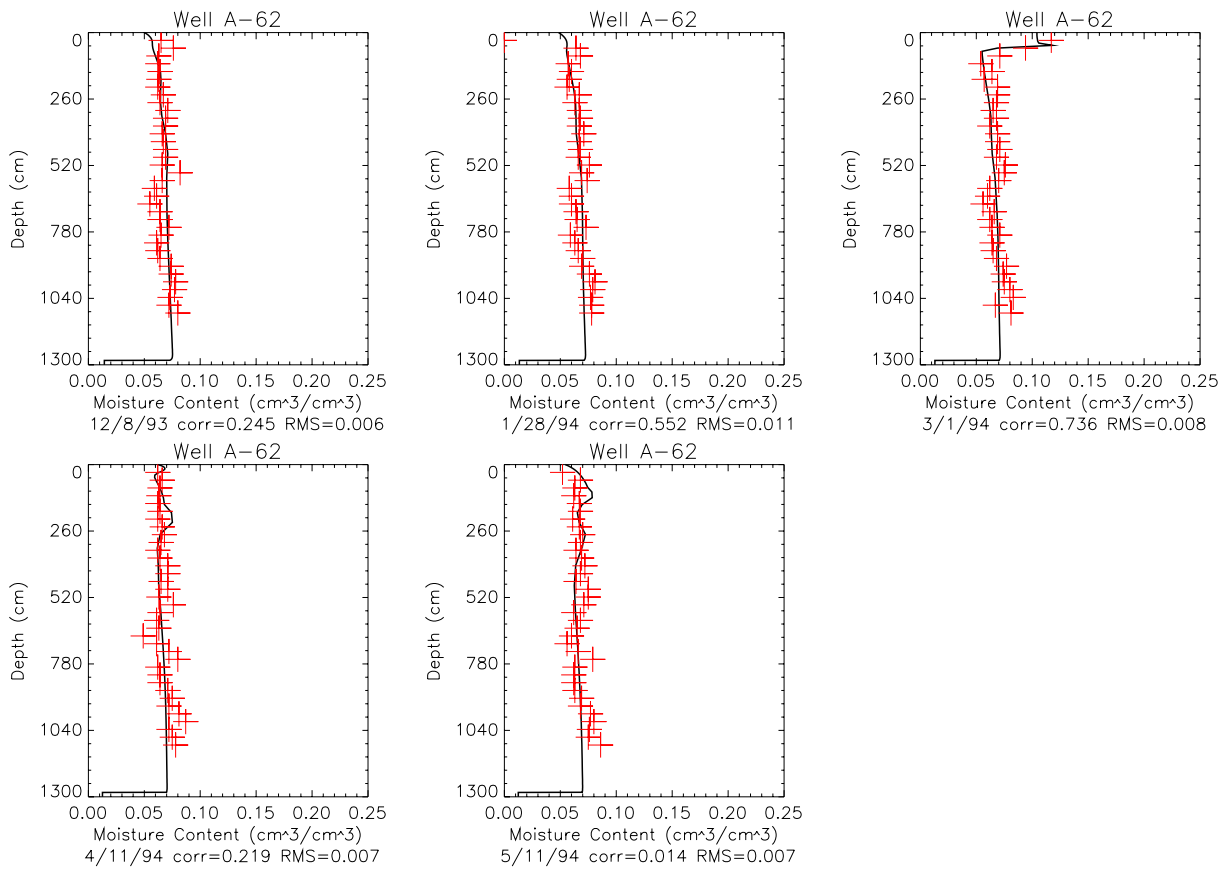


Figure B-10. Calibration results for Well A-62. (Simulated volumetric moisture contents are solid lines and field volumetric moisture contents are crosses.)

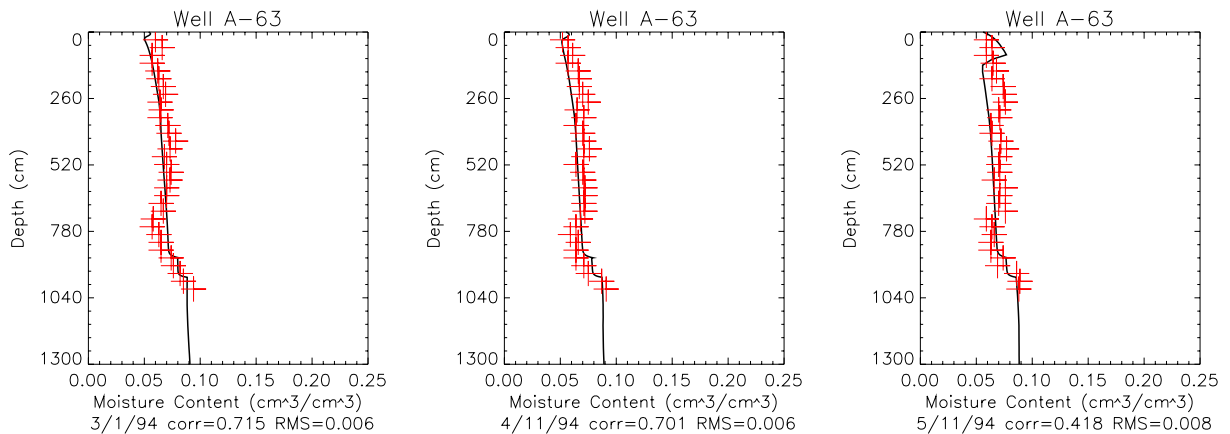


Figure B-11. Calibration results for Well A-63. (Simulated volumetric moisture contents are solid lines and field volumetric moisture contents are crosses.)

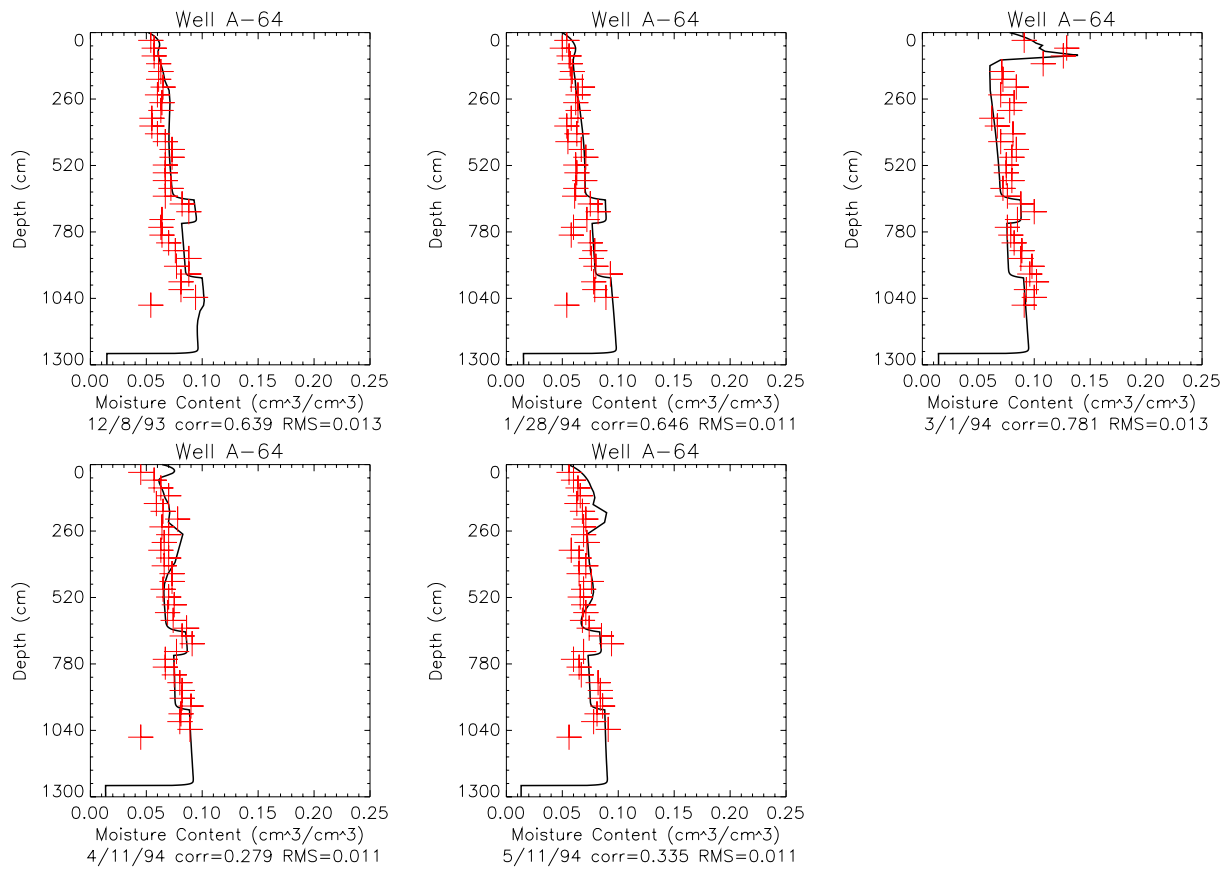


Figure B-12. Calibration results for Well A-64. (Simulated volumetric moisture contents are solid lines and field volumetric moisture contents are crosses.)

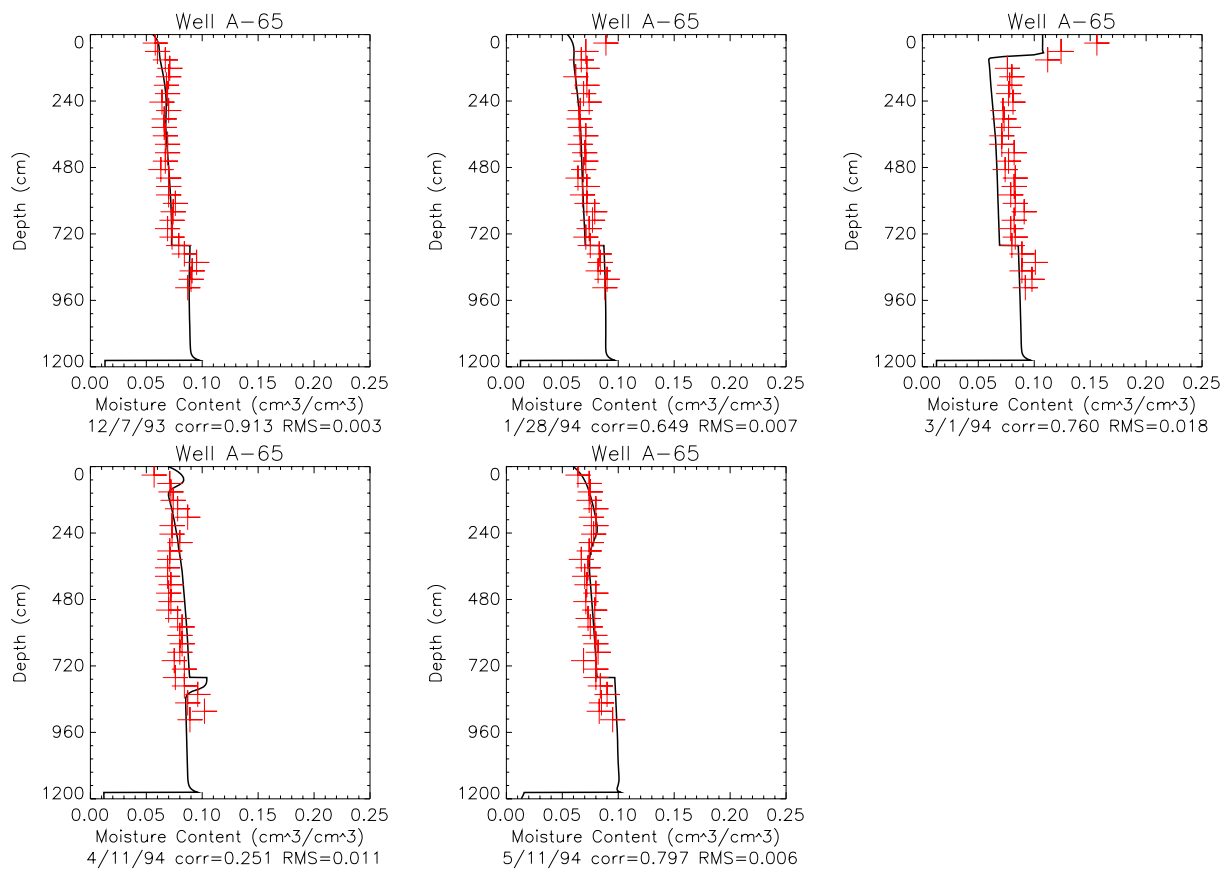


Figure B-13. Calibration results for Well A-65. (Simulated volumetric moisture contents are solid lines and field volumetric moisture contents are crosses.)

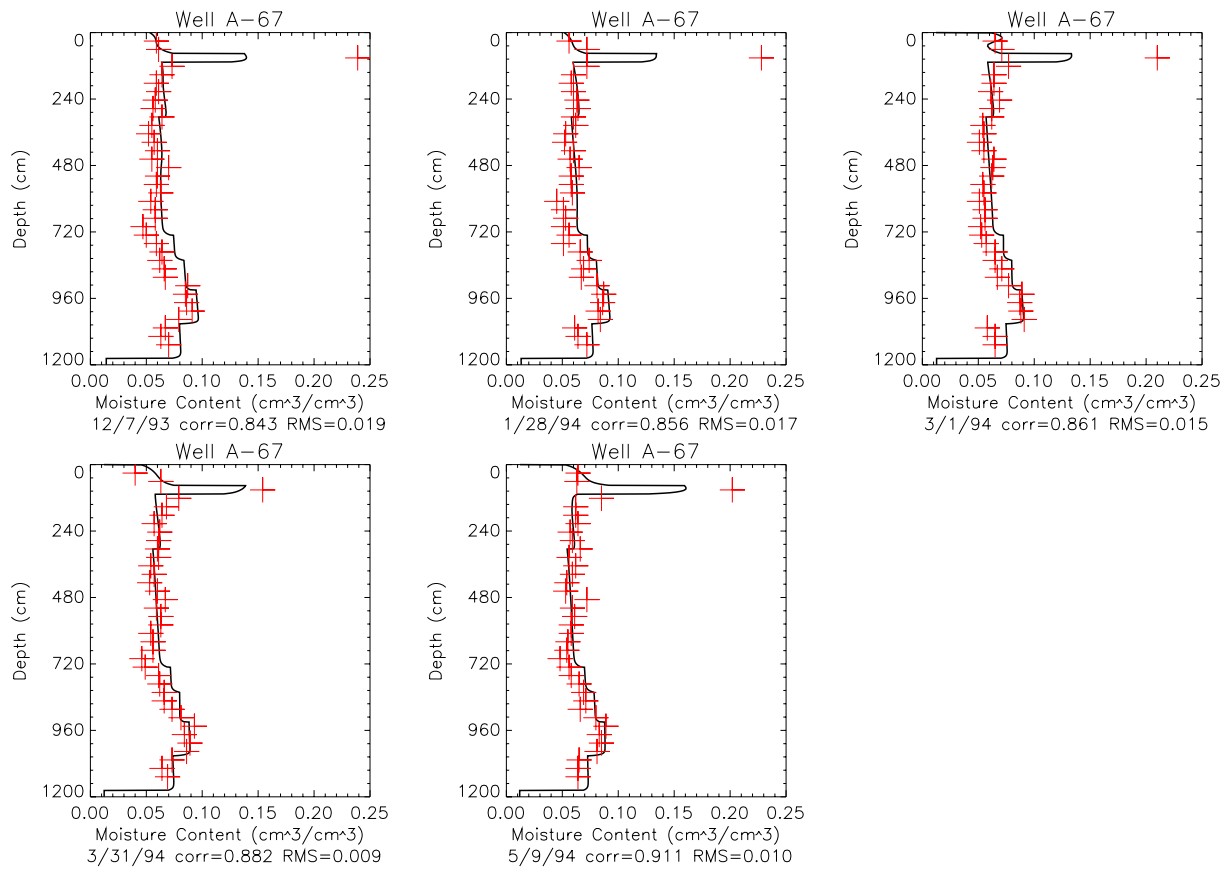


Figure B-14. Calibration results for Well A-67. (Simulated volumetric moisture contents are solid lines and field volumetric moisture contents are crosses.)

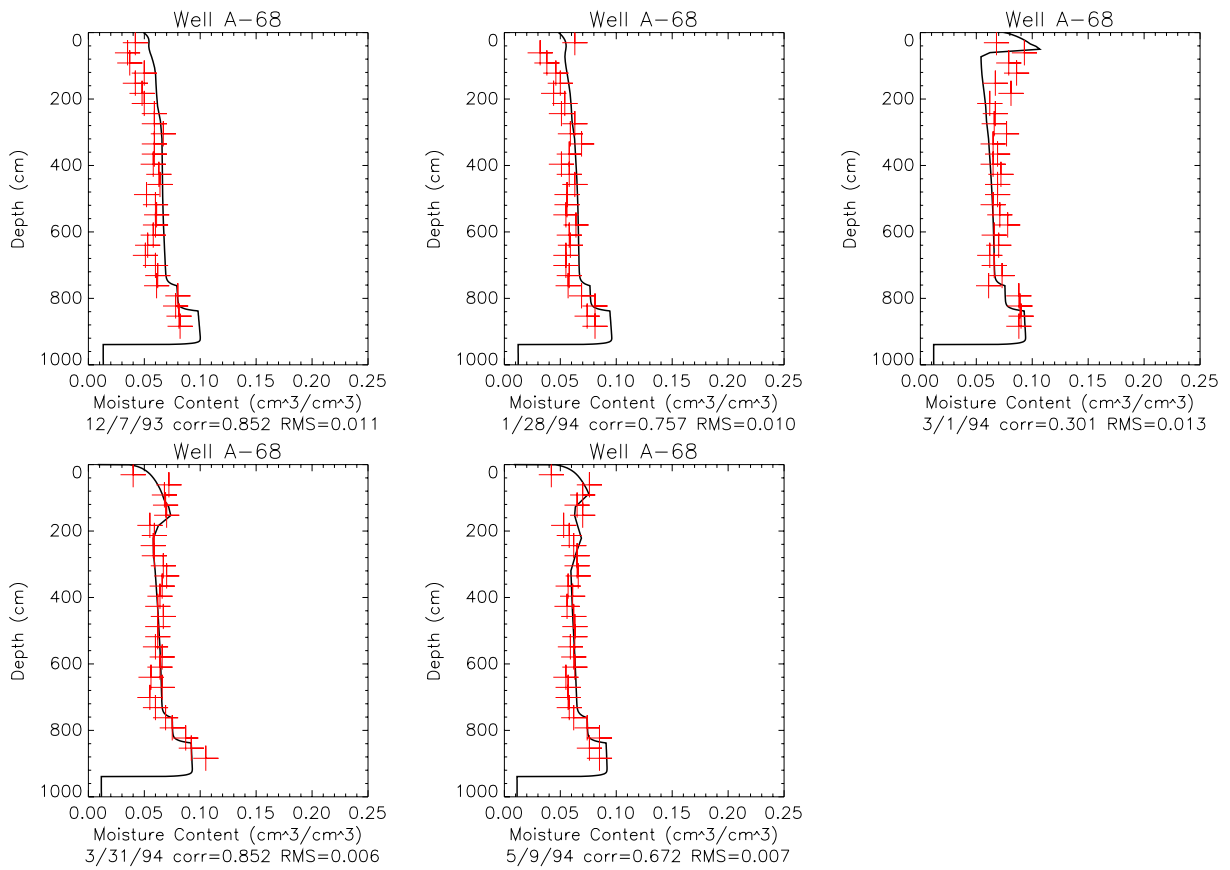


Figure B-15. Calibration results for Well A-68. (Simulated volumetric moisture contents are solid lines and field volumetric moisture contents are crosses.)

Table B-6. Calibration summary for wells located under the tank farm cover.

Well	Nonsnowpack Precipitation Multiplier	Snowpack Multiplier	Average Correlation Coefficient	Average RMS Error
81-02	1.	0.7	0.58	0.011
81-04	1.	0.4	0.92	0.014
81-05	0.2	0.2	0.86	0.006
81-10	0.1	0.1	0.53	0.011
81-15	0.5	0.5	0.67	0.009
81-17	0.	0.4	0.82	0.0078
81-21	1.	1.	0.49	0.011
A-60	1.	5.	0.62	0.014
A-62	1.	1.2	0.35	0.008
A-63	1.	0.	0.61	0.006
A-64	1.	2.	0.54	0.012
A-65	1.	5.	0.69	0.009

B-4.3.2 Outside Tank Farm Cover Area

The calibration results for the wells located under the tank farm cover are summarized in Table B-7 and illustrated in Figures B-14 and B-15. The observed soil moisture in Well A-67 (see Figure B-14) indicated the soil moisture at 91 cm below land surface was much higher than at all other depths. The high soil moisture suggests a finer material is present at this depth. However, the driller's log did not identify a distinct layer at this depth and specified the material as structureless well-graded gravel to well-graded sand through the profile. The calibrated model used finer soil hydraulic properties at this depth but did not attempt to match the very moist conditions at this depth because the observed soil moisture did respond to the infiltration pattern as expected. The observed soil moisture was highest during the winter and decreased with the spring snowmelt at this depth.

Table B-7. Calibration summary for wells located outside of the tank farm cover.

Well	Nonsnowpack Precipitation Multiplier	Snowpack Multiplier	Average Correlation Coefficient	Average RMS Error
A-67	1.	0.3	0.87	0.014
A-68	1.	1.	0.69	0.009

B-5 FINAL SIMULATIONS

The time period for the final simulations began in 1954, when the first tank was put in service, and extended through 2003. The final simulations represent two infiltration regimes for the wells located under the tank farm membrane and a single regime outside the tank farm. The infiltrate redistribution effect of the membrane, which was mimicked by adjusting the precipitation and snowpack, was not included in the premembrane period from 1954 through 1977. Evaporation was also simulated during this period. The final simulations for the two locations outside the tank farm did not include adjusting the snowpack because the simulations were performed to estimate the overall areal average recharge rate occurring outside the tank farm.

B-5.1 Simulation Results

The simulation results for the 1954-2003 period indicate that net infiltration through the alluvium is generally seasonal with most infiltration occurring during the spring snowmelt and spring rain. The drainage into basalt abruptly increases in the late spring or early summer as spring infiltrate exits the alluvium and enters the basalt. The low-magnitude infiltration events are dampened into a nearly constant baseline recharge and high-magnitude seasonal infiltration events from spring snowmelt, and rainstorms persist as discrete events down to the basalt interface. This can be seen in Figure B-16, which illustrates the daily infiltration and daily drainage into the basalt at Well A-68 for the years 1991 through 1995. The daily infiltration, daily drainage, and annual average drainage for all simulated well locations can be seen in Appendix B-B.

The amount of water that drains into the basalt is a good estimate of aquifer recharge because this water has almost no chance of returning to the surface via evapotranspiration. This is primarily due to the depth of the alluvium/basalt interface and the different soil moisture characteristics between the sediments and the basalts. The fractured basalt typically retains much less water and creates a capillary break at the interface.

The average annual INTEC precipitation for the period 1950 through 2003 was 21.1 cm. The average simulated annual drainage into the basalt at all locations inside or outside the tank farm was 18.4 cm, which is 87% of the average total precipitation. This high recharge estimate can be partly explained by the physical setting of the INTEC tank farm. The alluvial soil is gravelly sand, and vegetation does not exist within the tank farm. Construction activities may have increased the net infiltration rate by removing any natural soil horizons that could reduce the vertical permeability and hold moisture near the surface to more easily allow evaporation.

The tank farm cover appears to magnify infiltration events at some locations and reduce infiltration at other locations but may not significantly change the overall recharge rate. Wells A-65, A-64, and A-60 indicated a large recharge event occurred in the spring and the simulations required significantly increasing the snowpack to match the observed moisture content. Wells A-63, 81-17, 81-15, 81-10, 81-05, and 81-04 did not see the high-magnitude spring infiltration events and the snowpack was decreased. The average annual net simulated infiltration prior to installing the cover (1954-1976) was 18.7 cm and the average annual net infiltration after installing the cover was 18.3 cm. Table B-8 summarizes average annual drainage into basalt at each well location. Appendix B-B provides the annual drainage at each well over the simulation period (1954-2003).

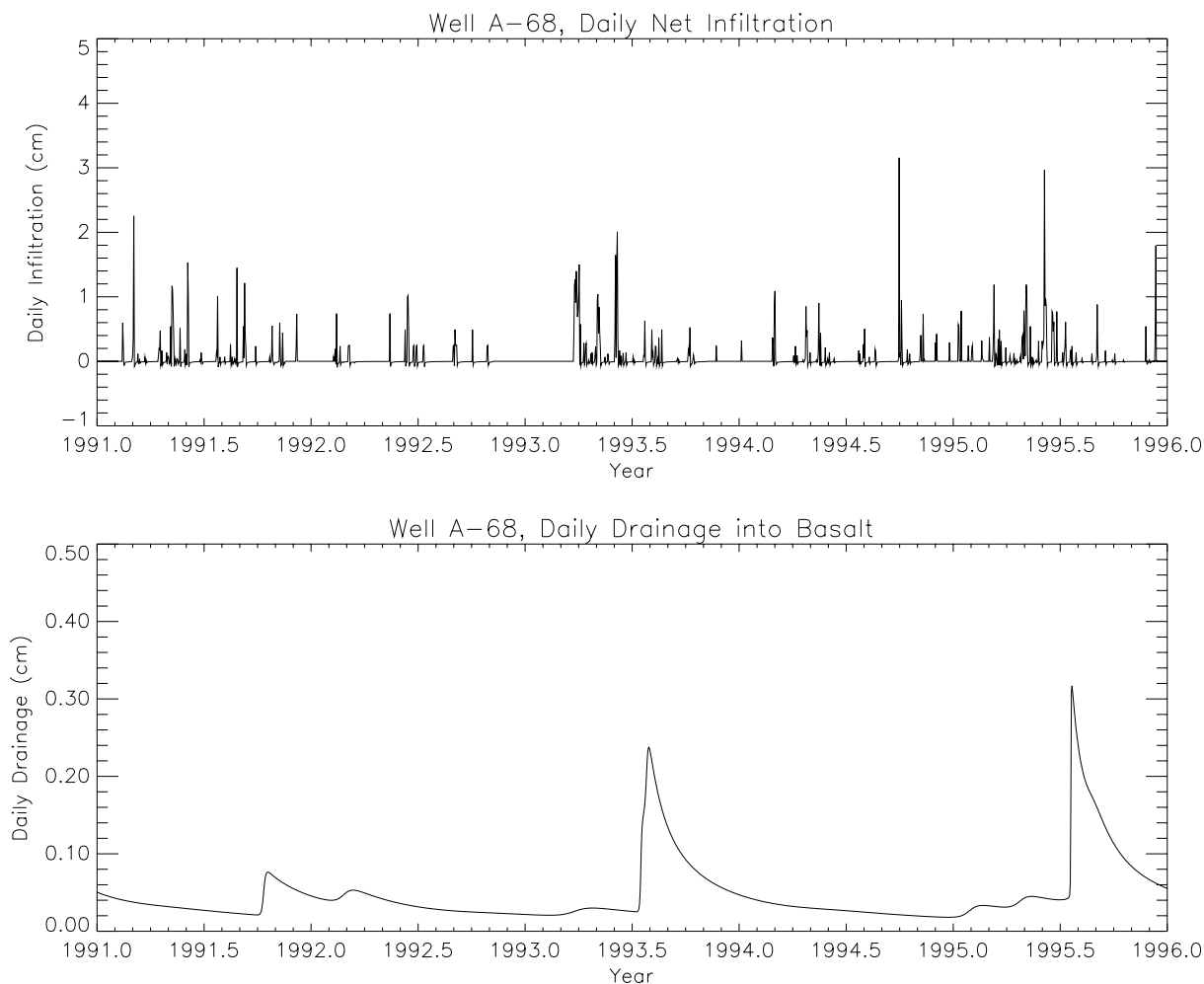


Figure B-16. Daily simulated infiltration, daily drainage, and annual average drainage at Well A-68.

Table B-8. Simulated average annual drainage into basalt.

Well	1954-1976 Average Annual Drainage (cm)	1977-2003 Average Annual Drainage (cm)	1954-2003 Average Annual Drainage (cm)
81-02	19.0	18.9	18.9
81-04	19.6	17.5	18.5
81-05	17.1	4.9	10.5
81-10	18.1	3.0	10.0
81-15	17.8	10.5	13.9
81-17	17.6	2.8	9.6
81-21	19.9	20.4	20.2
A-60	19.1	39.7	30.2
A-62	19.7	21.5	20.7
A-63	17.5	15.6	17.5
A-64	19.7	25.2	22.7
A-65	19.0	39.6	30.2
A-67 (outside tank farm)	18.5	17.3	17.3
A-68 (outside tank farm)	19.2	16.6	17.8

B-6 EVALUATION OF ALTERNATE INTEC ALLUVIUM SOIL MOISTURE DATA

There are two additional sources of INTEC alluvium moisture data, which could not be used to estimate the net infiltration through the INTEC alluvial sediments because the data were thought to be unreliable. These are neutron probe readings taken in the monitoring well (MW) series wells located outside of the tank farm and the tensiometer readings from the recent wells drilled during the Group 4 remedial work presented in the *Phase I Monitoring Well and Tracer Study Report for Operable Unit 3-13, Group 4, Perched Water* (MWTS report) (DOE-ID 2003c). The data and evaluation of the data for estimating net infiltration are discussed in this section.

B-6.1 Evaluation of MW Series Well Data

Neutron probe soil moisture readings were taken in the MW series wells during the same timeframe as the INTEC tank farm A- and 81- series alluvium well readings. Specifically, Wells MW-3, -7, -8, -9, -11, and -12 were monitored five times during the late winter 1993 through spring 1994. Many of these wells extended far below the alluvium and were logged to the well bottom, but only the alluvium soil moisture readings were of interest for estimating infiltration. Inspection of the reported volumetric moisture contents indicates soil moisture was often above 30% and rarely lower than 20%. These soil moisture readings were much higher than readings within the tank farm and laboratory analysis of cores collected during the Group 4 remedial work. Well logs for the MW- series wells suggested the alluvial material is not significantly different from that in the tank farm and the high soil moisture readings were most likely the result of the MW- series well construction. The MW- series wells used the same casing as the tank farm wells, but the well annular space was sealed with bentonite. The high soil moisture most likely represents water held in the bentonite backfill and not the alluvium.

The artificially higher soil moisture readings and possible nonuniform distribution of bentonite with depth, due to placing more bentonite in borehole collapse areas than other areas, make the data unsuitable for estimating infiltration. This is because of the following three reasons: (1) actual soil moisture cannot be

inferred from the readings because the probe was not calibrated to bentonite-sealed wells, (2) areas with additional bentonite may appear as soil horizons of different material, and (3) the bentonite will always retain a large amount of water as to remain near saturation and may not indicate the presence of a wetting front moving down and around the well casing.

B-6.2 Evaluation of the MWTS Report Data

The MWTS report presents the most recent well drilling and data collection activities within the INTEC fenceline (DOE-ID 2003c). Five vadose zone monitoring systems (21 wells) ranging from alluvium boreholes to aquifer wells were drilled and installed between November 16, 2000, and March 30, 2001. One of the main reasons for constructing these well sets was to obtain subsurface data to evaluate the hydrologic connection between recharge sources and the perched water bodies that lie beneath the INTEC. The five monitoring systems constructed for this purpose were identified as (1) Big Lost River (BLR) set, (2) Sewage Treatment Lagoon (STL) set, (3) Tank Farm (TF) set, (4) Central Set (CS), and (5) Percolation Pond (PP) set. Each set contained well completions in the alluvium, shallow perched, and deep perched zones. One monitoring well (the TF-Aquifer well, a.k.a., ICPP-MON-A-230) was completed into the SRPA. Each well set was equipped with tensiometers, lysimeters, and temperature sensors in the well completion intervals. A detailed description of the instrumentation, well locations, and well installation can be found in the MWTS report. A summary of the MWTS report alluvium tensiometers is presented in Table B-9.

Table B-9. INTEC alluvium tensiometer reading summary.

Tensiometer	Depth (ft bgs)	Average Reading (August 2001 to June 2002)	Comments
PP-AL	27.4	Positive to slightly negative pressure head	Mostly saturated conditions indicated
CS-AL	41.5	Consistently steady at ~+15 cm until March 2002	Always saturated conditions indicated
TF-AL	35.0	Relatively steady at ~+20 cm	Always saturated conditions indicated
STL-AL	26.5	Consistently steady at ~-40 cm	Always unsaturated conditions reported with two short periods of -100 cm during August 2001
BLR-AL	32.9	Consistently steady at ~+20 cm	Always saturated conditions indicated

All the alluvium tensiometer readings, except STL-AL, indicated a positive pressure head, i.e., saturated conditions. However, laboratory analysis of core samples taken from the alluvium wells indicated volumetric moisture contents in the range of 10% at most locations. These data indicate the tensiometers may not be working properly or they represent conditions only at the bottom of the alluvium. Water may be perching on the basalt/alluvium interface and the readings do not represent average conditions higher in the alluvium. Although the STL-AL tensiometer was indicating unsaturated conditions, it is still suspect because the reading was nearly constant throughout the year and less negative than expected. The tensiometer may not be working properly because the spring snowmelt event was not observed and the tension reading was lower than expected. A simple check data was performed on the STL-AL reading by calculating the volumetric moisture content using the tensiometer reading and the moisture characteristic curve obtained from laboratory analysis of core taken near this location (see Table B-2 and Well ICPP-SCI-P-251 for the STL-AL location van Genuchten parameters). Three core samples were analyzed in the laboratory from different depths from the STL well set. These cores were taken from 19-19.5 ft and 30.5-31 ft bgs. The calculated volumetric moisture content was 0.26, 0.21, and 0.14 at the reported tension. The absence of seasonal trends in the reported tension

and higher-than-expected moisture content at the indicated tension suggest the STL-AL tensiometer may not be working properly and should not be used to estimate infiltration rate.

B-7 MODEL SENSITIVITY TO SOIL HYDRAULIC PROPERTIES

The model sensitivity to hydraulic properties was evaluated to estimate a possible range in INTEC recharge from the range of measured alluvium hydraulic properties. This sensitivity study was performed to bound the possible recharge across the entire INTEC because the MW- series wells moisture content and alluvium tensiometer soil tension data collected outside the tank farm at the INTEC facility are unreliable and could not be used to estimate the net infiltration (see Section B-6).

The UNSAT-H software was used to construct one-dimensional simulation profiles of the INTEC alluvium and first few meters of basalt using the alluvium hydraulic properties measured from INTEC core samples. Each simulation profile used only one soil type for alluvium and the simulations were run for 50 years using the INTEC weather data discussed in Section 3.2.6. Well logs from the INTEC indicate the average alluvium thickness in the northern INTEC is approximately 40 ft and all the sensitivity simulations used this thickness and only two material types: (1) homogeneous alluvium parameterized from the laboratory core sample analysis and (2) fractured basalt. The fractured basalt properties were the same as those in the tank farm simulations. Each profile's initial conditions were determined from simulating the 50 years of weather data before beginning the final simulations. The 50-year initialization time period gave each profile sufficient time to reach quasi-equilibrium with meteorologic conditions at the start of the actual simulation period. The boundary conditions and the meteorologic data that were used in the sensitivity simulations are the same as those presented in Section B-3.2.6.

The classification of soil present in the INTEC alluvium cores ranged from silt/clay to gravel, and the measured hydraulic properties reflect a large variability in hydraulic properties. The saturated hydraulic conductivity measurements ranged from 6.7E-8 cm/sec from 51 ft bgs at Well ICPP-SCI-216 to 1.10E-1 cm/sec from 33 ft bgs at Well ICPP-SCI-226. Table B-10 summarizes the range of hydraulic parameters.

Table B-10. Range of measured INTEC alluvium hydraulic properties.

Soil Hydraulic Parameter	Value Range
Saturated hydraulic conductivity (cm/sec)	6.7E-8 to 1.10E-1
Effective porosity	0.22 to 0.42
Residual volumetric moisture content	0.0001 to 0.0642
Van Genuchten α (1/cm), approximately the inverse air entry potential	0.0002 to 1.97
Van Genuchten n parameter	1.1 to 4.2

The sensitivity simulation results for the 1954-2003 simulation period for all the locations, except ICPP-SCI-P-226, indicate that the large percentage of water from precipitation is drained into basalt. The simulations of the clayey-sand/silty-sand and silt/clay found in deep cores taken from Well ICPP-SCI-226 (CS-DP) were an exception. The drainage into basalt was near zero at these locations because of runoff and much higher evaporation totals. The very fine clay and sandy-clay-type soils can easily bring soil moisture back to the surface from deep in the alluvium during times of high potential evaporation, and the UNSAT-H software routes precipitation in excess of the saturated hydraulic conductivity to runoff. The core samples taken from CS-DP most likely represent the "old-alluvium" layer, which is usually a relatively thin layer found at the alluvium/basalt contact and is never found to extend from basalt to land surface at the INTEC. The

average annual runoff was zero for all other simulations. The average annual drainage, runoff, and evaporation are given in Table B-11.

Table B-11. Hydraulic property sensitivity simulation results.

Well Name (ICPP-SCI-P-)	Well Alias	Sample Depth	Unified Soil Classification	Average Annual Drainage (cm)	Average Annual Runoff (cm)	Average Annual Evaporation (cm)
216	BLR-AL	33-34	GW-GM	17.3	0.0	4.3
216	BLR-AL	34-35	GM	12.0	0.0	9.7
226	CS-DP	10-10.5	GW-GM	9.0	0.0	12.6
226	CS-DP	19-20	GP	13.9	0.0	7.7
226	CS-DP	45-46	SM-SC	0.5	16.0	5.0
226	CS-DP	51-52	ML-CL	0.	8.7	13.0
248	BLR-CH	10-10.5	GP	10.7	0.0	10.9
248	BLR-CH	18-18.5	GP-GM	15.7	0.0	5.8
250	PP-CH	15-15.5	GP	11.6	0.0	9.9
250	PP-CH	26-26.5	GW	6.7	0.0	14.9
250	PP-CH	31-31.5	GP-GM	9.7	0.0	12.0
251	STL-CH	19-19.5	GP	20.6	0.0	1.0
251	STL-CH	19-19.5	GW	6.3	0.0	15.
251	STL-CH	30.5-31	GP-GM	16.2	0.0	5.34
252	TF-CH	20-12	GP	12.2	0.0	9.51
252	TF-CH	26-27	GW	18.0	0.0	3.48
252	TF-CH	41-42.5	GP-GM	12.1	0.0	9.45

B-8 CONCLUSIONS AND RECOMMENDATIONS

The simulation results confirm previous observations that spring infiltration events from melting snow and rain account for a large proportion of the recharge occurring beneath the INTEC. The overall recharge rate inside and outside the tank farm appear similar. The recharge rate is a large percentage of the annual precipitation and may be approximately 18 cm/year (85% of the average annual precipitation). The effect of the tank farm membrane is mostly a redistribution of infiltration, which focuses the infiltration at membrane breaches and the membrane perimeter. The high infiltration rate predicted by the simulations is consistent with the need to pump the tank vault sumps. Approximately 0.5 cm/year recharge across the entire tank farm area (total area including tanks and surrounding area) is removed from the sumps even though the vaults have concrete roofs.

Radionuclide concentration profiles from the 2004 OU 3-14 RI/BRA field sampling could be used to validate the infiltration rates presented in this work. The depth of highly retarded radionuclide concentrations relative to less retarded radionuclide concentrations can provide estimates of pore water velocity and the recharge rate. However, the uncertainty of the radionuclide retardation factor may only allow validation to an order of magnitude. The highly intermittent nature of the INTEC infiltration and recharge entering the fractured basalt may further complicate using concentration profiles to validate the recharge rate because soil moisture is not constant, and rapidly occurring recharge may not allow the infiltrating water to reach equilibrium with the sorbed contaminants.

The calibrated NAT model at each location is nonunique. However, the modeling was consistent with the soil moisture observations and the measured soil properties. The numerical modeling was used to quantify infrequently observed soil moisture into the net infiltration rate. This net infiltration rate may need to be adjusted as more data are collected and the OU 3-14 vadose zone model is calibrated to observed perched water concentrations and elevation trends.

The sensitivity analysis confirms the measured soil hydraulic properties result in a large percentage of precipitation becoming recharge, but the soil within the tank farm alluvium may be more coarse and the recharge rate may be higher than other areas at the INTEC.

B-9 REFERENCES

- Baca, R. G. and S. O. Magnuson, 1990, *Independent Verification and Benchmark Testing of the UNSAT-H Computer Code, Version 2.0*, EGG-BEG-8811, EG&G Idaho, Inc., February 1990.
- Baca, R. G., S. O. Magnuson, H. D. Nguyen, and P. Martian, 1992, *A Modeling Study of Water Flow in the Vadose Zone Beneath the Radioactive Waste Management Complex*, EGG-GEO-10068, EG&G Idaho, Inc., January 1992.
- Clawson, K. L. G. E. Start, and N. R. Ricks, 1989, *Climatography of the Idaho National Engineering Laboratory*, 2nd Edition, DOE/ID-12118, U.S. Department of Energy Idaho Operations Office, December 1989.
- DOE-ID, 2003a, *Performance Assessment for the INEEL CERCLA Disposal Facility Landfill*, DOE/ID-10978, Rev. 0, U.S. Department of Energy Idaho Operations Office, August 2003.
- DOE-ID, 2003b, *INTEC Water Systems Engineering Study*, DOE/ID-11115, Rev. 0, U.S. Department of Energy Idaho Operations Office, December 2003.
- DOE-ID, 2003c, *Phase I Monitoring Well and Tracer Study Report for Operable Unit 3-13, Group 4, Perched Water*, DOE/ID-10967, Rev. 2, U.S. Department of Energy Idaho Operations Office, June 2003. [Note: Revision 2 is Official Use Only; Revision 1 is publicly available.]
- Fayer, M. J., 2000, *UNSAT-H Version 3.0: Unsaturated Soil Water and Heat Flow Model - Theory, User Manual, and Examples*, PNNL-13249, Pacific Northwest National Laboratory, June 2000.
- LITCO, 1995, *Report of 1993/1994 Tank Farm Drilling and Sampling Investigation at the Idaho Chemical Processing Plant*, INEL-95/0064, Lockheed Idaho Technologies Company, February 1995.
- Magnuson, S. O., 1993, *A Simulation of Moisture Movement in Proposed Barriers for the Subsurface Disposal Area*, INEL, EGG-WM-10974, EG&G Idaho, Inc., Idaho Falls, ID.
- Magnuson, S. O., 2004, "Regulatory Modeling for the Idaho National Engineering and Environmental Laboratory's Subsurface Disposal Area and Conceptual Model Uncertainty Treatment," *Vadose Zone Journal*, Volume 3, Issue 1, Soil Science Society of America.
- Martian, P., 1995, *UNSAT-H Infiltration Model Calibration at the Subsurface Disposal Area*, Idaho National Engineering Laboratory, INEL-95/0596, Idaho National Engineering and Environmental Laboratory, Lockheed Martin Idaho Technologies Company, October 1995.
- Martian, P. and S. O. Magnuson, 1993, *A Simulation Study of Infiltration Into Surficial Sediments at the Subsurface Disposal Area*, Idaho National Engineering Laboratory, EGG-WM-11250, EG&G Idaho, Inc., Idaho Falls, ID.
- Mockus, V., 1972, "Hydraulic Effects of Land Use and Treatment," Chapter 11, "Estimation of Direct Runoff from Snowmelt," *SCS National Engineering Handbook*, Section 4, "Hydrology," U.S. Department of Agriculture, Soil Conservation Service, Washington, D.C.
- Richards, B. T., 1993, *Analysis of ICPP Tank Farm Infiltration*, WINCO-1183, Westinghouse Idaho Nuclear Company, Inc., October 1993.
- Richards, L. A., 1931, "Capillary Conduction of Liquids Through Porous Mediums," *Physics*, Vol. 1, Issue 5, November 1931, pp. 318-333.

Richardson, C. W. and D. A. Wright, 1984, *WGEN: A Model for Generating Daily Weather Variables*, ARS-8, USDA Agricultural Research Service, August 1984.

Appendix B-A

Model Hydraulic Properties

Appendix B-A

Model Hydraulic Properties

This appendix contains the soil hydraulic properties for each well location obtained from the calibration exercises. The Hydraulic properties presented in Table B-A-1 consist of profile layering and the van Genuchten soil hydraulic parameters for each layer.

Table B-A-1. Model hydraulic properties for each simulated location.

Soil Layer	Layer Bottom (cm)	Saturated Hydraulic Conductivity (cm/hr)	Porosity	Residual Moisture Content	Alpha Parameter (1/cm)	n Parameter
81-02						
1	671.	400.	0.32	0.010	1.0	1.45
2	1228.	200.	0.32	0.012	1.0	1.45
3	1328.	1.0	0.05	0.00005	0.1	2.5
81-04						
1	229.	500.	0.32	0.006	1.0	1.50
2	290.	100.	0.32	0.010	1.0	1.40
3	351.	50.	0.32	0.012	1.0	1.35
4	1228.	50.	0.32	0.014	1.0	1.30
5	1328.	1.0	0.05	0.00005	0.1	2.5
81-05						
1	168.	400.	0.32	0.008	1.0	1.40
2	320.	300.	0.32	0.010	1.0	1.40
3	1228.	100.	0.32	0.012	1.0	1.40
4	1328.	1.0	0.05	0.00005	0.1	2.5
81-10						
1	305.	300.	0.32	0.010	1.0	1.40
2	457.	200.	0.32	0.010	1.0	1.38
3	671.	200.	0.32	0.010	1.0	1.38
4	1228.	400.	0.32	0.010	1.0	1.45
5	1328.	1.0	0.05	0.00005	0.1	2.5
81-15						
1	91.	400.	0.32	0.010	1.0	1.40
2	152.	150.	0.32	0.010	1.0	1.35
3	244.	400.	0.32	0.009	1.0	1.40
4	335.	500.	0.32	0.008	1.0	1.45
5	1228.	300.	0.32	0.010	1.0	1.40
6	1328.	1.0	0.05	0.00005	0.1	2.5
81-17						
1	381.	500.	0.32	0.006	1.0	1.4
2	472.	50.	0.32	0.012	1.0	1.4

Soil Layer	Layer Bottom (cm)	Saturated Hydraulic Conductivity (cm/hr)	Porosity	Residual Moisture Content	Alpha Parameter (1/cm)	n Parameter
3	1177.	500.	0.32	0.006	1.0	1.4
4	1277.	1.0	0.05	0.00005	0.1	2.5
81-21						
1	274.	300.	0.32	0.006	1.0	1.5
2	350.	600.	0.32	0.006	1.0	1.5
3	1393.	300.	0.32	0.006	1.0	1.3
4	1493.	1.0	0.05	0.00005	0.1	2.5
A-60						
1	152.	1200.	0.32	0.006	1.0	1.5
2	305.	1200.	0.32	0.015	1.0	1.5
3	752.	1200.	0.32	0.001	1.0	1.5
4	1228.	1200.	0.32	0.02	1.0	1.5
5	1328.	1.0	0.05	0.00005	0.1	2.5
A-62						
1	1283.	500.	0.32	0.006	1.0	1.5
2	1383.	1.0	0.05	0.00005	0.1	2.5
A-63						
1	884.	500.	0.32	0.008	1.0	1.5
2	960.	200.	0.32	0.006	1.0	1.5
3	1393.	100.	0.32	0.006	1.0	1.5
4	1493.	1.0	0.05	0.00005	0.1	2.5
A-64						
1	655.	500.	0.32	0.006	1.0	1.5
2	747.	100.	0.32	0.006	1.0	1.5
3	960.	300.	0.32	0.006	1.0	1.5
4	1256.	100.	0.32	0.006	1.0	1.5cd
5	1356.	1.0	0.05	0.00005	0.1	2.5
A-65						
1	762.	1500.	0.32	0.02	1.0	1.5
2	1177.	1500.	0.32	0.04	1.0	1.5
3	1277.	1.0	0.05	0.00005	0.1	2.5
A-67						
1	76.	500.	0.32	0.010	1.5	1.5
2	107.	10.	0.32	0.062	1.5	1.5
3	305.	500.	0.32	0.010	1.5	1.5
4	732.	600.	0.32	0.0030	1.5	1.5
5	823.	300.	0.32	0.0062	1.5	1.5
6	930.	150.	0.32	0.0062	1.5	1.5
7	1052.	75.	0.32	0.0062	1.5	1.5
8	1177.	300.	0.32	0.0062	1.5	1.5

Soil Layer	Layer Bottom (cm)	Saturated Hydraulic Conductivity (cm/hr)	Porosity	Residual Moisture Content	Alpha Parameter (1/cm)	n Parameter
9	1277.	1.0	0.05	0.00005	0.1	2.5
A-68						
1	762.	500.	0.32	0.0062	1.0	1.5
2	838.	200.	0.32	0.0062	1.0	1.5
3	939.	50.	0.32	0.0062	1.0	1.5
4	1039.	1.0	0.05	0.00005	0.1	2.5

Appendix B-B
Simulation Annual Drainage to Basalt

Appendix B-B

Simulation Annual Drainage to Basalt

This appendix contains the annual drainage into basalt for each simulated location and illustrates the water flux into and out of the simulation profiles. Table B-B-1 presents the annual drainage into basalt at each location for each simulation year (1954-2003). Figures B-B-1 through B-B-15 illustrate the daily infiltration, daily drainage, and annual drainage at each simulated location.

The effect of the impermeable membrane reducing infiltration after installation in 1977 can be seen in plots of drainage from Wells 81-05, 81-10, 81-15 and 81-17, which are illustrated in Figures B-B-3, B-B-4, B-B-5 and B-B-6, respectively. Wells A-60 and A-65 show a dramatic increase in infiltration after membrane installation and the drainage plots are illustrated in Figures B-8 and B-12, respectively.

Table B-B-1. Annual drainage into basalt at each simulated well.

Year	Total Drainage (cm)	Year	Total Drainage (cm)	Year	Total Drainage (cm)	Year	Total Drainage (cm)
81-02							
1954	12.3	1967	11.9	1980	22.9	1993	20.7
1955	13.1	1968	20.6	1981	25.1	1994	15.7
1956	11.5	1969	27.2	1982	16.4	1995	27.0
1957	25.2	1970	15.1	1983	22.6	1996	18.2
1958	17.0	1971	19.4	1984	33.1	1997	18.3
1959	13.0	1972	20.4	1985	19.1	1998	21.9
1960	17.5	1973	17.2	1986	30.2	1999	22.3
1961	14.8	1974	22.4	1987	22.4	2000	13.8
1962	28.0	1975	20.7	1988	16.5	2001	12.5
1963	29.3	1976	15.8	1989	10.3	2002	9.4
1964	20.8	1977	15.9	1990	19.5	2003	10.8
1965	28.1	1978	15.0	1991	17.6		
1966	14.8	1979	14.6	1992	17.7		
81-04							
1954	13.1	1967	11.1	1980	16.4	1993	14.7
1955	13.5	1968	18.3	1981	24.4	1994	18.5
1956	10.8	1969	30.0	1982	17.0	1995	21.5
1957	24.4	1970	17.3	1983	18.1	1996	19.8
1958	17.9	1971	17.9	1984	29.4	1997	17.2
1959	16.4	1972	21.9	1985	22.0	1998	17.9
1960	15.3	1973	17.8	1986	23.9	1999	20.4
1961	17.9	1974	23.4	1987	22.2	2000	17.6
1962	26.0	1975	20.8	1988	19.0	2001	10.5
1963	30.6	1976	17.4	1989	9.8	2002	9.9
1964	21.8	1977	18.0	1990	15.2	2003	8.1
1965	28.4	1978	11.3	1991	16.8		

Year	Total Drainage (cm)	Year	Total Drainage (cm)	Year	Total Drainage (cm)	Year	Total Drainage (cm)
1966	18.8	1979	14.8	1992	18.8		
81-05							
1954	11.0	1967	9.5	1980	3.5	1993	3.8
1955	11.6	1968	14.8	1981	3.7	1994	3.7
1956	8.1	1969	28.1	1982	4.1	1995	3.8
1957	22.3	1970	15.5	1983	5.1	1996	4.5
1958	15.6	1971	15.0	1984	4.4	1997	4.6
1959	14.0	1972	19.6	1985	5.0	1998	4.7
1960	12.2	1973	14.4	1986	6.5	1999	3.8
1961	15.6	1974	20.6	1987	4.9	2000	4.3
1962	22.4	1975	18.3	1988	6.2	2001	4.8
1963	27.4	1976	15.2	1989	4.9	2002	4.1
1964	18.6	1977	14.3	1990	4.1	2003	3.2
1965	25.8	1978	8.4	1991	3.3		
1966	17.1	1979	4.8	1992	3.0		
81-10							
1954	11.7	1967	10.4	1980	2.9	1993	1.7
1955	12.5	1968	19.6	1981	2.3	1994	1.7
1956	10.3	1969	26.9	1982	2.0	1995	1.8
1957	24.3	1970	14.5	1983	1.9	1996	1.9
1958	16.1	1971	18.4	1984	2.2	1997	2.0
1959	12.9	1972	19.9	1985	2.4	1998	2.2
1960	15.9	1973	16.2	1986	2.4	1999	2.6
1961	14.6	1974	21.5	1987	3.1	2000	2.3
1962	26.4	1975	19.8	1988	2.8	2001	2.1
1963	28.4	1976	14.9	1989	2.9	2002	2.3
1964	19.9	1977	15.4	1990	2.7	2003	2.3
1965	27.2	1978	7.3	1991	2.3		
1966	14.9	1979	4.2	1992	2.0		
81-15							
1954	11.5	1967	9.9	1980	9.5	1993	7.7
1955	12.3	1968	19.1	1981	11.9	1994	13.1
1956	9.9	1969	27.0	1982	12.2	1995	7.4
1957	23.9	1970	14.4	1983	10.1	1996	15.4
1958	15.8	1971	17.8	1984	15.2	1997	9.0
1959	13.0	1972	19.8	1985	15.5	1998	10.1
1960	15.2	1973	15.9	1986	12.9	1999	12.0
1961	14.6	1974	21.1	1987	14.6	2000	11.5
1962	25.8	1975	19.4	1988	11.0	2001	6.4
1963	28.1	1976	14.5	1989	6.8	2002	6.5
1964	19.6	1977	15.4	1990	8.0	2003	5.5

Year	Total Drainage (cm)	Year	Total Drainage (cm)	Year	Total Drainage (cm)	Year	Total Drainage (cm)
1965	26.7	1978	7.5	1991	9.7		
1966	15.1	1979	10.0	1992	9.3		
81-17							
1954	11.3	1967	10.6	1980	3.1	1993	1.5
1955	12.1	1968	19.3	1981	3.1	1994	1.7
1956	10.2	1969	26.0	1982	2.9	1995	1.5
1957	24.0	1970	13.9	1983	2.4	1996	1.3
1958	15.4	1971	18.0	1984	2.0	1997	1.3
1959	12.0	1972	19.2	1985	2.0	1998	1.7
1960	15.8	1973	15.6	1986	2.8	1999	1.6
1961	13.7	1974	20.8	1987	2.9	2000	1.5
1962	26.3	1975	19.4	1988	3.4	2001	1.5
1963	27.7	1976	14.4	1989	2.9	2002	1.8
1964	19.3	1977	14.3	1990	2.3	2003	2.0
1965	26.5	1978	6.8	1991	1.8		
1966	13.9	1979	3.9	1992	1.5		
81-21							
1954	13.2	1967	12.0	1980	24.2	1993	22.9
1955	13.9	1968	20.6	1981	26.4	1994	17.0
1956	12.3	1969	29.4	1982	18.7	1995	27.3
1957	25.6	1970	15.8	1983	24.0	1996	19.8
1958	18.3	1971	20.3	1984	35.0	1997	19.9
1959	14.3	1972	21.7	1985	22.1	1998	22.6
1960	17.9	1973	18.4	1986	33.0	1999	24.2
1961	16.4	1974	23.5	1987	22.5	2000	15.2
1962	28.4	1975	21.5	1988	18.3	2001	13.3
1963	30.7	1976	16.8	1989	11.5	2002	10.9
1964	22.0	1977	17.7	1990	20.5	2003	11.9
1965	29.0	1978	17.6	1991	17.8		
1966	16.6	1979	16.6	1992	19.1		
A-60							
1954	12.5	1967	15.0	1980	40.0	1993	65.3
1955	10.5	1968	22.2	1981	42.0	1994	24.9
1956	15.1	1969	25.6	1982	47.0	1995	46.2
1957	25.7	1970	15.1	1983	56.0	1996	34.0
1958	16.7	1971	19.3	1984	60.5	1997	34.2
1959	11.2	1972	19.4	1985	60.7	1998	46.2
1960	20.1	1973	19.1	1986	57.4	1999	46.2
1961	15.3	1974	20.7	1987	33.6	2000	26.5
1962	28.3	1975	21.6	1988	23.9	2001	28.1
1963	28.9	1976	15.9	1989	43.2	2002	28.2

Year	Total Drainage (cm)	Year	Total Drainage (cm)	Year	Total Drainage (cm)	Year	Total Drainage (cm)
1964	21.1	1977	24.5	1990	28.5	2003	23.6
1965	28.3	1978	57.2	1991	21.9		
1966	11.9	1979	47.3	1992	23.7		
A-62							
1954	13.1	1967	14.4	1980	25.5	1993	27.8
1955	13.2	1968	22.0	1981	27.2	1994	14.5
1956	13.5	1969	26.7	1982	20.2	1995	31.8
1957	26.3	1970	16.1	1983	27.1	1996	20.0
1958	17.6	1971	19.9	1984	36.7	1997	19.4
1959	12.0	1972	20.6	1985	24.4	1998	26.2
1960	20.0	1973	18.6	1986	33.4	1999	25.3
1961	14.3	1974	22.8	1987	24.1	2000	13.6
1962	30.4	1975	21.7	1988	15.0	2001	13.9
1963	30.0	1976	16.7	1989	16.1	2002	11.2
1964	21.7	1977	15.3	1990	21.3	2003	15.2
1965	28.9	1978	22.5	1991	18.4		
1966	13.7	1979	18.5	1992	16.9		
A-63							
1954	13.0	1967	11.8	1980	14.0	1993	11.8
1955	13.7	1968	20.9	1981	22.3	1994	16.7
1956	11.9	1969	28.4	1982	15.0	1995	21.2
1957	25.4	1970	15.7	1983	15.9	1996	17.6
1958	17.9	1971	20.1	1984	26.1	1997	15.1
1959	14.2	1972	21.4	1985	19.3	1998	17.2
1960	17.5	1973	18.0	1986	19.2	1999	18.0
1961	16.1	1974	23.2	1987	20.7	2000	14.9
1962	28.2	1975	21.2	1988	17.5	2001	9.8
1963	30.3	1976	16.6	1989	8.5	2002	8.4
1964	21.6	1977	17.2	1990	13.0	2003	6.1
1965	28.8	1978	9.9	1991	15.9		
1966	16.3	1979	11.4	1992	18.4		
A-64							
1954	12.9	1967	13.3	1980	28.7	1993	35.2
1955	13.7	1968	21.5	1981	30.4	1994	16.3
1956	12.7	1969	27.4	1982	25.6	1995	34.7
1957	26.1	1970	15.8	1983	32.3	1996	23.2
1958	17.7	1971	20.2	1984	41.5	1997	22.0
1959	12.9	1972	20.8	1985	31.5	1998	30.2
1960	19.1	1973	18.3	1986	38.9	1999	29.7
1961	14.9	1974	23.1	1987	25.5	2000	16.4
1962	29.5	1975	21.5	1988	17.6	2001	17.0

Year	Total Drainage (cm)	Year	Total Drainage (cm)	Year	Total Drainage (cm)	Year	Total Drainage (cm)
1963	30.1	1976	16.5	1989	21.2	2002	14.7
1964	21.7	1977	16.4	1990	22.7	2003	16.5
1965	28.9	1978	30.4	1991	18.9		
1966	14.6	1979	23.7	1992	18.5		
A-65							
1954	12.6	1967	15.3	1980	39.5	1993	65.4
1955	9.4	1968	22.7	1981	41.8	1994	24.8
1956	15.9	1969	24.9	1982	47.1	1995	46.6
1957	25.7	1970	15.0	1983	57.5	1996	33.6
1958	16.4	1971	19.2	1984	59.4	1997	34.9
1959	11.5	1972	19.3	1985	61.1	1998	45.9
1960	19.8	1973	19.4	1986	57.4	1999	46.0
1961	16.3	1974	20.0	1987	33.0	2000	26.4
1962	27.3	1975	21.8	1988	23.3	2001	28.0
1963	28.6	1976	15.8	1989	43.5	2002	28.4
1964	21.1	1977	24.5	1990	28.6	2003	23.5
1965	28.3	1978	57.0	1991	21.8		
1966	11.4	1979	48.0	1992	23.6		
A-67							
1954	13.0	1967	14.8	1980	20.7	1993	21.4
1955	13.0	1968	22.3	1981	23.0	1994	13.0
1956	14.3	1969	27.1	1982	15.3	1995	25.6
1957	26.3	1970	15.9	1983	20.4	1996	16.4
1958	17.7	1971	20.2	1984	31.3	1997	16.6
1959	11.9	1972	20.5	1985	18.7	1998	19.6
1960	20.9	1973	19.4	1986	29.1	1999	20.6
1961	14.7	1974	22.5	1987	19.1	2000	11.9
1962	30.3	1975	22.1	1988	14.3	2001	10.3
1963	30.1	1976	16.8	1989	10.3	2002	9.0
1964	22.0	1977	15.3	1990	17.0	2003	8.9
1965	29.2	1978	16.1	1991	14.7		
1966	13.5	1979	14.1	1992	15.0		
A-68							
1954	13.0	1967	14.8	1980	20.7	1993	21.4
1955	13.0	1968	22.3	1981	23.0	1994	13.0
1956	14.3	1969	27.1	1982	15.3	1995	25.6
1957	26.3	1970	15.9	1983	20.4	1996	16.4
1958	17.7	1971	20.2	1984	31.3	1997	16.6
1959	11.9	1972	20.5	1985	18.7	1998	19.6
1960	20.9	1973	19.4	1986	29.1	1999	20.6
1961	14.7	1974	22.5	1987	19.1	2000	11.9

Year	Total Drainage (cm)	Year	Total Drainage (cm)	Year	Total Drainage (cm)	Year	Total Drainage (cm)
1962	30.3	1975	22.1	1988	14.3	2001	10.3
1963	30.1	1976	16.8	1989	10.3	2002	9.0
1964	22.0	1977	15.3	1990	17.0	2003	8.9
1965	29.2	1978	16.1	1991	14.7		
1966	13.5	1979	14.1	1992	15.0		

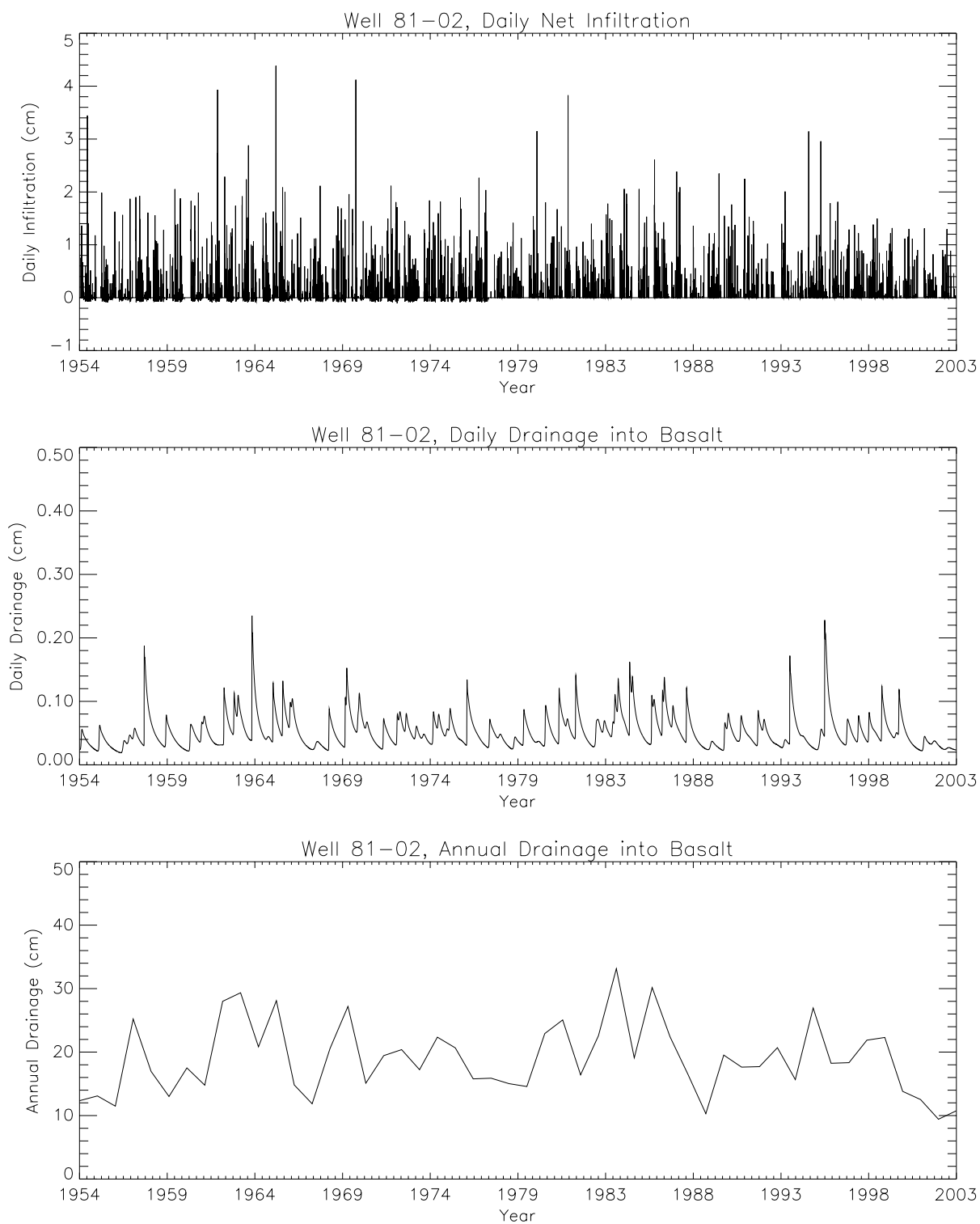


Figure B-B-1. Daily infiltration, daily drainage, and annual average drainage at Well 81-02.

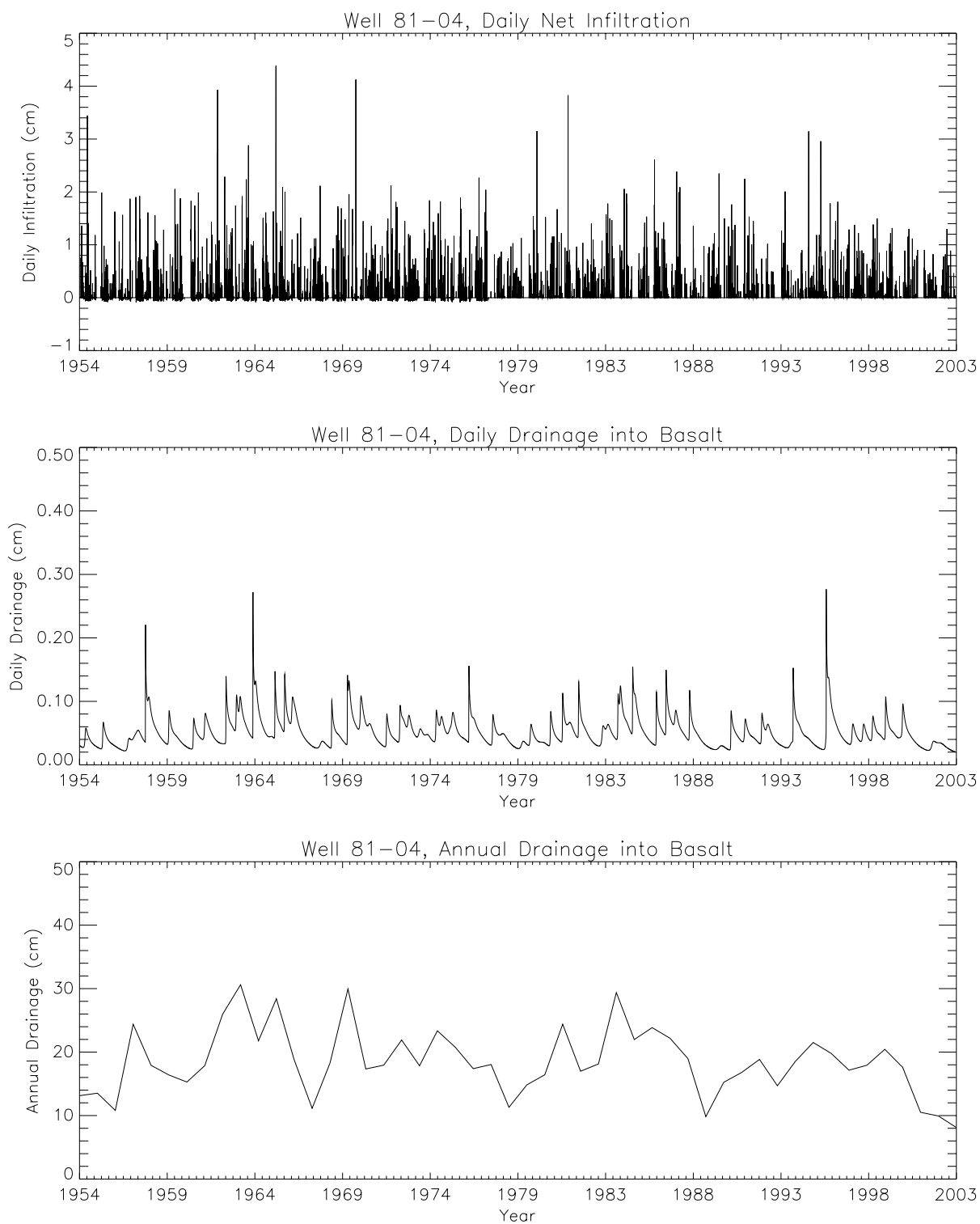


Figure B-B-2. Daily infiltration, daily drainage, and annual average drainage at Well 81-04.

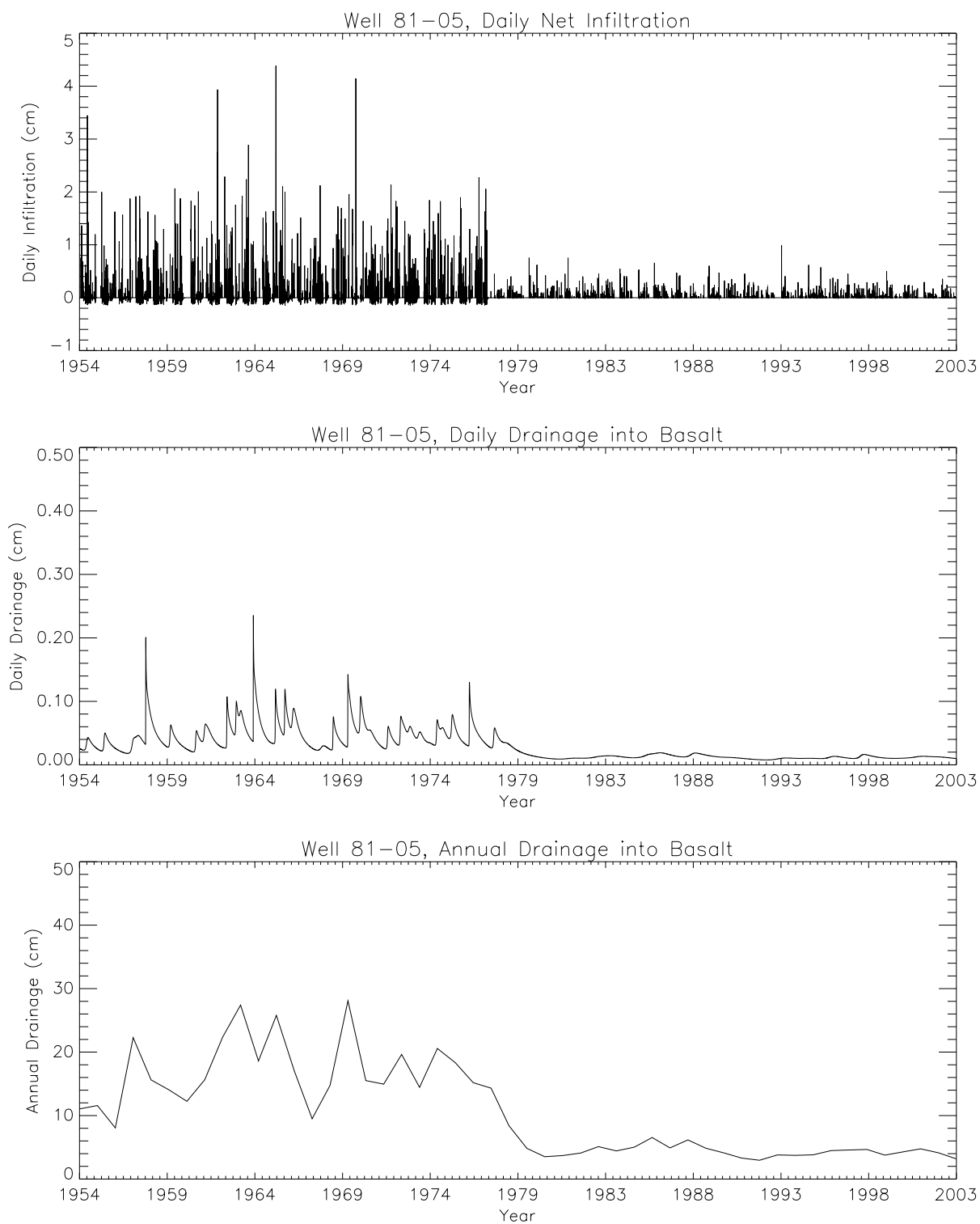


Figure B-B-3. Daily infiltration, daily drainage, and annual average drainage at Well 81-05.

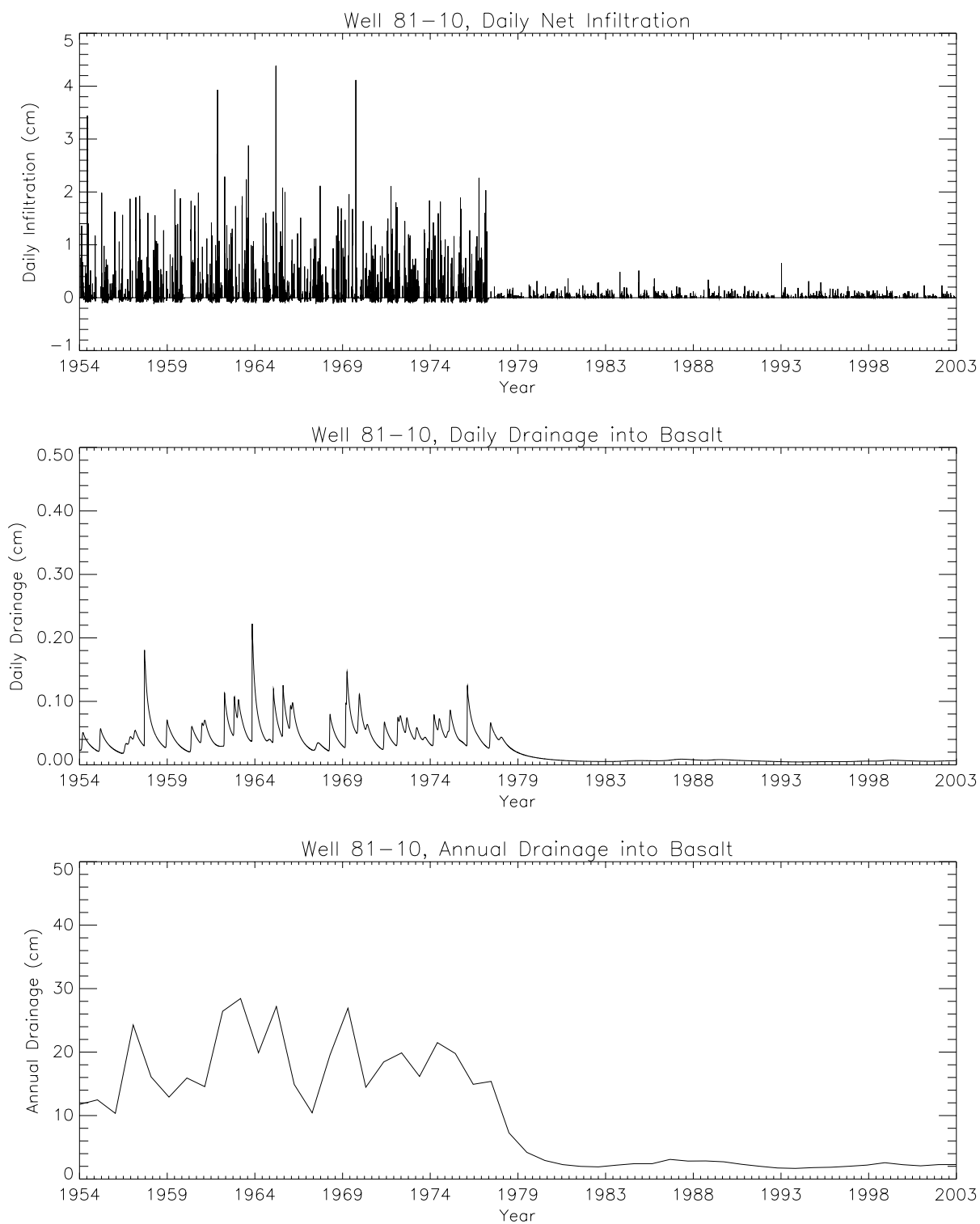


Figure B-B-4. Daily infiltration, daily drainage, and annual average drainage at Well 81-10.

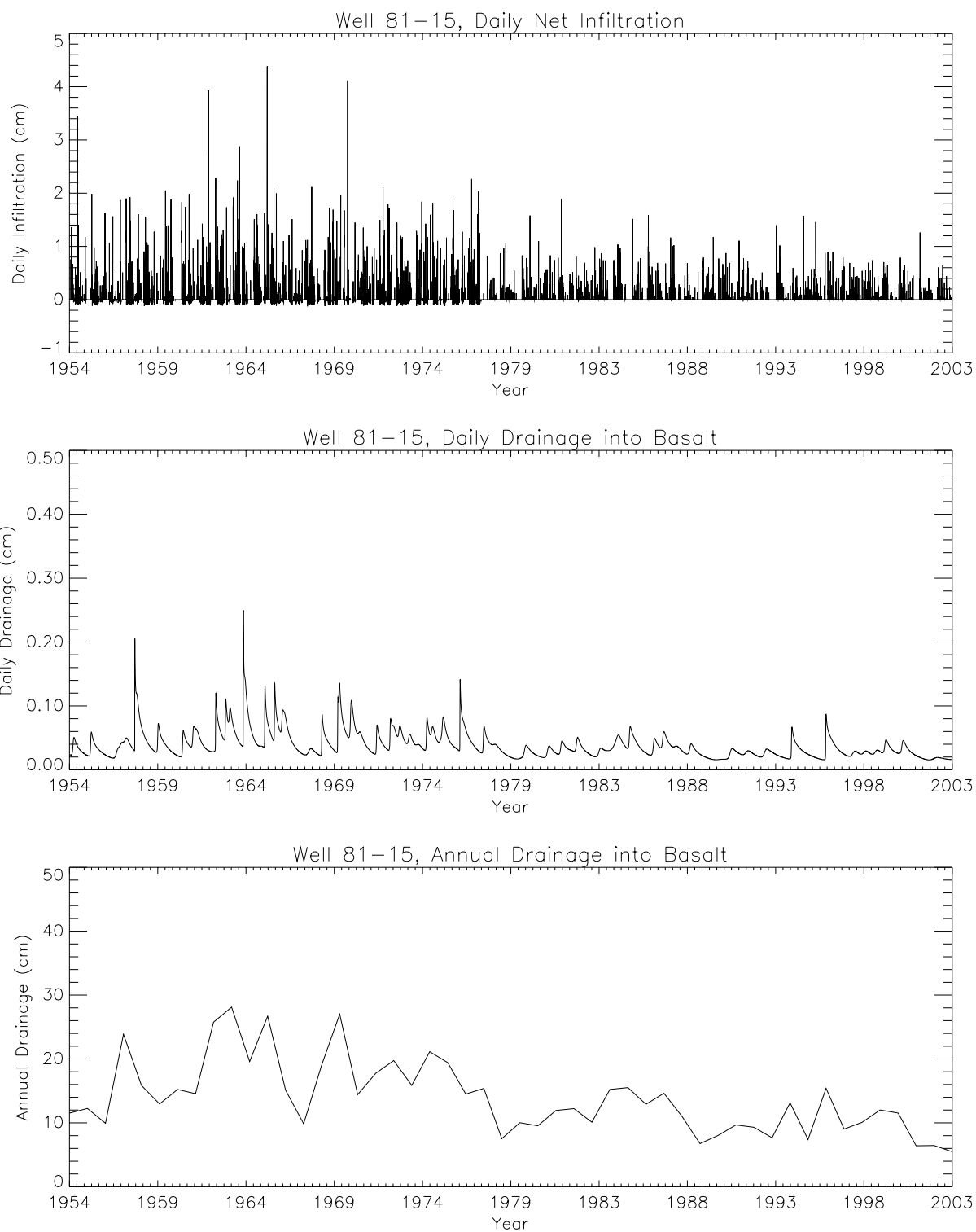


Figure B-B-5. Daily infiltration, daily drainage, and annual average drainage at Well 81-15.

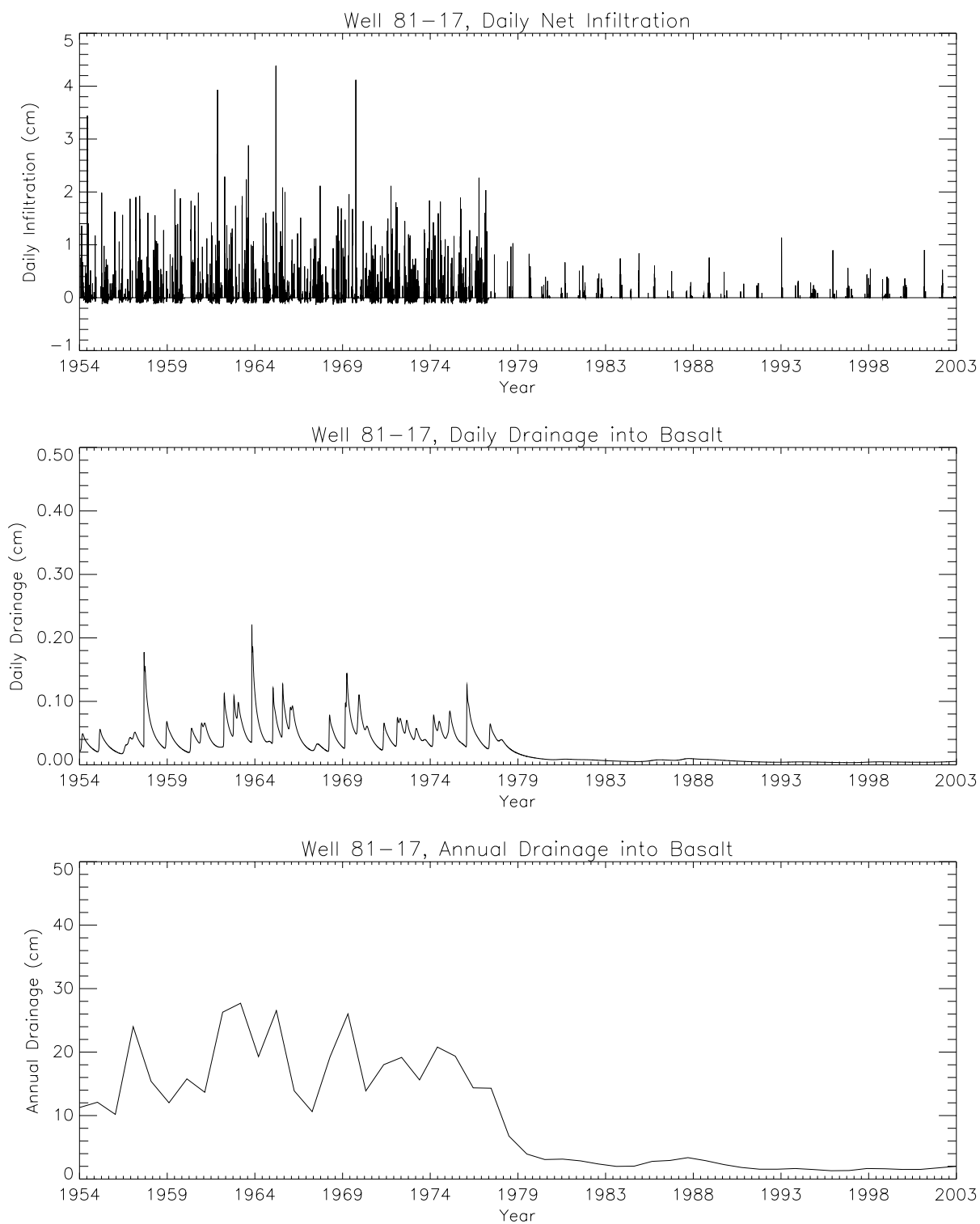


Figure B-B-6. Daily infiltration, daily drainage, and annual average drainage at Well 81-17.

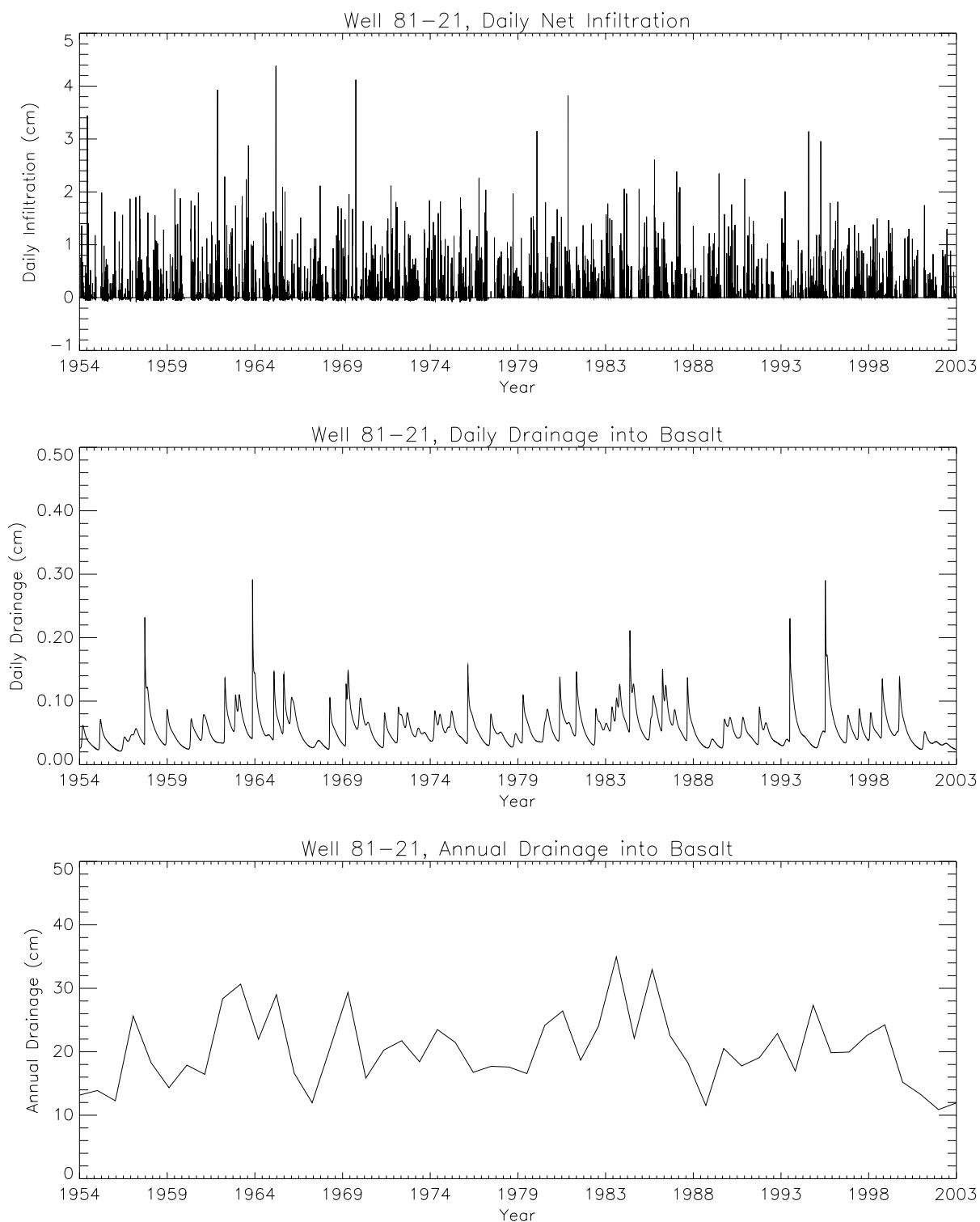


Figure B-B-7. Daily infiltration, daily drainage, and annual average drainage at Well 81-21.

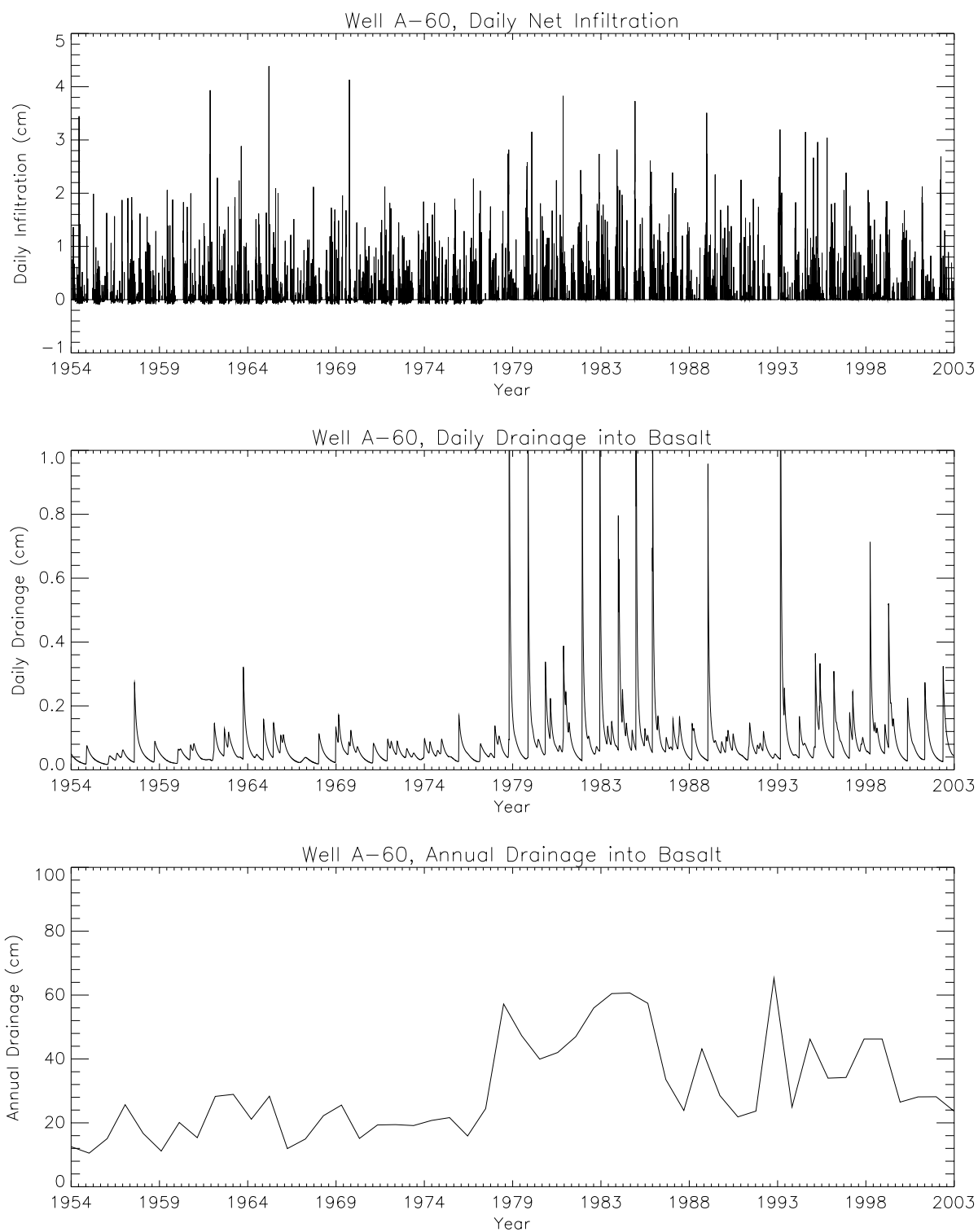


Figure B-B-8. Daily infiltration, daily drainage, and annual average drainage at Well A-60.

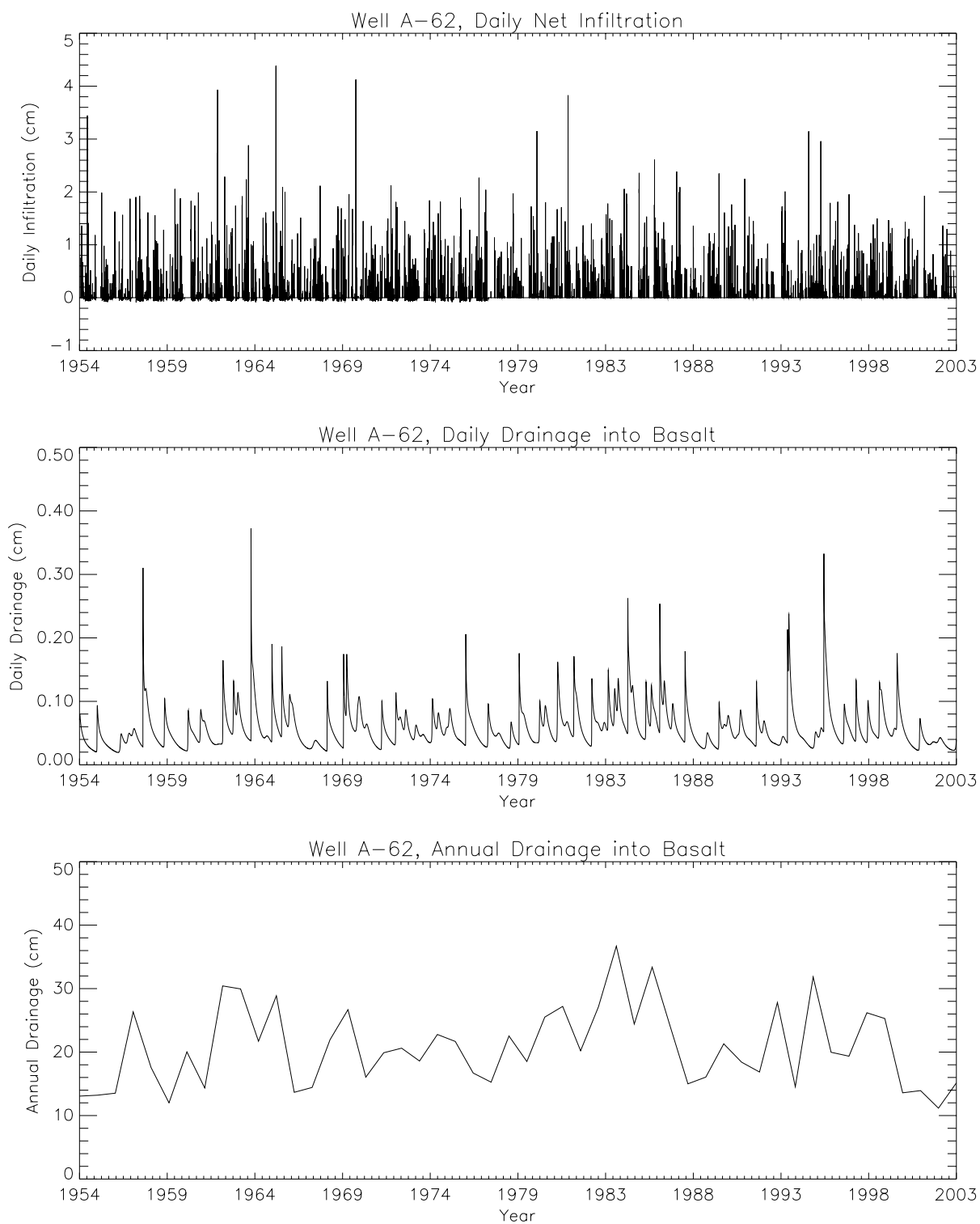


Figure B-B-9. Daily infiltration, daily drainage, and annual average drainage at Well A-62.

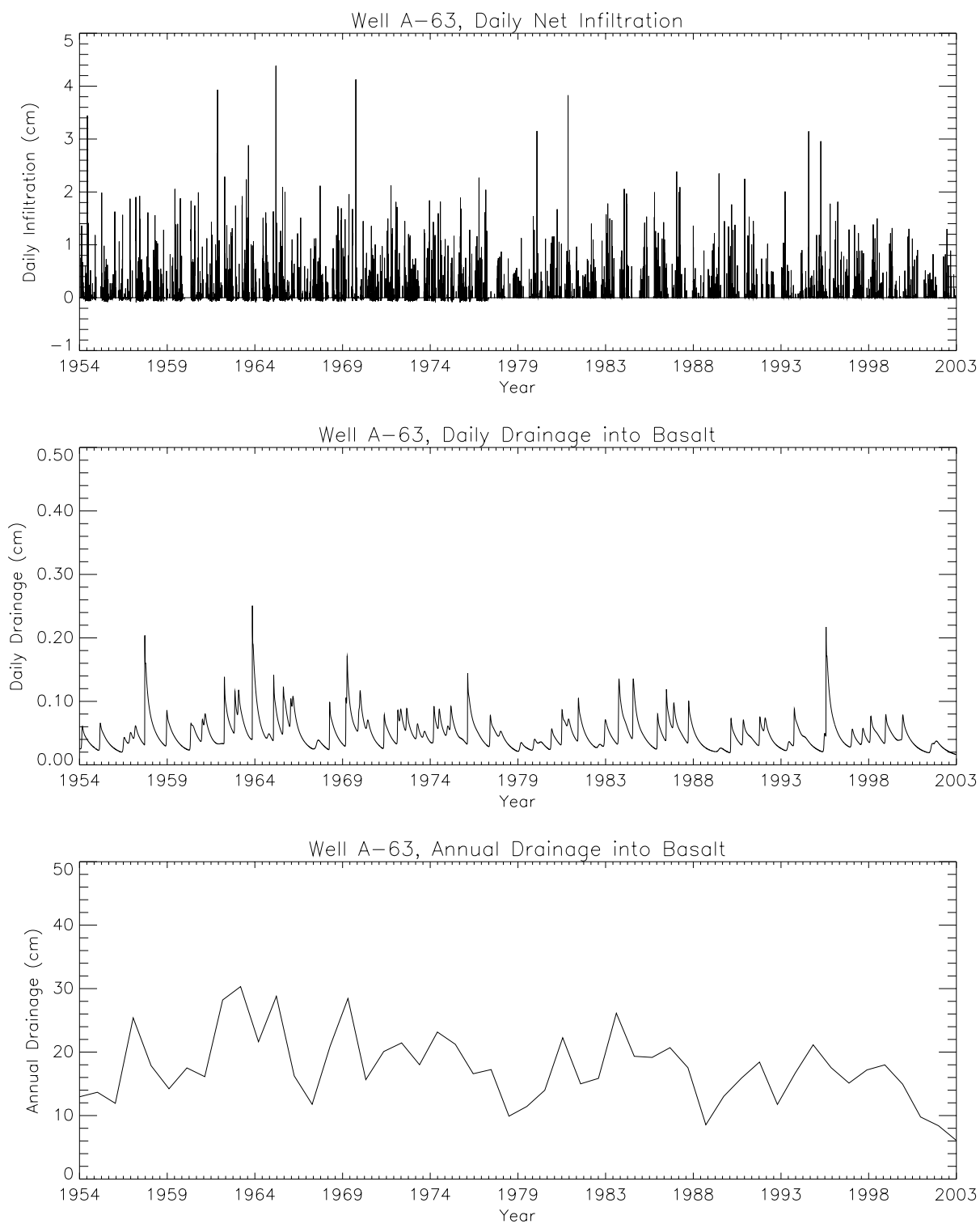


Figure B-B-10. Daily infiltration, daily drainage, and annual average drainage at Well A-63.

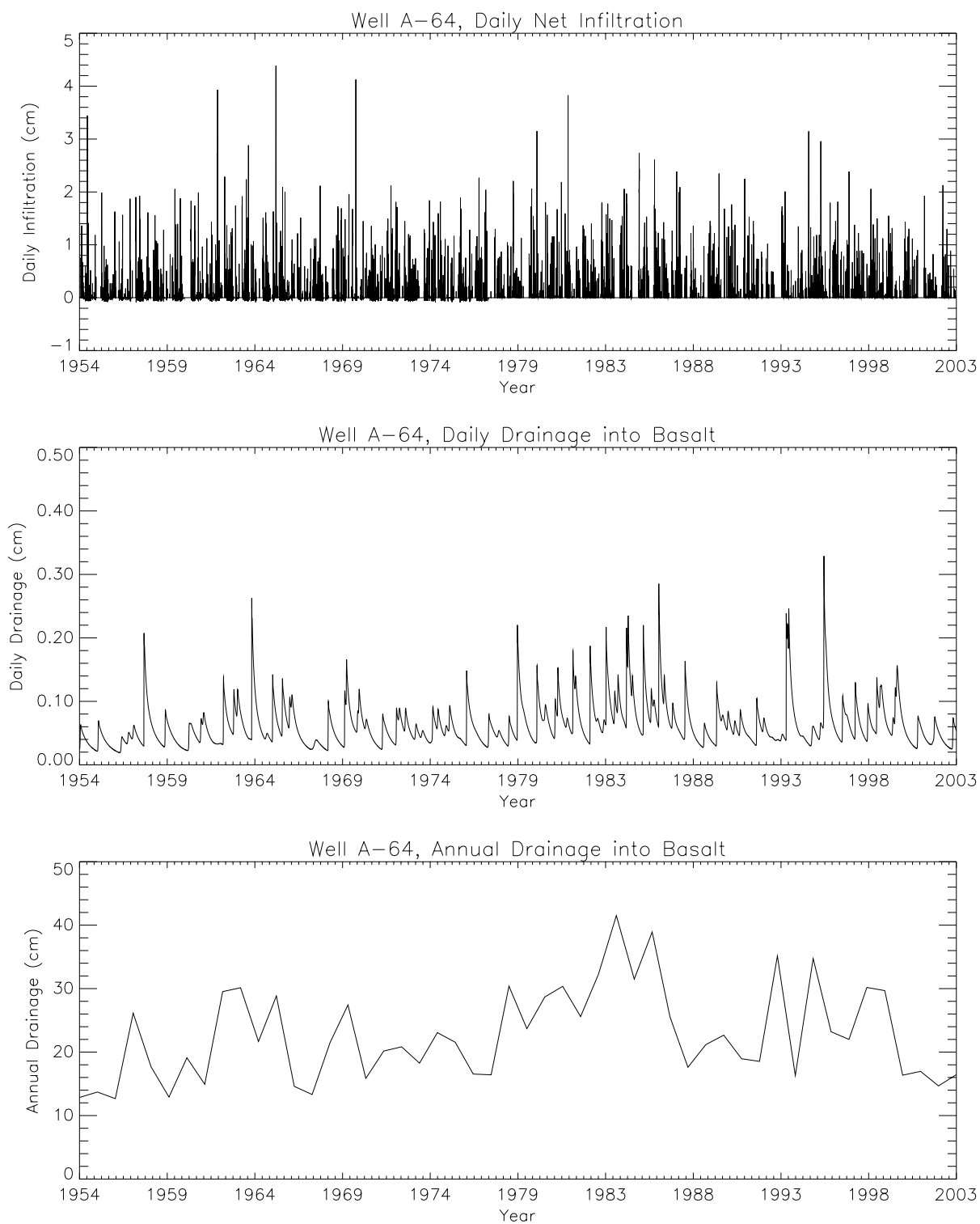


Figure B-B-11. Daily infiltration, daily drainage, and annual average drainage at Well A-64.

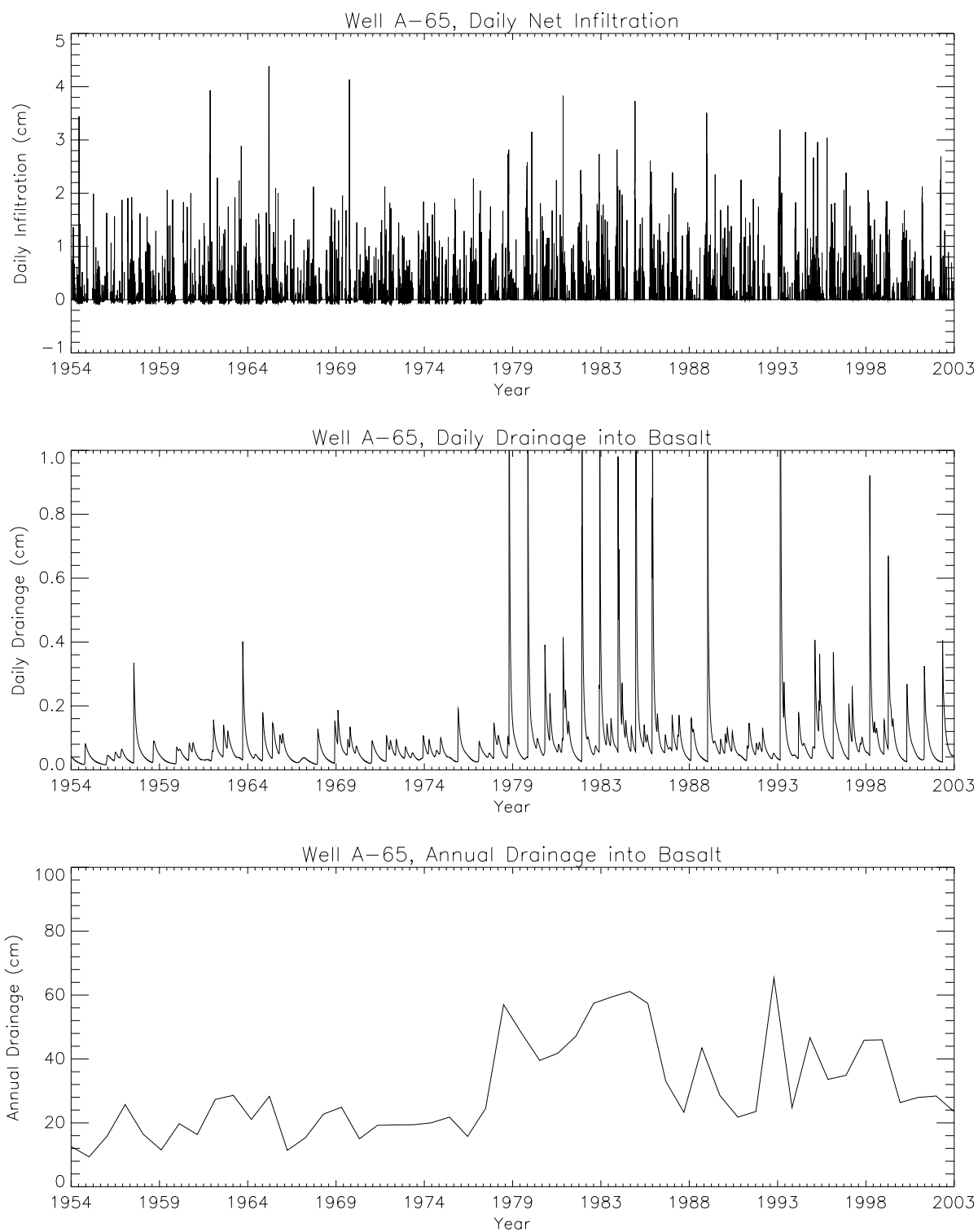


Figure B-B-12. Daily infiltration, daily drainage, and annual average drainage at Well A-65.

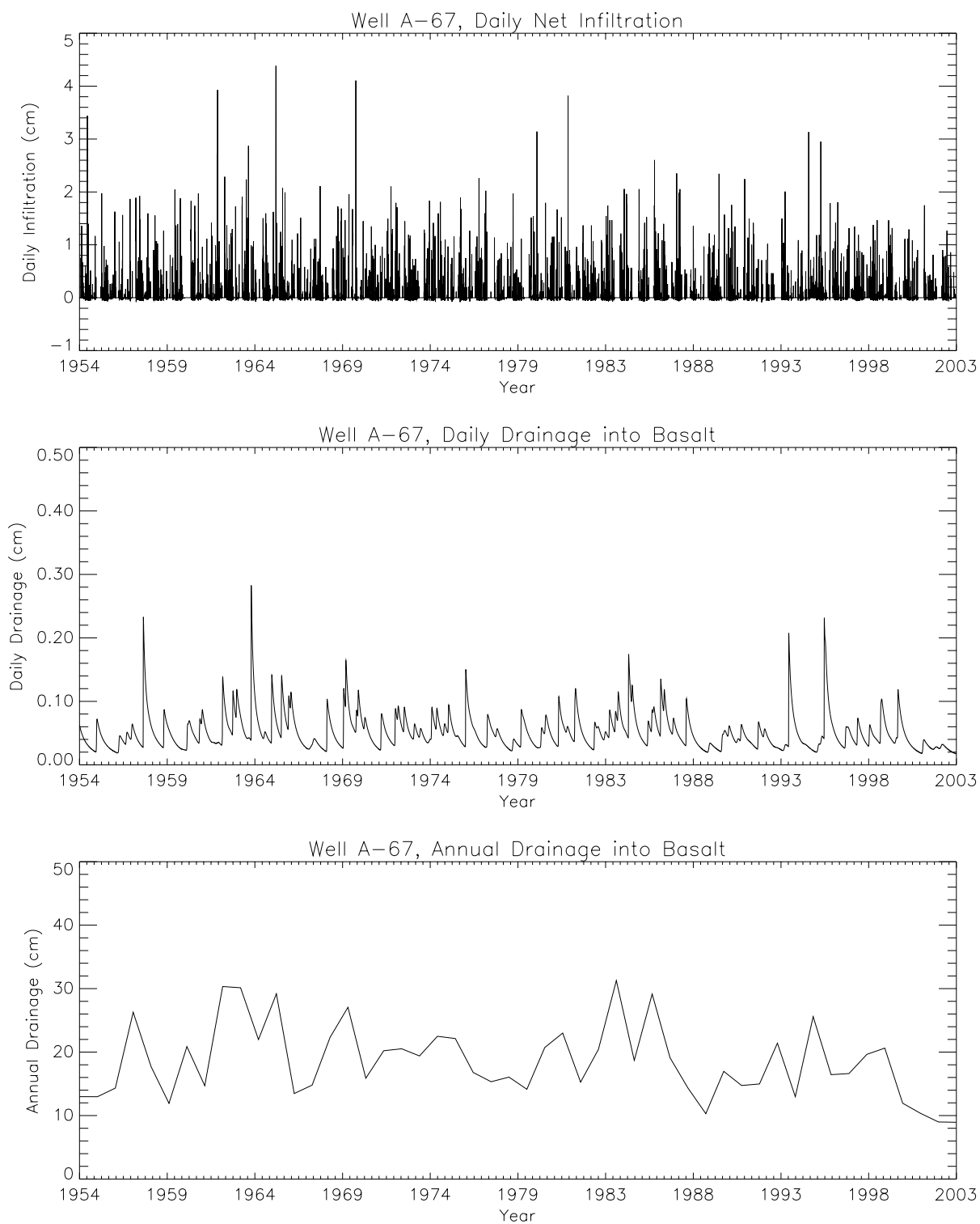


Figure B-B-13. Daily infiltration, daily drainage, and annual average drainage at Well A-67.

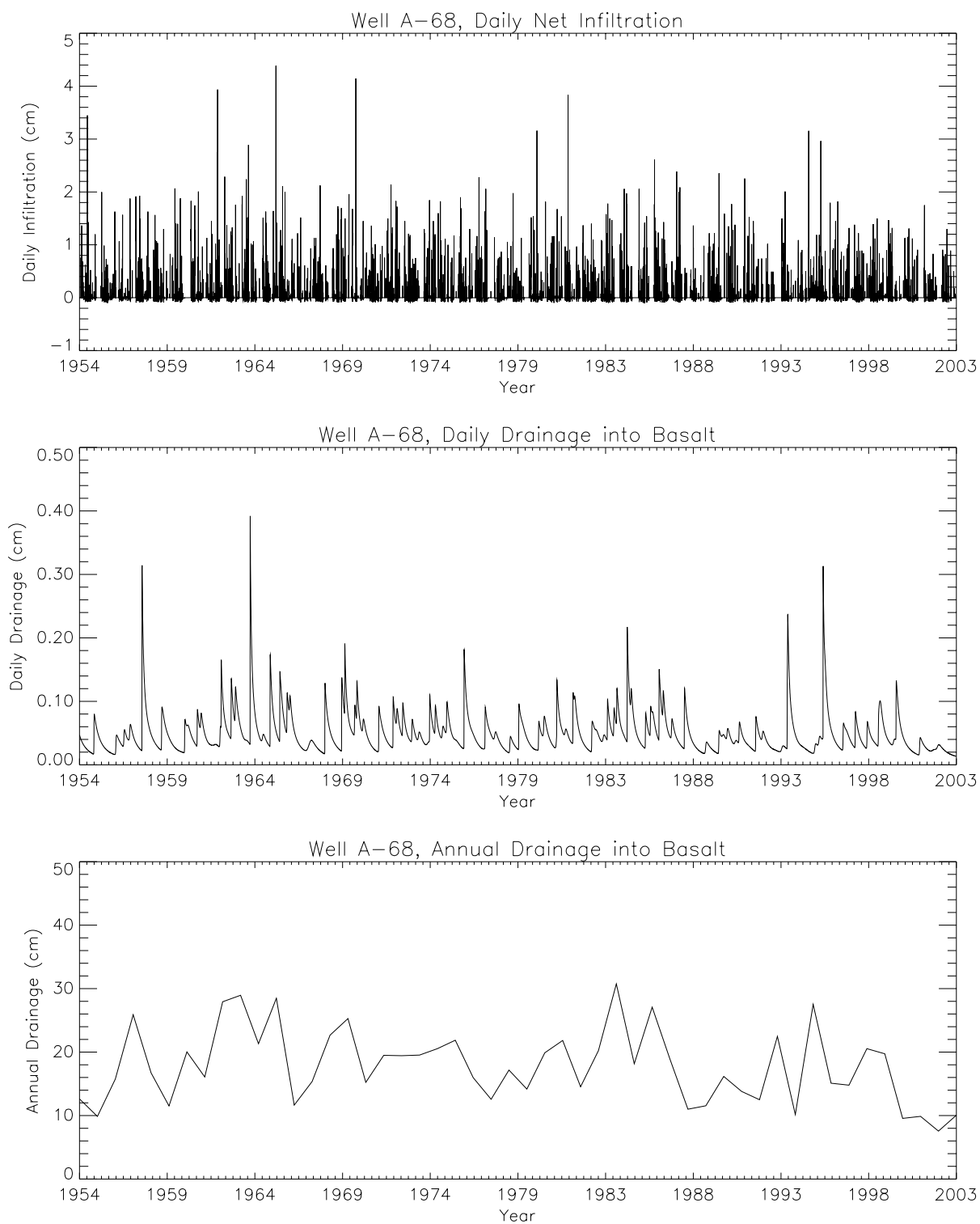


Figure B-B-14. Daily infiltration, daily drainage, and annual average drainage at Well A-68.

Appendix C

Geostatistical Modeling of Subsurface Characteristics in the Area of the Idaho Nuclear Technology and Engineering Center

Molly K. Leecaster

CONTENTS

C-1. INTRODUCTION	C-11
C-2. DATA	C-11
C-2.1 H-I Interbed	C-12
C-2.2 Aquifer Hydraulic Conductivity	C-12
C-2.3 Vadose Zone Lithology	C-12
C-2.4 Surface Elevation.....	C-16
C-3. METHODS.....	C-17
C-3.1 Data Assessment.....	C-17
C-3.2 Semivariograms	C-20
C-3.2.1 Empirical Semivariograms	C-20
C-3.2.2 Directional Semivariograms.....	C-21
C-3.2.3 Semivariogram Modeling.....	C-23
C-3.3 Kriging.....	C-24
C-3.4 Model Assessment.....	C-28
C-3.5 Prediction Uncertainty	C-30
C-4. RESULTS.....	C-31
C-4.1 H-I Interbed Top Elevation and Thickness.....	C-31
C-4.1.1 Data Assessment	C-31
C-4.1.2 Semivariograms.....	C-37
C-4.1.3 Kriging	C-37
C-4.1.4 Model Assessment	C-40
C-4.2 Aquifer Hydraulic Conductivity	C-45
C-4.2.1 Data Assessment	C-45
C-4.2.2 Semivariograms.....	C-48
C-4.2.3 Kriging and Model Assessment	C-48
C-4.3 Vadose Zone Lithology	C-54
C-4.3.1 Data Assessment	C-54
C-4.3.2 Semivariograms.....	C-55
C-4.3.3 Kriging	C-72
C-4.3.4 Model Assessment	C-72

C-4.3.5	Prediction Uncertainty.....	C-87
C-5.	DISCUSSION.....	C-89
C-5.1	H-I Interbed Thickness and Top Elevation.....	C-90
C-5.2	Aquifer Hydraulic Conductivity.....	C-90
C-5.3	Vadose Zone Lithology	C-91
C-6.	REFERENCES	C-92

FIGURES

C-1.	Well locations for sample results contained in the H-I interbed database	C-14
C-2.	Well locations for sample results contained in the aquifer hydraulic conductivity database.....	C-15
C-3.	Well locations for sample results contained in the subsurface lithology database	C-16
C-4.	Two prediction grids for subsurface lithology predictions	C-18
C-5.	Empirical semivariogram with model parameters labeled.....	C-23
C-6.	Empirical cumulative distribution of observed H-I interbed elevation, declustered data, predictions based on up to five sample locations (Krige5), predictions based on up to 10 sample locations (Krige10), and predictions based on all sample locations (KrigeAll)	C-27
C-7.	Histograms of observed H-I interbed thickness and predictions from ordinary kriging and trend plus kriging	C-31
C-8.	Declustering cell size versus declustered mean for H-I interbed thickness	C-32
C-9.	Empirical cumulative distribution for H-I interbed thickness observed values, kriging predictions, and declustered data	C-32
C-10.	Histograms of observed H-I interbed elevation and predictions from ordinary kriging and trend plus kriging	C-34
C-11.	Trend plus kriging predicted H-I interbed elevation, to compare to kriging predictions in Figure C-20. Black points represent sample locations.....	C-34
C-12.	Declustering cell size versus declustered mean for H-I interbed elevation	C-35
C-13.	Empirical cumulative distribution for observed H-I interbed elevation values, kriging predictions, and declustered data	C-35
C-14.	Histogram of observed H-I interbed thickness (m) values.....	C-36
C-15.	Histogram of observed H-I interbed elevation (m amsl) values	C-37

C-16.	Semivariograms for H-I interbed thickness	C-38
C-17.	Semivariograms for H-I interbed elevation	C-38
C-18.	Kriging predictions for H-I interbed thickness (m)	C-39
C-19.	Kriging variances (m^2) for H-I interbed thickness	C-39
C-20.	Kriging predictions for H-I interbed elevation	C-40
C-21.	Kriging variances (m^2) for H-I interbed elevation	C-41
C-22.	Histograms of observed H-I interbed thickness, hold-one-out predictions at sample locations, and kriging predictions on the grid	C-41
C-23.	Observed values versus the hold-one-out kriging predictions for H-I interbed thickness	C-42
C-24.	Histogram of hold-one-out errors (predicted minus observed) for H-I interbed thickness	C-43
C-25.	Histograms of observed H-I interbed elevation, hold-one-out predictions at sample locations, and kriging predictions on grid	C-44
C-26.	Observed values versus the hold-one-out predictions for H-I interbed elevation	C-44
C-27.	Histogram of hold-one-out errors (predicted minus observed) for H-I interbed elevation	C-45
C-28.	Histogram of observed aquifer hydraulic conductivity	C-46
C-29.	Histogram of the natural log of observed aquifer hydraulic conductivity	C-46
C-30.	Histogram of normal score transformed aquifer hydraulic conductivity	C-47
C-31.	Declustering cell size versus declustered mean for natural log transformed aquifer hydraulic conductivity	C-47
C-32.	Empirical cumulative distribution for natural log transformed aquifer hydraulic conductivity observed values, kriging predictions, and declustered data	C-48
C-33.	Semivariogram of normal score transformed aquifer hydraulic conductivity	C-49
C-34.	Back-transformed kriging predictions of aquifer hydraulic conductivity	C-49
C-35.	Back-transformed lower confidence limits for kriging predictions of natural log aquifer hydraulic conductivity	C-50
C-36.	Back-transformed upper confidence limits for kriging predictions of natural log aquifer hydraulic conductivity	C-50
C-37.	Back-transformed kriging predictions of aquifer hydraulic conductivity on finer, smaller grid around INTEC. Sample locations are included as black dots	C-51

C-38.	Back-transformed lower confidence limits of predicted aquifer hydraulic conductivity on finer, smaller grid around INTEC	C-51
C-39.	Back-transformed upper confidence limits of predicted aquifer hydraulic conductivity on finer, smaller grid around INTEC	C-52
C-40.	Histograms of natural log transformed observed aquifer hydraulic conductivity, hold-one-out predictions at sample locations, and kriging predictions on the grid	C-53
C-41.	Natural log observed aquifer hydraulic conductivity versus hold-one-out predictions	C-53
C-42.	Histograms of natural log transformed observed aquifer hydraulic conductivity, hold-one-out predictions at sample locations, and kriging predictions, all on the smaller prediction grid	C-54
C-43.	Histogram of observed surficial alluvium thickness values.....	C-55
C-44.	Histogram of observed 110-ft interbed thickness values	C-56
C-45.	Histogram of observed 140-ft interbed thickness values	C-56
C-46.	Histogram of observed BM interbed thickness values.....	C-57
C-47.	Histogram of observed 380-ft interbed thickness values	C-57
C-48.	Histogram of observed 110-ft interbed top elevation values	C-58
C-49.	Histogram of observed 140-ft interbed top elevation values	C-58
C-50.	Histogram of observed BM interbed top elevation values.....	C-59
C-51.	Histogram of observed 380-ft interbed top elevation values	C-59
C-52.	Surficial alluvium thickness semivariograms	C-61
C-53.	The 110-ft interbed thickness semivariograms	C-61
C-54.	The 140-ft interbed thickness semivariograms	C-62
C-55.	The BM interbed thickness semivariograms.....	C-62
C-56.	The 380-ft interbed thickness semivariograms	C-63
C-57.	The 110-ft interbed elevation semivariograms	C-63
C-58.	The 140-ft interbed elevation semivariograms	C-64
C-59.	The BM interbed elevation semivariograms	C-64
C-60.	The 380-ft interbed elevation semivariograms	C-65
C-61.	Surficial alluvium permeability category 3-D semivariograms	C-65

C-62.	The 110-ft interbed permeability category 3-D semivariograms	C-66
C-63.	The 140-ft interbed permeability category 3-D semivariograms	C-66
C-64.	The BM interbed permeability category 3-D semivariograms	C-67
C-65.	The 380-ft interbed permeability category 3-D semivariograms	C-67
C-66.	Permeability Category 3 (high-permeability interbed) 3-D semivariograms.....	C-68
C-67.	Permeability Category 4 (low-permeability interbed) 3-D semivariograms.....	C-68
C-68.	Permeability Category 5 (high-permeability basalt) 3-D semivariograms	C-69
C-69.	Permeability Category 6 (low-permeability basalt) 3-D semivariograms	C-69
C-70.	Permeability Category 3 (high-permeability interbed) 3-D vertical semivariograms.....	C-70
C-71.	Permeability Category 4 (low-permeability interbed) 3-D vertical semivariograms.....	C-70
C-72.	Permeability Category 5 (high-permeability basalt) 3-D vertical semivariograms	C-71
C-73.	Permeability Category 6 (low-permeability basalt) 3-D vertical semivariograms	C-71
C-74.	Combined kriging predicted subsurface soil layers	C-72
C-75.	Histograms of observed and predicted surficial alluvium thickness.....	C-73
C-76.	Histograms of observed and predicted 110-ft interbed thickness	C-73
C-77.	Histograms of observed and predicted 140-ft interbed thickness	C-74
C-78.	Observed and predicted BM interbed thickness	C-74
C-79.	Observed and predicted 380-ft interbed thickness	C-75
C-80.	Observed and predicted 110-ft interbed top elevation	C-75
C-81.	Observed and predicted 140-ft interbed top elevation	C-76
C-82.	Observed and predicted BM interbed top elevation.....	C-76
C-83.	Observed and predicted 380-ft interbed top elevation	C-77
C-84.	Observed surficial alluvium thickness versus hold-one-out kriging predictions	C-77
C-85.	Observed 110-ft interbed thickness versus hold-one-out kriging predictions.....	C-78
C-86.	Observed 140-ft interbed thickness versus hold-one-out kriging predictions.....	C-78
C-87.	Observed BM interbed thickness versus hold-one-out kriging predictions.....	C-79

C-88.	Observed 380-ft interbed thickness versus hold-one-out kriging predictions.....	C-79
C-89.	Observed 110-ft interbed top elevation versus hold-one-out kriging predictions.....	C-80
C-90.	Observed 140-ft interbed top elevation versus hold-one-out kriging predictions.....	C-80
C-91.	Observed BM interbed top elevation versus hold-one-out kriging predictions	C-81
C-92.	Observed 380-ft interbed top elevation versus hold-one-out kriging predictions.....	C-81
C-93.	Histogram of surficial alluvium thickness hold-one-out errors (predicted minus observed).....	C-82
C-94.	Histogram of 110-ft interbed thickness hold-one-out errors (predicted minus observed)	C-82
C-95.	Histogram of 140-ft interbed thickness hold-one-out errors (predicted minus observed)	C-83
C-96.	Histogram of BM interbed thickness hold-one-out errors (predicted minus observed).....	C-83
C-97.	Histogram of 380-ft interbed thickness hold-one-out errors (predicted minus observed)	C-84
C-98.	Histogram of 110-ft interbed top elevation hold-one-out errors (predicted minus observed) ...	C-84
C-99.	Histogram of 140-ft interbed top elevation hold-one-out errors (predicted minus observed) ...	C-85
C-100.	Histogram of BM interbed top elevation hold-one-out errors (predicted minus observed).....	C-85
C-101.	Histogram of 380-ft interbed top elevation hold-one-out errors (predicted minus observed) ...	C-86
C-102.	Transport-retardant extreme combined spatial stochastic simulation subsurface soil layers.....	C-88
C-103.	Transport-conductive extreme combined spatial stochastic simulation subsurface soil layers	C-89

TABLES

C-1.	Subsurface characteristic variables used in modeling.....	C-13
C-2.	Characteristics of omnidirectional empirical semivariograms.....	C-22
C-3.	Horizontal and vertical search radius specifications used for kriging	C-26
C-4.	Summary statistics for H-I interbed thickness: observed values, ordinary kriging predictions, and trend plus kriging predictions	C-33
C-5.	Summary statistics for H-I interbed elevation: observed values, ordinary kriging predictions, and trend plus kriging predictions.....	C-36
C-6.	Cross-validation statistics for H-I interbed thickness and top elevation.....	C-42
C-7.	Cross-validation statistics for aquifer hydraulic conductivity	C-54

C-8.	Semivariogram model parameters for vadose zone lithology variables	C-60
C-9.	Cross-validation summary statistics for continuous vadose zone lithology variables	C-86
C-10.	Relative frequency of permeability categories for all prediction grids.....	C-87
C-11.	Relative frequency of permeability categories on 1-m vertical grid for adjusted observed, kriging predictions, and simulated realizations for thin soil and high-permeability category and for thick soil and low-permeability category	C-88

Appendix C

Geostatistical Modeling of Subsurface Characteristics in the Area of the Idaho Nuclear Technology and Engineering Center

C-1. INTRODUCTION

The flow and transport model described in Appendix A of this report requires a framework for the vadose zone and aquifer lithology. The subsurface in and around the Idaho Nuclear Technology and Engineering Center (INTEC) is dominated by extreme heterogeneity in the vadose zone and aquifer consisting of interbedded basalts and sediments. The basalt and interbed layers, as well as the soil subtypes within, are characterized by differing hydraulic conductivity and transport pathways.

Realistic predictions of subsurface characteristics improve decision-making based on predicted risk to the aquifer. The predictions for depth of subsurface sediment and basalt layers and aquifer hydraulic conductivity are required at a small scale over the entire area of interest in order to predict flow and transport on a scale that supports decision-making. These variables are measured at only a sample of sites. Predictions between and beyond those sample sites must be made because the flow and transport model extends to the whole area of interest.

Previous efforts (DOE-ID 1997) used a relatively simplistic model for the vadose zone lithology. This approach assigned the combined interbed thickness to four layers, or effective interbeds, and the remaining volume of the vadose zone as unfractured basalt, which is highly permeable. Although this approach might have used a reasonable total volume of interbed, the placement in four relatively continuous layers is not realistic given the new data that lateral transport in the vadose zone from the former INTEC percolation ponds was less than predicted. Since the previous modeling effort, new data have been collected and interpreted upon which to base kriging predictions for subsurface characteristics. The values used in the model for aquifer hydraulic conductivity were not based on kriging predictions. Hydraulic conductivity may portray spatial correlation that would improve predictions (Leecaster and Hull 2004).

The current approach for predicting subsurface characteristics improves on the previous effort in two ways: data completeness and modeling rigor. The data sets for modeling contain all existing well data. The vadose zone lithology data are interpreted for each foot of depth and categorized as two permeabilities for each of surficial alluvium, interbed, and basalt. The predictions are based on kriging models that use spatial correlation information from the data and are applied to the vadose zone as a layered volume (instead of lumped into four effective interbeds).

This appendix summarizes the data sets, data assessment, semivariogram calculation and modeling, kriging models, model assessment, and prediction uncertainty.

C-2. DATA

Four separate data sets are assembled and analyzed. These correspond to the three spatial modeling efforts (H-I interbed within the aquifer, aquifer hydraulic conductivity, and vadose zone lithology) and the surface elevation. The three spatial modeling efforts are presented separately because the prediction scales are different for the aquifer and the vadose zone, and the two aquifer variables are independent.

All data sets have clustered locations: dense within the INTEC fence, some locations NE and SW to follow the groundwater flow path, and very few or no locations NW and SE of the INTEC fence (Table C-1). These locations were preferentially chosen to represent areas of interest, not preferentially chosen to provide specific data values (like hotspot sampling). Thus, although the data locations are clustered, the clustering should not correspond to the measured values, but declustering of the data values was explored during data assessment.

C-2.1 H-I Interbed

The H-I interbed is a widespread layer of sediment overlying Basalt Flow Group I. The interbed tends to dip in the southeast direction when viewed from a large scale (OU 3-13 RI/BRA aquifer model domain), and the interbed tends to become thicker and more continuous in the southeast direction. Well logs from Wells SPERT-IV and Site-09 (southeast of INTEC) indicate the interbed can be approximately 90 ft thick in some areas. The spatial model of this interbed is based on 55 sample locations (Figure C-1) with top elevation and thickness measurements (Anderson 1989, Anderson 1991, and DOE-ID 2002). The well data have five zero thickness values, and the top elevation ranges from 1,212 to 1,395 m amsl (3,977 to 4,577 ft) and in depth from 100 to 290 m (328 to 951 ft) bgs. Six of the wells did not fully penetrate the HI interbed, so the thickness values were qualified as > the depth of the well. These values were used without attempts to estimate the true thickness.

C-2.2 Aquifer Hydraulic Conductivity

The permeability property for the aquifer is represented by the hydraulic conductivity (K, ft/day) within the H basalt layer. The H basalt layer is directly above the H-I interbed and is completely within the saturated zone. The top elevation of the H basalt layer is from 1,297 to 1,393 m amsl (4,255 to 4,570 ft) and from 3 to 35 m (10 to 120 ft) in thickness. These aquifer hydraulic conductivity data are from 128 wells and provided in Appendix A of this report (Table A-4-2 in Appendix A). Of these, 53 wells are within the prediction grid (Figure C-2). The measured values range from 0.01 to 7,379 ft/day.

C-2.3 Vadose Zone Lithology

The vadose zone geologic characteristics of the area were combined from various sources and interpreted^a.

Some of the permeability categories within interbed layers were modified after the interpretations were finalized. The changes were made to correspond to measured perched water data; water perches on low-permeability areas. The changes were relatively few (affected 25 wells at 1 to 30 ft in thickness for a total of about 200 ft) but were important to ensure the well data would reflect the presence/absence of perched water.

a. Cahn, L.C., CH2M-WG Idaho, LLC, Interoffice Memorandum, to R. Bowser, CH2M-WG Idaho, LLC, April 21, 2005, "Transmittal of Operable Unit 3-14 Geologic Data Base for a Vadose Zone Model," LSC-01-05. Note: This may contain Official Use Only data and is not available to the public.

Table C-1. Subsurface characteristic variables used in modeling.

Variable Name	Number of Wells with Data	Depth Interval (m)	Average Well Spacing (m)	Minimum Well Spacing (m)	Maximum Well Spacing (m)
H-I Interbed Top Elevation	55	1,212–1,395	5,179	28	20,932
H-I Interbed Thickness	55	0–27	5,179	28	20,932
Aquifer Hydraulic Conductivity	128	Not available	23,962	6	66,084
Surficial Alluvium Thickness	120 or 119	1–21	915	1	3,026
Surficial Alluvium Permeability Category	120 or 119	1,474–1,503	915	1	3,026
110-ft Interbed Top Elevation	84	1,457–1,472	929	1	3,026
110-ft Interbed Thickness	93	0–17	1,000	1	3,026
110-ft Interbed Permeability Category	84	1,449–1,472	929	1	3,026
140-ft Interbed Top Elevation	59	1,445–1,461	1,077	13	3,026
140-ft Interbed Thickness	73	0–13	1,077	1	3,026
140-ft Interbed Permeability Category	59	1,441–1,461	1,077	13	3,026
BM Interbed Top Elevation	58	1,362–1,405	1,136	1	2,995
BM Interbed Thickness	60	0–12	1,115	1	2,995
BM Interbed Permeability Category	60	1,362–1,405	1,115	1	2,995
380-ft Interbed Top Elevation	18	1,364–1,380	926	16	2,995
380-ft Interbed Thickness	62	0–9	1,124	1	3,026
380-ft Interbed Permeability Category	18	1,359–1,380	926	16	2,995
Permeability Category 3	42	1,366–1,485 17–133	1,133	1	2,906
Permeability Category 4	52	1,364–1,489 7–137	969	1	3,026
Permeability Category 5	120	1,358–1,498 2–137	915	1	3,026
Permeability Category 6	28	1,358–1,488 11–137	817	16	2,727

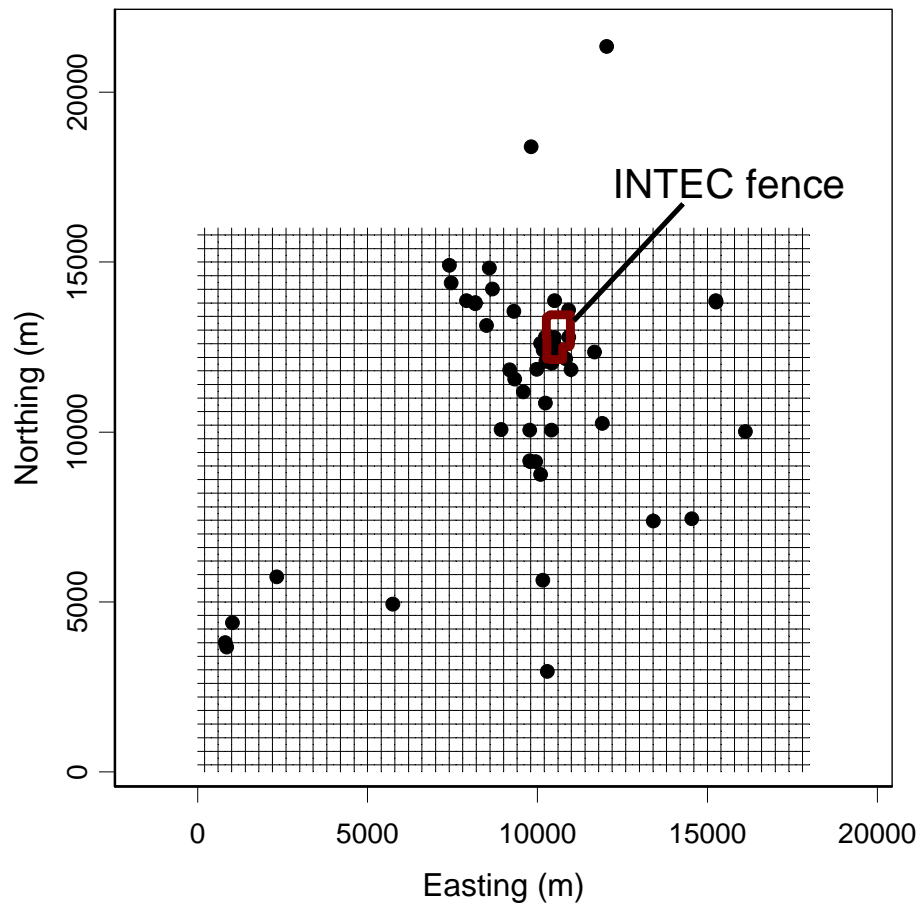


Figure C-1. Well locations for sample results contained in the H-I interbed database. Small points represent the prediction grid used in kriging. Coordinates are relative to the figure and, although they represent meters, they do not correspond to a land surface location.

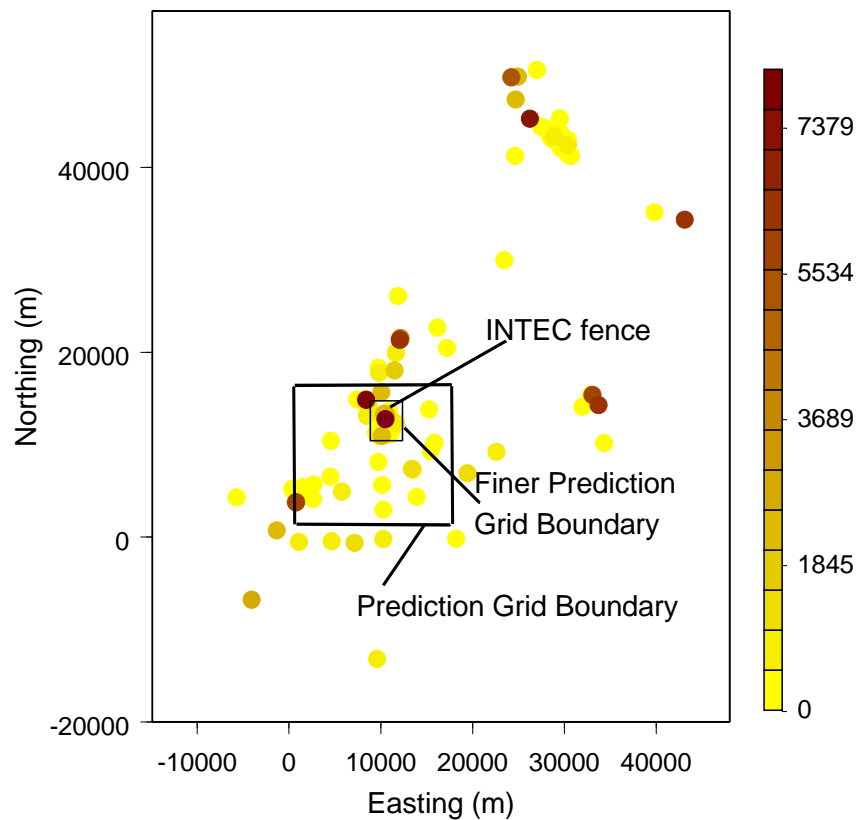


Figure C-2. Well locations for sample results contained in the aquifer hydraulic conductivity database. Color corresponds to hydraulic conductivity. Square outline is the prediction grid boundary. Coordinates are relative to the figure and, although they represent meters, they do not correspond to a land surface location.

The final data set has 121 wells, to varying depths (Figure C-3), with named layers for each foot. Almost half of the wells extend to the assumed depth of the aquifer (130 m), while almost 80% are at least 30 m deep. The dataset includes well location, depth, elevation, material type, permeability category, as well as background information such as well-type, material description, and other information available (such as gamma log).

The dataset is used in two ways. The first is to separate out the mostly continuous soil layers. These are the surficial alluvium, 110-ft interbed, 140-ft interbed, the interbed below the middle massive basalt (BM interbed), and the 380-ft interbed. These soil layers are modeled separately from the other vadose zone material to retain their continuity. For surficial alluvium, the thickness values are parsed (the surface elevation is obtained separately). For the interbeds, the elevation at the tops of the interbeds and thicknesses are parsed. For wells that do not have a particular interbed, the thickness is assigned zero, and there is no corresponding top elevation value. The second way the dataset is used is to predict permeability categories using indicator kriging. This is done for the five soil layers separately and for the remainder of the vadose zone volume. These models are discussed in detail in the Section C-3.

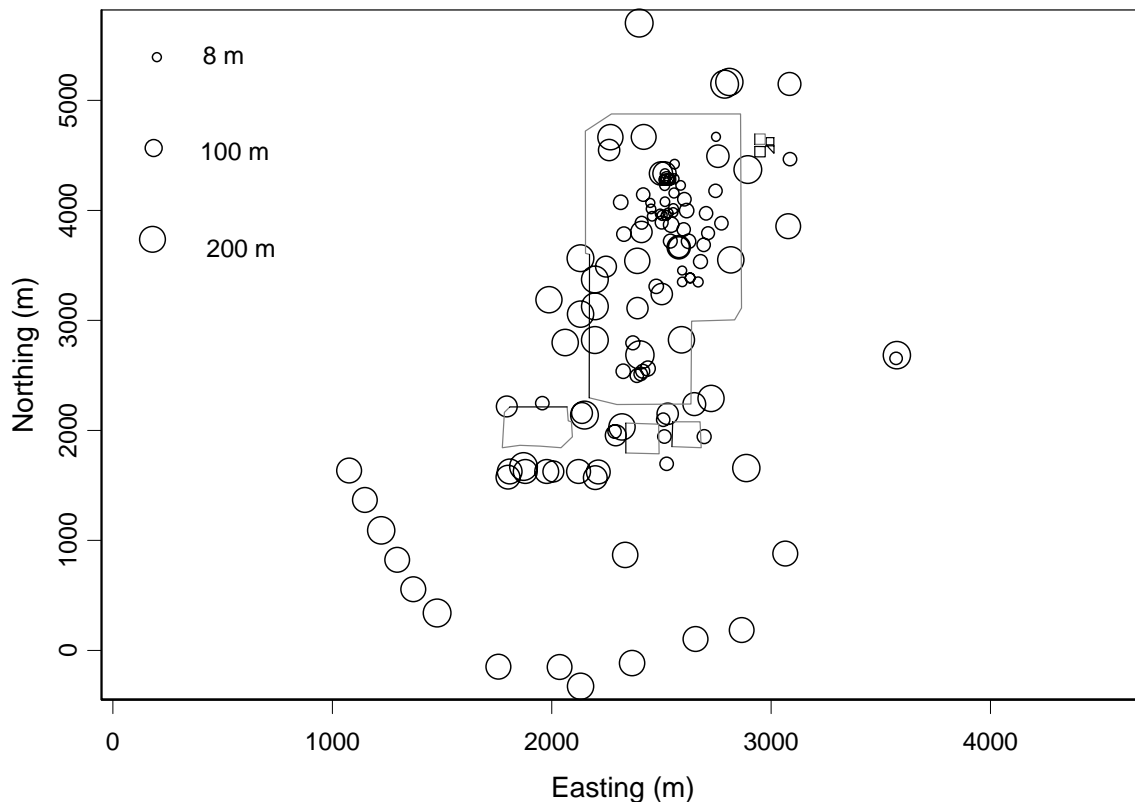


Figure C-3. Well locations for sample results contained in the subsurface lithology database. The INTEC fence, ICDF, and former percolation ponds are outlined in gray. The size of the circles represents well depth. Coordinates are relative to the figure and, although they represent meters, they do not correspond to a land surface location.

These models use 15 variables to predict vadose zone lithology. These variables are the surficial alluvium thickness, top elevation and thickness of the four main interbeds (110-ft, 140-ft, BM, and 380-ft), permeability category within each of these five soil layers, and permeability category in the remaining vadose zone volume.

C-2.4 Surface Elevation

The surface elevation data were obtained from digital elevation models. The data were on a grid of 10×10 m, but the flow and transport model uses a grid of 100×100 m over the whole ground surface domain and 50×50 m in the refined portion of the model. So the ground surface elevation data were averaged over the defined prediction blocks (see Section C-3 for a description of the prediction areas).

C-3. METHODS

The goal of predicting subsurface characteristics over this volume of interest was achieved through many steps: (1) the data were assessed, (2) spatial correlation was investigated and modeled, (3) the kriging predictions were calculated, (4) the kriging predictions were assessed, and (5) prediction uncertainty was estimated. These five steps are detailed in the five subsections that follow. The methods for the steps are presented in general, with specifics to data sets discussed as necessary. The overarching ideas and study boundaries to the prediction volume are presented here first.

Kriging models were used to predict values of lithologic concern and aquifer hydraulic conductivity at unsampled locations. Kriging uses the spatial relationship among sample locations to improve prediction over a grid. Although several variations of kriging on various layers were attempted, the predictions were based on a combination of 2D ordinary kriging and 3D indicator kriging. Predicting some soil layers separately produced the most reasonable results; predictions agreed with geologic expectations. Also in support of this, Bouma and Finke (1993) suggest that “[geostatistics] is most effective when applied separately within different soil units of the soil map.”

The H-I interbed top elevation and thickness were predicted onto site-specific coordinates covering 18,000 m in the W-E direction and 16,000 m in the N-S direction. Each grid cell was 400×400 m (consistent with the aquifer flow and transport model), so there were 45 grid cells in the W-E direction and 40 in the N-S direction.

The aquifer hydraulic conductivity values were predicted on the grid specified for the H-I interbed and a finer grid over a smaller area (Figure C-2). The finer grid had 36×44 cells of size 100×100 m.

The vadose zone lithology predictions were made on four 3-D grids: two horizontal grids (100×100 m and 50×50 m) and two vertical grids (1 and 2 m). These four grids were all used in the flow and transport model in separate volumes. The two horizontal grids have different ranges. The 100×100 -m grid covers just beyond the INTEC fence and the 50×50 -m grid range is smaller and in the north part of the INTEC (Figure C-4). The 1-m grids were used for upper elevations and 2-m grids for lower elevations. These were used for both of the horizontal grids. The vertical grid ranges from the surface to 130 m (450 ft), the approximate depth to the aquifer.

All semivariograms were calculated and modeled, kriging predictions calculated, cross validation performed, and uncertainty estimated in *GSLIB: Geostatistical Software Library* (Deutsch and Journel 2000).

C-3.1 Data Assessment

The three data sets (H-I interbed within the aquifer, aquifer hydraulic conductivity, and vadose zone lithology) were assessed separately. All data were assessed for normality because kriging relies on data being symmetric, and, ideally, normally distributed (Goovaerts 1997). In addition, the vadose zone lithology data were assessed for consistency among wells and depths and parsed in preparation for the various models used to create the volume of vadose zone predictions. Also, data were assessed for trend using regression on easting and northing coordinates. If a significant trend was found, then it was included in the modeling process. Finally, the data were declustered to investigate whether the sample locations affected the distribution of the data values.

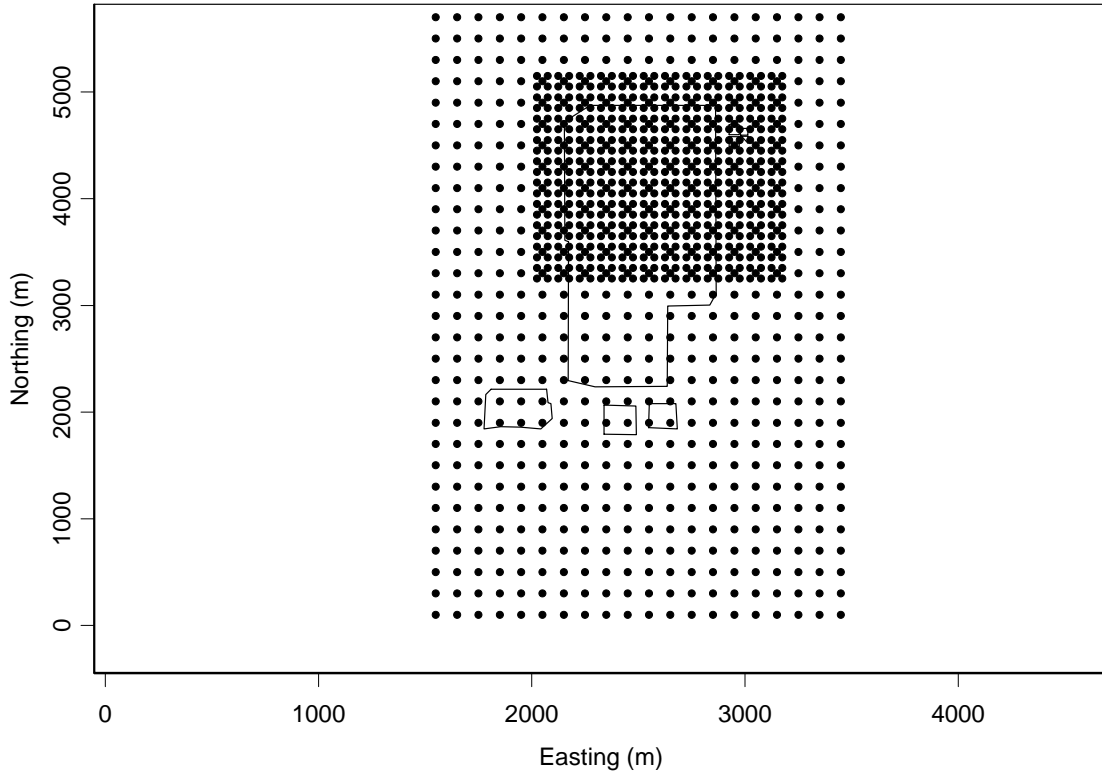


Figure C-4. Two prediction grids for subsurface lithology predictions. The INTEC fence, ICDF, and former percolation ponds are outlined. Coordinates are relative to the figure and, although they represent meters, they do not correspond to a land surface location.

The data were assessed for symmetry by looking at histograms. If the data were skewed, then a Shapiro-Wilk test for lognormality was conducted. If the data were lognormal, then they were natural log-transformed, $y = \ln(x)$, where x is the original variable. If the data were not lognormal, then a normal score transform was used. The normal score transformation is

$$y_i = G^{-1}\left(\frac{c_i + c_{i-1}}{2}\right), \quad (\text{C-1})$$

where

G^{-1} = inverse standard normal function

c_i = empirical cumulative probability associated with the i^{th} largest data value.

The back-transformation for the kriging predictions is

$$z_i = F^{-1}(G(y_i)), \quad (C-2)$$

where

F^{-1} = declustered cumulative distribution function of the original data.

In lieu of back-transforming the kriging variance, confidence limits (y_i^{LCL} , y_i^{UCL}) are back-transformed, using Equation C-2, for use in uncertainty/sensitivity analysis of the flow and transport model.

Additional data assessment and management were required for the vadose zone lithology database due to the greater complexity. Preliminary modeling efforts to predict permeability categories over the entire vadose zone volume at once were unsuccessful. The continuous nature of the surficial alluvium and main interbeds was very different than the rest of the volume, which was characterized by small disjointed interbedded materials. These initial predictions had the surficial alluvium merging with the first interbed and the main interbeds and very discontinuous. Thus, the surficial alluvium and the four main interbeds were separated from the remaining vadose zone lithology data. This process is detailed below.

The surficial alluvium data were parsed from the main database. The surface elevation was used as the top elevation of the surficial alluvium. The surficial alluvium thickness was determined by counting the number of surficial alluvium records (each represented 1 ft) in the database for each well. All wells had recorded surficial alluvium except USGS-81, where data began at 8 ft bgs with recorded basalt. Thus, the surficial alluvium was assumed to be 8 ft thick for this well.

The four main interbeds were parsed from the main database into four data sets. The top elevation and thickness for each main interbed in each well were extracted. The top elevation was obtained by taking the maximum elevation record for each main interbed within each well. The thickness was obtained by counting the number of records for each main interbed for each well. If a well did not have the interbed, then the top elevation record was a missing value, and the thickness was zero. Thus, there were, for each main interbed, more data for thickness than for top elevation.

For the surficial alluvium and four main interbeds, the permeability categories were also parsed into separate data sets. These data, simply lifted from the main database, were used to predict permeability category within those soil layers, separately from the rest of the volume.

The remaining vadose zone lithology data were retained, but with the surficial alluvium and four interbeds removed. Thus, the vadose zone lithology data set had large areas of missing data. This discouraged predicted joining of the main soil layers to the smaller interbeds.

There were 15 sets of data for which semivariograms and models were calculated: the surficial alluvium thickness and permeability; the thickness, top elevation, and permeability for each of the four main interbeds; and the permeability for the remaining vadose zone lithology. The predictions were combined back into one data set, with the surficial alluvium and main interbed predictions taking precedence over the predictions on the remaining volume.

Trend in sample values was assessed through regression analysis on the easting and northing coordinates, their interaction, and quadratic forms. A backward selection algorithm was used to determine a best model; first the full model was fit and successively insignificant (t-test $p > 0.05$) terms were

removed until a significant (F-test $p < 0.05$) model with all significant (t-test $p < 0.05$) terms remained. The residuals from the final regression model were spatially modeled, and the kriging predictions of the residuals were added to the regression predictions to create the final predictions. These were compared to the kriging predictions on the data values to assess the impact of modeling a trend.

The data locations were not systematic, and they did not cover the entire prediction range. The clustering of data locations may be related to a clustering of the data values. Data value clustering may cause bias in the predictions, so was investigated. To determine if the clustering of locations was related to clustering of values, cell declustering analyses were performed. Declustered data were weighted by the degree of isolation of the sample location; values that were located far from others had a greater weight than values closely surrounded by others. The cell declustering method uses cells of a specified size, overlaid on the sample locations. The weights for values from locations within a cell were assigned a weight of 1 over the number of locations within the cell. These weights were then normalized, so they summed to the number of sample locations. The cell sizes were chosen to achieve a minimum or maximum declustered data mean, allowing for the maximum utility of the declustering. This was accomplished by plotting the cell size versus the declustered mean. The empirical cumulative distribution (ecd) of the data was compared to the ecd of declustered data. If the ecd of the weighted values was similar to the unweighted values, then it was assumed the clustering of sample locations was not related to clustering of data values. A Kolmogorov-Smirnov two-sample test was used to determine if the distributions were significantly different. These ecds were also compared to the ecd of the predictions.

C-3.2 Semivariograms

The empirical semivariogram for a set of data is the corresponding values of lag distance and variance between pairs of values at that approximate lag distance. The empirical semivariogram was fit with a model whose estimated parameters were used to calculate kriging predictions. Although the terms semivariogram and variogram are often used interchangeably, the correct use for the values and plots used in this report is semivariogram.

C-3.2.1 Empirical Semivariograms

The empirical semivariogram is equal to one-half the variance of paired sample differences taken at lag distance, h , plus or minus a tolerance,

$$\gamma(h) = \frac{1}{2} E \left[\{x_i - x_{i+h}\}^2 \right], \quad (C-3)$$

where

E = expectation function

x_i = observed value at location i

x_{i+h} = observed value at lag h from i .

The empirical semivariogram depended on four characteristics that were specified prior to calculation. These were the lag distances, the lag tolerance, the minimum number of pairs required to estimate the semivariogram at a lag, and the maximum distance at which to calculate the semivariogram. Each will be described separately although their impacts on the empirical semivariogram were not independent.

The distance lags (distance between two data locations used for calculating the semivariogram) were generally specified to provide an empirical semivariogram that had obvious structure but was not oversmoothed or undersmoothed. The lags were set to be small enough to discern the structure but large enough to avoid having sporadic imprecise estimates of variance that form a “jumpy” semivariogram. Another approach to selection of lags was to coordinate them to the prediction grid. This was applied for the H-I interbed top elevation and thickness and the aquifer hydraulic conductivity. The grid was on 400- × 400-m intervals, so that was used for the lag distance.

The lag tolerance was the interval around the lag distance for which pairs at that distance were included in that lag distance. The lag tolerance was set to 1/2 the lag so that pairs were used in only one lag distance.

The minimum number of pairs required to estimate the semivariogram at a lag was set to provide reliable estimates at all lags. This minimum was especially an issue at short lag distances, where often few pairs existed. This parameter was specified in coordination with the lag distance in order to achieve a reliable semivariogram. A rule of thumb is to have at least 30 pairs for each lag distance.

The maximum distance for semivariograms is generally specified as 1/2 the range of locations or prediction grid because the number of pairs at greater distance decreases rapidly. The maximum distance can also be specified as smaller than 1/2 the range to account for limited data or to reduce the scope of the semivariogram. The vital part of the semivariogram is at short lag distances, where strong spatial correlation exists. These relatively few, close data locations were used in the actual kriging equations, as explained below.

Note that all four characteristics were investigated simultaneously for their influence on the semivariogram. The effect of changing the values was assessed by looking at the semivariogram plots. Values were chosen to provide the semivariogram that was representative and could be modeled. The values used in the final semivariograms are in Table C-2.

C-3.2.2 Directional Semivariograms

Directional semivariograms were computed to investigate the assumption of isotropy. Isotropic data had spatial correlation that was independent of direction. To check this assumption, empirical semivariograms were calculated using only pairs that fell in specific directions (azimuths). These directional semivariograms were compared to an omnidirectional semivariogram. Similar semivariograms indicated the assumption of isotropy was valid. For a directional semivariogram, the direction was specified along with a tolerance. Azimuths of every 15° (with 10° tolerance) were considered for investigating anisotropy, but only four of these directions are presented. The four directional semivariograms were north-south (0°), northeast-southwest (45°), east-west (90°), and northwest-southeast (135°). The directional semivariogram was calculated using only pairs that were in the specified direction, plus or minus a tolerance angle of 22.5°, half the difference between azimuths.

Because some of the data were used in three-dimensional kriging, three-dimensional semivariograms were calculated. The difference for three-dimensional semivariograms was in specification of directional semivariograms. For data used in three-dimensional kriging, depth semivariograms were compared. The dip was the specified angle in the vertical direction and had an associated dip tolerance. The dips considered here were horizontal (0°), slanted (45°), and vertical (90°). The dip tolerance was specified as 22.5°. For these semivariograms, a vertical lag distance of 10 m, with tolerance of 5 m, was used.

Table C-2. Characteristics of omnidirectional empirical semivariograms. The surficial alluvium categories are 1 and 2, interbed categories are 3 and 4, and basalt categories are 5 and 6.

Variable Name	Dimension	Total Number of Lags	Lag Distance (m)	Lag Tolerance (m)	Maximum Distance (m)
H-I Interbed Top Elevation	2	12	400	200	4,800
H-I Interbed Thickness	2	12	400	200	4,800
Aquifer Hydraulic Conductivity	2	16	600	400	9,600
Surficial Alluvium Thickness	2	12	150	75	1,800
Surficial Alluvium Permeability Category (high or low)	3	15	60	30	900
110-ft Interbed Top Elevation	2	10	60	30	600
110-ft Interbed Thickness	2	10	60	30	600
110-ft Interbed Permeability Category	3	20	30	15	600
140-ft Interbed Top Elevation	2	15	60	30	900
140-ft Interbed Thickness	2	15	60	30	900
140-ft Interbed Permeability Category	3	20	30	15	600
BM Interbed Top Elevation	2	30	30	15	900
BM Interbed Thickness	2	20	60	30	1,200
BM Interbed Permeability Category	3	20	60	30	1,200
380-ft Interbed Top Elevation	2	20	90	45	1,800
380-ft Interbed Thickness	2	20	60	30	1,200
380-ft Interbed Permeability Category	3	20	90	45	1,800
Permeability Category 3 (high-permeability interbed)	3	20	100	50	2,000
Permeability Category 4 (low-permeability interbed)	3	20	100	50	2,000
Permeability Category 5 (high-permeability basalt)	3	20	100	50	2,000
Permeability Category 6 (low-permeability basalt)	3	20	100	50	2,000

C-3.2.3 Semivariogram Modeling

The empirical semivariograms were modeled by specifying model forms and estimating parameters. The estimated parameters of the semivariogram model were used in the kriging equations to weight data values used to predict values at unsampled locations.

The semivariogram model parameters are, except for special models, the nugget, sill, and range (Figure C-5). The nugget is the small-scale variance and is estimated as the variance at lag distance 0. If the sample locations are close enough, then this is easily estimable. Often this is considered equal to the measurement variance. A zero nugget is reasonable if the variance of the data is large compared to the measurement variance. The sill is the variance between pairs of values that are assumed to be independent. The estimated sill can be larger or smaller than the variance of the data overall, depending on the sample locations. For many close locations, the overall variance will provide an underestimate of the sill. For many distant locations, the overall variance may overestimate the sill. Models generally specify the partial sill, which is the sill minus the nugget. The range is the lag distance at which the sill is attained; the distance where values are independent.

The common models are the spherical, Gaussian, and exponential. The difference between these is the shape for close data points (near the origin of the semivariogram): the Gaussian is concave, the exponential is convex, and the spherical is almost linear. These models relay different behaviors in the spatial correlation of values. The Gaussian model implies that spatial correlation remains strong at increasing lag distances, the exponential implies that the spatial correlation drops off quickly at increasing lag distances, and the spherical model implies that the spatial correlation reduces almost linearly with increasing lag distance.

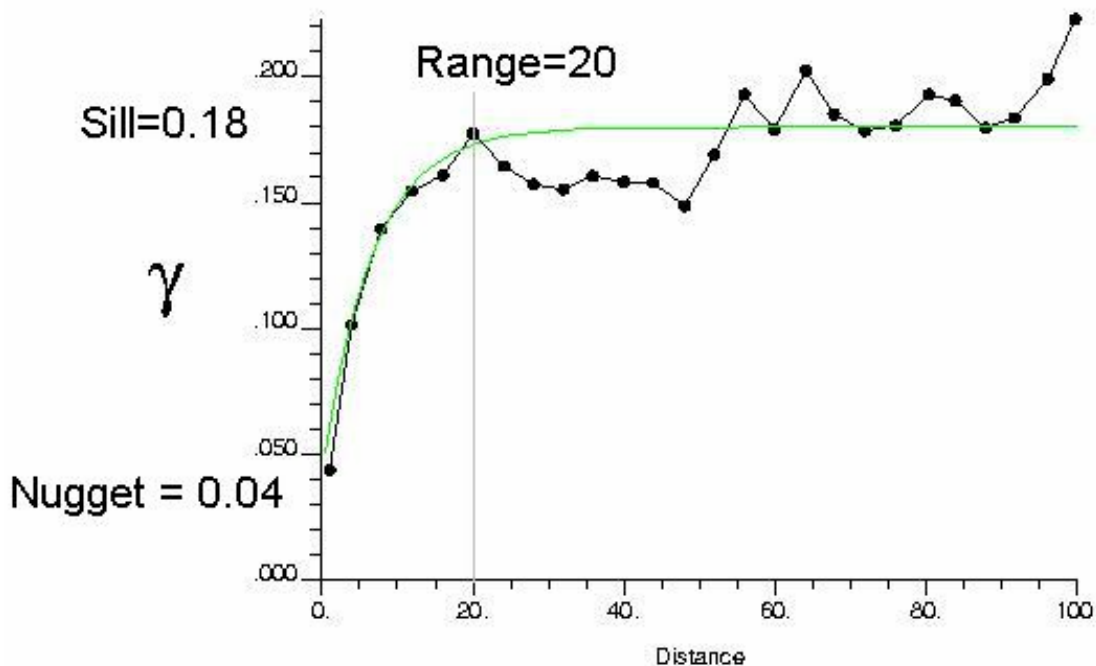


Figure C-5. Empirical semivariogram with model parameters labeled.

The model can be fit to the empirical semivariogram by automated fitting algorithms or “by eye.” The automated fitting algorithms are generally based on least squares or maximum likelihood. The least squares method is nonparametric and can be improved by weighting semivariogram points by lag distance or number of pairs used in the estimate. The maximum likelihood methods require the data to be normally distributed, which is often a problem even if they are symmetric. Regardless, these methods are often implemented in current software programs without knowledge of the intricacies of fitting a semivariogram. Fitting a semivariogram model by eye is labor-intensive and requires knowledge of the models and parameters. This approach produces a model that is closer to the empirical semivariogram than automated fitting algorithms and eliminated blatant errors. The models fit by eye may not be exactly reproducible by another geostatistician, but the fits would be close. The semivariogram models in this report were all fit by eye.

A series of directional semivariograms for one variable can be fit with a corresponding series of models and used in the kriging predictions. If the variable is anisotropic, then this complexity must be accounted for in the kriging predictions. The weights in the kriging equations will depend on the distance between prediction location and sample locations, but also the direction between them. This was done for the permeability categories, which used 3-D semivariograms and kriging.

C-3.3 Kriging

Kriging was used to predict values at unsampled locations as a weighted average of observed data. The kriging prediction for x_0 is

$$\hat{x}_0 = \sum_{i=1}^n \lambda_i x_i, \quad (C-4)$$

where

the weights, λ_i , are chosen so that

$$\sum_{i=1}^n \lambda_i = 1 \quad (C-5)$$

and the prediction variance is minimized.

The weight assigned to each observation was based on its distance from the prediction location and the semivariogram parameters. Observations closer to the prediction location had greater weight because they were assumed, according to the semivariogram, to have greater correlation. This section presents assumptions, input parameters, types of kriging, and kriging variance.

The two assumptions made for kriging were (1) spatial correlation was location-invariant (i.e., stationarity) and (2) spatial correlation was independent of direction (i.e., isotropy). Local stationarity, instead of global stationarity, was sufficient and assumed but isotropy was verified through investigation of directional semivariograms. Additionally, continuous variables were assumed to be symmetric but not necessarily normally distributed.

Kriging predictions were averaged over blocks instead of being reported for all points. The flow and transport modeling assumed a value over a block (grid cell), instead of at a point, so block kriging corresponded with its final use. The average prediction over the block was more realistic than the prediction at the center point of the block.

The kriging algorithm required input parameters to specify the minimum and maximum number of data points to use in each prediction and the search radius for data point to use in the prediction. These input parameters depended on the other's definition.

The minimum and maximum number of data points to use in each prediction was specified to prevent oversmoothing in the predictions. Theoretically, kriging is a global predictor, meaning all data points were used to make predictions. In practice, a few sample points were used to calculate predictions. The number of data points used depended on the density of the data, coverage of the sample locations, and the smoothness desired. Our data were patchy; there were many sample locations inside the INTEC and few outside of that area. We used between one and five sample points to calculate each prediction. Note that the weights from the semivariogram were used on these five points, so that closer locations had greater influence. The use of more sample locations did not overly influence the kriging variance but tended to smooth predictions toward the overall mean while extending the range of predictions beyond the range of data due to extending of, possibly unfounded, trends.

The search radius determines how many data points were used, between one and five, in each prediction. The search radius limited the data points from being too far away from the prediction location and prevented oversmoothing. We defined the search radius to be from 40 to 10,000 m depending on the value and the axis (horizontal or vertical); at least 10 times smaller radii were specified for vertical than horizontal (Table C-3). These values were specified to ensure that every grid point could be predicted (that at least one sample value was within that distance) and that the predictions were not overly influenced by far-reaching sample values. This was a difficult balance because often prediction locations are far from data locations, and at least one is needed to make a prediction. Because of this, the number of data points to use worked in combination with the search radius to prevent oversmoothing, while maintaining predictability. Note that these are loosely related to the maximum distance used for the semivariogram (Table C-2).

To illustrate the effect of the maximum number of sample locations and search radius, results using up to 10 sample locations and all sample locations are presented for H-I interbed elevation. The predictions from global predictions do not follow the same distribution as the declustered data (or raw data), while the kriging with up to 5 or up to 10 are closer (Figure C-6). The distribution of predictions from kriging with up to five locations is closer to the distribution of declustered data. This effect is seen for all modeled variables.

The input parameters used reflect differences in prediction grids and the use of 2-D or 3-D kriging. The H-I interbed top elevation and thickness and aquifer hydraulic conductivity were predicted on a much larger grid and displayed larger semivariogram range than the vadose zone lithology. The Other Permeability Category variable contained the information on disjointed interbeds and basalts, which displayed a shorter spatial range. The permeability category variables were modeled with 3-D kriging, so the vertical search radius was included and was generally small, as were the vertical spatial range parameters.

Table C-3. Horizontal and vertical search radius specifications used for kriging. Well locations that are farther away from the prediction location than this distance are not used in the kriging prediction. Only permeability categories are three-dimensional and require a vertical radius.

Variable Name	Horizontal Search Radius (m)	Vertical Search Radius (m)
H-I Interbed Top Elevation	10,000	NA ^a
H-I Interbed Thickness	10,000	NA
Aquifer Hydraulic Conductivity	10,000	NA
Surficial Alluvium Thickness	1,200	NA
Surficial Alluvium Permeability Category	1,000	25
Four Main Interbeds Top Elevation	1,500	NA
Four Main Interbeds Thickness	1,000	NA
Four Main Interbeds Permeability Category	2,000	40
<u>Other Subsurface Permeability Category</u>	500	50
a. NA = not applicable for 2-dimensional variables.		

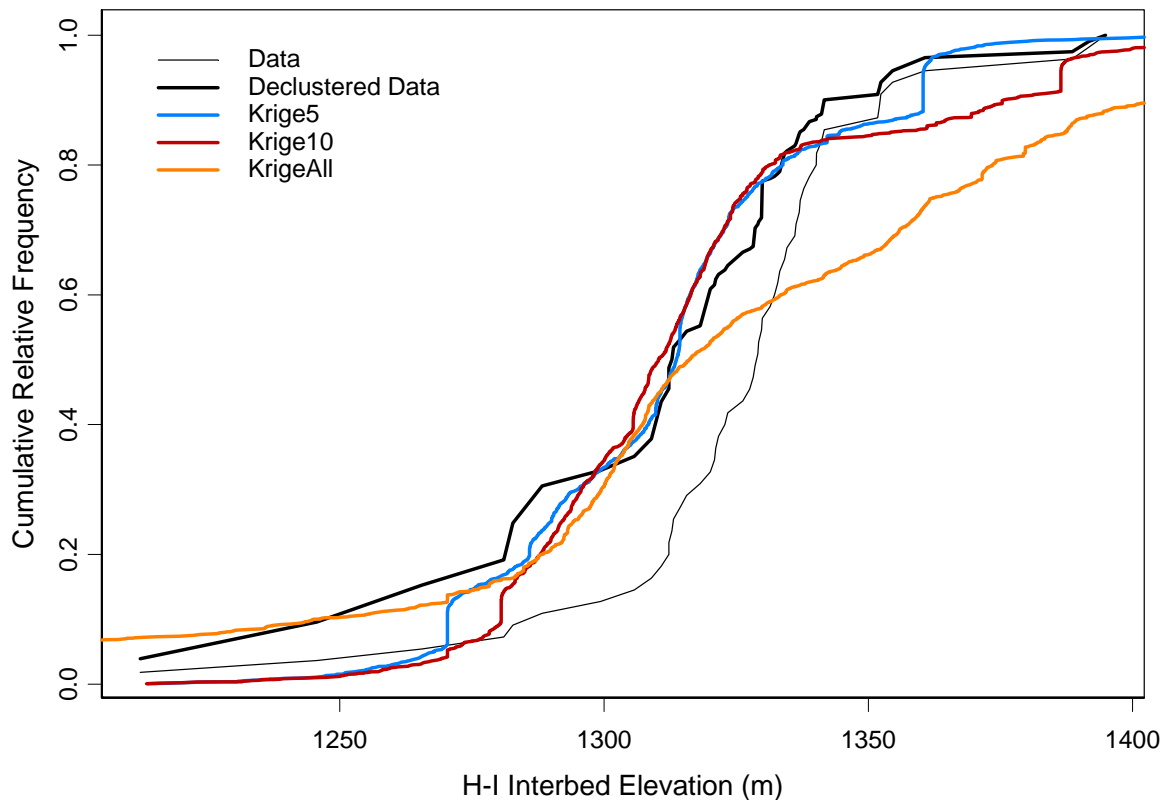


Figure C-6. Empirical cumulative distribution of observed H-I interbed elevation, declustered data, predictions based on up to five sample locations (Krige5), predictions based on up to 10 sample locations (Krige10), and predictions based on all sample locations (KrigeAll). This illustrates the importance of specifying the number of sample locations to use in kriging.

There were two forms of kriging used to account for the type of data and the assumptions made: ordinary kriging and indicator kriging. Ordinary kriging was used for continuous variables. The continuous variables were top elevation and thickness for the five main interbeds (including the H-I), surficial alluvium thickness, and aquifer hydraulic conductivity, which were modeled with 2-D kriging. The two assumptions specific to ordinary kriging were (1) locally unknown mean and (2) coefficients in the kriging equation sum to one. The first assumption was a relaxation of the assumption that the mean was known and applied globally. The second assumption ensured uniform unbiasedness in the predictions. Indicator kriging was used for categorical variables. The main interbed and surficial alluvium permeability values were binary and the permeability values for the rest of the vadose zone had four values. Indicator kriging made no additional assumptions. The indicator semivariograms were more labor-intensive because each category required an empirical (including directional) semivariogram and model.

C-3.4 Model Assessment

The predictions from the kriging models were assessed in two ways. The first was to compare the relative frequency of the predicted values to the observed values. Comparison of the distributions serves to ensure that the same population was represented by the predictions as was observed. If the observed values represented the population of interest, then the predicted values would follow the same distribution. This was performed on combined results, so, for vadose zone lithology, the relative frequency of permeability categories was compared. The second approach was through cross-validation using a hold-one-out approach. This analysis assessed the ability to predict specific values, not the population overall. This was done on all variables, prior to combination of vadose zone lithology models, so 18 separate analyses were performed.

The distributions of observed and predicted values were compared visually for H-I interbed top elevation and thickness and aquifer hydraulic conductivity and in a table for the vadose zone lithology permeability categories. For the vadose zone lithology, in particular, the observed values were not representative of the population due to drilling depth limitations. For instance, not all wells were drilled to aquifer depth, so that deeper ranges were underrepresented in the sample. Also, many wells were only drilled to the first basalt layer, so that the surficial alluvium was overrepresented in the sample. An adjusted relative frequency of observed permeability categories was compared to the predictions to account for this. The adjusted relative frequency for permeability category k , where

$$k = \begin{cases} 1 & \text{high permeability alluvium} \\ 2 & \text{low permeability alluvium} \\ 3 & \text{high permeability interbed} \\ 4 & \text{low permeability interbed} \\ 5 & \text{high permeability basalt} \\ 6 & \text{low permeability basalt} \end{cases}, \quad (\text{C-6})$$

was defined as

$$f_k = \frac{\sum_{i=1}^{121} \sum_{j=1}^{450} \frac{I_k(i, j)}{w_j}}{\sum_{i=1}^{121} \sum_{j=1}^{450} \frac{1}{w_j}}, \quad (\text{C-7})$$

where

$$I_k(i, j) = \begin{cases} 1 & \text{depth } j \text{ of well } i \text{ is permeability category } k \\ 0 & \text{otherwise} \end{cases}$$

$$w_j = \sum_{i=1}^{121} \frac{I_j(i)}{121}$$

$$I_j(i) = \begin{cases} 1 & \text{well } i \text{ extends to depth } j \\ 0 & \text{otherwise} \end{cases}.$$

This adjustment was based on 121 wells and depths up to 450 ft. Thus, the adjusted relative frequency was a weighted sum of presence of permeability categories where the weights were the proportion of wells at depths. The weighting factor was at least 1, with depths having little sample data receiving greater weight.

Cross-validation using the hold-one-out approach was performed on all 18 models. Point predictions were made for each sample location, without using that sample location in the prediction. Point instead of block kriging was used to compare points to points, instead of points to means. Each sample location (including each foot of lithology data) had an associated hold-one-out error equal to the hold-one-out prediction minus the observed value. Large errors indicated the model was unable to predict at that location. Generally, large errors were associated with sample locations that had large influence on the model. A sample location value had large influence if it was extreme with respect to nearby values or if it was far from other sample locations.

Although the kriging model was assessed through a cross-validation effort, the semivariogram was not. The semivariogram modeling was investigated as part of semivariogram model fitting. Thus, one set of semivariogram model parameters was used to predict the value at each sample location in the hold-one-out effort.

The hold-one-out errors from this exercise were reported using five statistics: mean error, median of the errors as percent of observed value, mean square error (MSE), square root of the reduced MSE (RRMSE), and mean absolute error (MAE). The error as percent of observed value adjusted for larger values generally having larger errors and smaller values generally having smaller errors. The MSE is defined as

$$MSE = \frac{\sum_{i=1}^n (\hat{x}_{-i} - x_i)^2}{n}, \quad (C-8)$$

where

\hat{x}_{-i} = the hold-one-out prediction at sample location i .

The reduced root of the MSE is

$$RRMSE = \sqrt{\frac{\sum_{i=1}^n \frac{(\hat{x}_{-i} - x_i)^2}{Var(\hat{x}_{-i})}}{n}}, \quad (C-9)$$

where

$Var(\hat{x}_{-i})$ = the kriging variance at the hold-one-out sample location.

For a good-fitting model the RRMSE was near unity and within the limits $1 \pm 2\sqrt{2/n}$ (Magnuson and Sondrup 1998). The MAE provided a measure of the size of the error without regard to the sign of the error.

The cross-validation results were also investigated visually using graphs. The observed values were plotted against the hold-one-out predictions to assess the accuracy of the predictions. The histograms of hold-one-out errors were used to assess model adequacy by looking for outliers, skewness, and multimodality. Histograms of observed values and hold-one-out predictions were compared for relative frequency of values and range of values.

C-3.5 Prediction Uncertainty

The uncertainty from the modeling process was estimated and used to judge the usefulness of the model predictions. Two methods for determining uncertainty were (1) through estimation of kriging variance or confidence intervals based on kriging variance and (2) production of a distribution of realizations. Kriging methods generally allowed for determination of uncertainty, in terms of the kriging variances (variance differed by prediction location). The kriging variance at prediction location 0 is

given by $Var(\hat{x}_0) = 2 \sum_{i=1}^n \lambda_i \gamma(x_i, x_0) - \sum_{i=1}^n \sum_{j=1}^n \lambda_i \lambda_j \gamma(x_i, x_j)$. The kriging variances were a function of

the semivariogram parameters (including the variance of the data through the nugget and sill) and the distance between the prediction and observed locations. These kriging variances were computable for kriging on continuous variables. The kriging variances for categorical variables would have been computed from the predictions themselves, so the variances would not depend on the distance between prediction and observation locations.

As an alternative to estimating the kriging variances, a distribution of possible realizations through spatial stochastic simulation was developed. Stochastic simulation is a Monte Carlo method for generating values for a random variable given its distribution. Spatial stochastic simulation generates values using the added information of spatial correlation. The resulting realizations provide a range of probable values. This range is analogous to a prediction interval based on variance estimates. An added benefit of spatial stochastic simulation was that it conditioned on the existing data, therefore reproduced observed data. Kriging did not necessarily reproduce the observed data, due to smoothing.

The uncertainties in H-I interbed top elevation and thickness predictions were quantified using the kriging variances. These kriging variances were summarized with plots (Section C-4.1.3).

The uncertainties for the aquifer hydraulic conductivity were quantified using the back-transformed confidence limits. These were summarized with plots within the kriging section of the results (Section C-4.2.3).

The uncertainties for the vadose zone lithology predictions were based on spatial stochastic simulation. The spatial stochastic simulations were performed for each of the 15 models and then combined. Each model was run 100 times using the same semivariogram models as were used for kriging. The combination of results followed the same layer ordering as combination of the kriging models.

The simulation predictions from the models were combined in ways to produce a range of realizations to describe the vadose zone lithology. The range of realizations was with respect to the frequency of lowest permeability categories. One end of the range had the most volume with low-permeability categories both among and within layer types (surficial alluvium, interbed, and basalt). So, for instance, a realization with the thickest 110-ft interbed was chosen along with a realization with the most volume of low-permeability 110-ft interbed. This was described as a thick soils and low-permeability category realization. On the other end of the range were realizations that had the least volume of low-permeability categories both among and within layer types. This was described as a thick soils and high-permeability category realization.

Uncertainty bounds for the vadose zone lithology were set as a thick soils and low-permeability category realization on one end and a thin soils and high-permeability category realization on the other end. We assumed that these realizations, from the 100 simulations performed, provided reasonable bounds without being too extreme.

The uncertainty for vadose zone lithology was summarized by comparing the relative frequencies of the permeability categories among realizations, kriging predictions, and adjusted observed values.

C-4. RESULTS

The results will be presented separately for the H-I interbed, aquifer hydraulic conductivity, and vadose zone lithology. For each section, data assessment, semivariograms, kriging, model assessment, and uncertainty will be summarized.

C-4.1 H-I Interbed Top Elevation and Thickness

C-4.1.1 Data Assessment

The H-I interbed thickness values were highly positively skewed (Figure C-7) but were not lognormal (Shapiro-Wilks test p-value = 0.0002). No transformation was used on the data, but care was taken to ensure the distribution of sample values and predictions were similar.

The sample locations and thickness values seemed to be somewhat clustered, although the resulting predictions followed the distribution of declustered values. The H-I interbed thickness values were declustered using a cell size of 2,500 m (Figure C-8). The distribution of the declustered data was significantly different than the distribution of the observed data (Kolmogorov-Smirnov $p < 0.05$) (Figure C-9). The distribution of the predictions, however, was very close to the distribution of the declustered data.

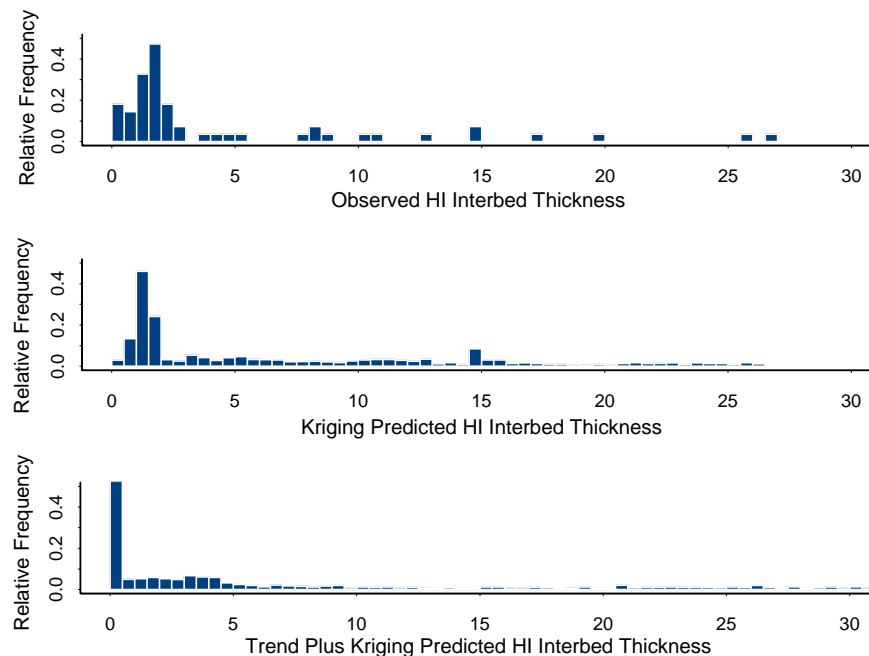


Figure C-7. Histograms of observed H-I interbed thickness and predictions from ordinary kriging and trend plus kriging. Y-axis is relative frequency.

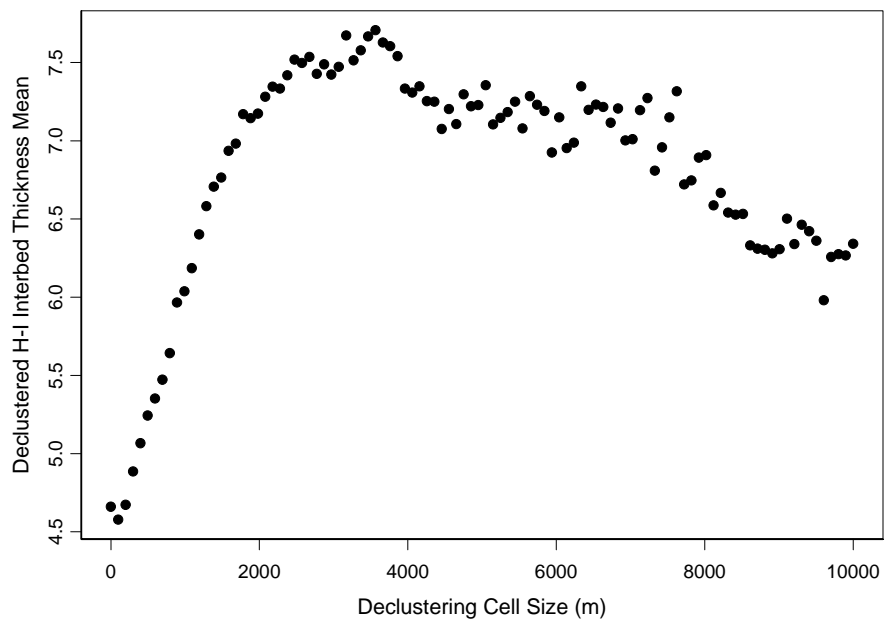


Figure C-8. Declustering cell size versus declustered mean for H-I interbed thickness. The declustered mean reaches the approximate asymptote at 2,500 m.

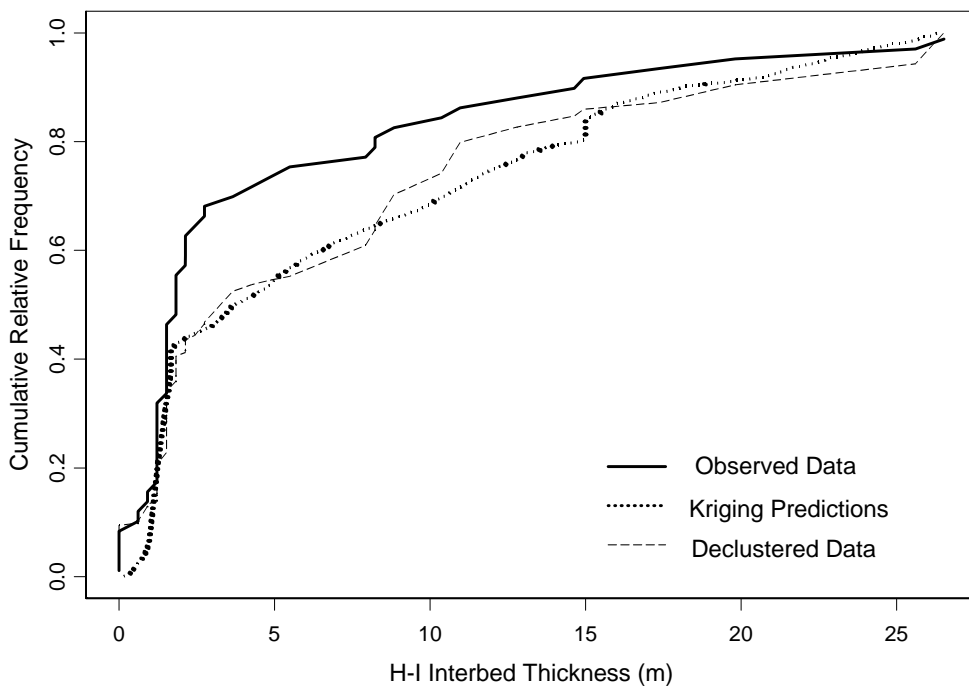


Figure C-9. Empirical cumulative distribution for H-I interbed thickness observed values, kriging predictions, and declustered data.

The regression of H-I interbed thickness resulted in a model including easting, easting², and northing. The semivariogram of the residuals was modeled and kriging predictions were calculated. The trend plus kriging predictions exceeded the range of the observed data in the areas of no sampling, in the NW and SE corners of the prediction grid (Table C-4, Figure C-10). Accounting for trend reduced kriging variance, but, when the regression prediction variance was added to the kriging variance, the total variance was larger. For these reasons, trend was not included in the model.

The H-I interbed top elevation values had long tails, with slight negative skewness (Figure C-11), and were significantly nonnormal. No transformation to the data was made because the asymmetry was slight.

The sample locations and elevation values seemed to be somewhat clustered, although the resulting predictions followed the distribution of declustered values. The H-I interbed elevation values were declustered using a cell size of 2,500 m (Figure C-12). The distribution of the declustered data was significantly different than the distribution of the observed data (Kolmogorov-Smirnov $p < 0.01$) (Figure C-13). The distribution of the predictions, however, was very close to the distribution of the declustered data.

The regression of H-I interbed elevation resulted in a model including easting, northing, and northing². The semivariogram of the residuals was modeled and kriging predictions were calculated. The trend plus kriging predictions exceeded the range of the observed data in the areas of no sampling, in the NW and SE corners of the prediction grid (Table C-5, Figures C-14 and C-15). Accounting for trend reduced kriging variance, but, when the regression prediction variance was added to the kriging variance, the total variance was larger; for elevation, the ordinary kriging variance is, on average, 30% less than the total variance for modeling trend plus kriging. For these reasons, trend was not included in the model.

There were two sample locations (S5G-Test and WE-INEL-1) north of the prediction range (Figure C-1). The values from these wells were used in semivariogram estimation and kriging to improve the predictions on the northern prediction border.

Table C-4. Summary statistics for H-I interbed thickness: observed values, ordinary kriging predictions, and trend plus kriging predictions.

	Range	Mean	Median	Standard Deviation
Observed data	0 – 27	4.7	1.8	6.3
Ordinary kriging (sample locations)	0 – 22	4.3	1.8	5.2
Trend plus kriging (sample locations)	0 – 265	10.4	1.6	37.7
Ordinary kriging (prediction grid)	0 – 26	7.2	3.7	7.2
Trend plus kriging (prediction grid)	0 – 622	18.6	3.3	53.0

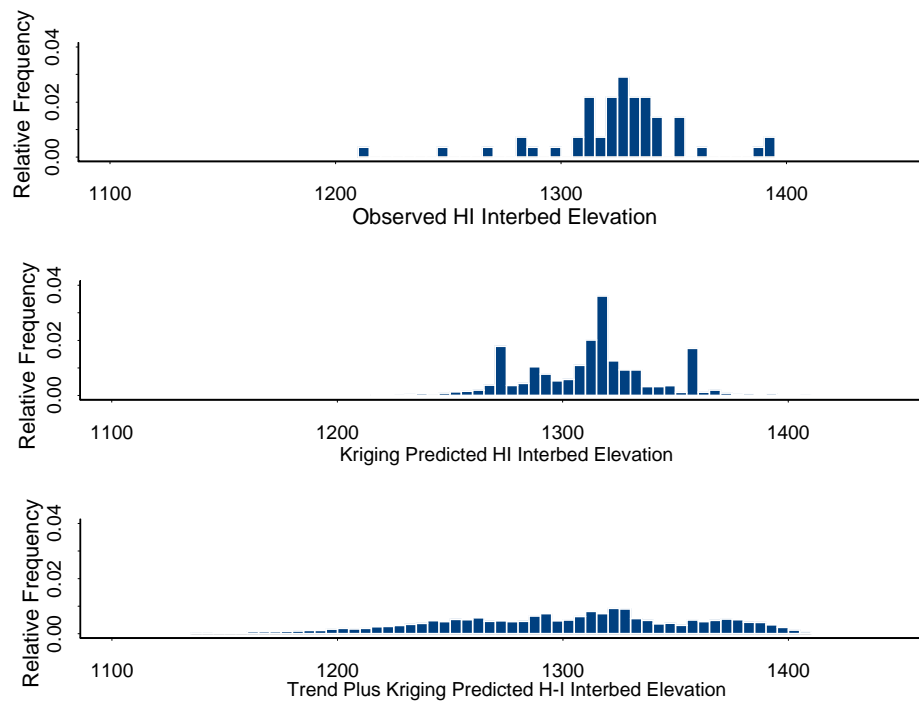


Figure C-10. Histograms of observed H-I interbed elevation and predictions from ordinary kriging and trend plus kriging. Y-axis is relative frequency.

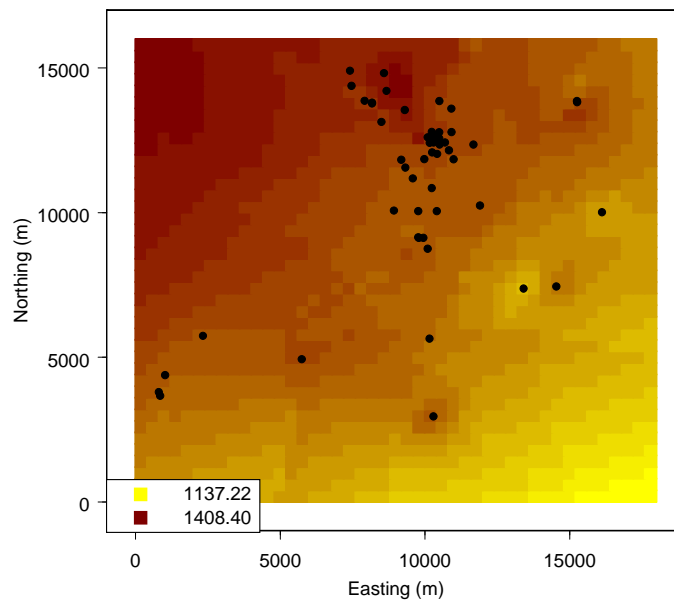


Figure C-11. Trend plus kriging predicted H-I interbed elevation, to compare to kriging predictions in Figure C-20. Black points represent sample locations. Coordinates are relative to the figure, and, although they represent meters, they do not correspond to a land surface location.

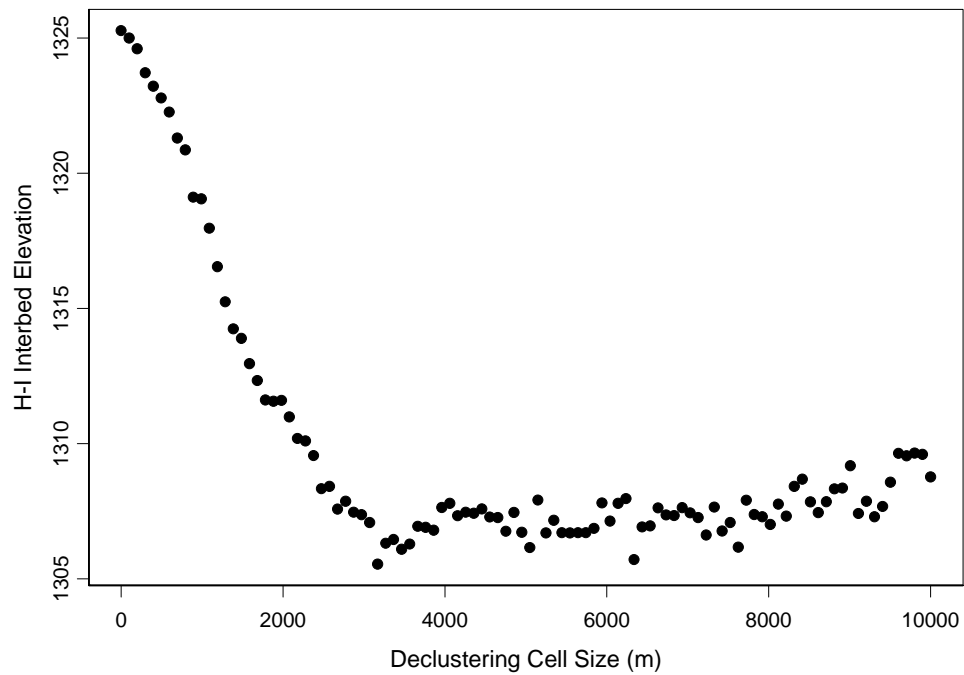


Figure C-12. Declustering cell size versus declustered mean for H-I interbed elevation. The declustered mean reaches the approximate asymptote at 2,500 m.

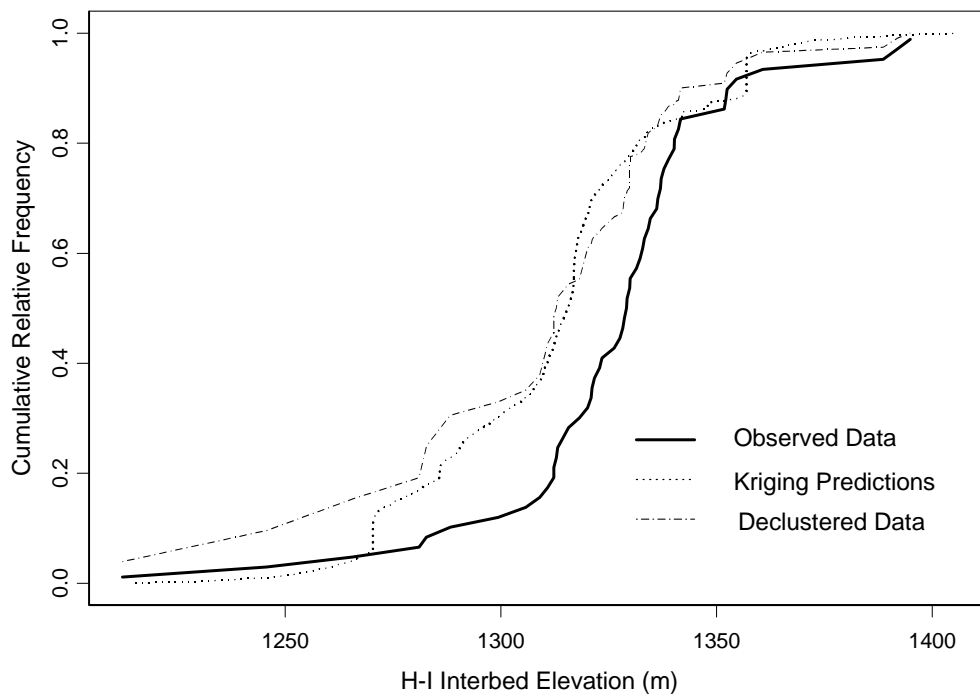


Figure C-13. Empirical cumulative distribution for observed H-I interbed elevation values, kriging predictions, and declustered data.

Table C-5. Summary statistics for H-I interbed elevation: observed values, ordinary kriging predictions, and trend plus kriging predictions.

	Range	Mean	Median	Standard Deviation
Observed data	1212 – 1395	1325	1329	30.5
Ordinary kriging (sample locations)	1244 – 1397	1329	1329	23.7
Trend plus kriging (sample locations)	1215 – 1318	1324	1327	31.2
Ordinary kriging (prediction grid)	1215 – 1407	1312	1315	29.0
Trend plus kriging (prediction grid)	1137 – 1408	1300	1307	57.0

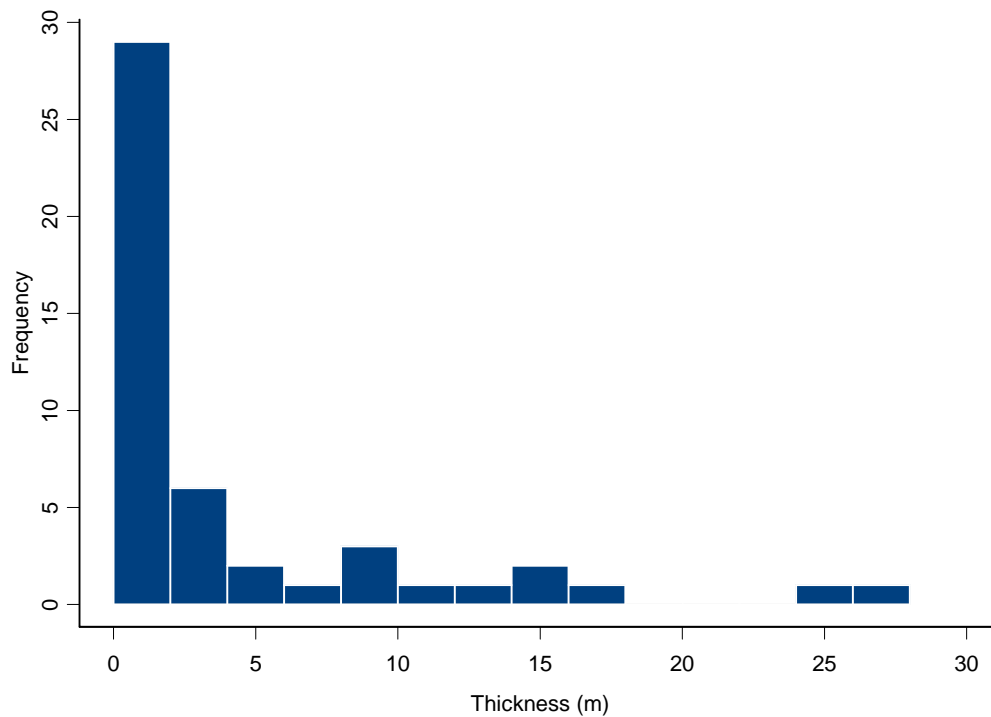


Figure C-14. Histogram of observed H-I interbed thickness (m) values.

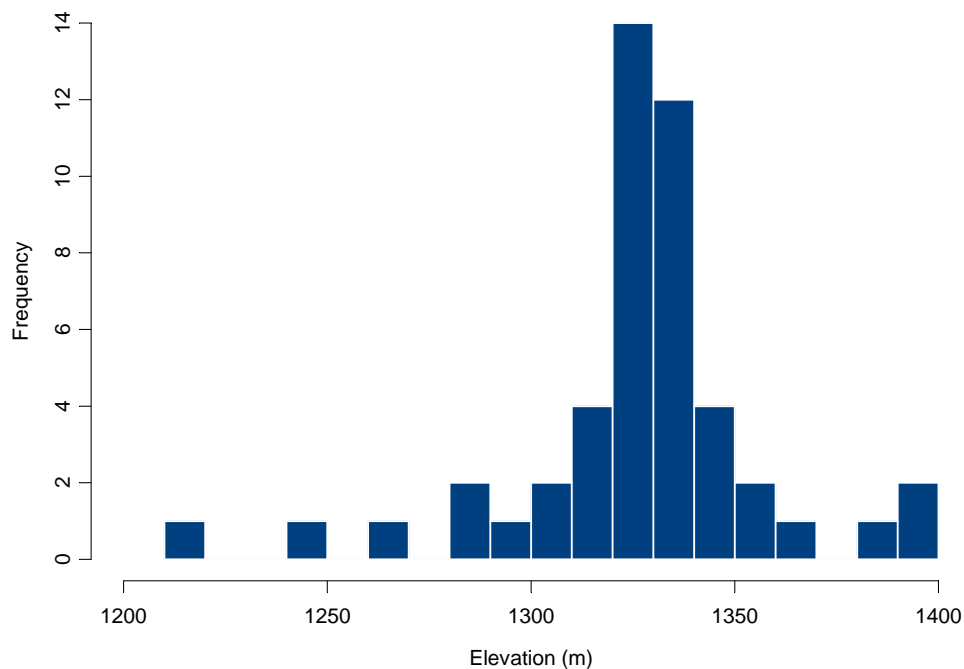


Figure C-15. Histogram of observed H-I interbed elevation (m amsl) values.

C-4.1.2 Semivariograms

The semivariogram for H-I interbed thickness was modeled with an anisotropic model. The direction of greatest spatial continuity (largest range) was N-S and least spatial continuity was E-W (Figure C-16). The N-S empirical semivariogram was fit with a Gaussian model with 0 nugget, sill of 50, and range of 4,750 m. The E-W empirical semivariogram was fit with a spherical model with 0 nugget, sill of 15, and range of 3,500 m. The directional semivariograms become erratic after the 5,000-m lag due to limited number of pairs.

The semivariogram for H-I interbed top elevation was modeled with an anisotropic model. The direction of greatest spatial continuity was NW-SE and least spatial continuity was NE-SW (Figure C-17). The NW-SE empirical semivariogram was fit with a Gaussian model with 0 nugget, sill of 700, and range of 2,500 m. The NE-SW empirical semivariogram was fit with a spherical model with 0 nugget, sill of 100, and range of 1,000 m.

C-4.1.3 Kriging

The kriging predictions for H-I interbed thickness (Figure C-18) suggested a thick interbed in the east central area of the prediction grid, extending further west in the south than in the north. Almost the whole west side of the grid had very thin H-I interbed soil with no H-I interbed soil in the north central region. The predictions followed the sample values quite well for thickness but there were large areas with no sample points, mostly in the NW and SE corners. These extrapolated areas could be far from the truth, as reflected by the increased kriging variance there (Figure C-19).

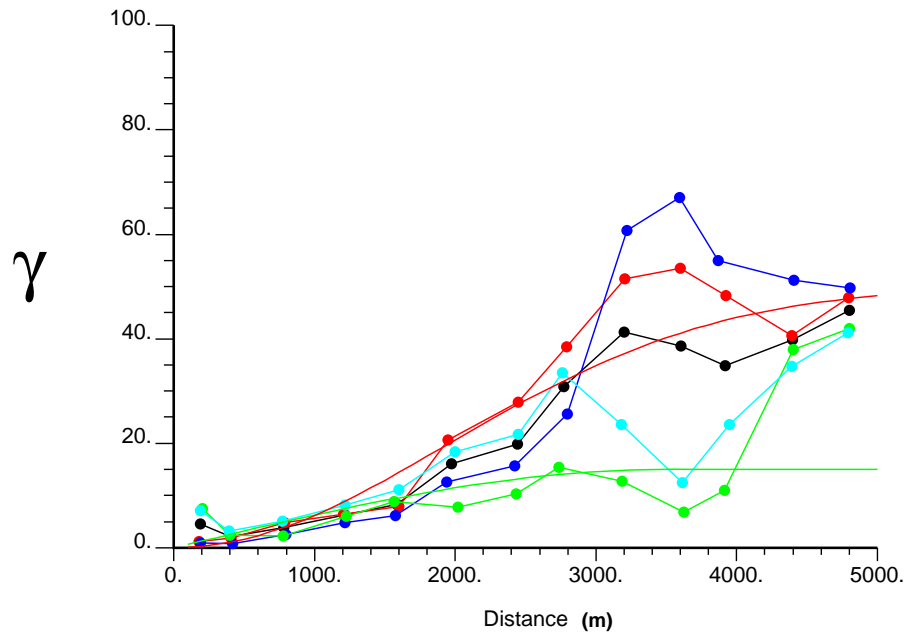


Figure C-16. Semivariograms for H-I interbed thickness. Black is omnidirectional, red is 0°, dark blue is 45°, green is 90°, and light blue is 135°. Dashed lines with associated colors for anisotropic semivariogram.

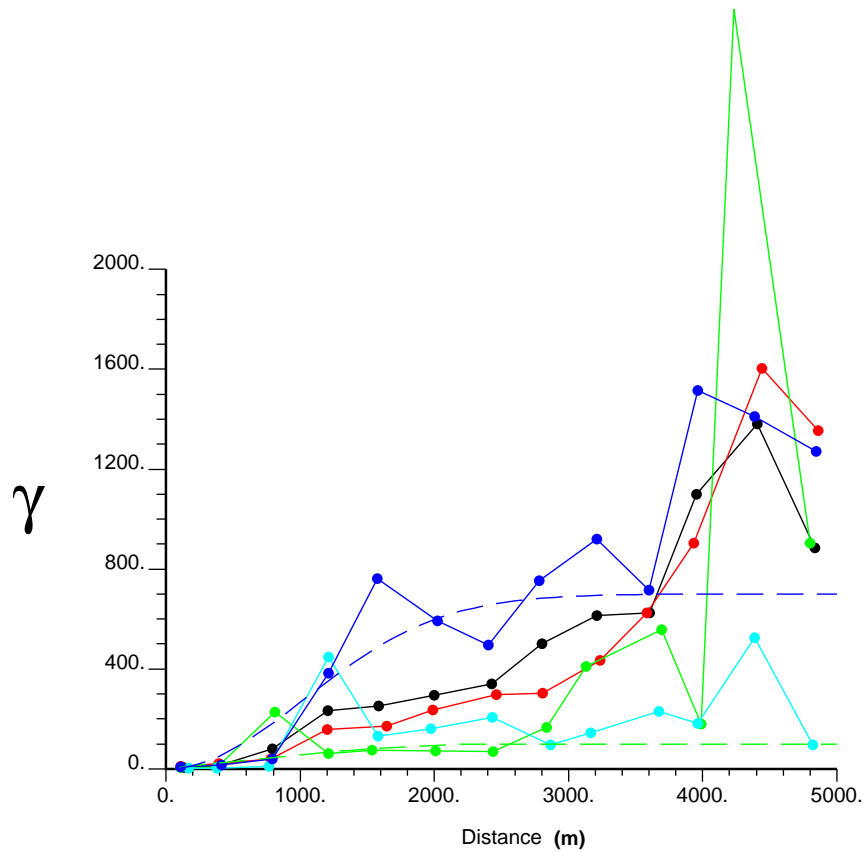


Figure C-17. Semivariograms for H-I interbed elevation. Black is omnidirectional, red is 0°, green is 45°, light blue is 90°, and dark blue is 135°. Dashed lines with associated colors for anisotropic semivariogram.

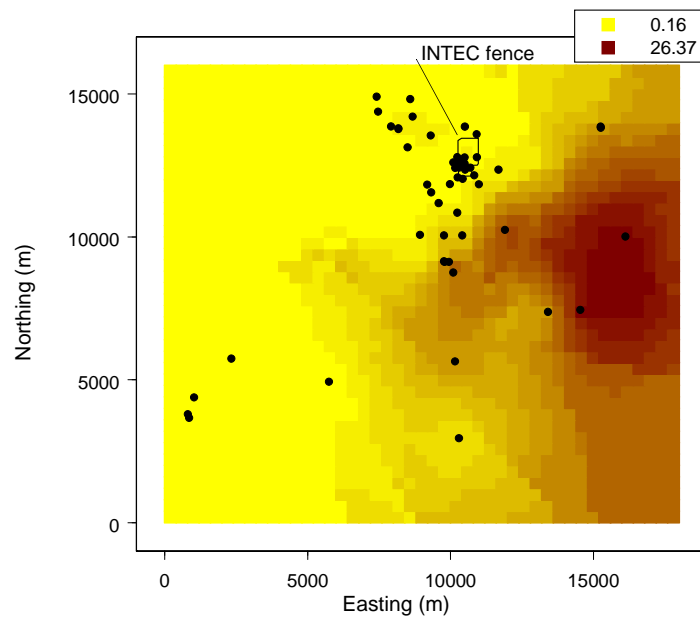


Figure C-18. Kriging predictions for H-I interbed thickness (m). Black points represent sample locations. Coordinates are relative to the figure and, although they represent meters, they do not correspond to a land surface location.

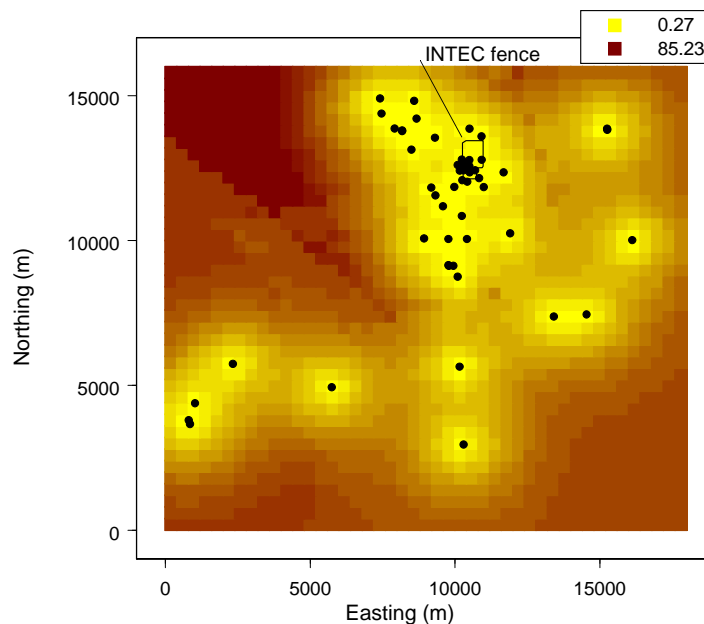


Figure C-19. Kriging variances (m^2) for H-I interbed thickness. Black points represent sample locations. Coordinates are relative to the figure and, although they represent meters, they do not correspond to a land surface location.

The kriging predictions for H-I interbed top elevation (Figure C-20) suggested a low area on the east section of the grid, a ridge running from the center of the southern border to the NE corner, and a level area with a bump on the center north boundary. The predictions followed the sample values quite well for top elevation but there were large areas with no sample points, mostly in the NW and SE corners. These extrapolated areas could be far from the truth, as reflected by the increased kriging variance there (Figure C-21).

The low-elevation areas in the SE corresponded to the thick interbed areas. Generally, soil deposits in valleys during nonvolcanic time periods. Thus, the low-elevation areas would correspond to areas of thick interbed soil.

C-4.1.4 Model Assessment

The distribution of predicted H-I interbed thickness matched the distribution of observed values (Figure C-22). The range of values matched almost exactly (observed 0 - 26.5, predicted 0.16 - 26.4). There were, proportionally, more high predicted values than observed; the long right tail was thicker for the predictions histogram. This was expected due to the smoothing effect of kriging and the large areas with no observed data.

The cross-validation statistics indicated the model fits the data well (Table C-6). The median error was less than 1% of the observed values. The square root of the reduced MSE was above the limits based on a sample size of 55, but the kriging variance was quite small in areas of clustered samples.

The plot of observed versus hold-one-out predictions showed no systematic bias or large differences (Figure C-23). The histogram of hold-one-out errors was symmetric with tails not exceeding 15 m (Figure C-24). Also the histogram of hold-one-out predictions matched the observed and kriging predictions well (Figure C-22).

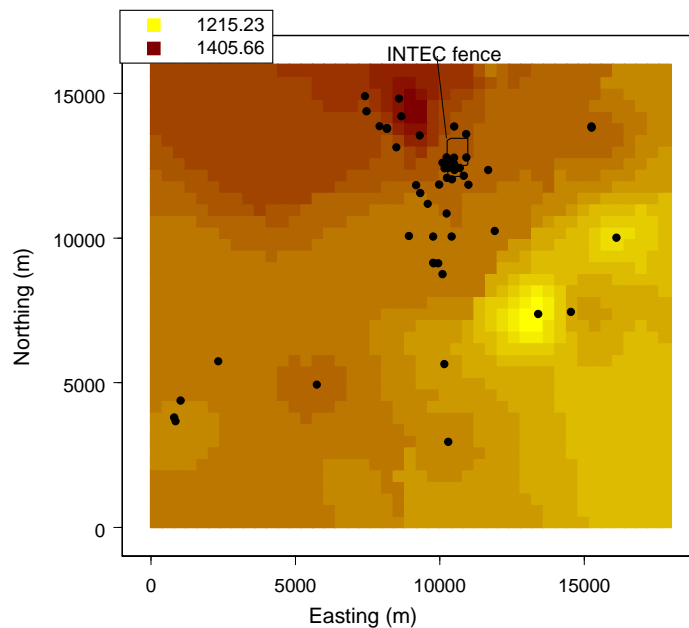


Figure C-20. Kriging predictions for H-I interbed elevation. Black points represent sample locations. Coordinates are relative to the figure and, although they represent meters, they do not correspond to a land surface location.

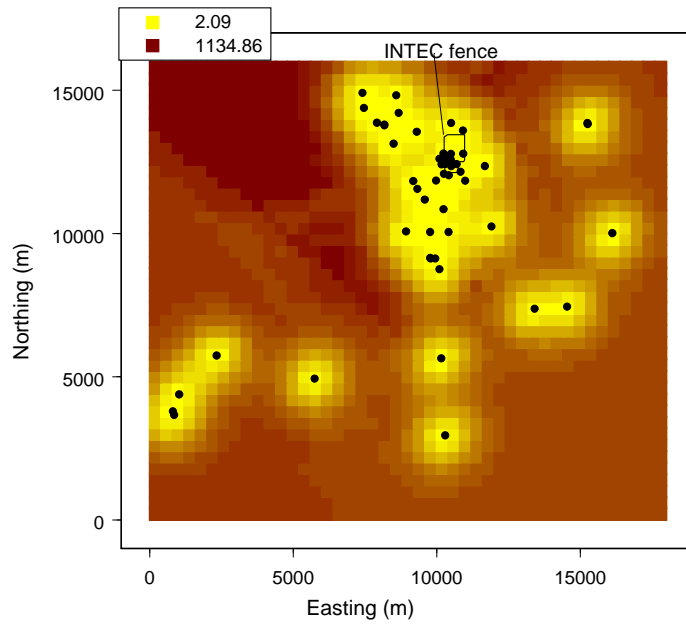


Figure C-21. Kriging variances (m^2) for H-I interbed elevation. Black points represent sample locations. Coordinates are relative to the figure and, although they represent meters, they do not correspond to a land surface location.

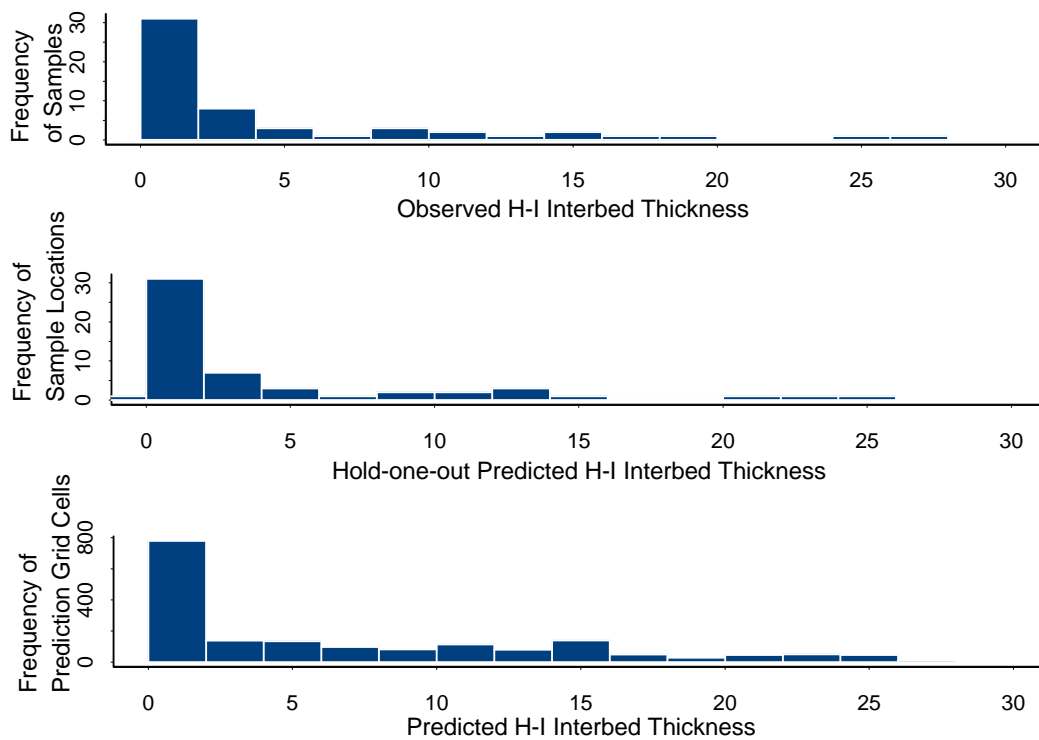


Figure C-22. Histograms of observed H-I interbed thickness, hold-one-out predictions at sample locations, and kriging predictions on the grid.

Table C-6. Cross-validation statistics for H-I interbed thickness and top elevation. Range for a good fitting model using RRMSE in parentheses.

Statistic	Thickness	Top Elevation
Mean error (m)	-0.4	3.3
Median error as % of observed (%)	0.4%	< 0.1%
MSE (m ²)	22	366
RRMSE (m) Ideal range (0.6 – 1.4)	4.26	1.04
MAE (m)	2.9	9.6

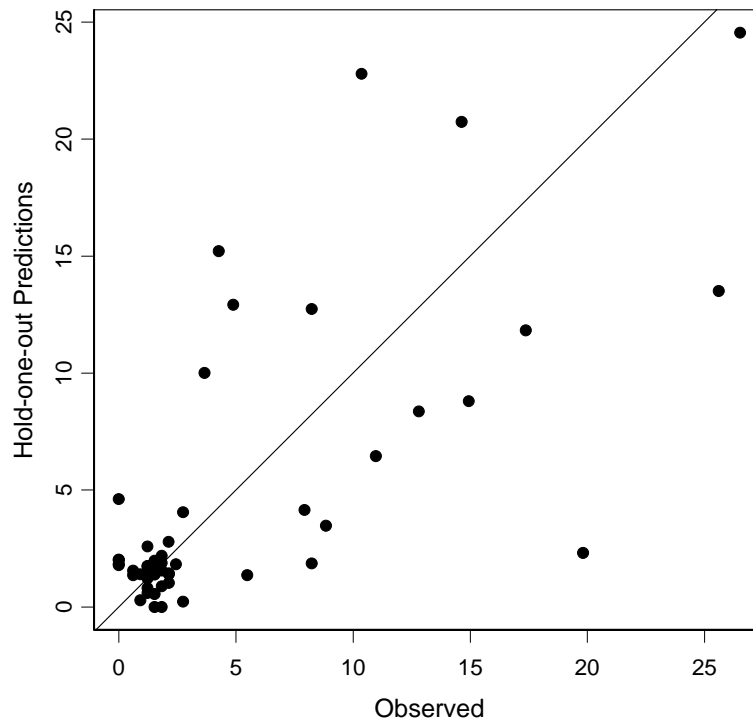


Figure C-23. Observed values versus the hold-one-out kriging predictions for H-I interbed thickness. The line represents perfect correlation between observed and predicted.

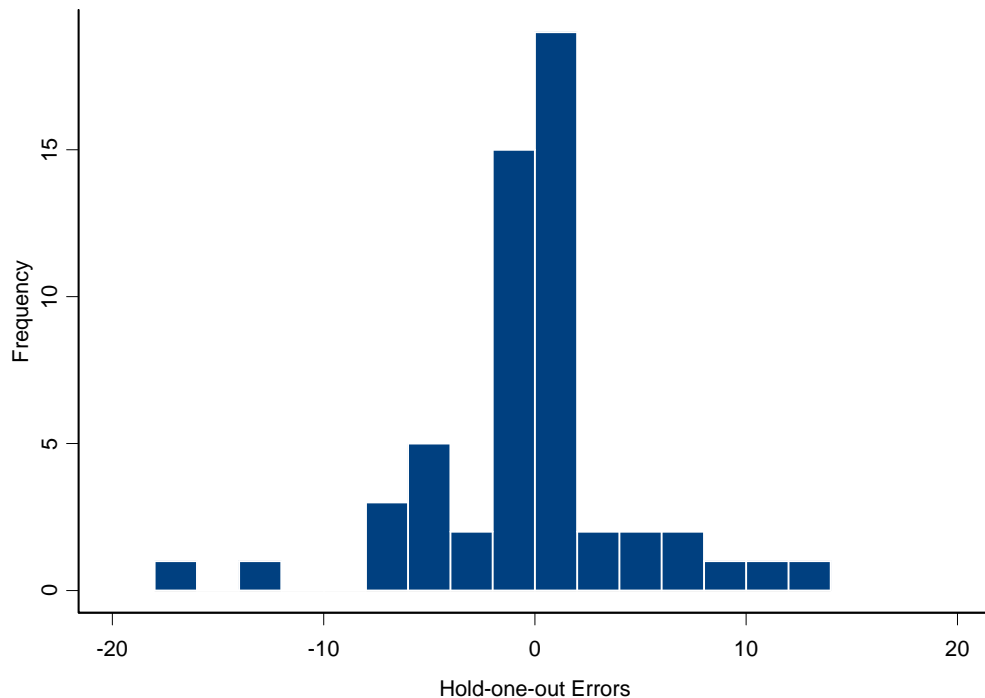


Figure C-24. Histogram of hold-one-out errors (predicted minus observed) for H-I interbed thickness.

The distribution of predicted H-I interbed top elevation was similar to the distribution of observed values (Figure C-25). The range of values matched well (observed 1,212 – 1,395, predicted 1,215 – 1,405). The distributions had approximately the same mode, but the predictions displayed more than one mode, the most prominent was at approximately 1,270 m. These modes corresponded to the large areas with no observed values.

The cross-validation statistics indicated the model fits the data well (Table C-6). The median error was less than 1% of the observed values and the square root of the reduced MSE was within the limits based on a sample size of 55.

The plot of observed versus hold-one-out predictions showed no systematic bias or large differences (Figure C-26). The histogram of hold-one-out errors was symmetric with tails not exceeding 80 m (Figure C-27). Also the histogram of hold-one-out predictions matched the observed and kriging predictions well (Figure C-25).

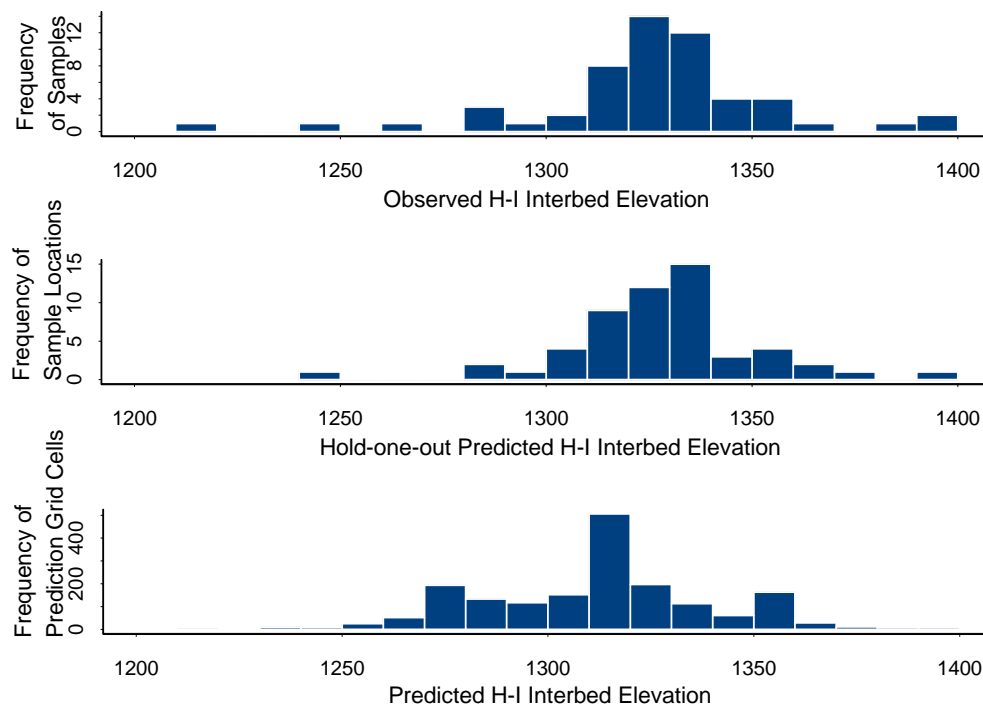


Figure C-25. Histograms of observed H-I interbed elevation, hold-one-out predictions at sample locations, and kriging predictions on grid.

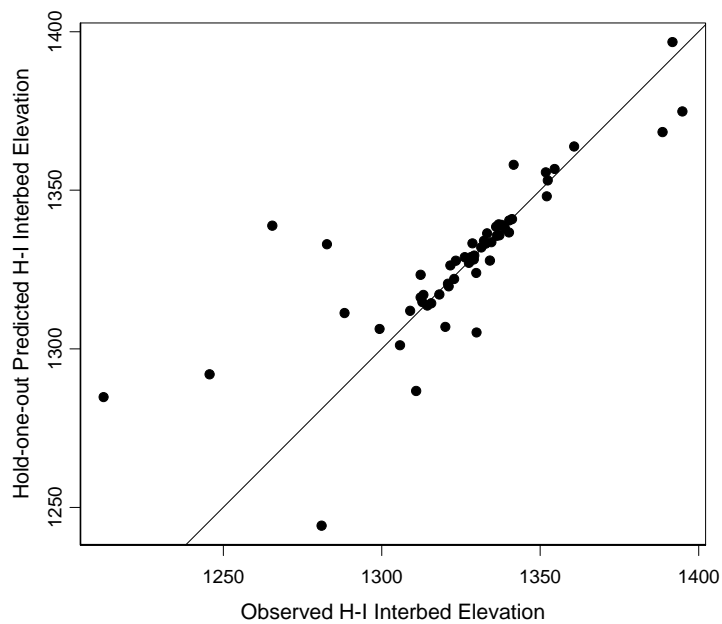


Figure C-26. Observed values versus the hold-one-out predictions for H-I interbed elevation. The line represents perfect correlation between observed and predicted.

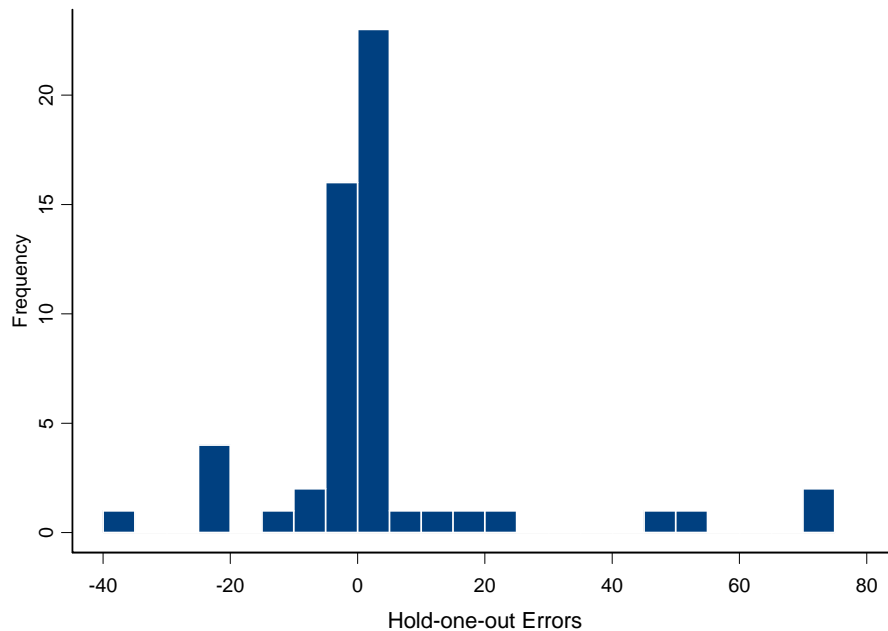


Figure C-27. Histogram of hold-one-out errors (predicted minus observed) for H-I interbed elevation.

C-4.2 Aquifer Hydraulic Conductivity

C-4.2.1 Data Assessment

There were 128 sample locations for aquifer hydraulic conductivity. Of these, 54 are within the prediction grid (Figure C-2). All data are used because the outlying locations added valuable information to the edges of the prediction grid and there were no differences in spatial correlation or levels found between the whole set and the subset within the prediction grid.

The distribution of aquifer hydraulic conductivity values were highly skewed to the right (Figure C-28). A natural log transformation improved the symmetry but resulted in a slightly left-skewed distribution (Figure C-29). The data were not lognormal (Shapiro-Wilk test p-value < 0.0001). A normal score transformation was used to attain symmetry (Figure C-30). The kriging predictions were back-transformed for use in the flow and transport model and for presentation here. Despite the nonlognormality, the data and results were generally presented as natural log transformed to allow for easier comparison and visualization.

Although the locations were clustered, the aquifer hydraulic conductivity values were not. A cell size of 1,500 m was used to decluster the aquifer hydraulic conductivity values (Figure C-31). The distribution of the declustered data was not significantly different than the distribution of the observed data (Kolmogorov-Smirnov $p > 0.05$) (Figure C-32). The distribution of the predictions was different than the distribution of the raw and declustered data.

No significant models were found for regressing aquifer hydraulic conductivity, natural log transformed aquifer hydraulic conductivity, or normal score transformed aquifer hydraulic conductivity. There were some individual coefficients that significantly differed from zero.

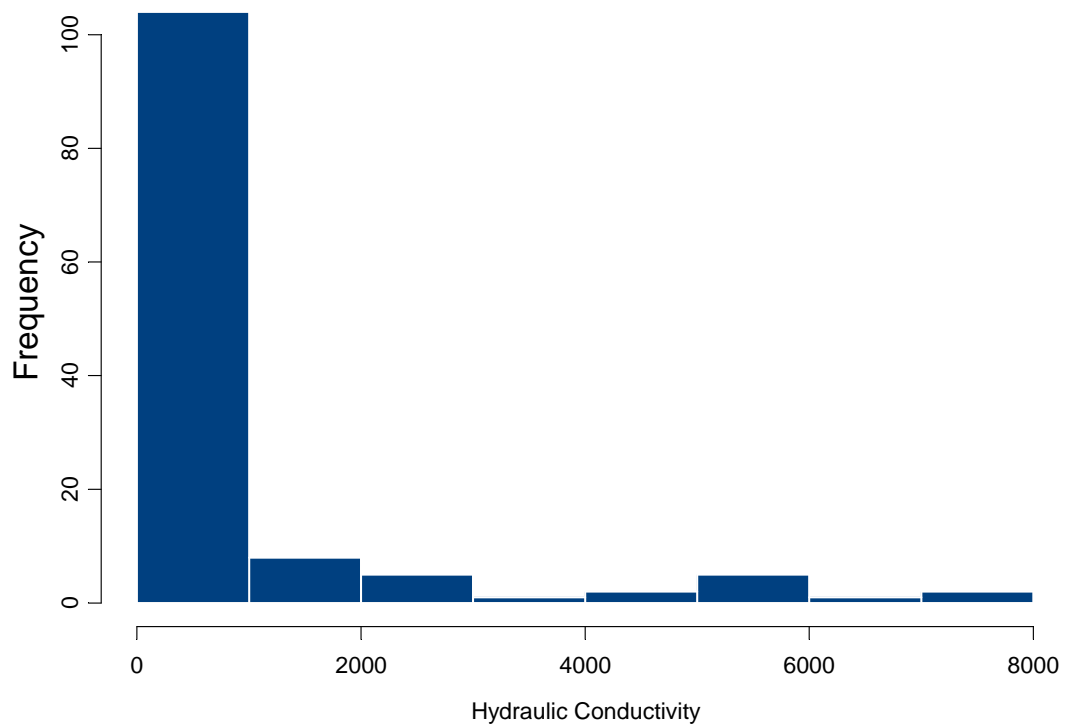


Figure C-28. Histogram of observed aquifer hydraulic conductivity.

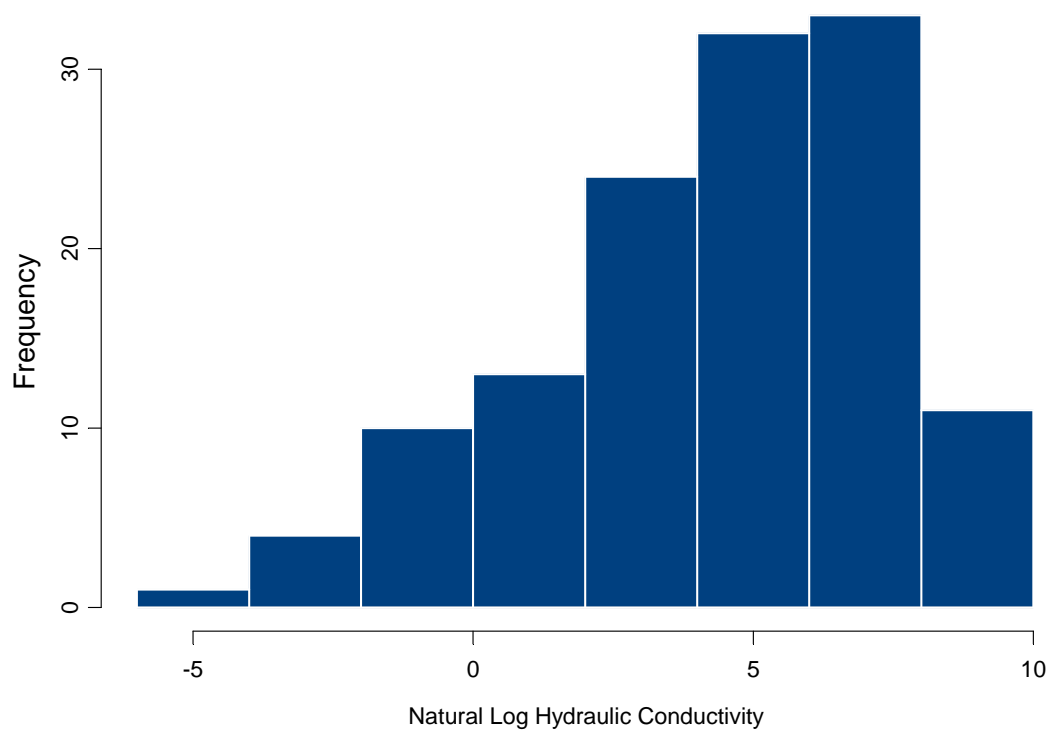


Figure C-29. Histogram of the natural log of observed aquifer hydraulic conductivity.

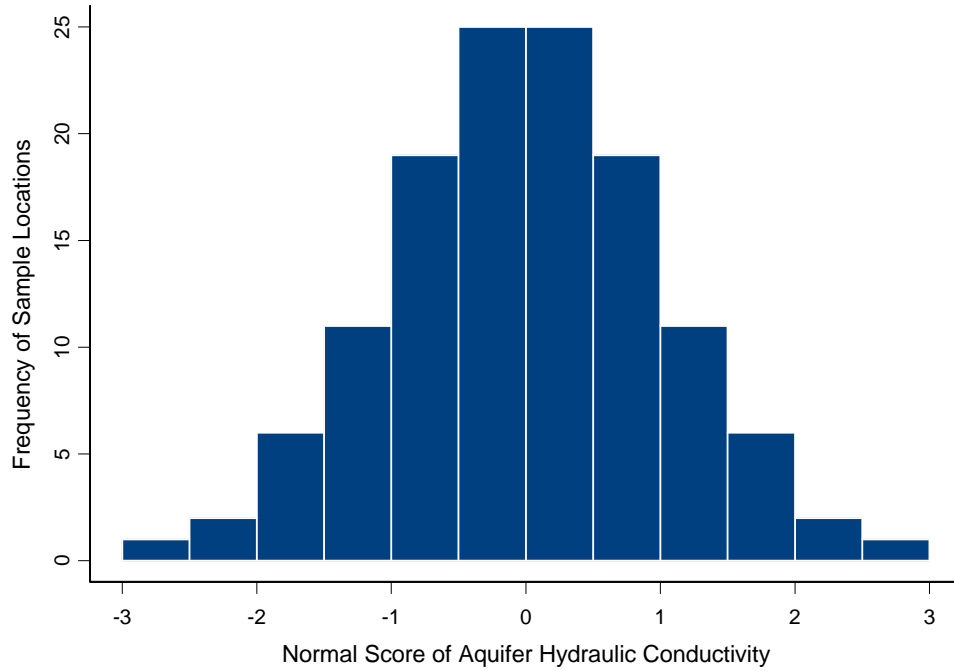


Figure C-30. Histogram of normal score transformed aquifer hydraulic conductivity.

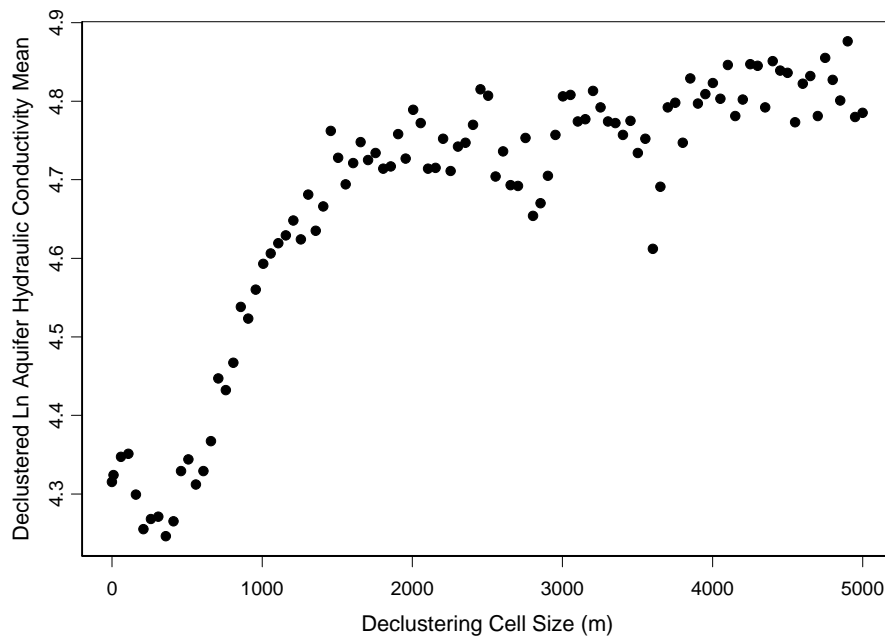


Figure C-31. Declustering cell size versus declustered mean for natural log transformed aquifer hydraulic conductivity. The declustered mean reaches the approximate asymptote at 1,500 m.

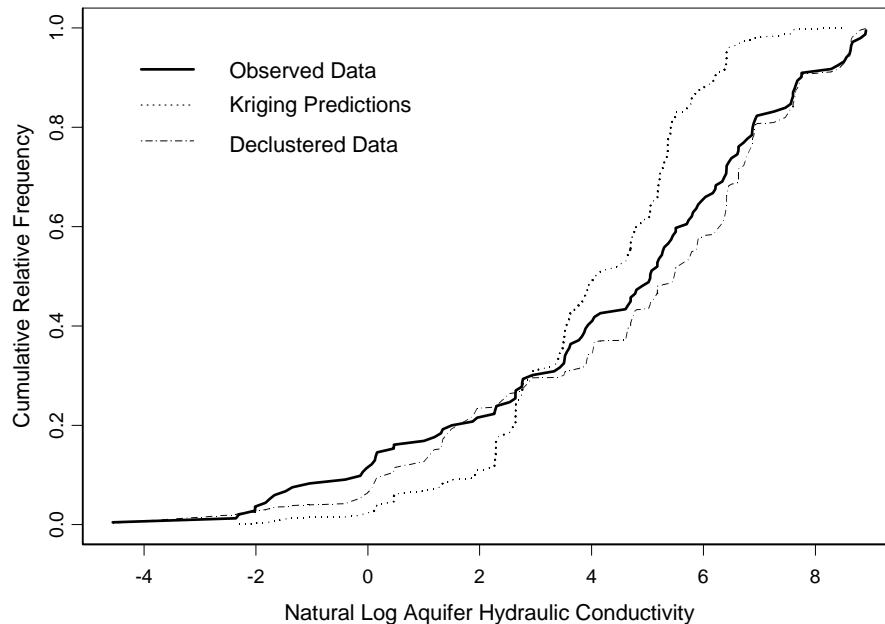


Figure C-32. Empirical cumulative distribution for natural log transformed aquifer hydraulic conductivity observed values, kriging predictions, and declustered data.

C-4.2.2 Semivariograms

The semivariogram for normal score transformed aquifer hydraulic conductivity was modeled with an anisotropic model (Figure C-33). The NW-SE direction had the greatest spatial continuity and was modeled with a Gaussian model with 0.2 nugget, sill of 0.8, and range of 5,000 m. The NE-SW direction had the least spatial continuity and was modeled with a Gaussian model with 0.2 nugget, sill of 0.8, and range of 1,000 m.

C-4.2.3 Kriging and Model Assessment

The kriging predictions of back-transformed aquifer hydraulic conductivity are presented in Figure C-34, with the lower confidence limits and upper confidence limits in Figures C-35 and C-36. The predictions and confidence limits on the smaller grid are shown in Figures C-37 through C-39. All figures show the NW-SE elliptical pattern modeled from the anisotropic semivariogram, most pronounced for the smaller grid and the upper confidence limits for both sets of predictions.

The predicted aquifer hydraulic conductivity values were generally low (0.1 – 4,758 ft/day, with 75% of predictions less than 212 ft/day), with higher values in the north central and southwest regions of the prediction grid.

For purposes of flow and transport modeling, a finer grid just near INTEC was defined for predictions. This 36×44 grid of 100- \times 100-m cells was based on the same semivariograms. These predictions were generally higher than the full grid predictions, with a range of 0.2 to 5,705 ft/day, with 75% less than 525 ft/day. These higher values follow a high-permeability trough through the INTEC (Figure C-37).

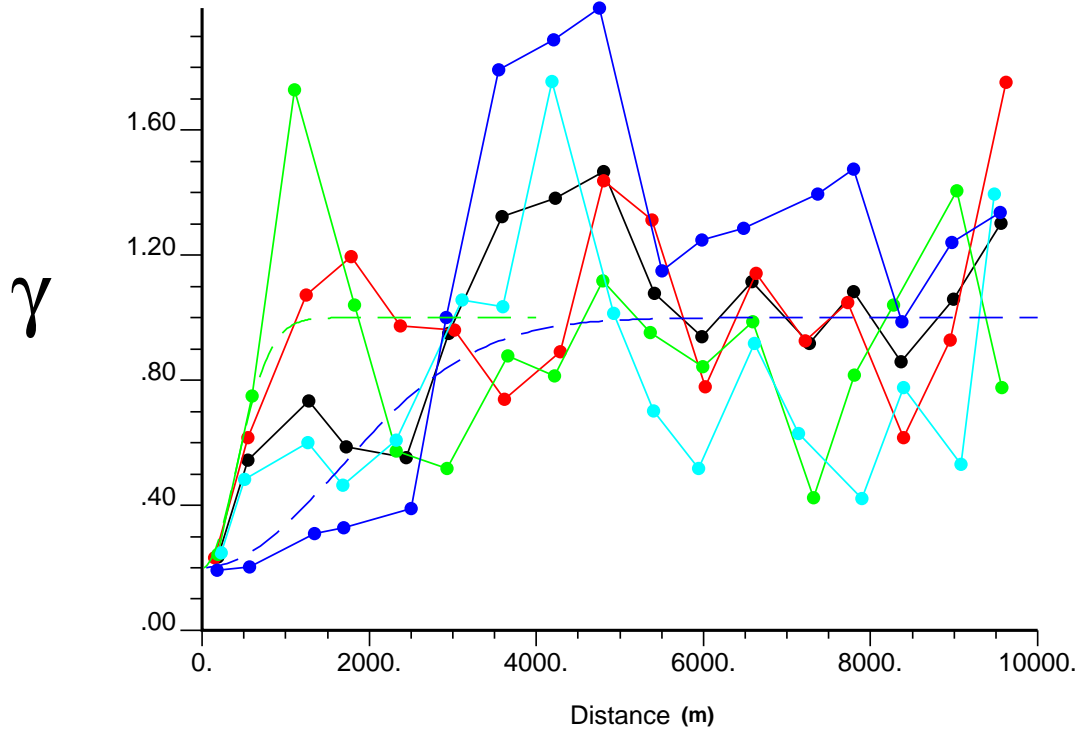


Figure C-33. Semivariogram of normal score transformed aquifer hydraulic conductivity. Black is omnidirectional, red is 0°, green is 45°, light blue is 90°, and dark blue is 135°. Dashed lines with associated colors are for anisotropic semivariogram.

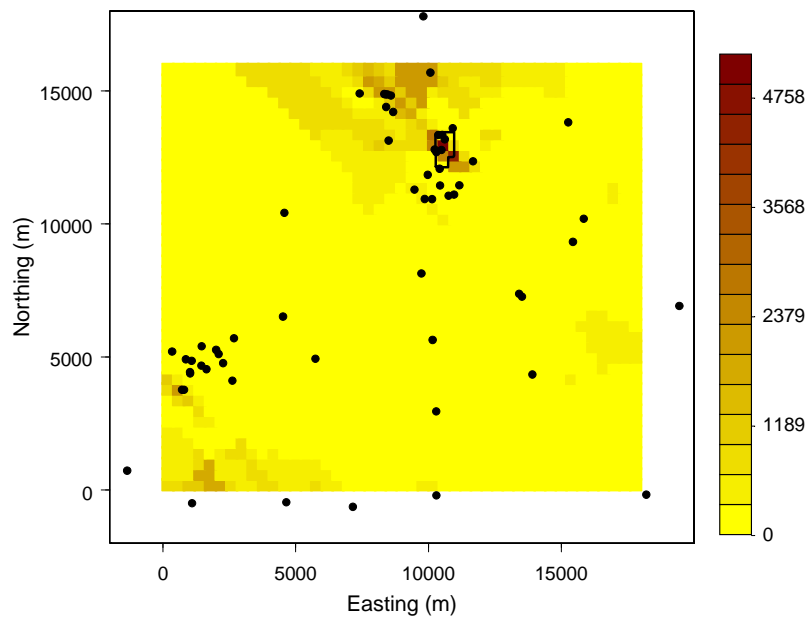


Figure C-34. Back-transformed kriging predictions of aquifer hydraulic conductivity. Coordinates are relative to figure, and, although they represent meters, they do not correspond to a land surface location.

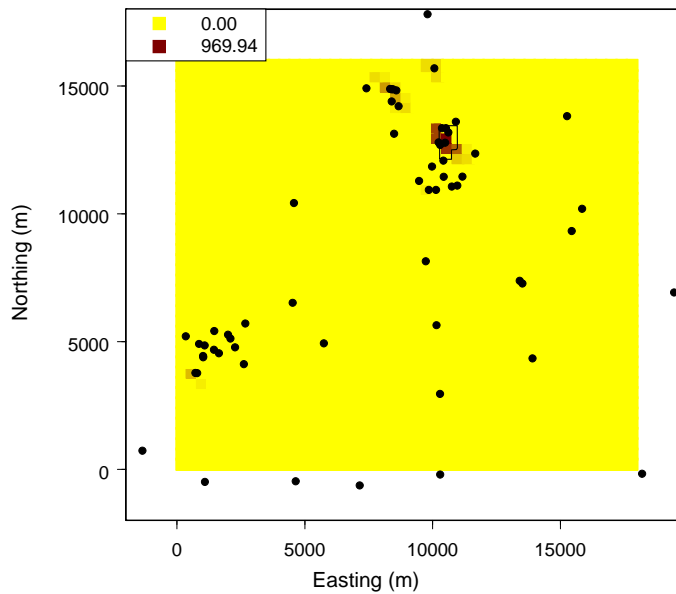


Figure C-35. Back-transformed lower confidence limits for kriging predictions of natural log aquifer hydraulic conductivity. Black points are well locations. Coordinates are relative to the figure, and, although they represent meters, they do not correspond to a land surface location.

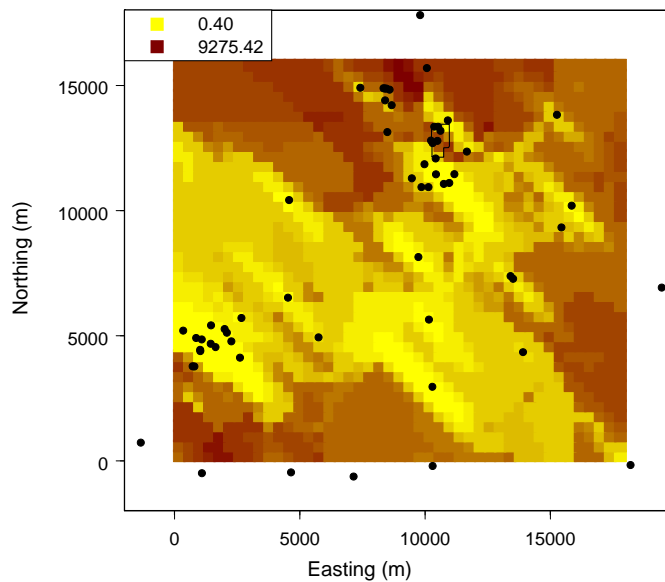


Figure C-36. Back-transformed upper confidence limits for kriging predictions of natural log aquifer hydraulic conductivity. Black points are well locations. Coordinates are relative to the figure, and, although they represent meters, they do not correspond to a land surface location.

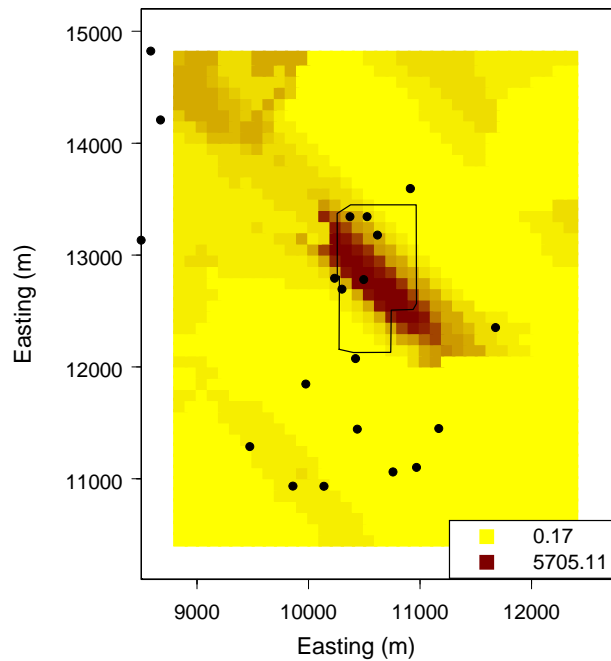


Figure C-37. Back-transformed kriging predictions of aquifer hydraulic conductivity on finer, smaller grid around INTEC. Sample locations are included as black dots. Coordinates are relative to the figure, and, although they represent meters, they do not correspond to a land surface location.

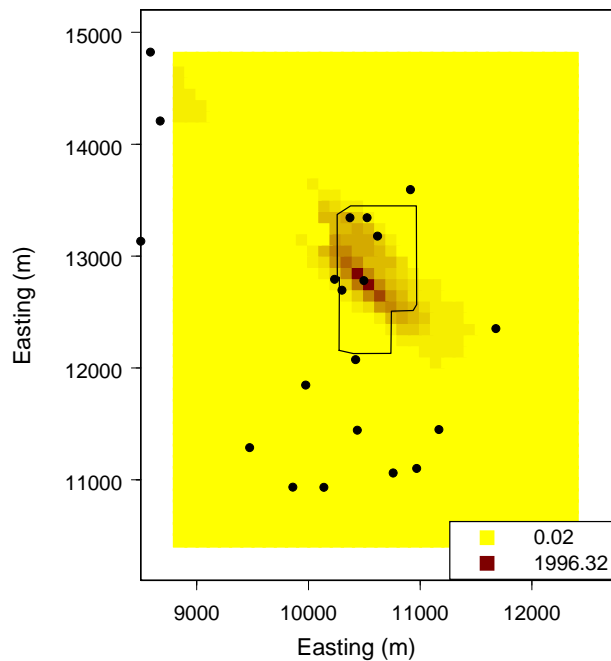


Figure C-38. Back-transformed lower confidence limits of predicted aquifer hydraulic conductivity on finer, smaller grid around INTEC. Sample locations are included as black dots. Coordinates are relative to the figure, and, although they represent meters, they do not correspond to a land surface location.

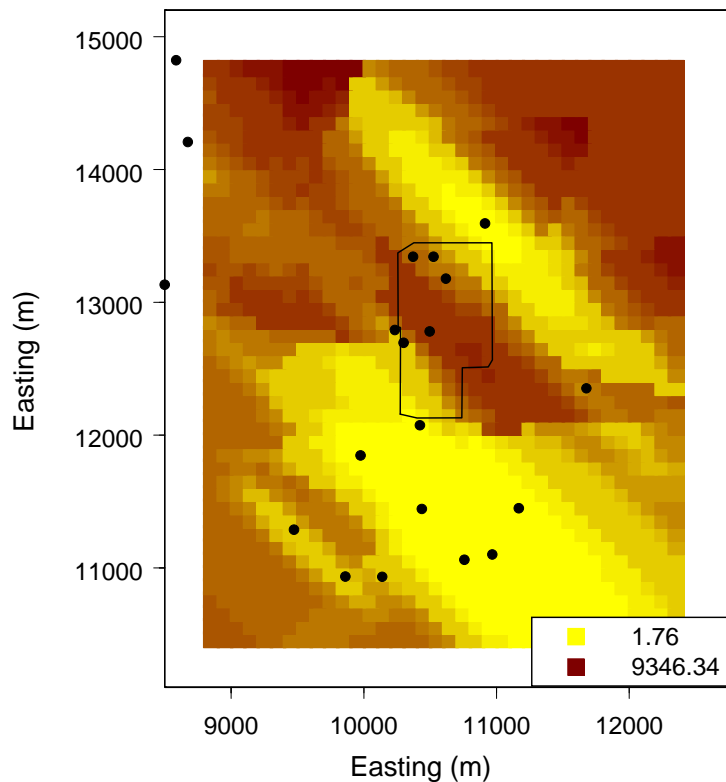


Figure C-39. Back-transformed upper confidence limits of predicted aquifer hydraulic conductivity on finer, smaller grid around INTEC. Sample locations are included as black dots. Coordinates are relative to the figure, and, although they represent meters, they do not correspond to a land surface location.

The hold-one-out predictions match fairly well to the observed aquifer hydraulic conductivity; although the distribution of predictions is slightly more leptokurtic (more peaked) than observed (Figure C-40). The distribution of kriging predictions on the grid differ more from the observed; the central tendency is slightly smaller and the distribution leptokurtic like the hole-one-out predictions (Figure C-40). This is expected from kriging, which smoothes predictions toward the mean. The plot of natural log transformed observed aquifer hydraulic conductivity and natural log transformed hold-one-out predictions shows a reasonable correlation (Figure C-41). The predictions (hold-one-out and on the prediction grid) on the finer grid in a smaller area have the same leptokurtic distribution, but there is not bias in the central tendency (Figure C-42).

The cross-validation statistics demonstrate that the large variance in the aquifer hydraulic conductivity observations are present in the predictions (Table C-7). The median error as percent of observed value, however, is only -1.4%, which is reasonably low, indicating a good fit.

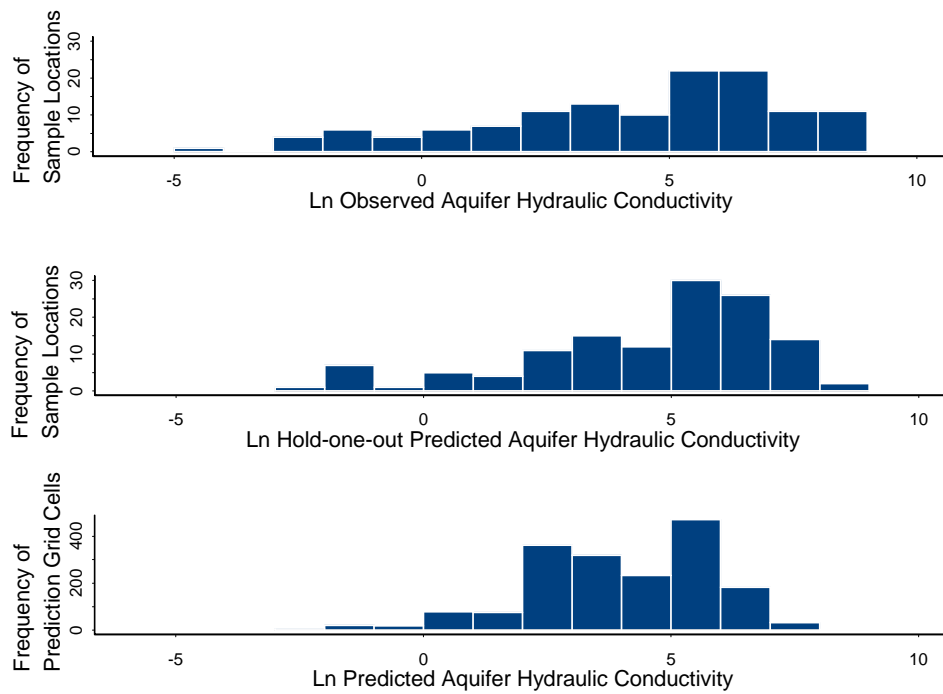


Figure C-40. Histograms of natural log transformed observed aquifer hydraulic conductivity, hold-one-out predictions at sample locations, and kriging predictions on the grid.

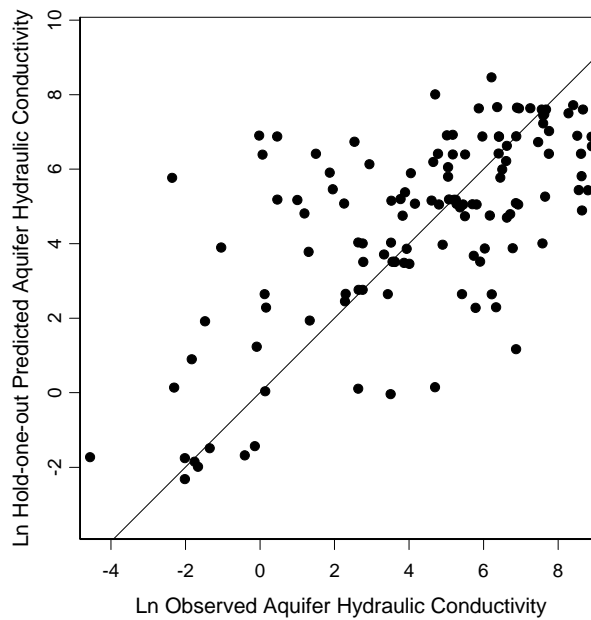


Figure C-41. Natural log observed aquifer hydraulic conductivity versus hold-one-out predictions. The line represents perfect correlation between observed and predicted.

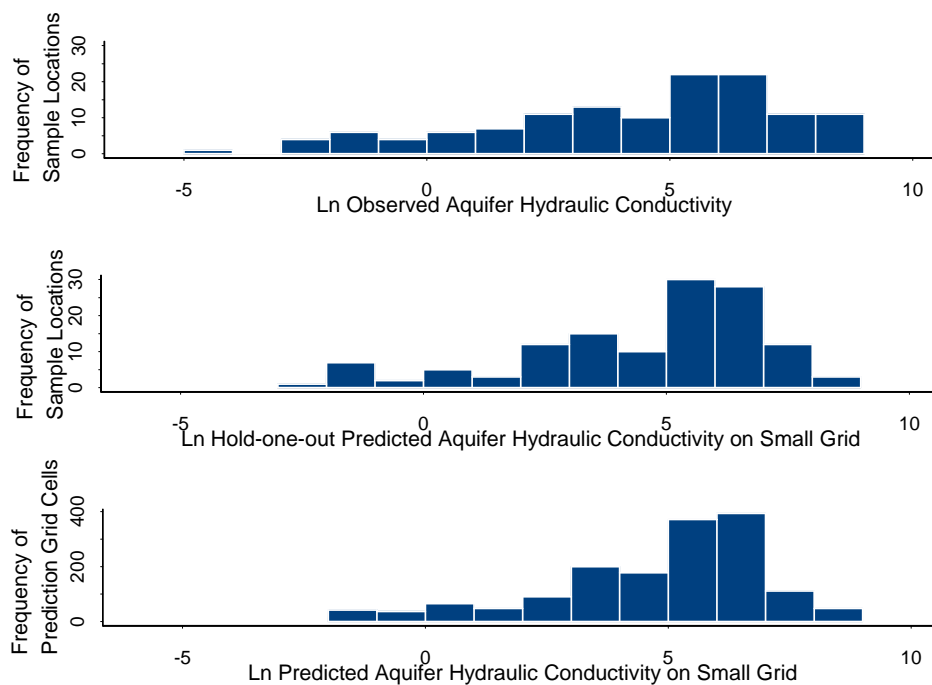


Figure C-42. Histograms of natural log transformed observed aquifer hydraulic conductivity, hold-one-out predictions at sample locations, and kriging predictions, all on the smaller prediction grid.

Table C-7. Cross-validation statistics for aquifer hydraulic conductivity.

Statistic	Hydraulic Conductivity
Mean error	-354 ft/day
Median error percent of observed	-1.4%
MSE	2,597,287 (ft/day) ²
MAE	753 ft/day

C-4.3 Vadose Zone Lithology

C-4.3.1 Data Assessment

The vadose zone lithology consisted of 15 different subsets: surficial alluvium thickness, surficial alluvium permeability category, 110-ft interbed top elevation, 110-ft interbed thickness, 110-ft permeability category, 140-ft interbed top elevation, 140-ft interbed thickness, 140-ft interbed permeability category, below massive basalt (BM) interbed top elevation, BM interbed thickness, BM interbed permeability category, 380-ft interbed top elevation, 380-ft interbed thickness, 380-ft interbed permeability category, and all other vadose zone permeability category. Each subset of data was assessed and modeled separately. The continuous variables (thicknesses and top elevations) were assessed for symmetry. The categorical data were checked for logical correctness, but no formal assessment is presented here.

The thickness variables were skewed to the right, with the exception of the surficial alluvium thickness (Figures C-43 through C-47). The four main interbeds had many observed zero thickness values. These values, which included zero values, lent themselves to a 3-parameter lognormal distribution or a mixture distribution, but neither was conducive to kriging. The top elevation variables were symmetric, with the exception of the 380-ft interbed (Figures C-48 through C-51). The 380-ft interbed top elevation had few (18) data points and appeared to be almost uniform. The predictions for all subsets were carefully compared to the observed values to ensure the distribution of values was maintained.

C-4.3.2 Semivariograms

The 15 data subsets required 19 variables whose semivariograms needed to be modeled because the categorical variables required more than one semivariogram (surficial alluvium and four main interbeds had one each but the other vadose zone permeability category subset had four). For variables modeled in 2-D (thickness and top elevation), directional semivariograms were considered. For variables modeled in 3-D (permeability categories), directional and vertical semivariograms were considered.

The semivariogram parameters (Table C-8) describe the semivariogram models (Figures C-52 through C-73) used for kriging. Only the surficial alluvium permeability category was fit with an anisotropic model; all other variables were assumed horizontally isotropic. The surficial alluvium data set was larger, providing the ability to confidently discern anisotropy. All other vadose zone permeability categories displayed vertical anisotropy, so a shorter range was used for a dip of 90°, corresponding to straight up and down.

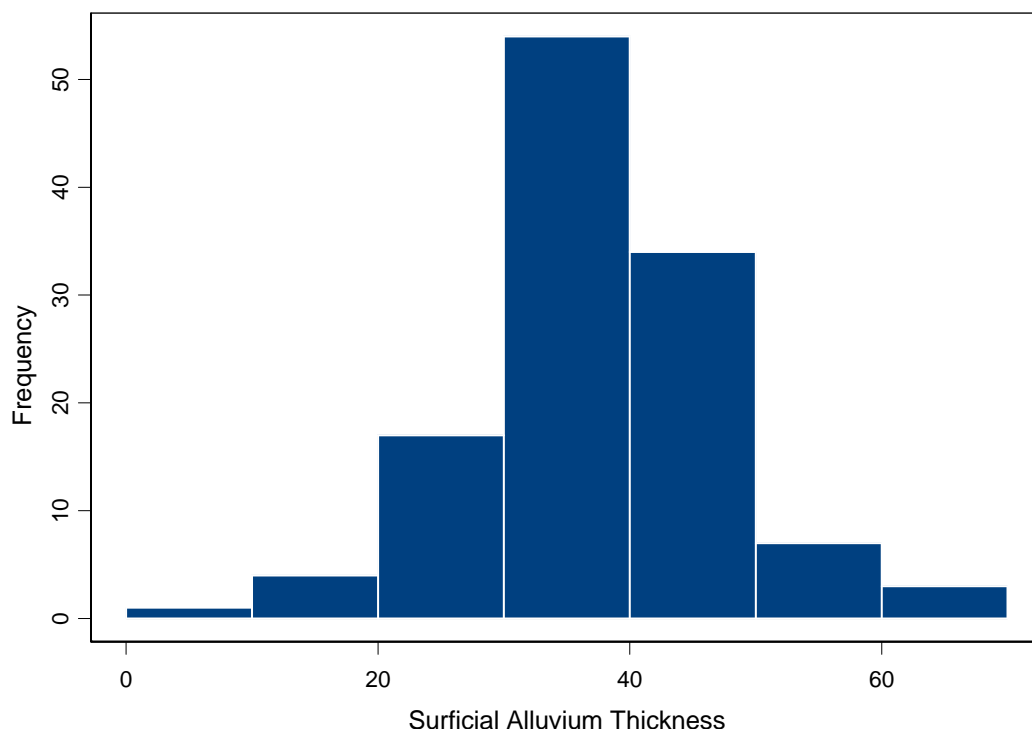


Figure C-43. Histogram of observed surficial alluvium thickness values.

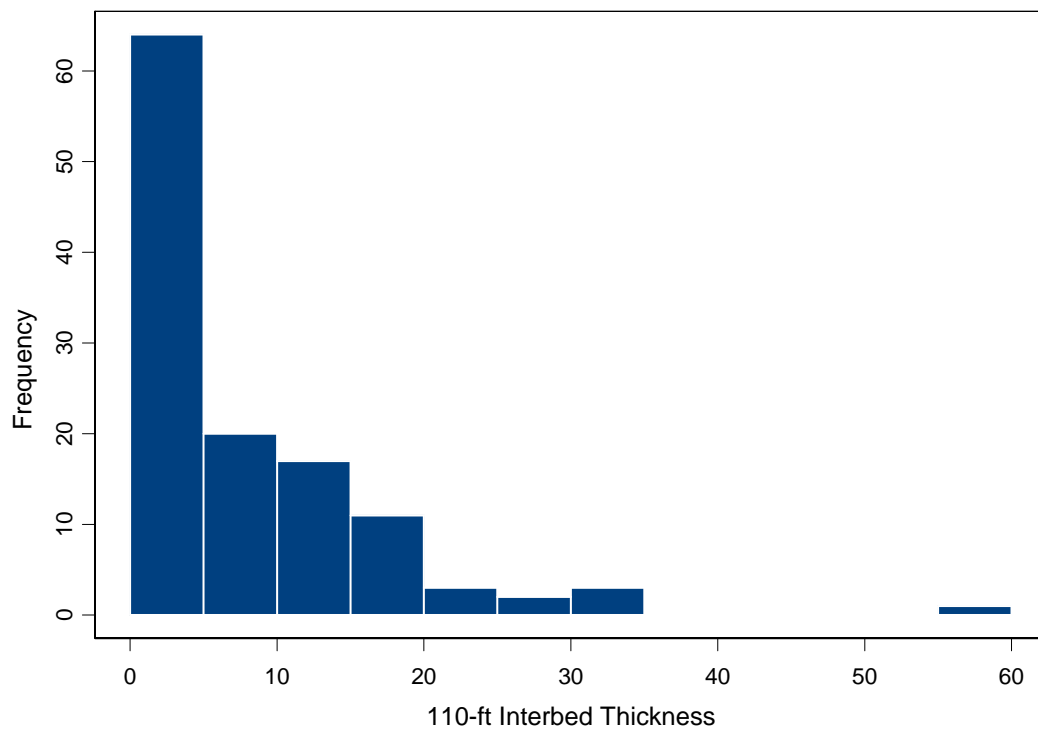


Figure C-44. Histogram of observed 110-ft interbed thickness values.

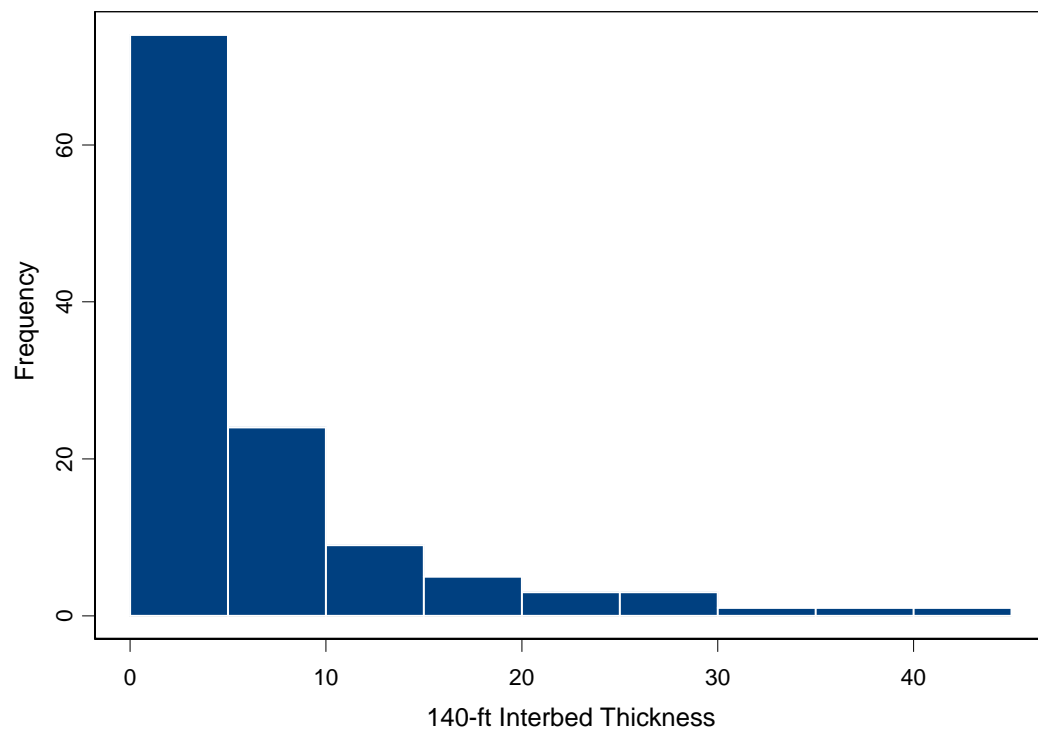


Figure C-45. Histogram of observed 140-ft interbed thickness values.

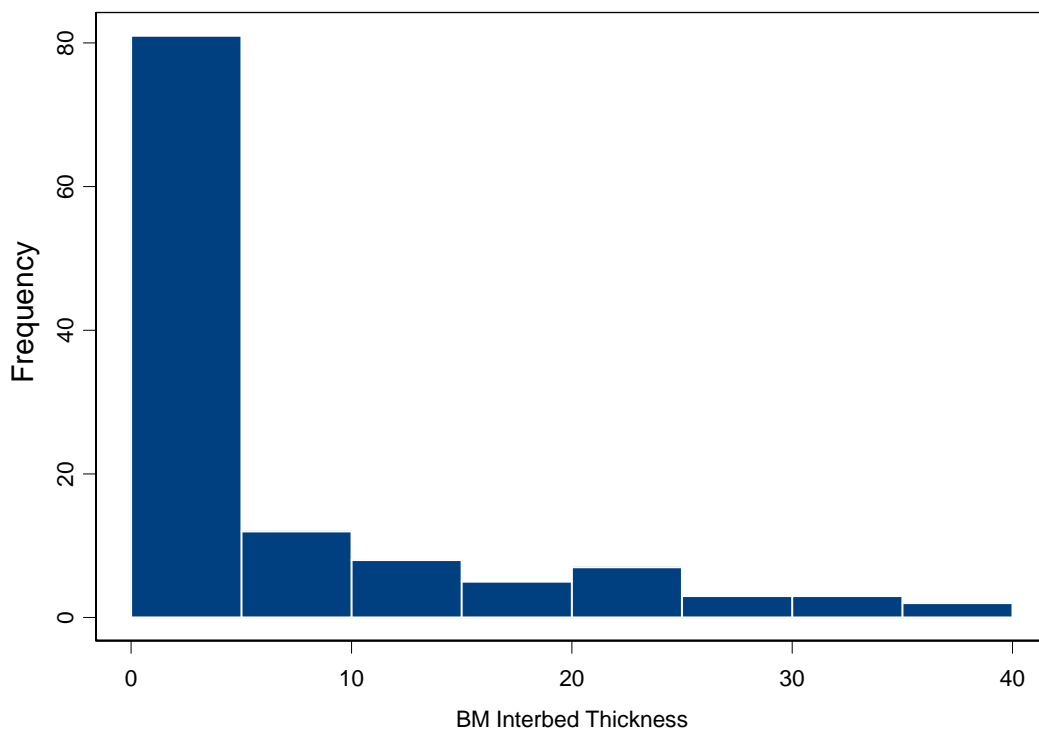


Figure C-46. Histogram of observed BM interbed thickness values.

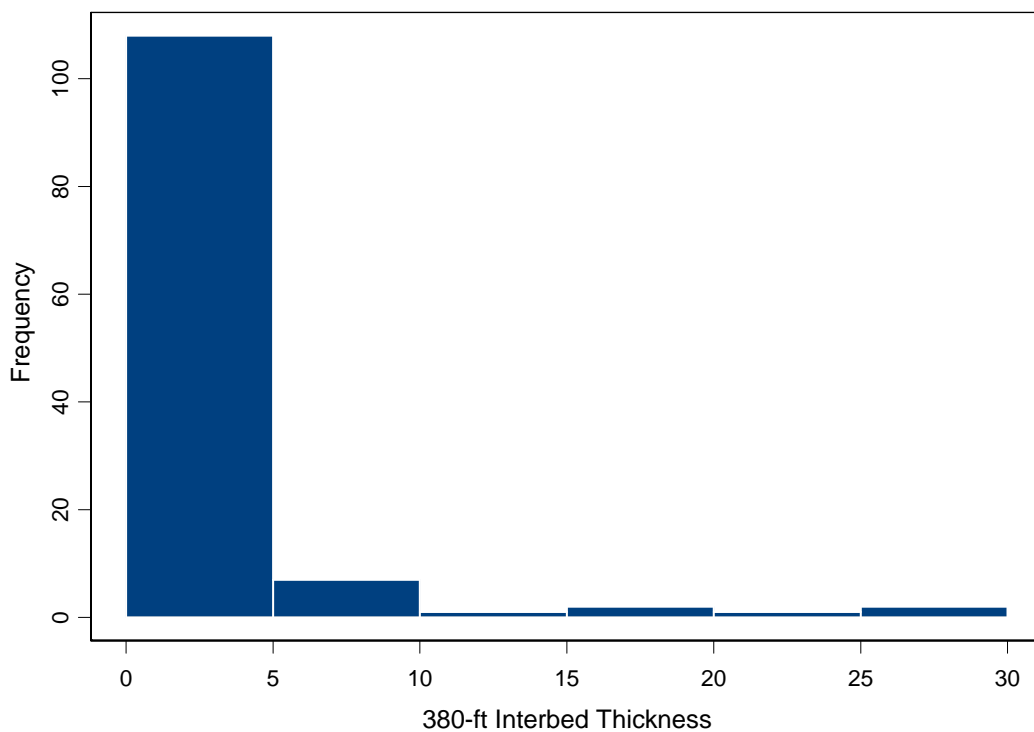


Figure C-47. Histogram of observed 380-ft interbed thickness values.

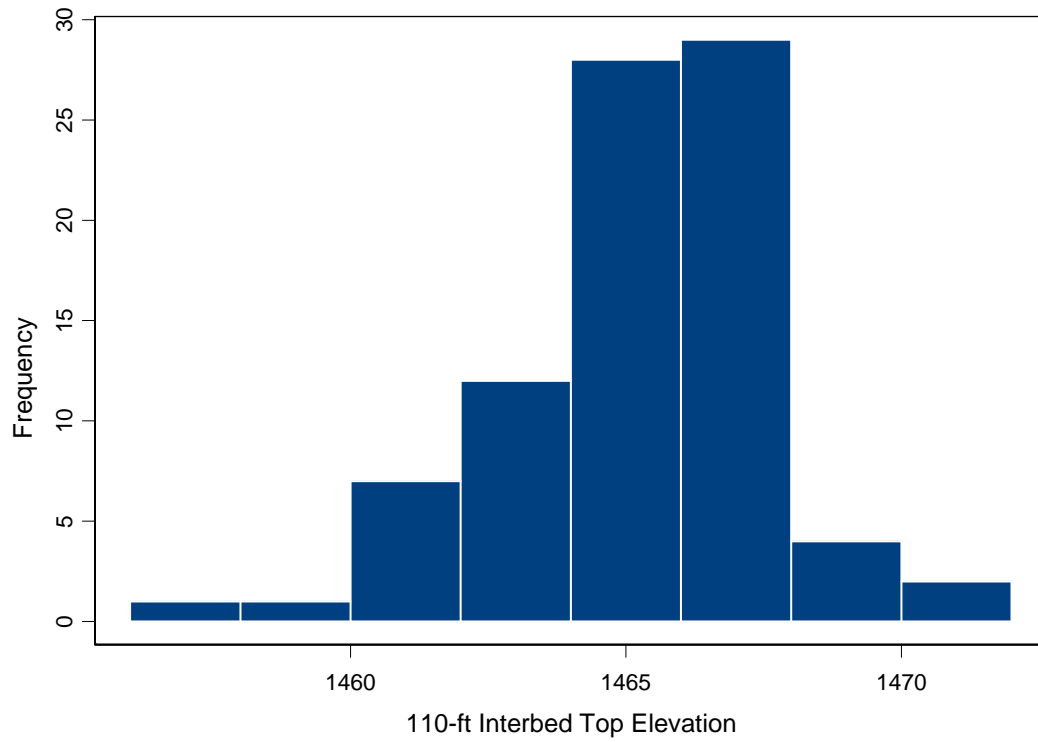


Figure C-48. Histogram of observed 110-ft interbed top elevation values.

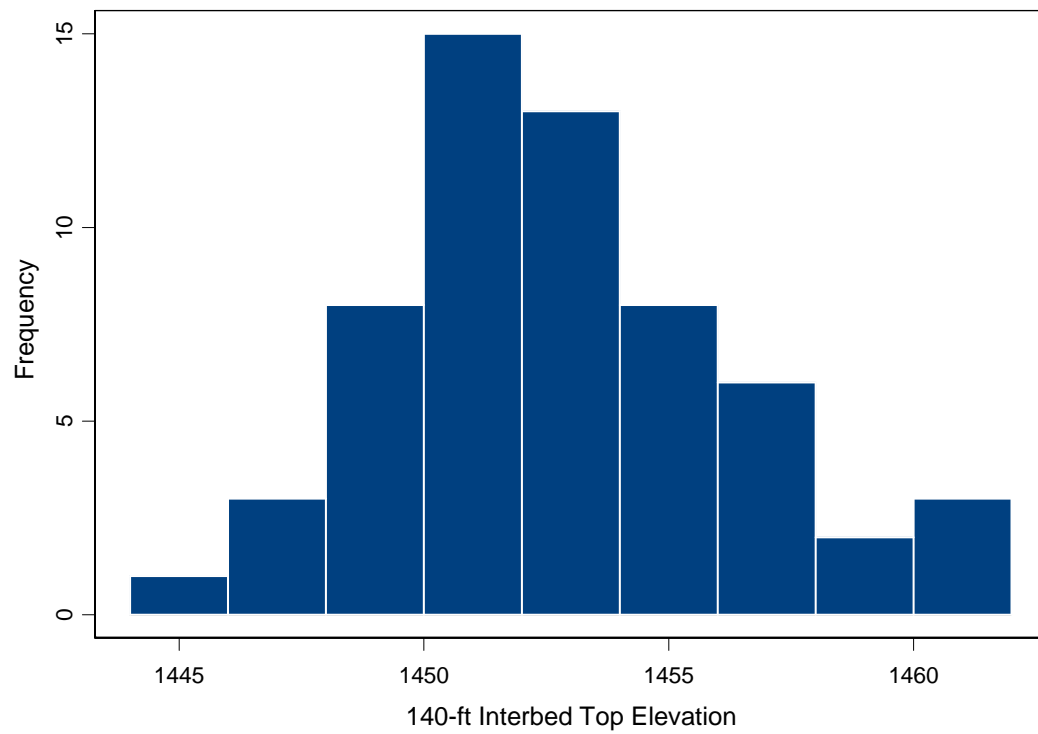


Figure C-49. Histogram of observed 140-ft interbed top elevation values.

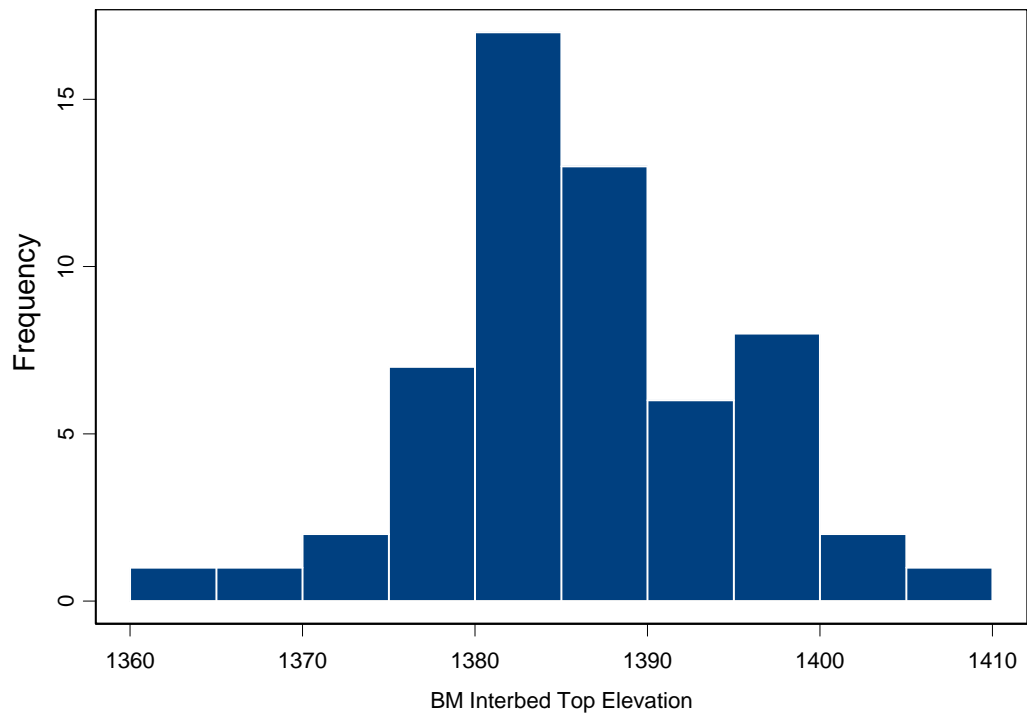


Figure C-50. Histogram of observed BM interbed top elevation values.

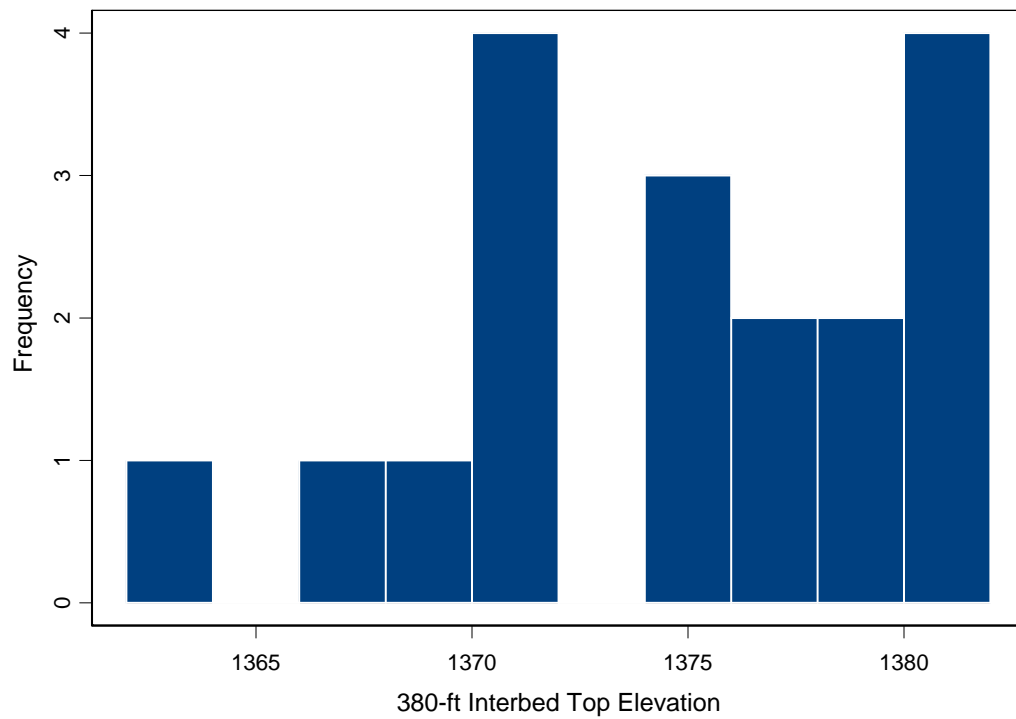


Figure C-51. Histogram of observed 380-ft interbed top elevation values.

Table C-8. Semivariogram model parameters for vadose zone lithology variables. The nugget and sill are in unit² with units given in parentheses after the variable name.

Variable Name	Model	Nugget (unit ²)	Partial Sill (unit ²)	Range (m)	Vertical Range (m)
Surficial Alluvium Thickness (m)	Spherical	0	10	600	NA ^a
110-ft Interbed Thickness (m)	Spherical	1	5.5	350	NA
140-ft Interbed Thickness (m)	Gaussian	0	7	200	NA
BM Interbed Thickness (m)	Spherical	0	11	250	NA
380-ft Interbed Thickness (m)	Spherical	0	3.7	550	NA
110-ft Interbed Top Elevation (m amsl)	Spherical	1	5	550	NA
140-ft Interbed Top Elevation (m amsl)	Spherical	0	10	400	NA
BM Interbed Top Elevation (m amsl)	Spherical	0	40	400	NA
380-ft Interbed Top Elevation (m amsl)	Spherical	0	25	600	NA
Surficial Alluvium Permeability Category (NE-SW and E-W)	Spherical	0	0.05	300	NA
Surficial Alluvium Permeability Category (NW-SE and N-S)	Spherical	0.01	0.03	300	NA
110-ft Interbed Permeability Category	Spherical	0	0.2	100	NA
140-ft Interbed Permeability Category	Spherical	0	0.2	100	NA
BM Interbed Permeability Category	Spherical	0	0.25	400	NA
380-ft Interbed Permeability Category	Spherical	0	0.2	300	NA
Permeability Category 3 (high-permeability interbed)	Exponential	0.008	0.01	100	30
Permeability Category 4 (low-permeability interbed)	Exponential	0	0.028	100	30
Permeability Category 5 (high-permeability basalt)	Exponential	0	0.09	80	30
Permeability Category 6 (low-permeability basalt)	Exponential	0	0.055	80	30

a. NA = not applicable for two-dimensional variables.

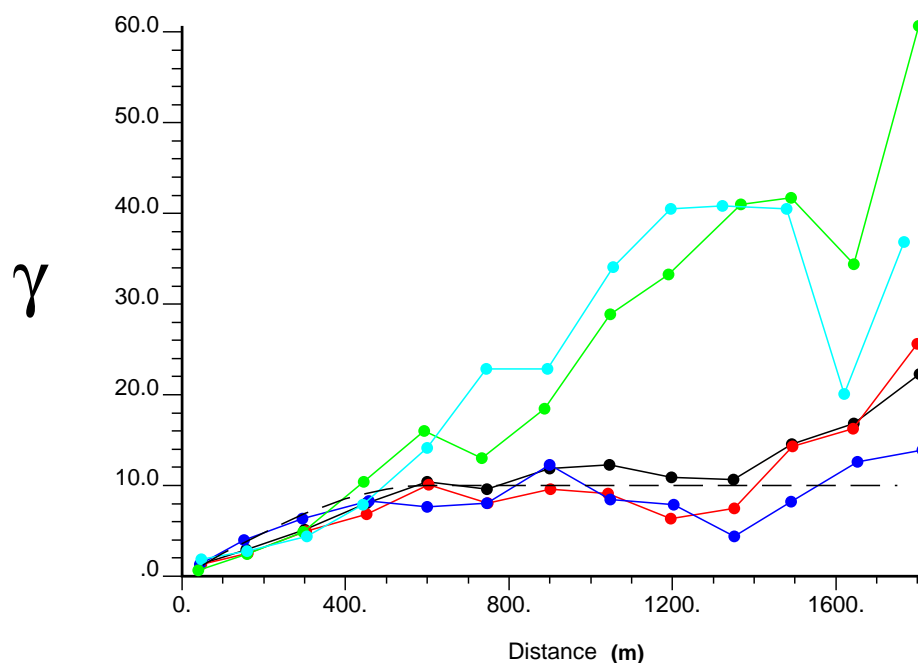


Figure C-52. Surficial alluvium thickness semivariograms. γ is the semivariance of surficial alluvium thickness at various distance lags. Black dots with connecting lines are the omnidirectional semivariogram. Red is N-S, dark blue is NE-SW, green is E-W, and light blue is NW-SE. The large-dash line semivariogram is spherical (0, 10, 600).

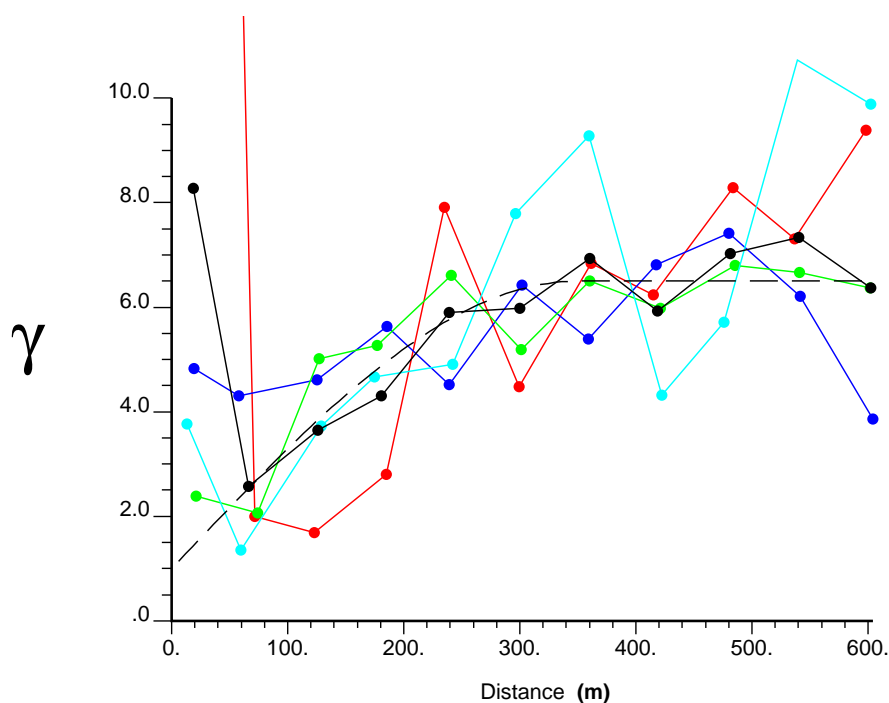


Figure C-53. The 110-ft interbed thickness semivariograms. γ is the semivariance of 110-ft interbed thickness at various distance lags. Black dots with connecting lines are the omnidirectional semivariogram. Red is N-S, dark blue is NE-SW, green is E-W, and light blue is NW-SE. The large-dash line semivariogram is spherical (1, 5.5, 350).

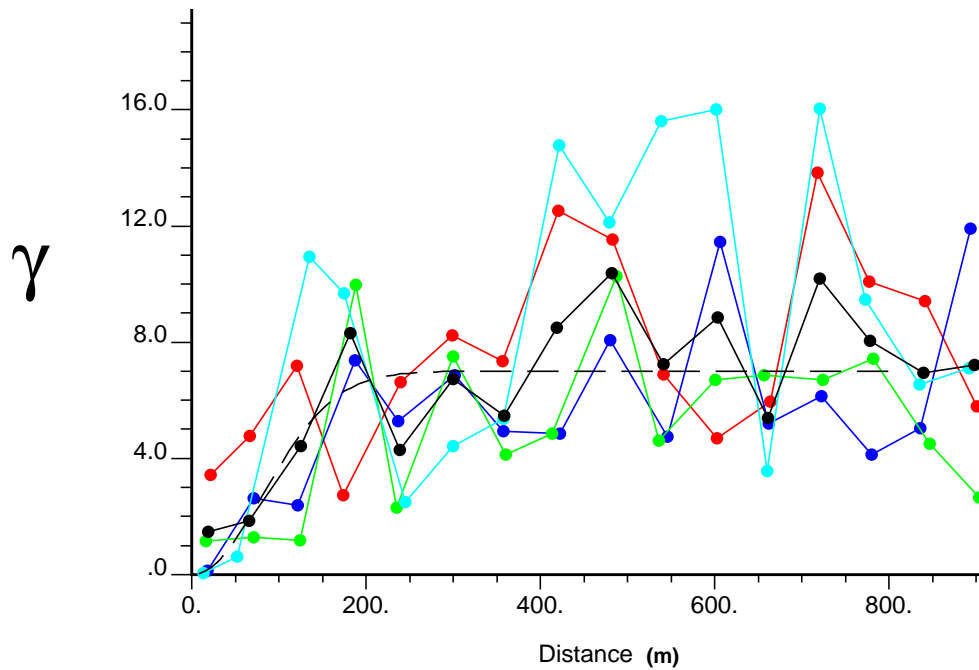


Figure C-54. The 140-ft interbed thickness semivariograms. γ is the semivariance of 140-ft interbed thickness at various distance lags. Black dots with connecting lines are the omnidirectional semivariogram. Red is N-S, dark blue is NE-SW, green is E-W, and light blue is NW-SE. The large-dash line semivariogram is Gaussian (0, 7, 200).

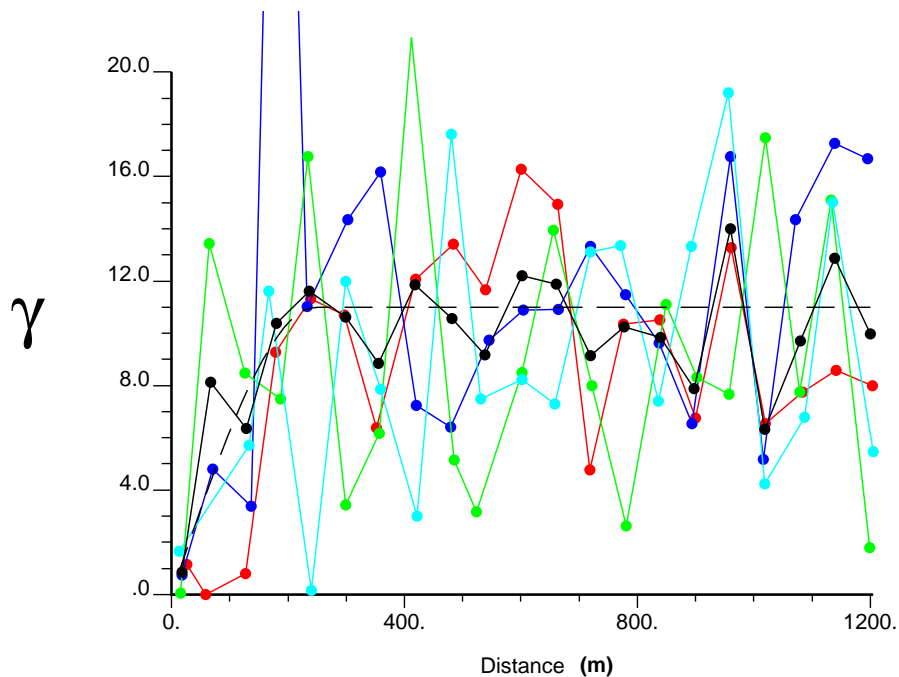


Figure C-55. The BM interbed thickness semivariograms. γ is the semivariance of BM interbed thickness at various distance lags. Black dots with connecting lines are the omnidirectional semivariogram. Red is N-S, dark blue is NE-SW, green is E-W, and light blue is NW-SE. The large-dash line semivariogram is spherical (0, 11, 250).

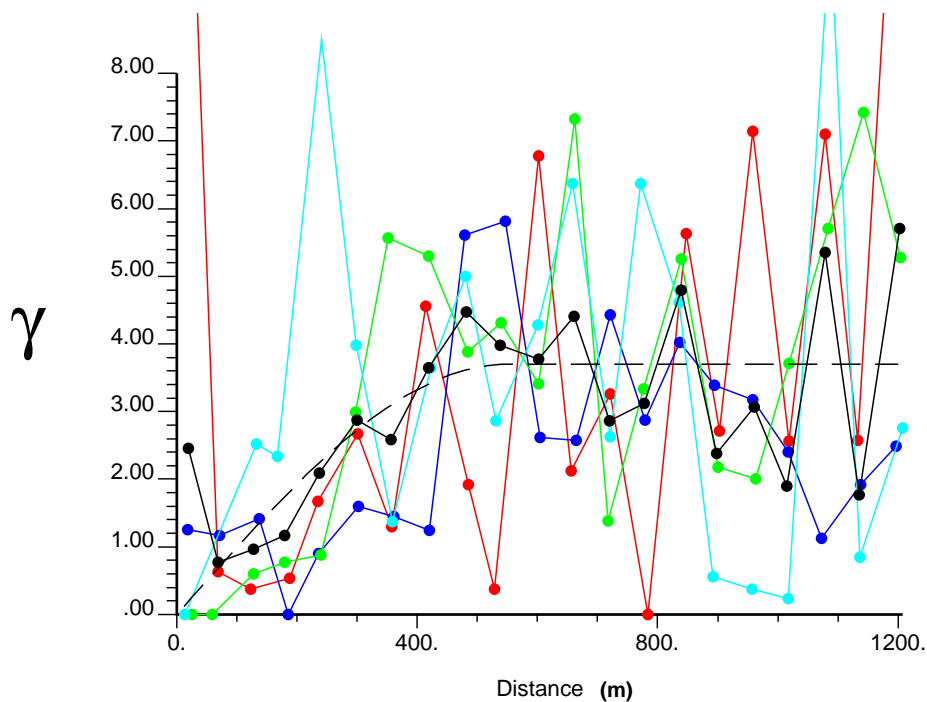


Figure C-56. The 380-ft interbed thickness semivariograms. γ is the semivariance of 380-ft interbed thickness at various distance lags. Black dots with connecting lines are the omnidirectional semivariogram. Red is N-S, dark blue is NE-SW, green is E-W, and light blue is NW-SE. The large-dash line semivariogram is spherical (0, 3.7, 550).

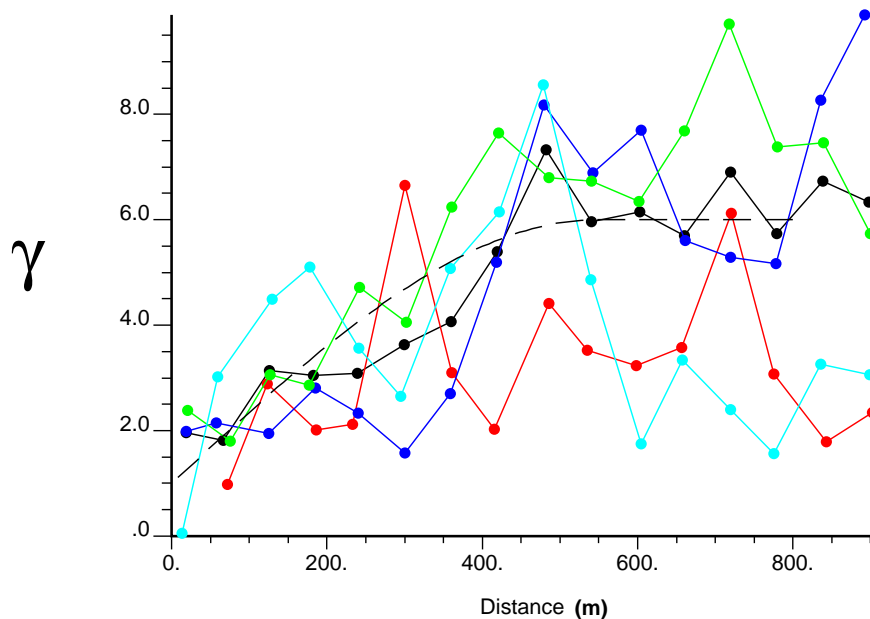


Figure C-57. The 110-ft interbed elevation semivariograms. γ is the semivariance of 110-ft interbed elevation at various distance lags. Black dots with connecting lines are the omnidirectional semivariogram. Red is N-S, dark blue is NE-SW, green is E-W, and light blue is NW-SE. The large-dash line semivariogram is spherical (1, 5, 550).

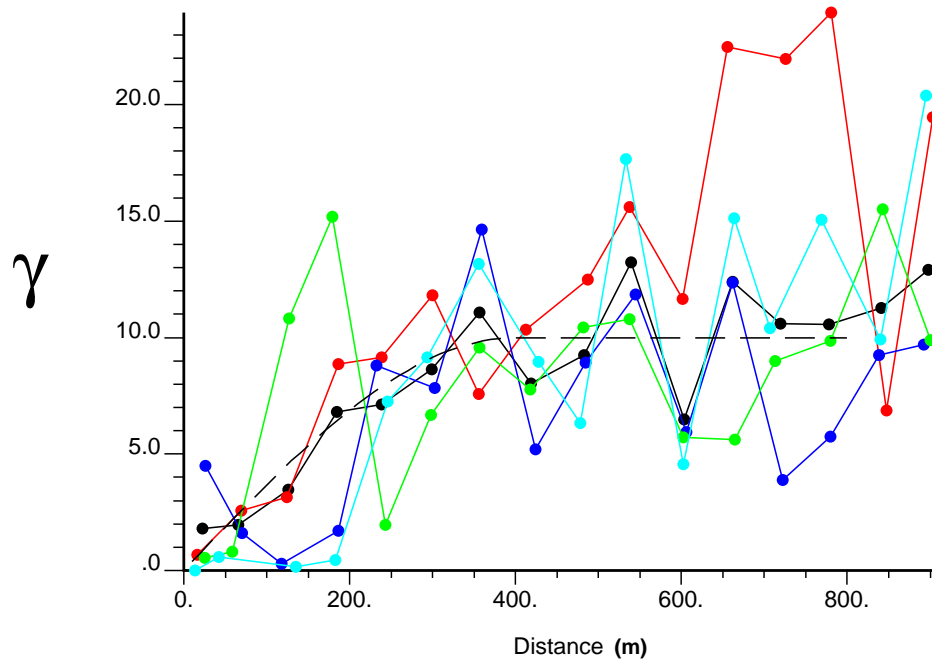


Figure C-58. The 140-ft interbed elevation semivariograms. γ is the semivariance of 140-ft interbed elevation at various distance lags. Black dots with connecting lines are the omnidirectional semivariogram. Red is N-S, dark blue is NE-SW, green is E-W, and light blue is NW-SE. The large-dash line semivariogram is spherical (0, 10, 400).

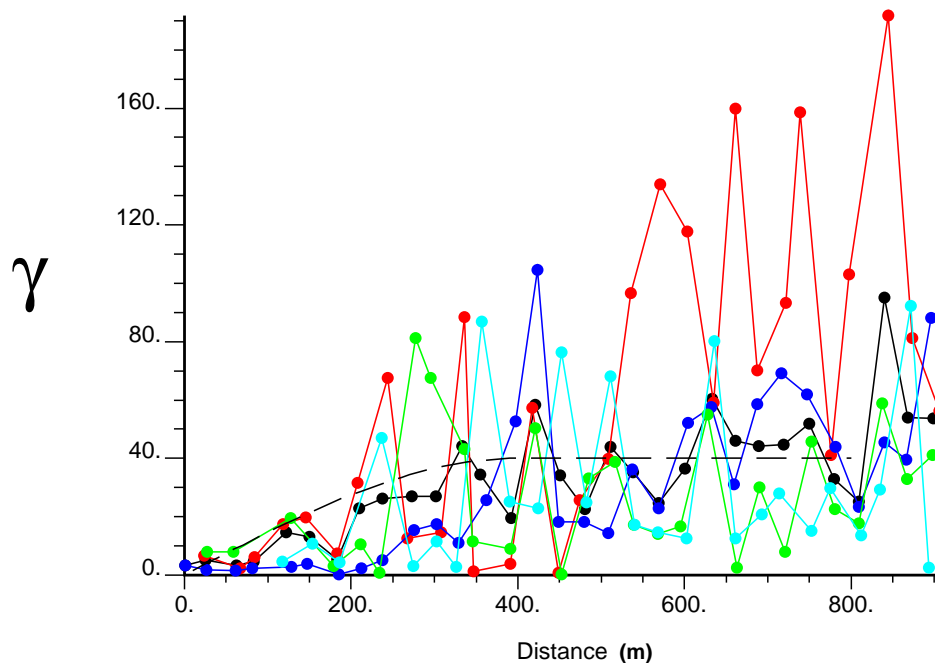


Figure C-59. The BM interbed elevation semivariograms. γ is the semivariance of BM interbed elevation at various distance lags. Black dots with connecting lines are the omnidirectional semivariogram. Red is N-S, dark blue is NE-SW, green is E-W, and light blue is NW-SE. The large-dash line semivariogram is spherical (0, 40, 400).

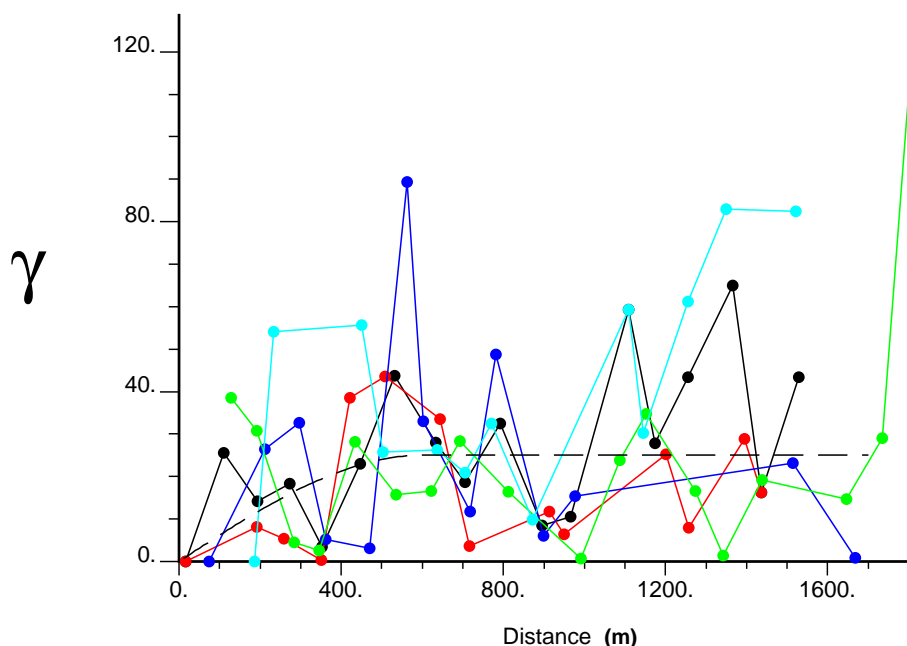


Figure C-60. The 380-ft interbed elevation semivariograms. γ is the semivariance of 380-ft interbed elevation at various distance lags. Black dots with connecting lines are the omnidirectional semivariogram. Red is N-S, dark blue is NE-SW, green is E-W, and light blue is NW-SE. The large-dash line semivariogram is spherical (0, 0.05, 300).

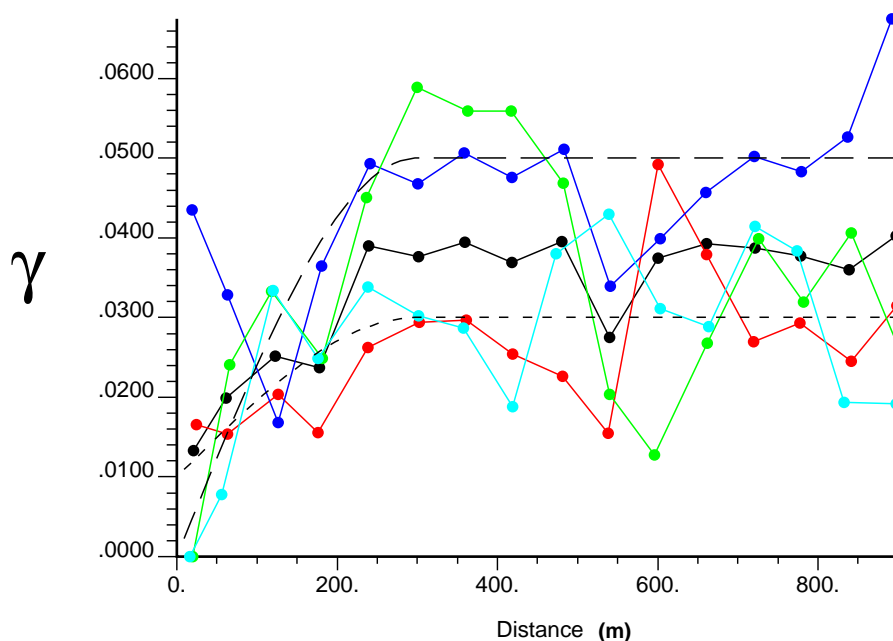


Figure C-61. Surficial alluvium permeability category 3-D semivariograms. γ is the semivariance of permeability category (1 – 6) at various distance lags. Black dots with connecting lines are the omnidirectional semivariogram. Red is N-S, dark blue is NE-SW, green is E-W, and light blue is NW-SE. The large-dash line semivariogram is spherical (0.01, 0.03, 300) and the small-dash semivariogram is spherical (0.01, 0.03, 300). These two semivariograms represent the anisotropic semivariance of the surficial alluvium permeability category data.

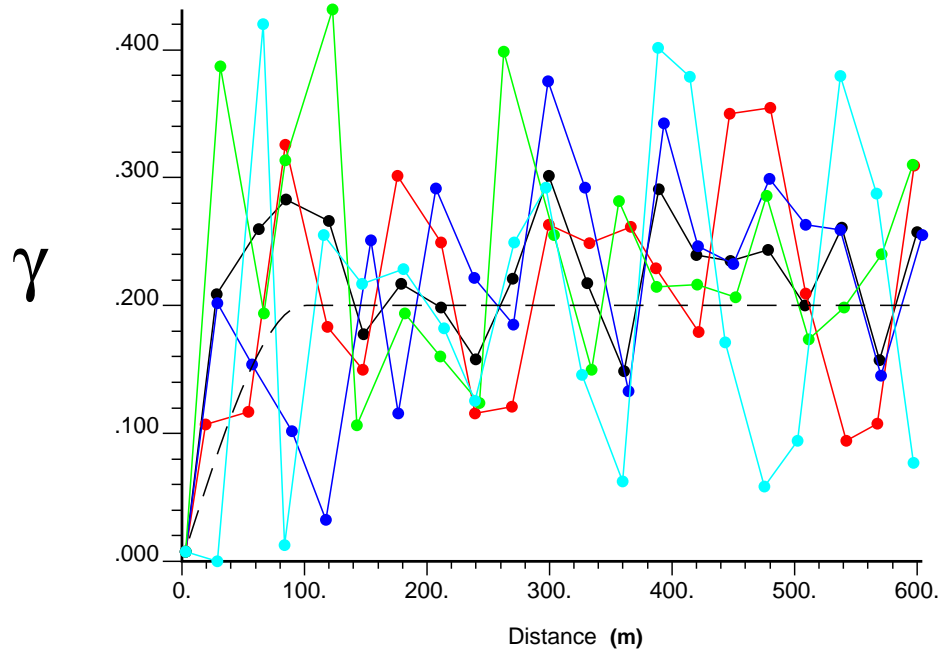


Figure C-62. The 110-ft interbed permeability category 3-D semivariograms. γ is the semivariance of permeability category (1 – 6) at various distance lags. Black dots with connecting lines represent the omnidirectional semivariogram. Red is N-S, dark blue is NE-SW, green is E-W, and light blue is NW-SE. The large-dash line semivariogram is spherical (0, 0.2, 100).

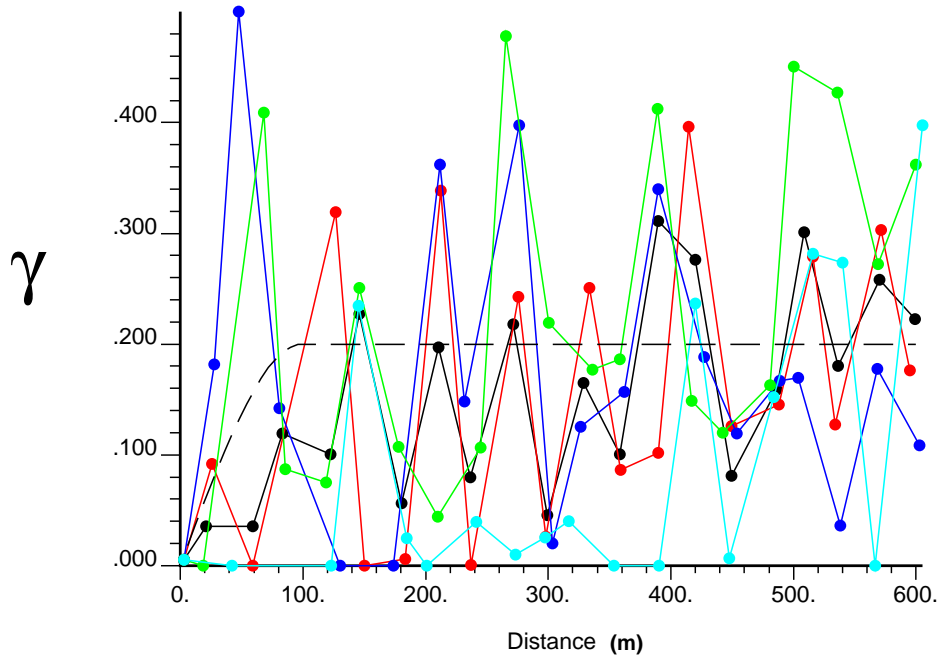


Figure C-63. The 140-ft interbed permeability category 3-D semivariograms. γ is the semivariance of permeability category (1 – 6) at various distance lags. Black dots with connecting lines are the omnidirectional semivariogram. Red is N-S, dark blue is NE-SW, green is E-W, and light blue is NW-SE. The large-dash line semivariogram is spherical (0, 0.2, 100).

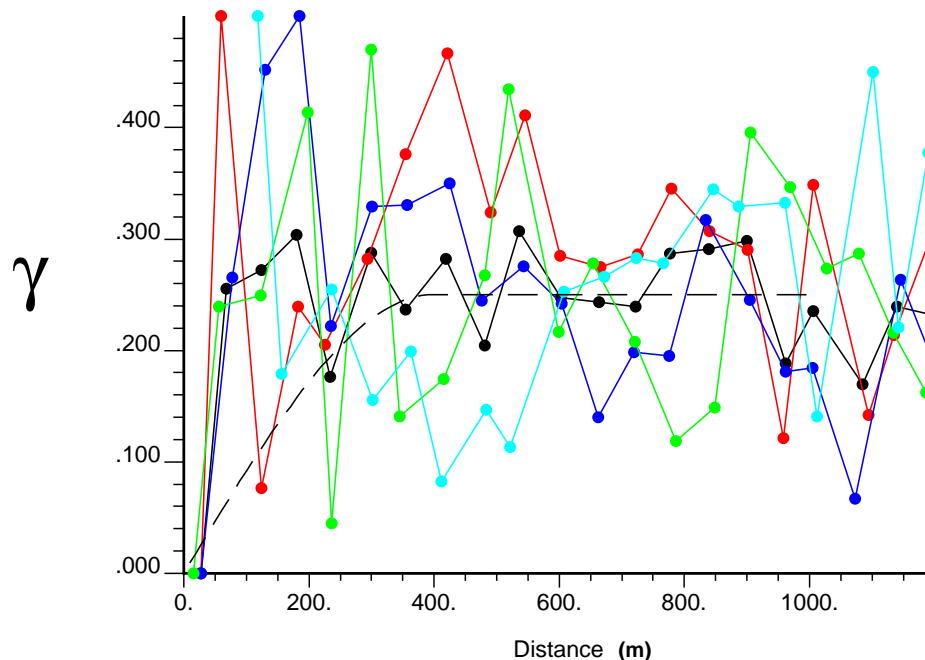


Figure C-64. The BM interbed permeability category 3-D semivariograms. γ is the semivariance of permeability category (1 – 6) at various distance lags. Black dots with connecting lines are the omnidirectional semivariogram. Red is N-S, dark blue is NE-SW, green is E-W, and light blue is NW-SE. The large-dash line semivariogram is spherical (0, 0.25, 400).

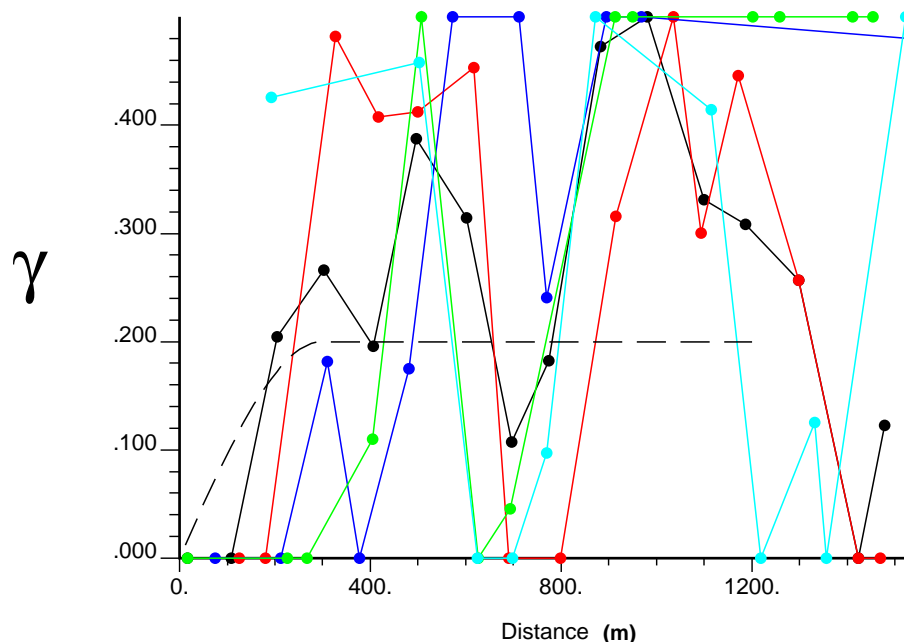


Figure C-65. The 380-ft interbed permeability category 3-D semivariograms. γ is the semivariance of permeability category (1 – 6) at various distance lags. Black dots with connecting lines are the omnidirectional semivariogram. Red is N-S, dark blue is NE-SW, green is E-W, and light blue is NW-SE. The large-dash line semivariogram is spherical (0, 0.2, 300).

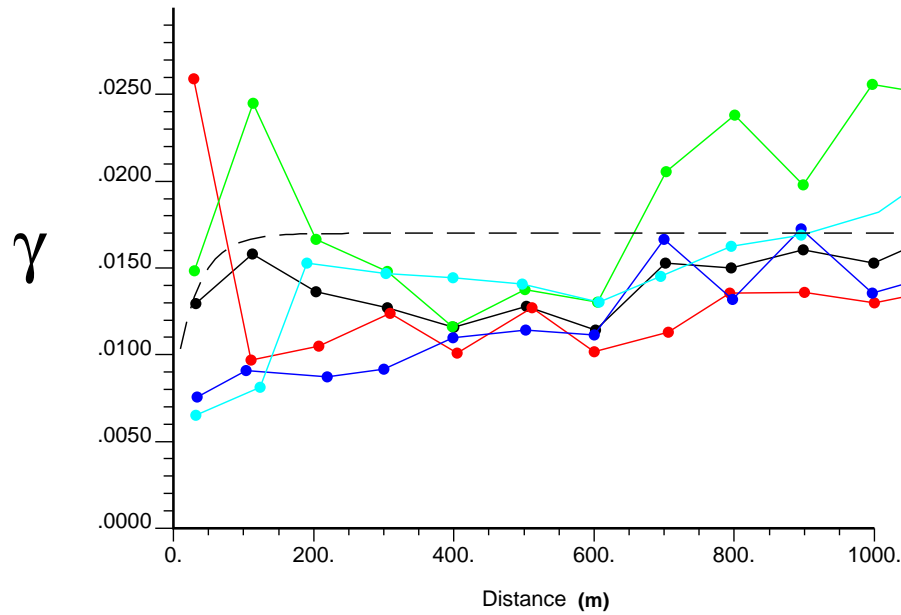


Figure C-66. Permeability Category 3 (high-permeability interbed) 3-D semivariograms. γ is the semivariance of permeability Category 3 at various distance lags. Black dots with connecting lines are the omnidirectional semivariogram. Red is N-S, dark blue is NE-SW, green is E-W, and light blue is NW-SE. The large-dash line semivariogram is exponential (0.008, 0.01, 100).

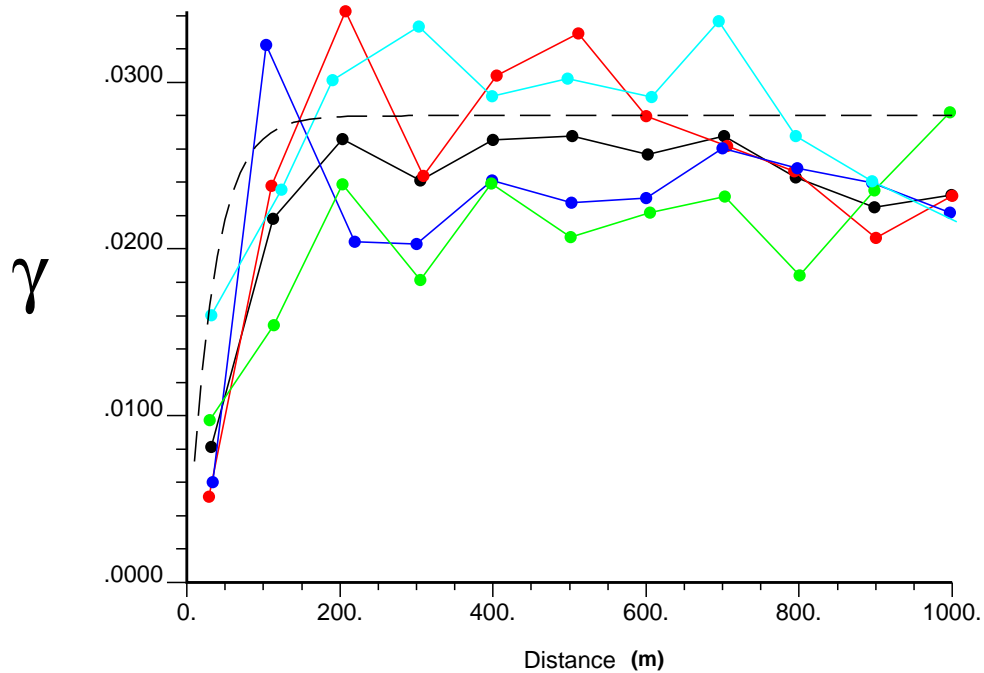


Figure C-67. Permeability Category 4 (low-permeability interbed) 3-D semivariograms. γ is the semivariance of permeability Category 4 at various distance lags. Black dots with connecting lines are the omnidirectional semivariogram. Red is N-S, dark blue is NE-SW, green is E-W, and light blue is NW-SE. The large-dash line semivariogram is exponential (0, 0.028, 100).

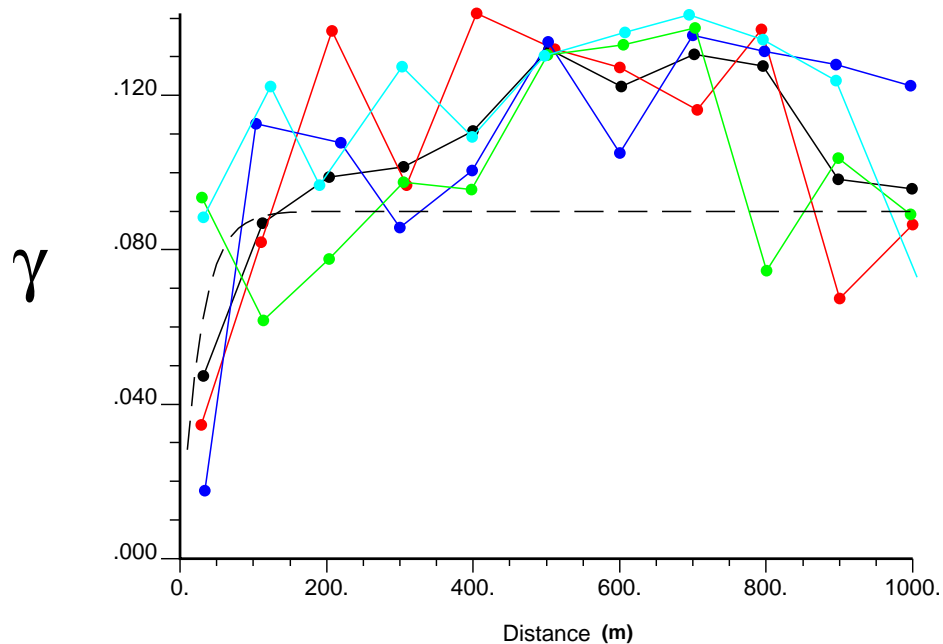


Figure C-68. Permeability Category 5 (high-permeability basalt) 3-D semivariograms. γ is the semivariance of permeability Category 5 at various distance lags. Black dots with connecting lines are the omnidirectional semivariogram. Red is N-S, dark blue is NE-SW, green is E-W, and light blue is NW-SE. The large-dash line semivariogram is exponential (0, 0.09, 80).

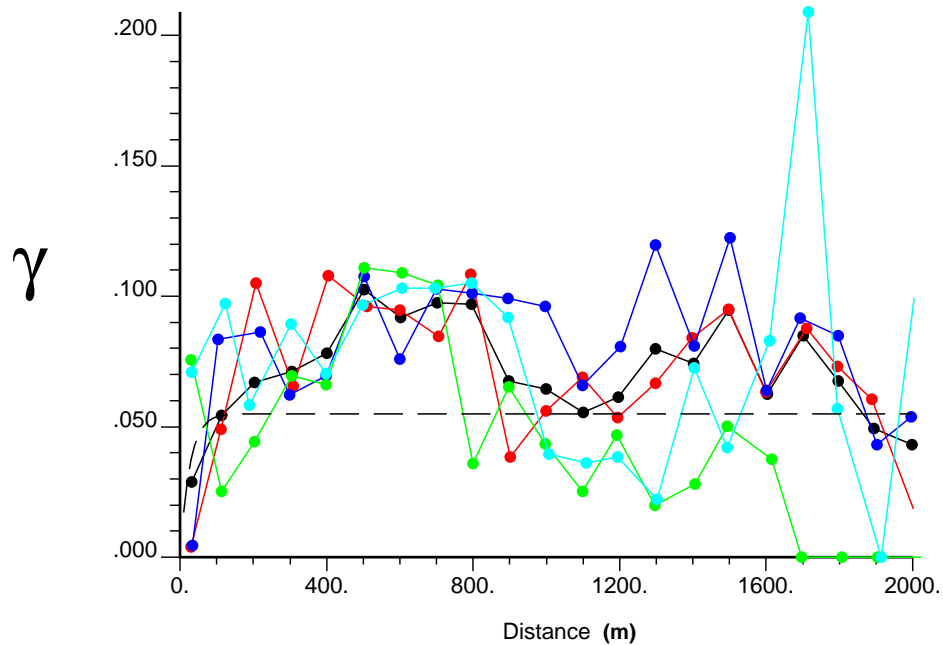


Figure C-69. Permeability Category 6 (low-permeability basalt) 3-D semivariograms. γ is the semivariance of permeability Category 6 at various distance lags. Black dots with connecting lines are the omnidirectional semivariogram. Red is N-S, dark blue is NE-SW, green is E-W, and light blue is NW-SE. The large-dash line semivariogram is exponential (0, 0.055, 80).

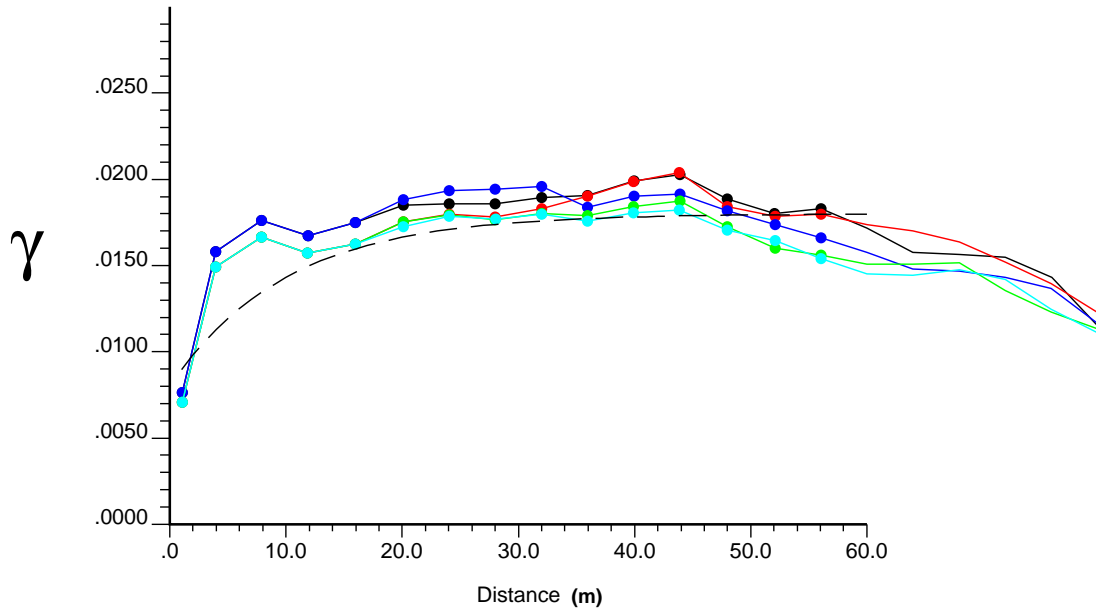


Figure C-70. Permeability Category 3 (high-permeability interbed) 3-D vertical semivariograms. γ is the semivariance of permeability Category 3 at various depth lags. Black dots with connecting lines are the omnidirectional semivariogram. Red is N-S, dark blue is NE-SW, green is E-W, and light blue is NW-SE. The large-dash line semivariogram is exponential (0.008, 0.01, 30).

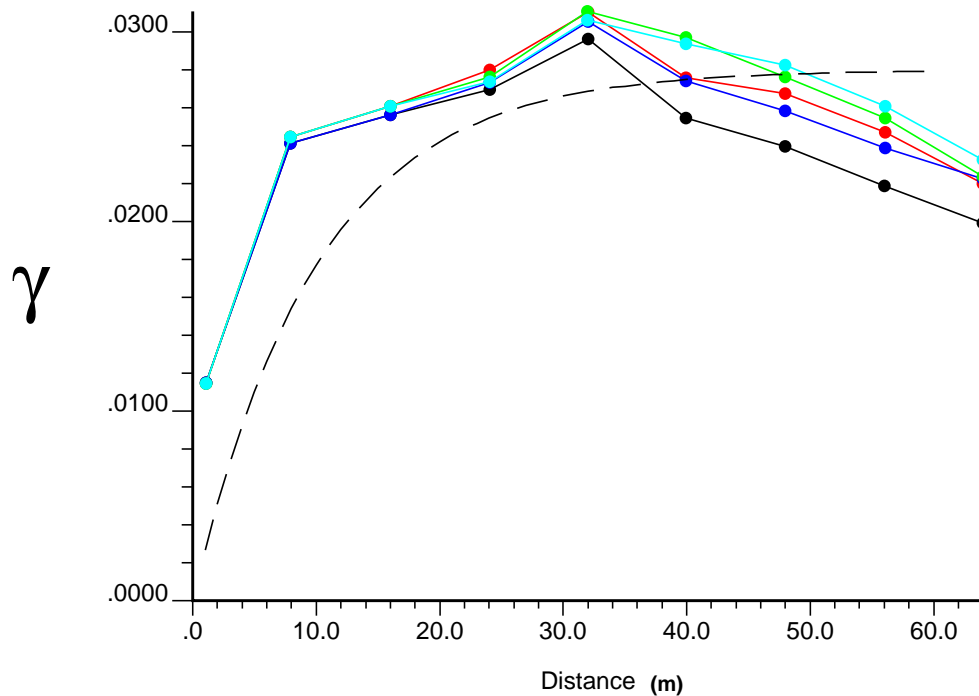


Figure C-71. Permeability Category 4 (low-permeability interbed) 3-D vertical semivariograms. γ is the semivariance of permeability Category 4 at various depth lags. Black dots with connecting lines are the omnidirectional semivariogram. Red is N-S, dark blue is NE-SW, green is E-W, and light blue is NW-SE. The large-dash line semivariogram is exponential (0, 0.028, 30).

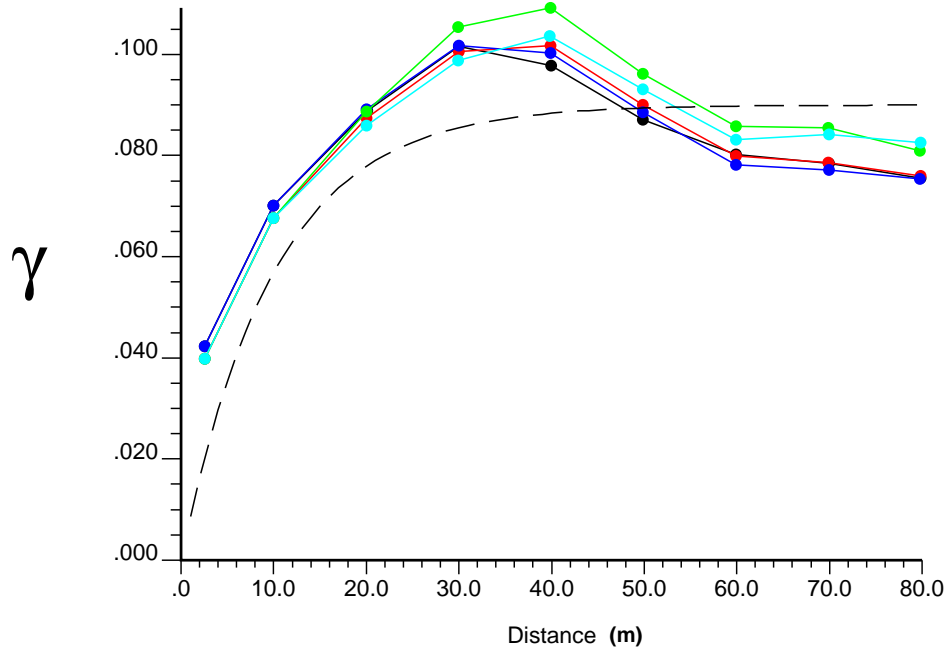


Figure C-72. Permeability Category 5 (high-permeability basalt) 3-D vertical semivariograms. γ is the semivariance of permeability Category 5 at various depth lags. Black dots with connecting lines are the omnidirectional semivariogram. Red is N-S, dark blue is NE-SW, green is E-W, and light blue is NW-SE. The large-dash line semivariogram is exponential (0, 0.09, 30).

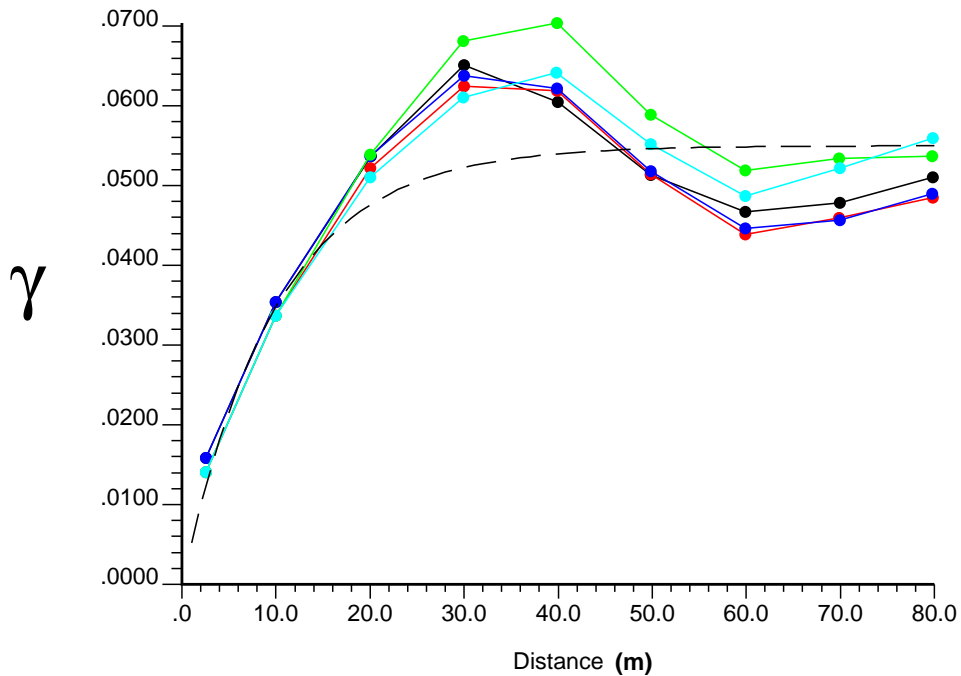


Figure C-73. Permeability Category 6 (low-permeability basalt) 3-D vertical semivariograms. γ is the semivariance of permeability Category 6 at various depth lags. Black dots with connecting lines are the omnidirectional semivariogram. Red is N-S, dark blue is NE-SW, green is E-W, and light blue is NW-SE. The large-dash line semivariogram is exponential (0, 0.055, 30).

C-4.3.3 Kriging

The combined kriging predictions resulted in a full volume picture of the vadose zone lithology (Figure C-74). Only the soil was pictured; all other volume represented basalt.

C-4.3.4 Model Assessment

The predictions of continuous variables (top elevation and thickness) were compared to the observed values by looking at distributions and by cross validation. The predictions of categorical variables (permeability category) were compared to the observed values by looking at a relative frequency table. The 1-m vertical grid predictions were used for comparisons.

The distributions of the observed and predicted values were similar for all thickness and top elevation variables (Figures C-75 through C-83). All predicted thickness values had thicker tails, which is expected from kriging, which is a smoother. But the range and mean for predicted thickness values was very similar to observed. The range and/or mean of predictions for top elevations differed somewhat from the observed. This was due to smaller data sets and the location of areas without sample values in relation to the closest observed values.

The cross-validation plots and statistics generally supported a good-fitting model. The hold-one-out predictions generally followed the observed values (Figures C-84 through C-92), but the correspondence was not extremely close for the thickness values. The histograms of hold-one-out errors were generally small (between -5 and 5) and symmetric (Figures C-93 through C-101). The cross-validation statistics (Table C-9) were generally low, but four of the nine variables had RRMSE outside the ideal range for that statistic. Only surficial alluvium thickness and 380-ft interbed thickness RRMSE values were extremely large. This was due to relatively small variance estimates compared to the hold-one-out errors.

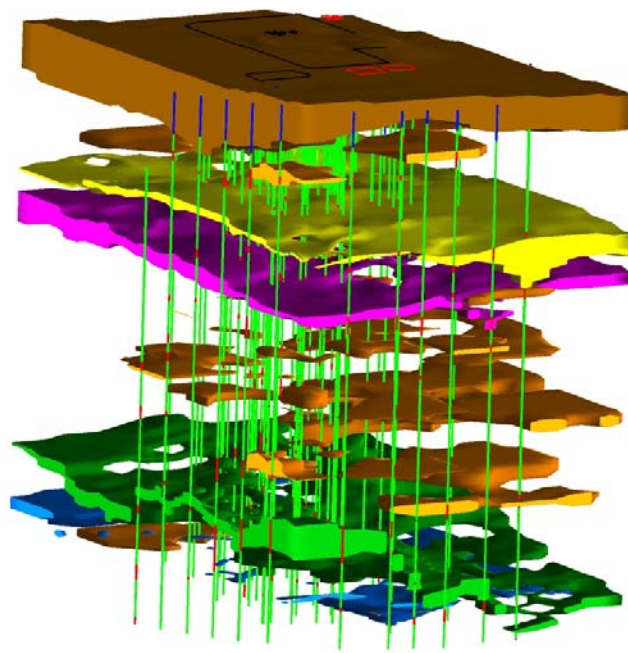


Figure C-74. Combined kriging predicted subsurface soil layers. Surficial alluvium is brown, 110-ft interbed is yellow, 140-ft interbed is pink, BM interbed is green, 380-ft interbed is blue, and other interbed soils are orange. The wells are represented with blue surficial alluvium, green basalt, and red interbed. The INTEC fence, former percolation ponds, and ICDF are outlined on the surface.

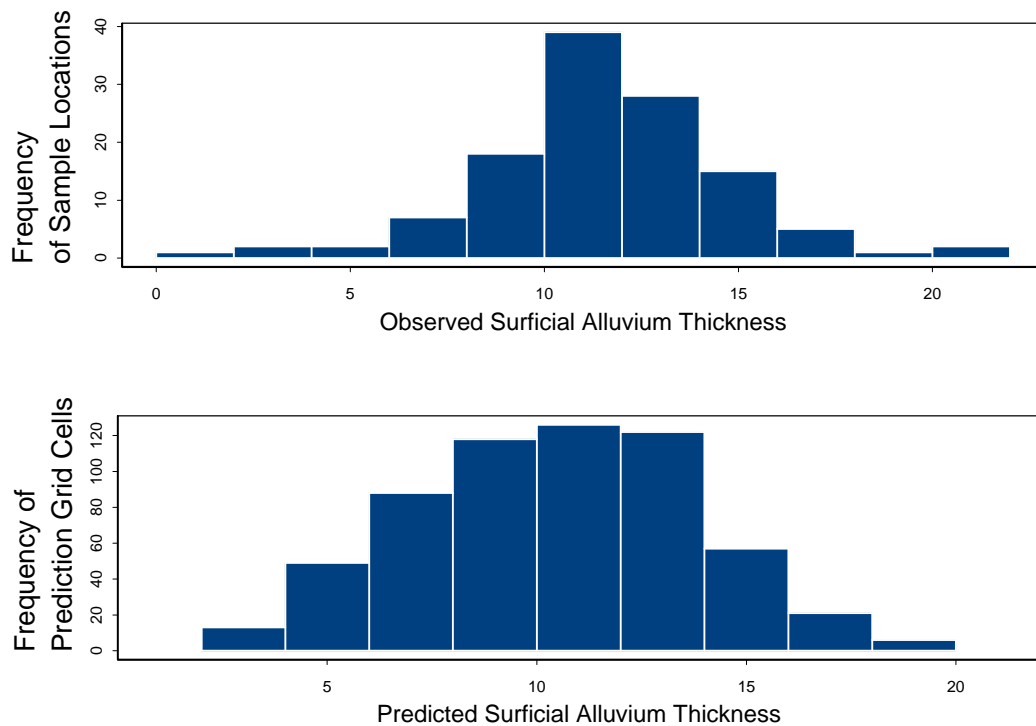


Figure C-75. Histograms of observed and predicted surficial alluvium thickness.

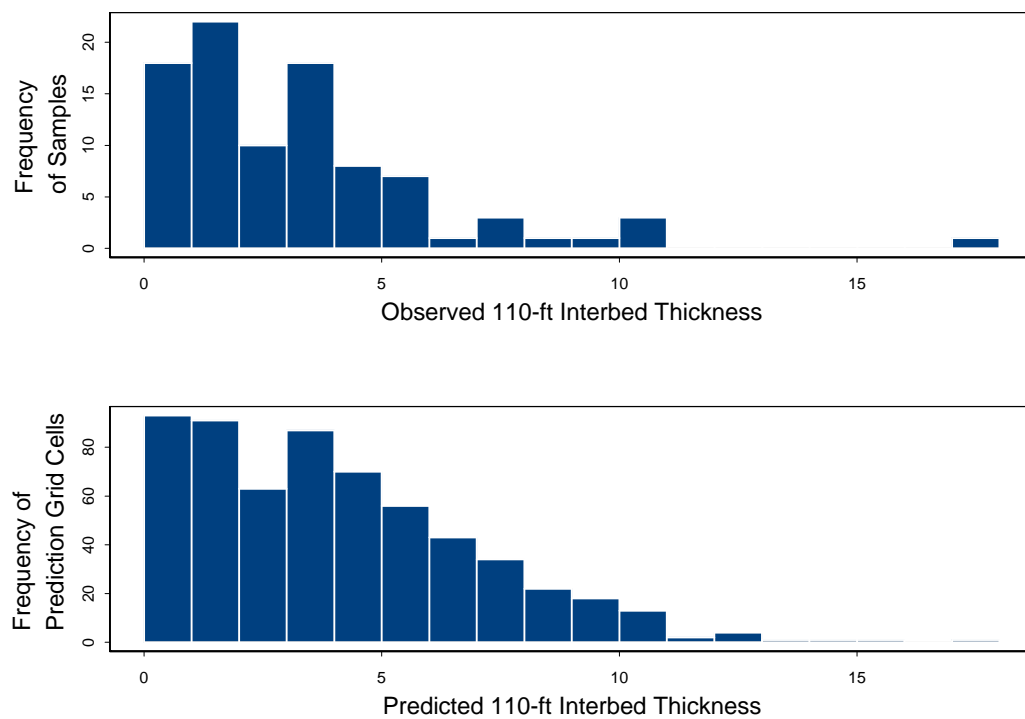


Figure C-76. Histograms of observed and predicted 110-ft interbed thickness.

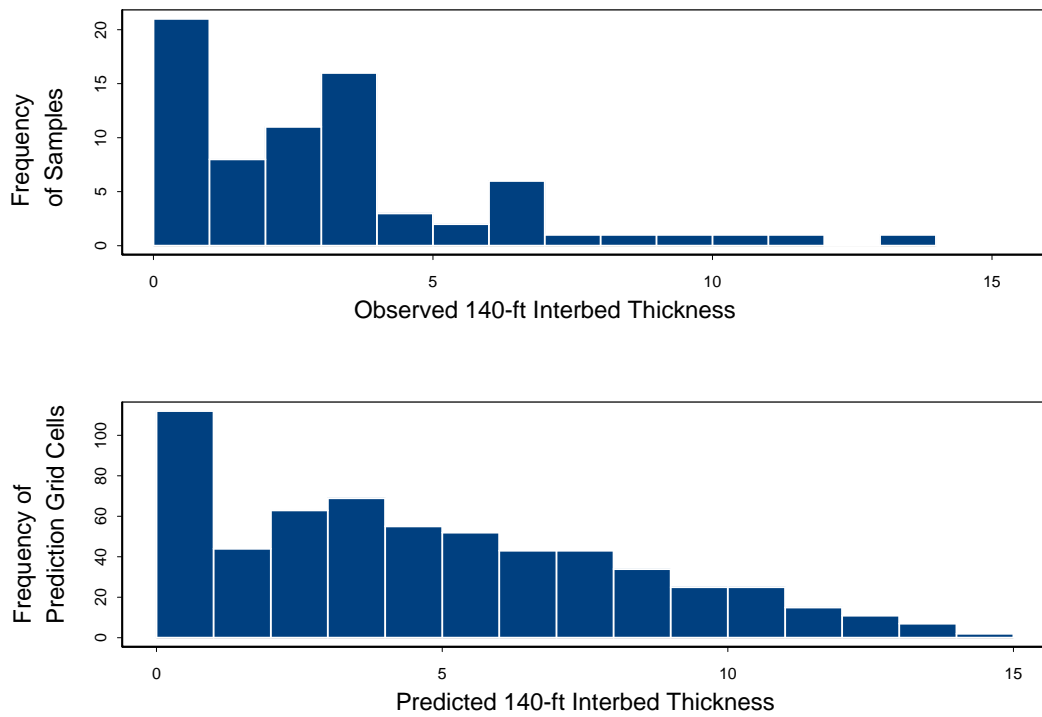


Figure C-77. Histograms of observed and predicted 140-ft interbed thickness.

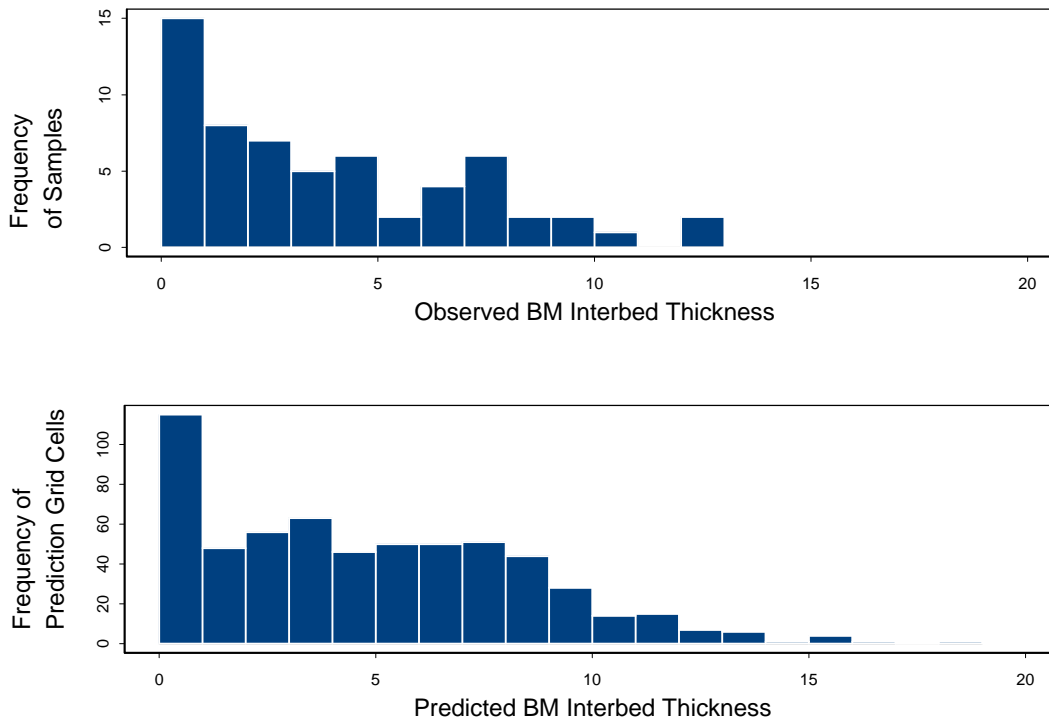


Figure C-78. Observed and predicted BM interbed thickness.

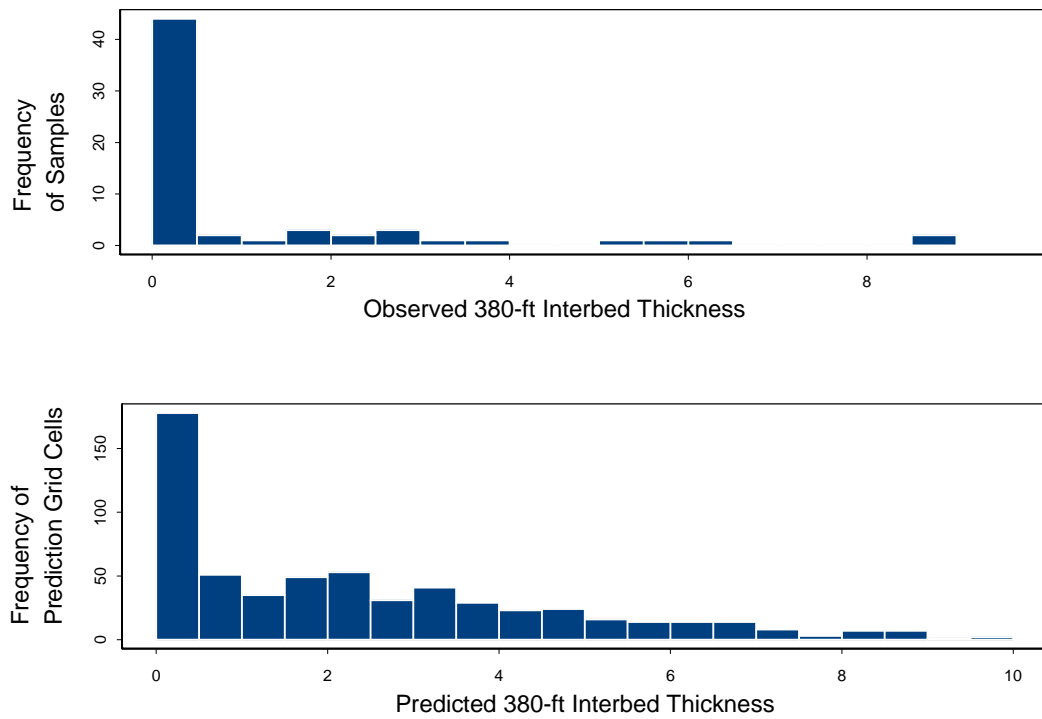


Figure C-79. Observed and predicted 380-ft interbed thickness.

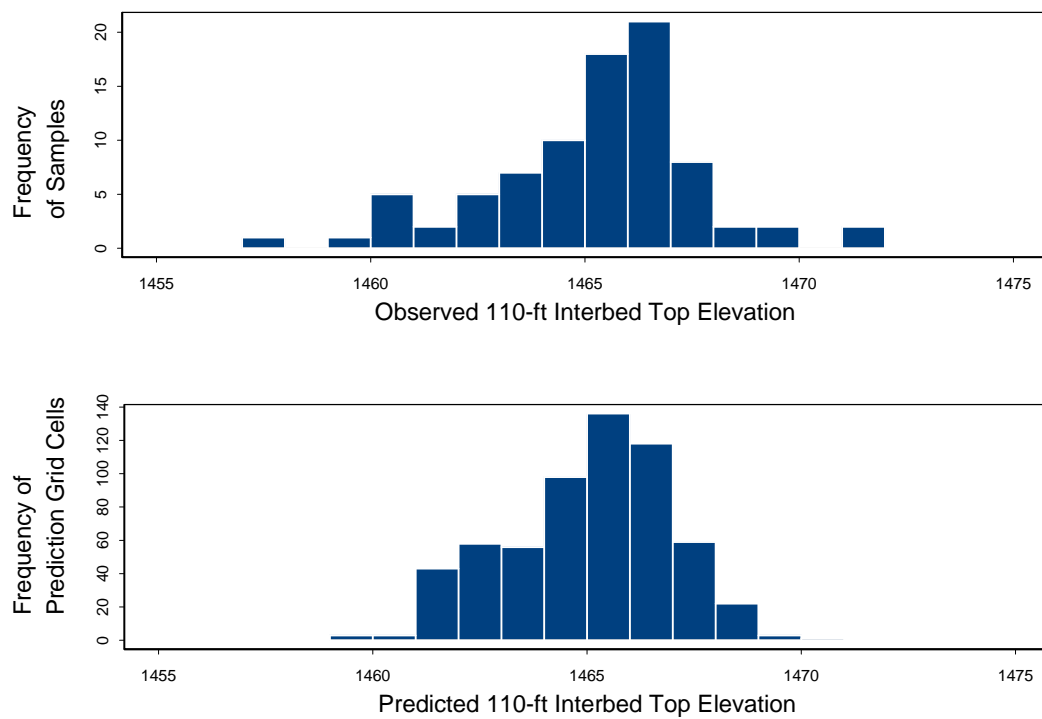


Figure C-80. Observed and predicted 110-ft interbed top elevation.

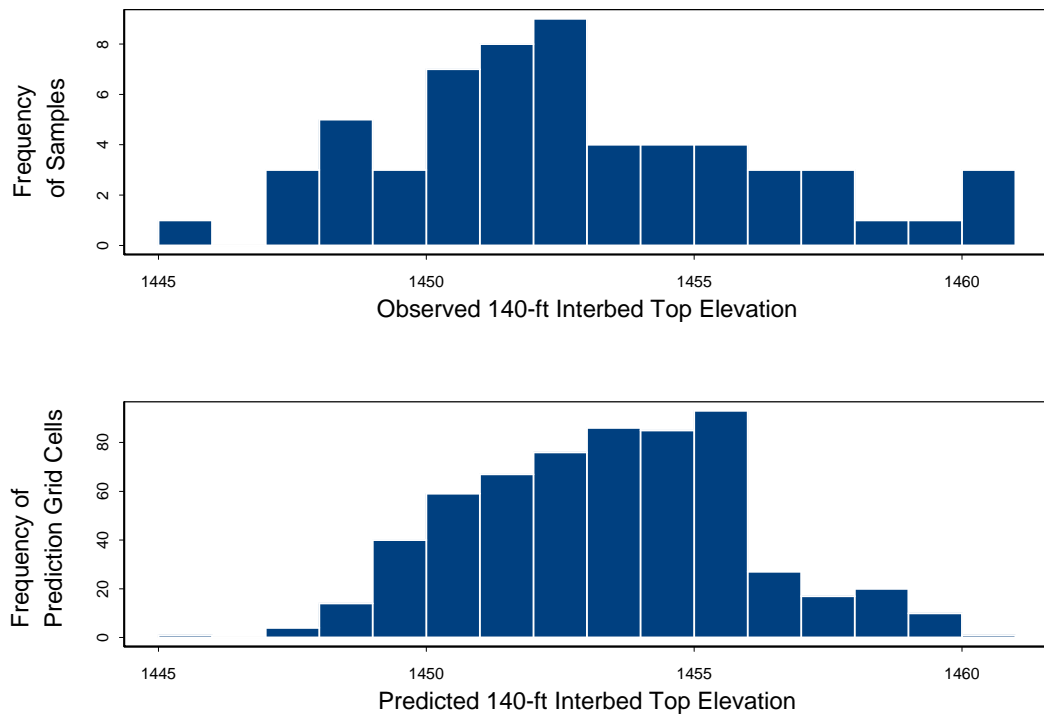


Figure C-81. Observed and predicted 140-ft interbed top elevation.

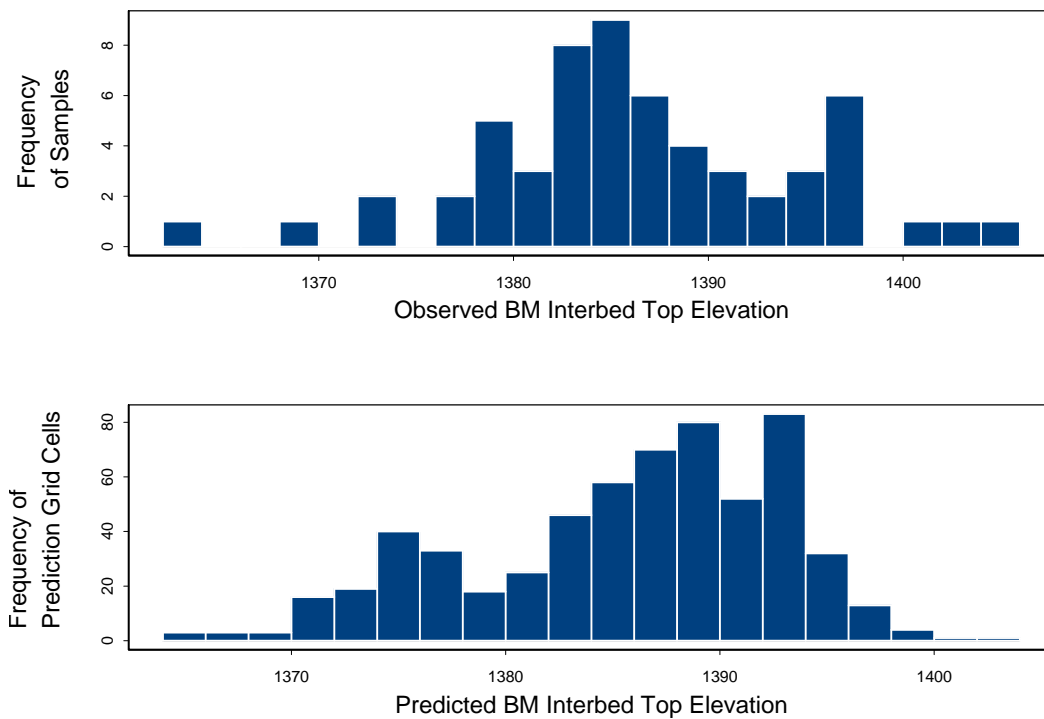


Figure C-82. Observed and predicted BM interbed top elevation.

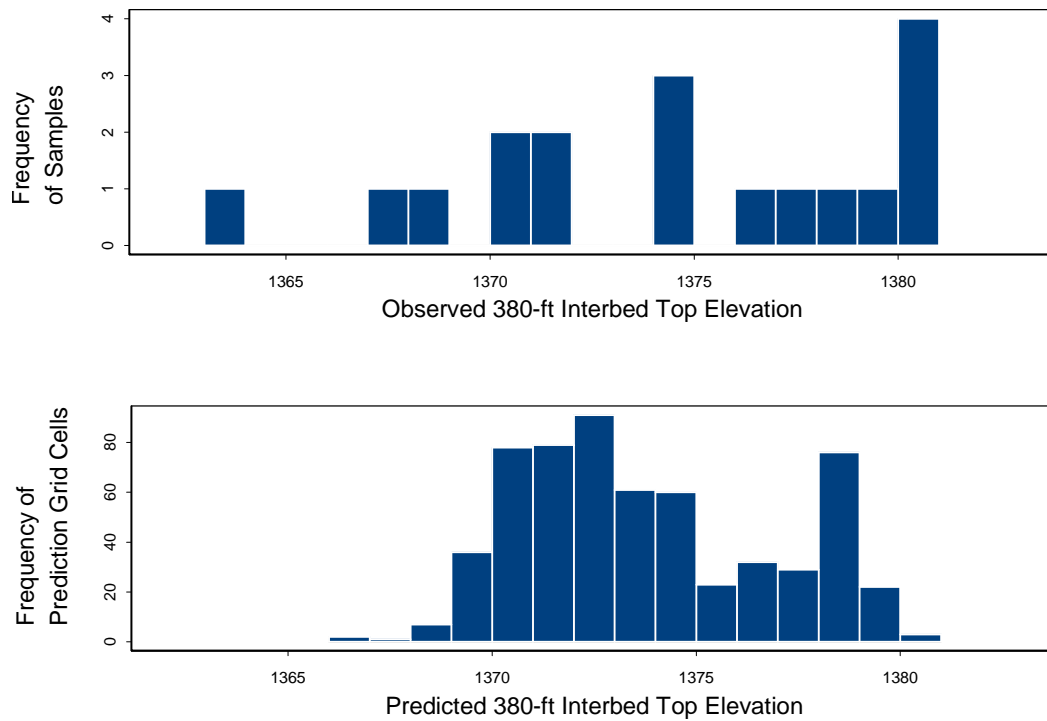


Figure C-83. Observed and predicted 380-ft interbed top elevation.

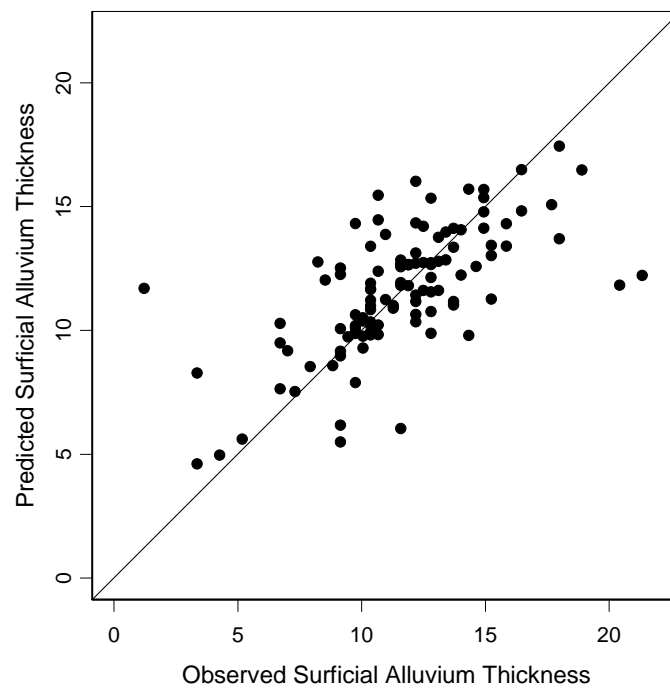


Figure C-84. Observed surficial alluvium thickness versus hold-one-out kriging predictions. The line represents perfect correlation between observed and predicted.

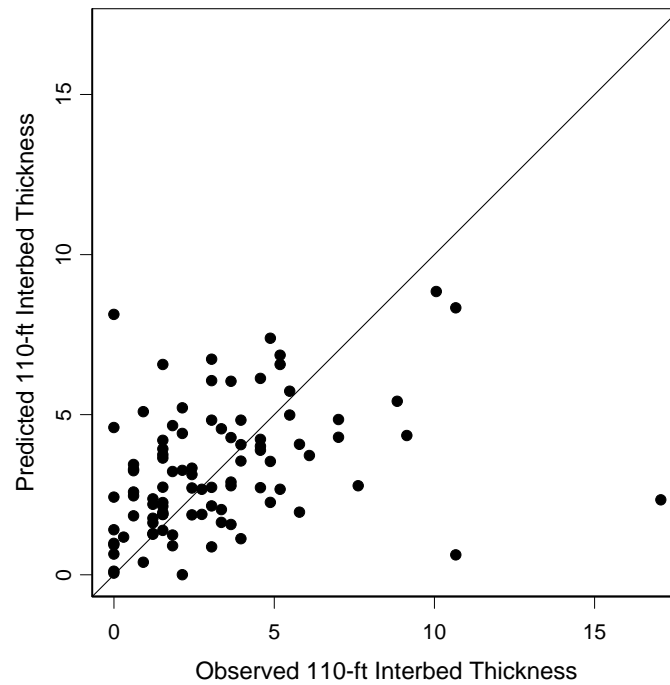


Figure C-85. Observed 110-ft interbed thickness versus hold-one-out kriging predictions. The line represents perfect correlation between observed and predicted.

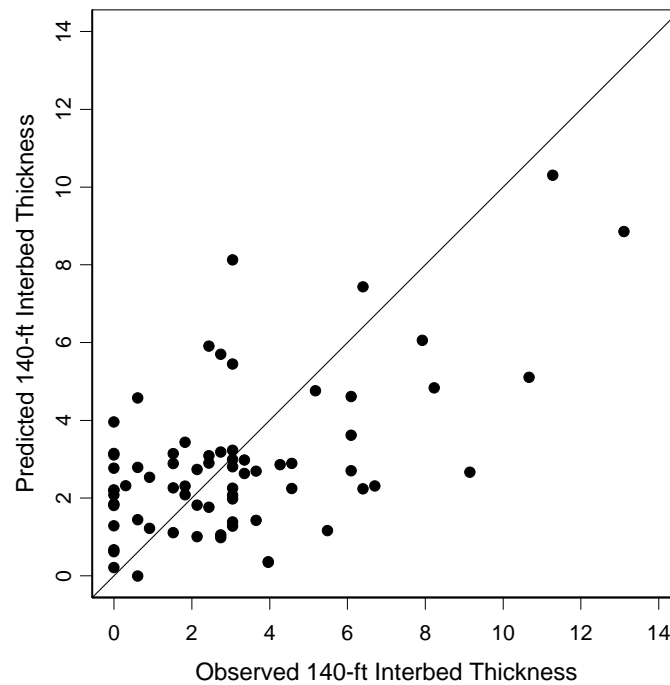


Figure C-86. Observed 140-ft interbed thickness versus hold-one-out kriging predictions. The line represents perfect correlation between observed and predicted.

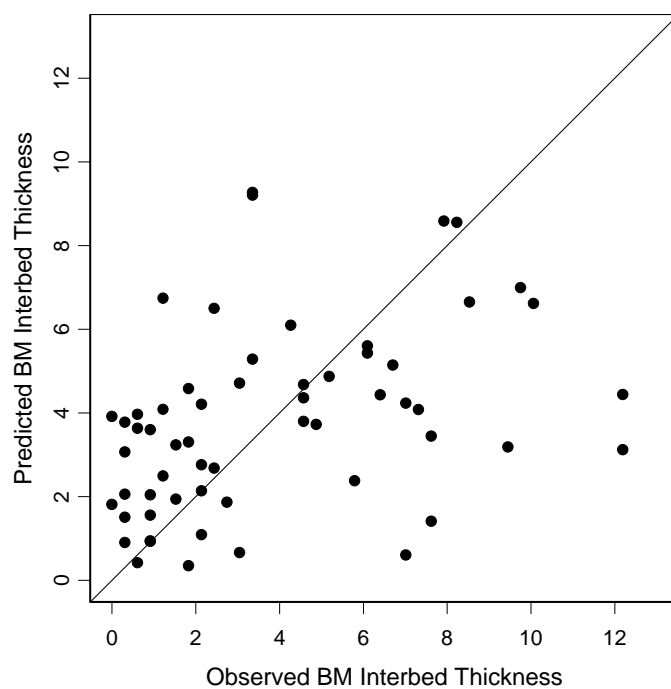


Figure C-87. Observed BM interbed thickness versus hold-one-out kriging predictions. The line represents perfect correlation between observed and predicted.

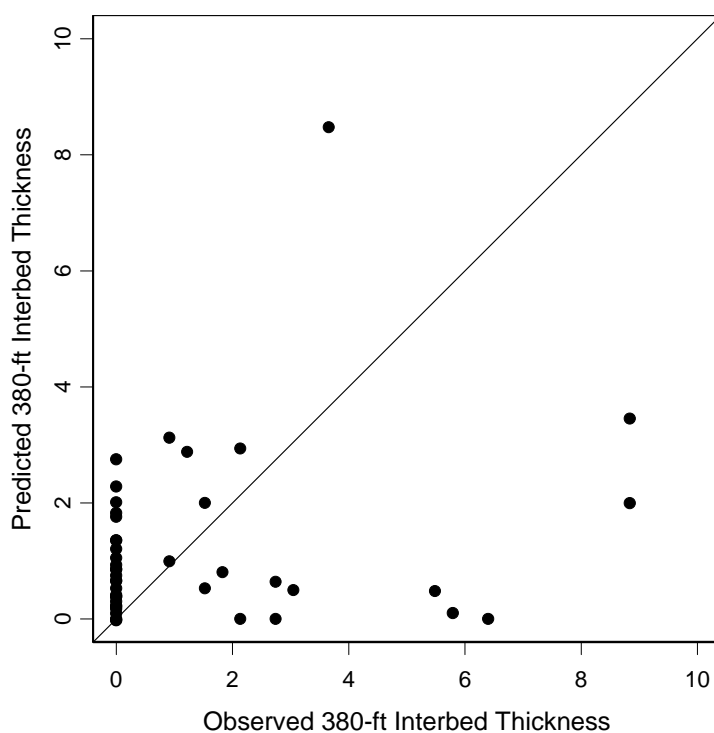


Figure C-88. Observed 380-ft interbed thickness versus hold-one-out kriging predictions. The line represents perfect correlation between observed and predicted.

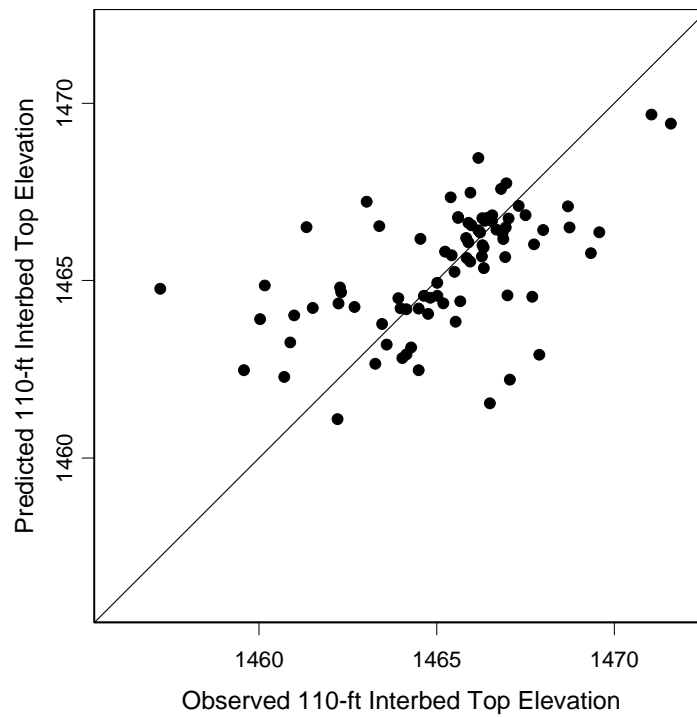


Figure C-89. Observed 110-ft interbed top elevation versus hold-one-out kriging predictions. The line represents perfect correlation between observed and predicted.

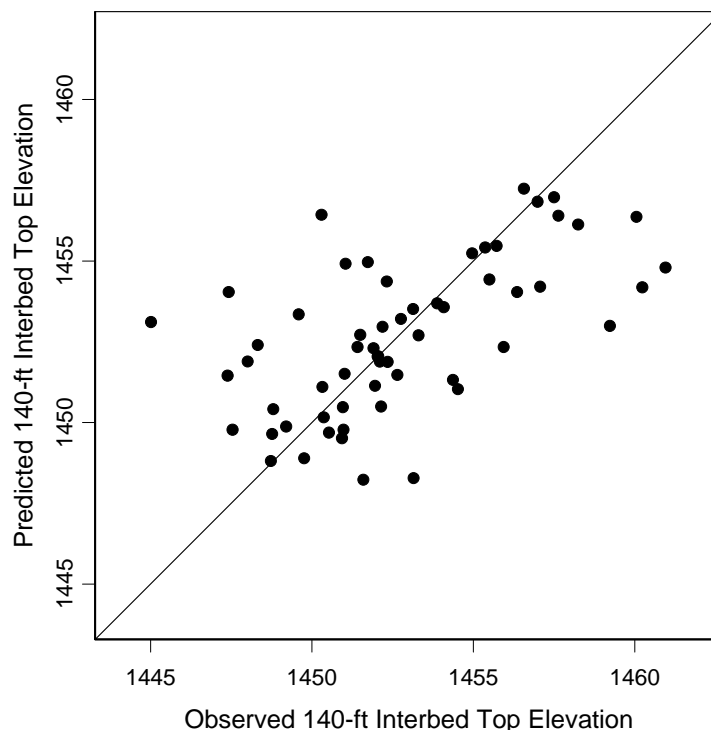


Figure C-90. Observed 140-ft interbed top elevation versus hold-one-out kriging predictions. The line represents perfect correlation between observed and predicted.

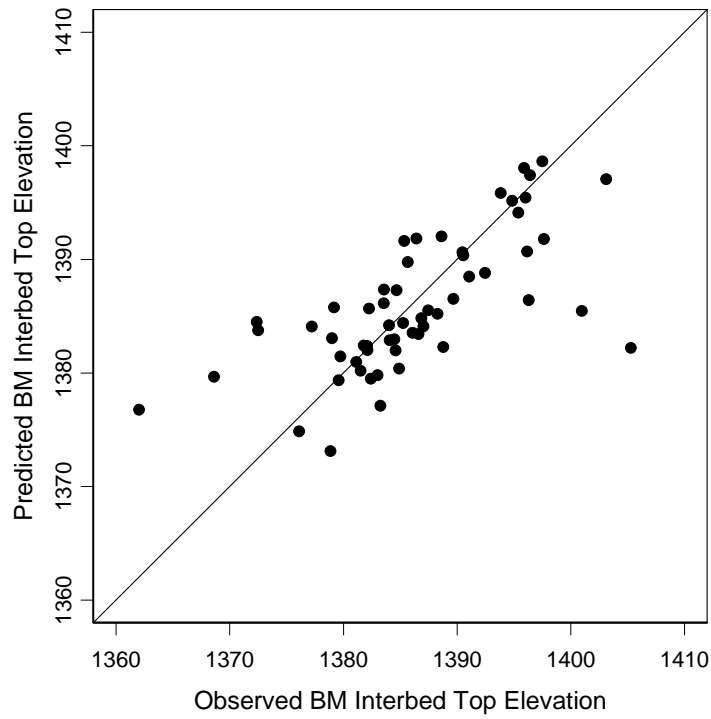


Figure C-91. Observed BM interbed top elevation versus hold-one-out kriging predictions. The line represents perfect correlation between observed and predicted.

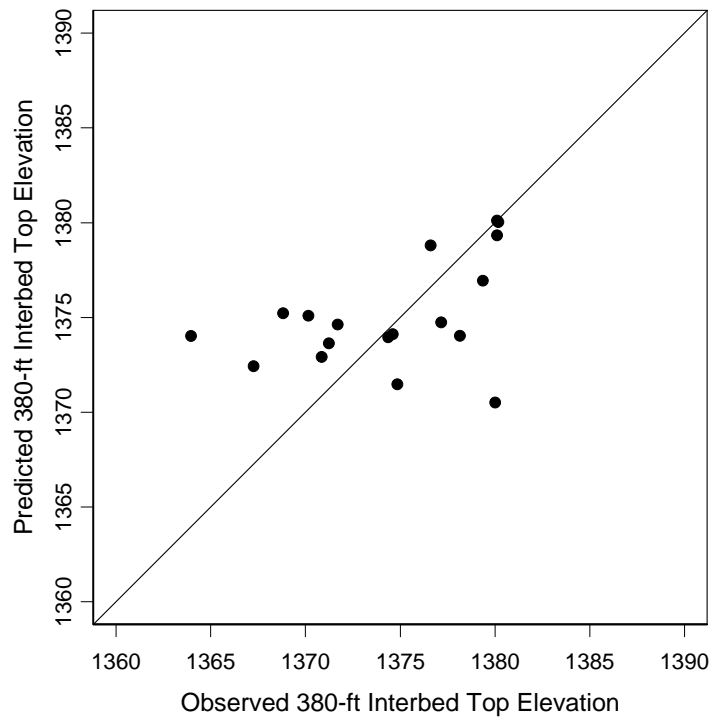


Figure C-92. Observed 380-ft interbed top elevation versus hold-one-out kriging predictions. The line represents perfect correlation between observed and predicted.

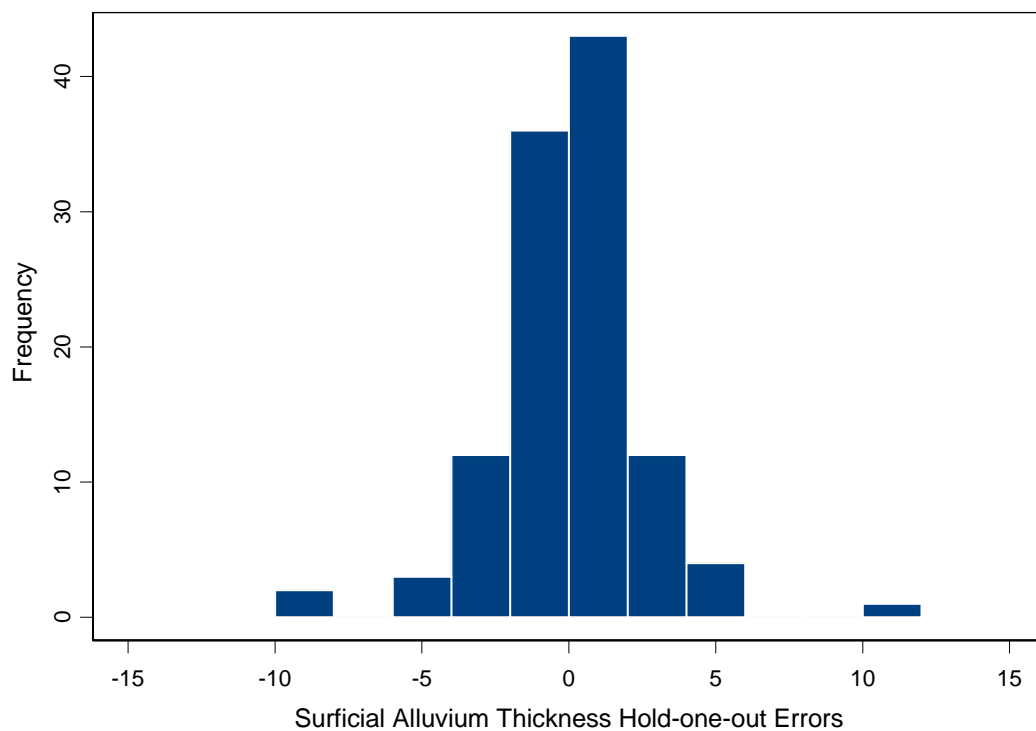


Figure C-93. Histogram of surficial alluvium thickness hold-one-out errors (predicted minus observed).

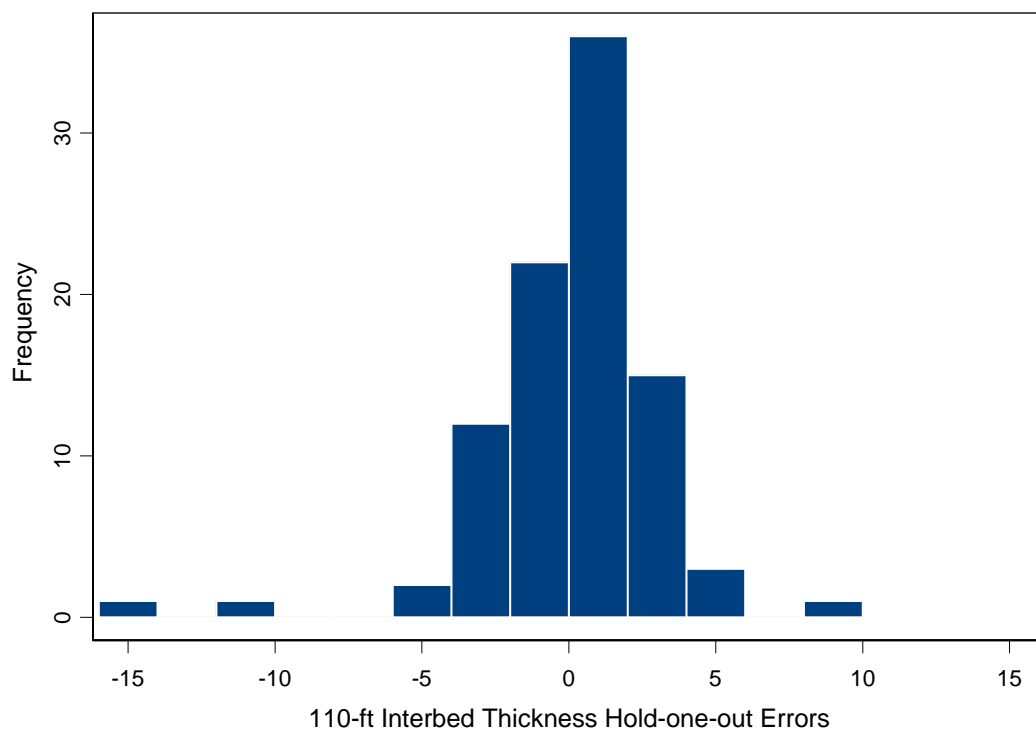


Figure C-94. Histogram of 110-ft interbed thickness hold-one-out errors (predicted minus observed).

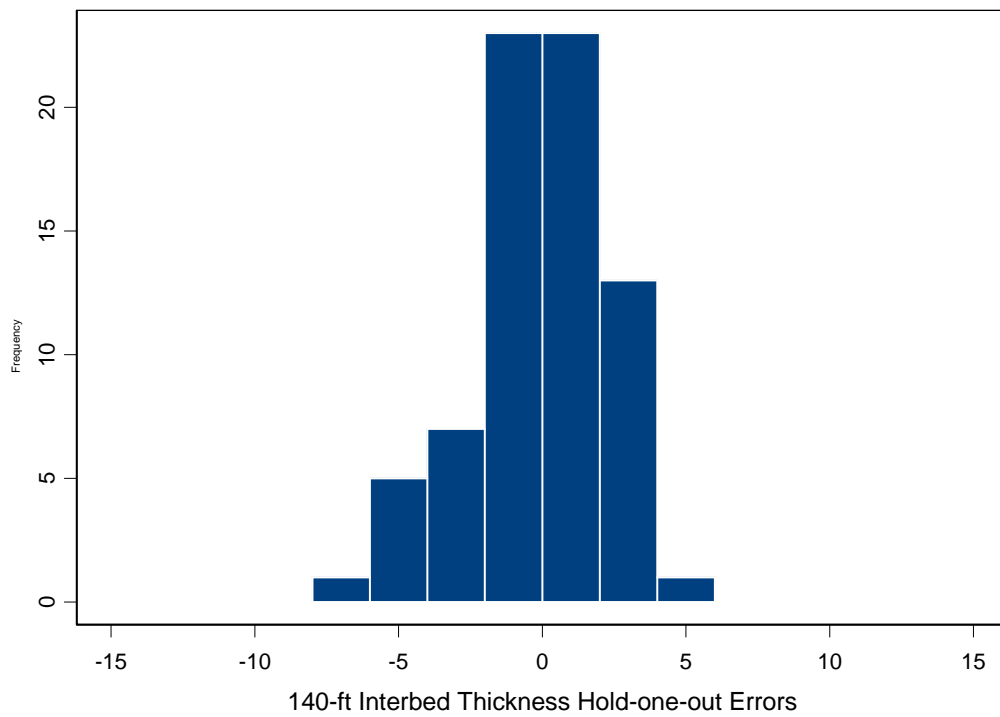


Figure C-95. Histogram of 140-ft interbed thickness hold-one-out errors (predicted minus observed).

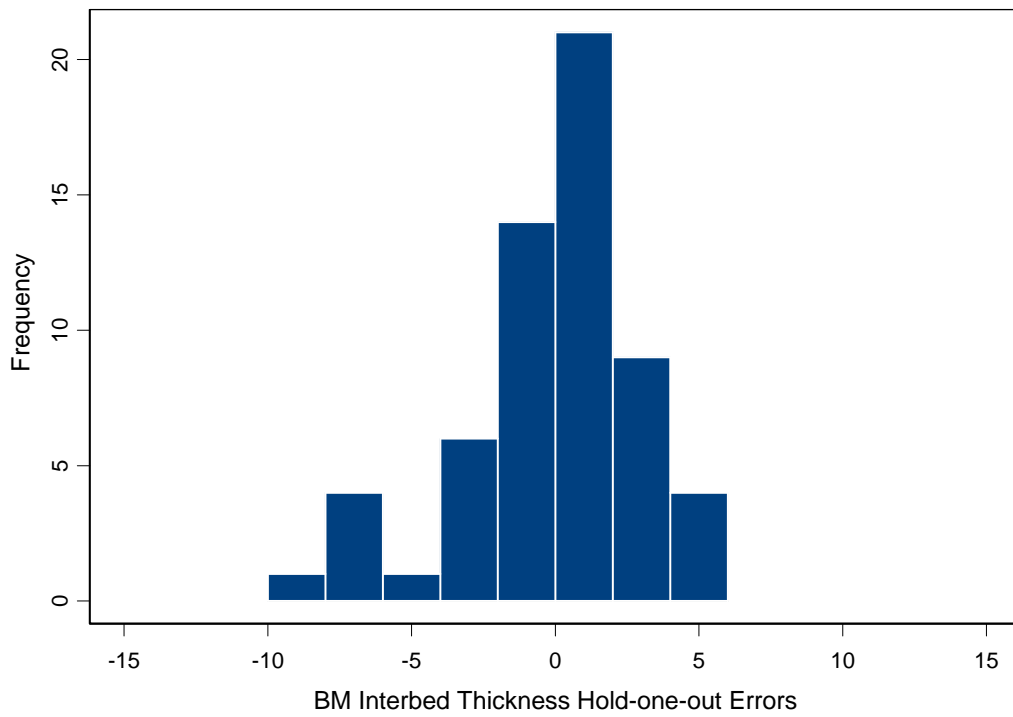


Figure C-96. Histogram of BM interbed thickness hold-one-out errors (predicted minus observed).

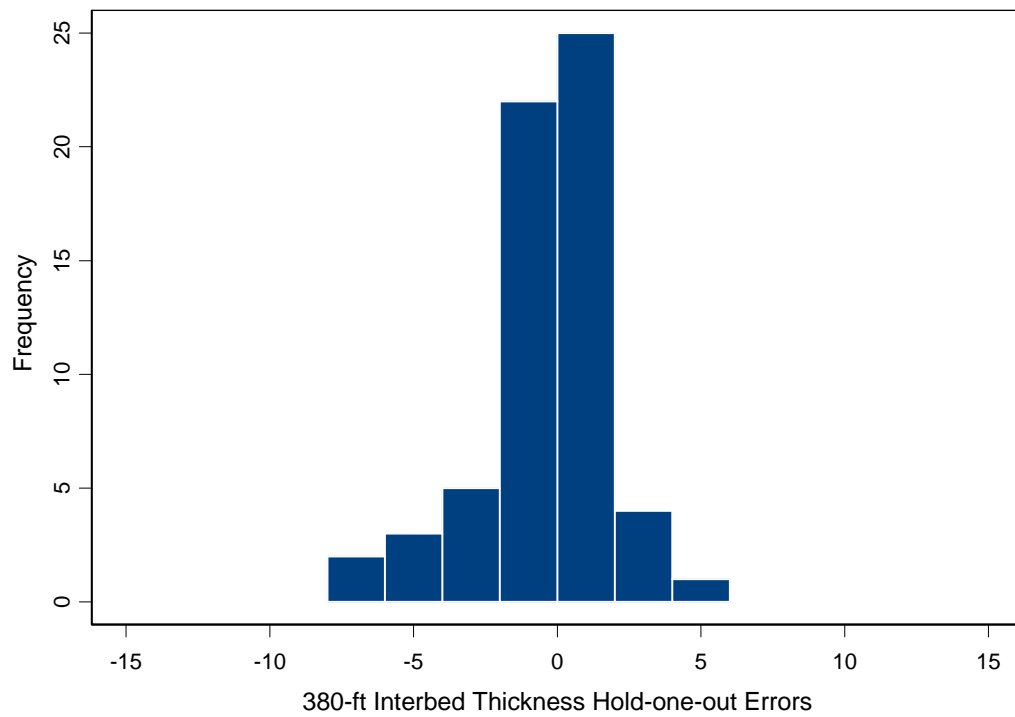


Figure C-97. Histogram of 380-ft interbed thickness hold-one-out errors (predicted minus observed).

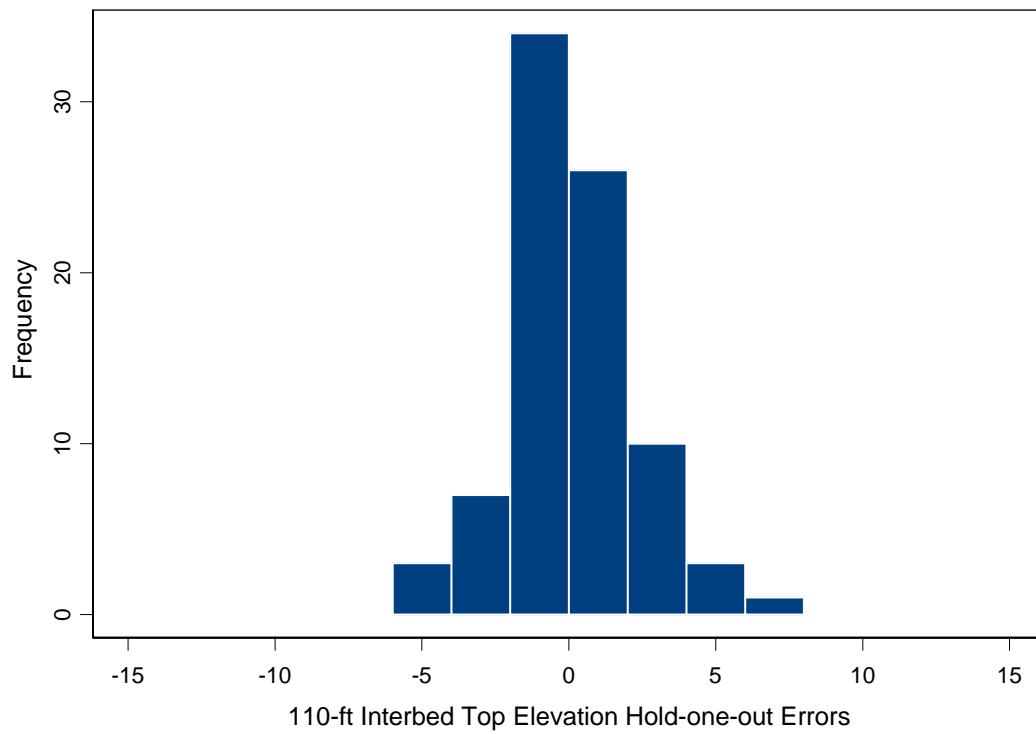


Figure C-98. Histogram of 110-ft interbed top elevation hold-one-out errors (predicted minus observed).

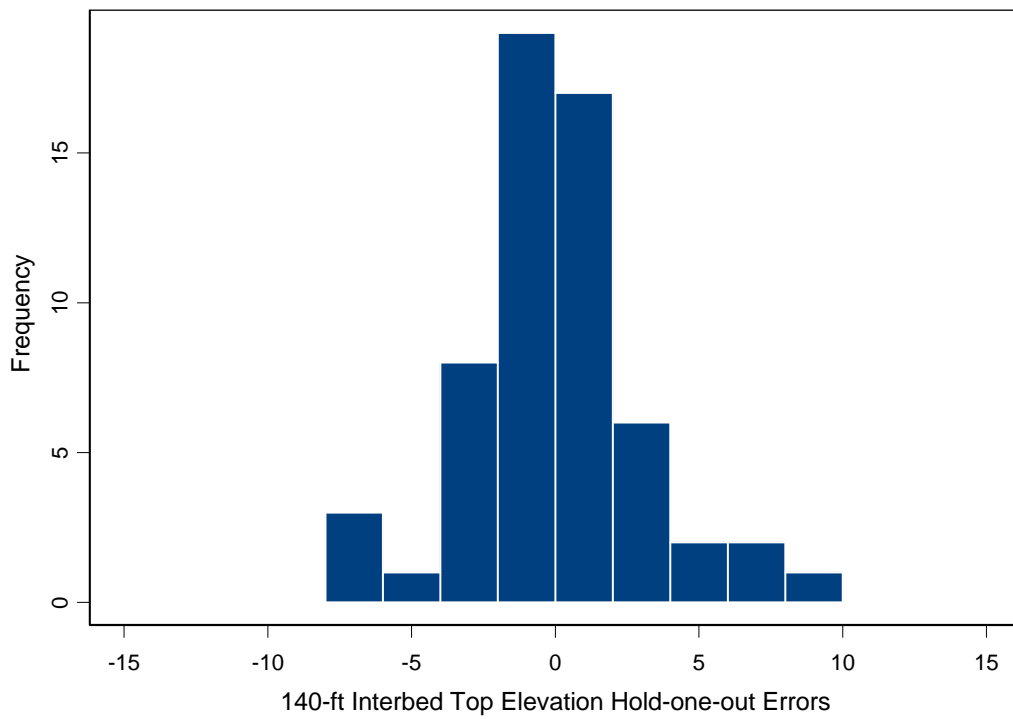


Figure C-99. Histogram of 140-ft interbed top elevation hold-one-out errors (predicted minus observed).

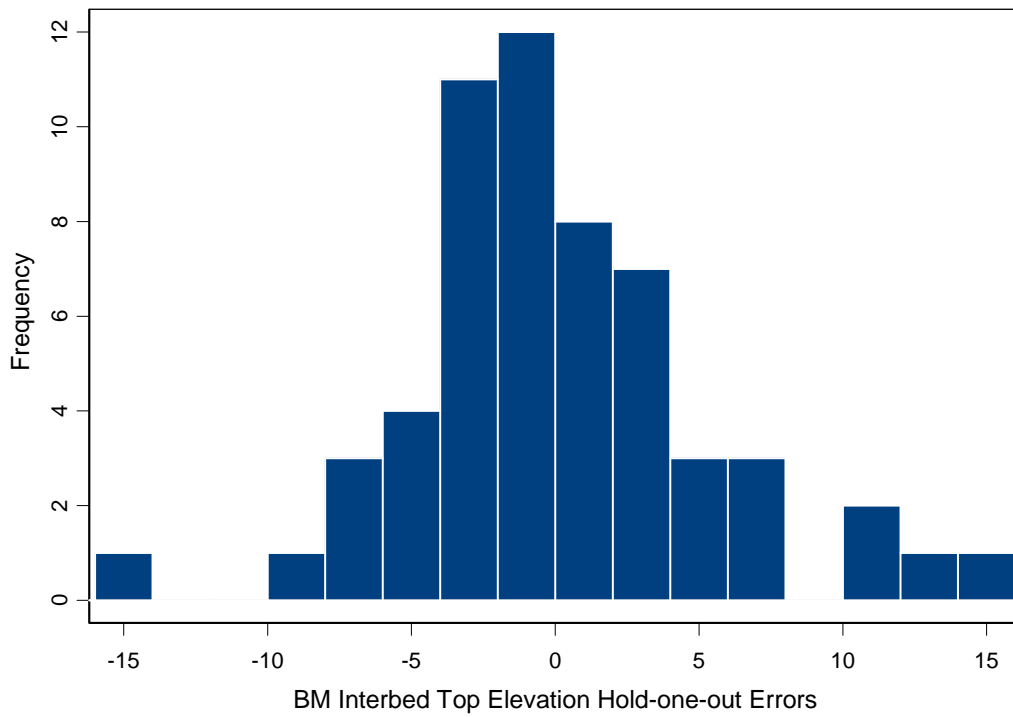


Figure C-100. Histogram of BM interbed top elevation hold-one-out errors (predicted minus observed).

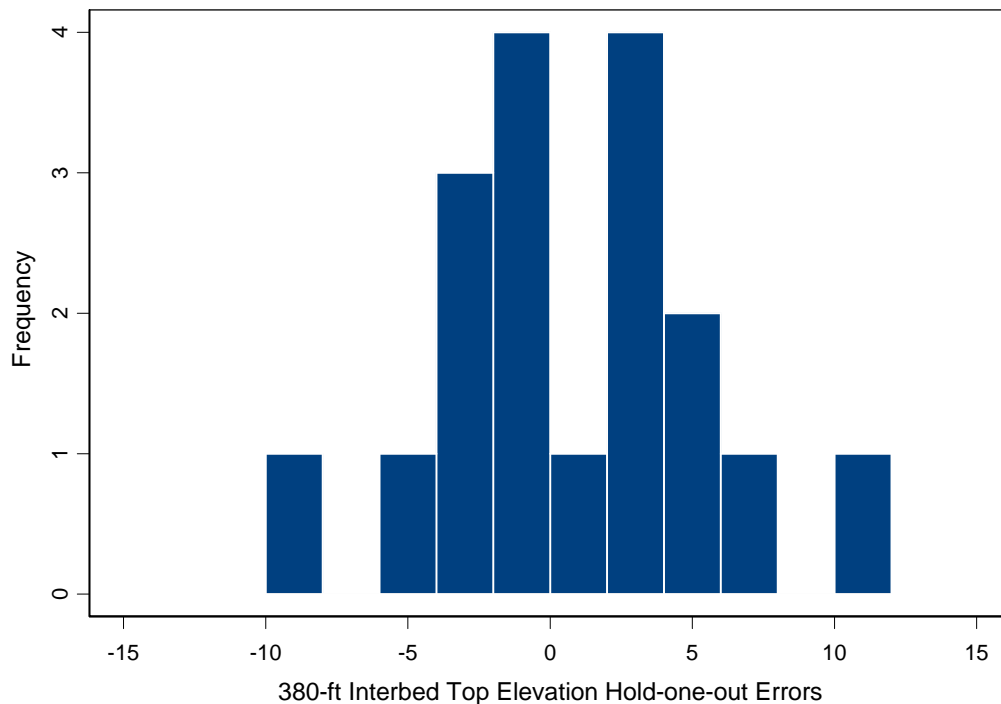


Figure C-101. Histogram of 380-ft interbed top elevation hold-one-out errors (predicted minus observed).

Table C-9. Cross-validation summary statistics for continuous vadose zone lithology variables. Median error as percent of observed is not calculated for thickness values because there are many observed zero thickness values, which would be in the denominator. The ideal ranges of RRMSE are provided in parentheses and bold RRMSE are outside of this range.

Variable Name	Mean Error (m)	Median Error Percent of Observed (%)	MSE (m ²)	RRMSE (m) (ideal range)	MAE (m)
Surficial Alluvium Thickness	0.04	1.2%	6.3	3.4 (0.73 – 1.27)	1.7
110-ft Interbed Top Elevation	0.10	<0.00%	4.4	1.1 (0.69 – 1.31)	1.5
140-ft Interbed Top Elevation	-0.07	-0.01%	8.4	1.1 (0.63 – 1.37)	2.0
BM Interbed Top Elevation	-0.41	-0.02%	36.0	1.4 (0.63 – 1.37)	4.1
380-ft Interbed Top Elevation	0.69	<0.00%	19.4	1.1 (0.33 – 1.67)	3.3
110-ft Interbed Thickness	0.09	a	7.8	1.5 (0.71 – 1.29)	1.9
140-ft Interbed Thickness	-0.15	a	5.3	1.1 (0.67 – 1.33)	1.9
BM Interbed Thickness	-0.05	a	9.6	1.2 (0.63 – 1.37)	2.3
380-ft Interbed Thickness	-0.17	a	4.4	4.4 (0.64 – 1.36)	1.2

a. Not reported because there are many observed zero thickness values.

The relative frequencies of predicted permeability categories matched well with the adjusted observed values (Table C-10).

Table C-10. Relative frequency of permeability categories for all prediction grids. Small refers to the south portion that was predicted on a smaller horizontal grid. The 1 m or 2 m defines the vertical grid spacing.

Permeability Category	Adjusted Observed (%)	All 1 m (%)	Small 1 m (%)	All 2 m (%)	Small 2 m (%)
Permeability Category 1 (high-permeability surficial alluvium)	8.3	7.2	8.8	7.1	9.3
Permeability Category 2 (low-permeability surficial alluvium)	0.3	0.1	0.2	0.2	0.3
Permeability Category 3 (high-permeability interbed)	5.1	5.0	4.6	5.8	5.6
Permeability Category 4 (low-permeability interbed)	6.9	6.4	6.2	7.8	7.8
Permeability Category 5 (high-permeability basalt)	72.3	73.7	71.1	71.8	68.3
Permeability Category 6 (low-permeability basalt)	7.1	7.6	9.1	7.3	8.7

C-4.3.5 Prediction Uncertainty

The uncertainty in the vadose zone lithology predictions were based on spatial stochastic simulation on the 15 variables. The simulations were combined to present a range of vadose zone realizations. These were presented (1) as relative frequencies for the permeability categories and (2) graphically. Although this was performed on the 1-m and 2-m vertical grid, only the 1-m results were shown.

The simulations indicated that it was reasonable to expect between 6.85% and 8.78% of the volume to be surficial alluvium, between 9.96% and 15.08% of the volume to be interbed, and between 76.15% and 83.19% of the volume to be basalt (Table C-11). There was no confidence level associated with these ranges because they were combined across many simulated layers. Based on having 100 simulations of each layer, there was assurance that these combined realizations represented almost the full range of possibilities.

The realization with thin soils and high-permeability categories displays a vadose zone with narrow interbeds that were more disjointed (Figure C-102). The realization with thick soils and low-permeability categories displays a vadose zone with thicker interbeds that were more continuous (Figure C-103). Both sets of realizations were used in the flow and transport model sensitivity and uncertainty runs (Appendix A of this document).

Table C-11. Relative frequency of permeability categories on 1-m vertical grid for adjusted observed, kriging predictions, and simulated realizations for thin soil and high-permeability category and for thick soil and low-permeability category.

Permeability Category	Adjusted Observed (%)	Kriging Predictions (%)	Simulated Realization: Thin Soil and High-Permeability Category (%)	Simulated Realization: Thick Soil and Low-Permeability Category (%)
Permeability Category 1 (high-permeability surficial alluvium)	8.30	7.08	6.68	8.03
Permeability Category 2 (low-permeability surficial alluvium)	0.30	0.17	0.17	0.75
Permeability Category 3 (high-permeability interbed)	5.10	5.77	4.64	5.43
Permeability Category 4 (low-permeability interbed)	6.90	7.77	5.33	9.65
Permeability Category 5 (high-permeability basalt)	72.30	71.84	72.71	64.86
Permeability Category 6 (low-permeability basalt)	7.10	7.37	10.48	11.29
All surficial alluvium	8.60	7.25	6.85	8.78
All interbed	12.00	13.54	9.96	15.08
All basalt	79.40	79.21	83.19	76.15

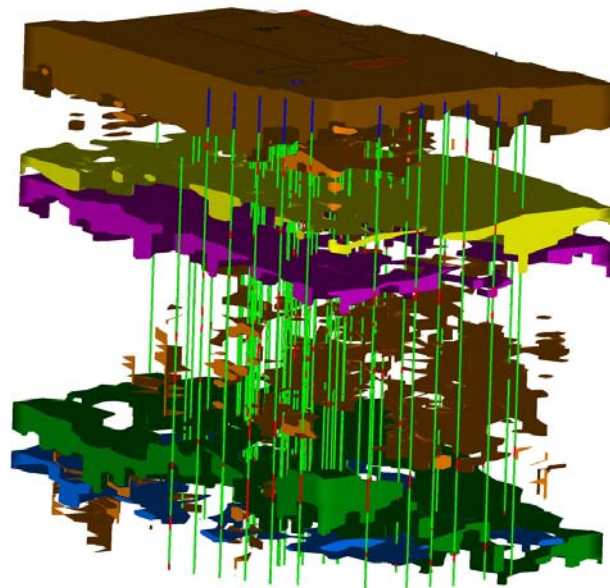


Figure C-102. Transport-retardant extreme combined spatial stochastic simulation subsurface soil layers. Surficial alluvium is brown, 110-ft interbed is yellow, 140-ft interbed is pink, BM interbed is green, 380-ft interbed is blue, and other interbed soils are orange. The wells are represented with blue surficial alluvium, green basalt, and red interbed. The INTEC fence, former percolation ponds, and ICDF are outlined on the surface.

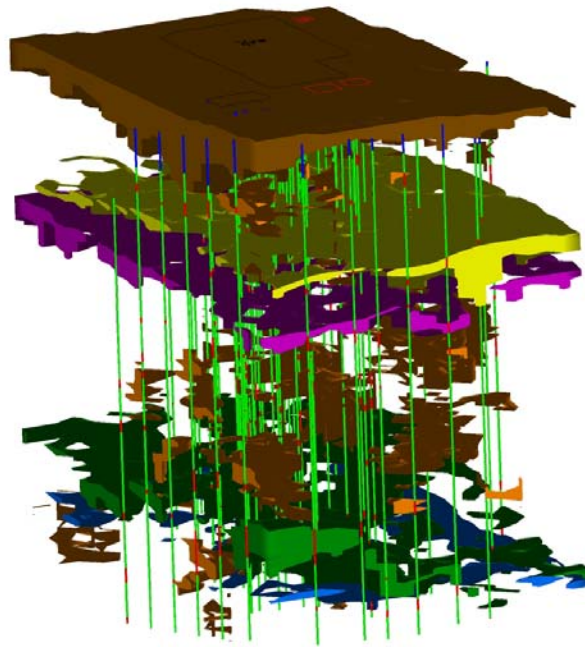


Figure C-103. Transport-conductive extreme combined spatial stochastic simulation subsurface soil layers. Surficial alluvium is brown, 110-ft interbed is yellow, 140-ft interbed is pink, BM interbed is green, 380-ft interbed is blue, and other interbed soils are orange. The wells are represented with blue surficial alluvium, green basalt, and red interbed. The INTEC fence, former percolation ponds, and ICDF are outlined on the surface.

C-5. DISCUSSION

The results presented here provide predictions for use in the flow and transport models. The methods provide estimates of prediction variance, confidence limits, or range of predictions (through simulation) for use in sensitivity and uncertainty analyses for the flow and transport models. The prediction methods use the data to determine weights (based on semivariograms) instead of using an assumed spatial correlation (as in inverse distance weighting). Thus, this represents a rigorous approach to the problem. Because there are choices made in the modeling process, there will never be one best set of predictions or a truth to the predictions. Here, we discuss the choices made and how they might have affected the predictions and also what future choices might be made to improve predictions. We present general discussion items first and then those specifically related to the three data sets.

Some of the regressions on spatial coordinates resulted in statistically significant trend, but these trends were not included. The trends were not included for two reasons. The first is the location of samples. They form a trend of their own (most are along a NE-SW axis), which makes accurate determination of trend difficult because there are few data in the NW-SE direction, causing a bias in the estimated coefficients of the regression. Also, these areas without sample locations are predicted to have trend, without any information to support it. The second reason is that the kriging predictions, without accounting for trend, do, in part, predict the same type of trend in the areas with sample data but do not extend these moderate trends to the areas without sample data.

The kriging variance is a function of the variance of the data (through the estimated nugget and sill of the semivariogram model) and the distance from the prediction location to the sample locations. Thus, the differences in kriging variance across the area of interest depend only upon the sample locations (because nugget and sill are not spatially dependent). Predictions close to sample locations have a small kriging variance. Predictions at increasing distance from sample locations have increasing kriging variance (e.g., Figure C-19). This results in maps of kriging variance generally having bull's-eyes around sample locations unless they are close to other samples. The perception of the size of these bull's-eyes depends on the range of kriging variance values; extreme values of the kriging variance will produce a map with smaller-looking bull's-eyes. In considering the kriging variance, it is important to recall that at the distance of the estimated semivariogram range, the data are assumed to be spatially uncorrelated.

Spatial modeling benefits from sample locations on a regular grid over the whole area of interest. The data used to predict subsurface characteristics in the area of the INTEC were from locations that were not regular and did not cover the whole prediction area. This type of sample design affects the predictions in several ways. First, stationarity is assumed but is questionable in areas of no information. There could be heterogeneities in these areas that are never discovered. The tendency of these sample locations to be mainly in the NE and SW, but lacking in the NW and SE, makes determination of large-scale spatial trends difficult to discern as well. The uncertainty in those areas with little data is large and should be used when reporting final fate and transport model results.

Additional sample locations would improve the predictions. These additional sample locations could be few if strategically placed. They should cover the areas currently lacking and also be spaced for optimal kriging variance based on the estimated semivariogram model parameters (McBratney, Webster, and Burgess 1981).

The semivariograms developed using these data can be used beyond this study. The results can be compared to previous efforts within the INL Site (Leecaster 2004), larger-scope projects (Welhan, Clemo, and Gého 2002 and Welhan et al. 2002) and also be used in future work in the Snake River Plain Aquifer region.

C-5.1 H-I Interbed Thickness and Top Elevation

The predicted H-I interbed dimensions produce a picture of an interbed that is thin and high on the west side and thick and low on the east side. Although the predictions match well with the observed values, both in distribution and for the cross validation, these are based on extrapolation, which is rarely a reliable method of prediction. The large areas without sample locations have large uncertainties, which should be included in their use. Given the variable nature of the interbeds, the information available does not describe the parameters in the extrapolation areas.

C-5.2 Aquifer Hydraulic Conductivity

The sample locations greatly affect spatial analysis. The sample locations for aquifer hydraulic conductivity are highly clustered and there are large areas without samples. This affects the kriging predictions in at least four ways. The first impact of sample location is in calculation and modeling of the semivariogram. Although there are plenty of sample locations for semivariogram calculation and modeling (usual recommendation is at least 100), their locations are not nearly optimal. Optimal locations would be approximately evenly spread over the area of interest, with some additional locations clustered to estimate small lags for the semivariogram. Note that semivariograms are calculated using only locations within the prediction grid and all locations, but no differences are found. Secondly, the clustered nature of the sample locations hinders the calculation and modeling of directional semivariograms, making it difficult to investigate anisotropy. Most directional semivariograms have too few pairs of

locations to adequately characterize directional spatial correlation. Thirdly, only 53 of the 128 locations are within the prediction grid, although many lie along the border. The far-reaching locations are used in semivariogram estimation but not in kriging predictions (given the number and distance constraints discussed in the Section C-3, Methods). The kriging predictions are based on a small number of sample locations. Fourth, the kriging variance increases as sample spacing increases. The kriging variance is larger than might be expected from having so many sample locations because of the poor sample spacing.

The anisotropy established in this study was slightly different than what has been found in models of larger regions. Welhan and Reed (1997) looked at spatial correlation of aquifer hydraulic conductivity over a large area of the Snake River Plain Aquifer. Because their interest is in a larger region, they use a lag of 3,000 m for the empirical semivariogram. Using this large lag, they are able to discern isotropy with the N15° W direction having larger range (approximately 5,800 m) and the N75° E direction having smaller range (approximately 1,450 m). They also see a larger sill, which could be an artifact of the large lags. Such a large region may be more likely to be nonstationary as well.

Two possible improvements could be made in these predictions: more samples and an alternative model. Like most models, these predictions would benefit from more sample locations, especially in those areas that are sparsely sampled. These samples would improve the semivariogram model and decrease the kriging variance as well as improve the accuracy of predictions in those areas. The model used here is based on symmetric, continuous data. Perhaps the values could be categorized into hydraulic conductivity levels with some importance for flow and transport modeling. Then an indicator kriging approach could be used and the skewness issue would disappear.

C-5.3 Vadose Zone Lithology

Isotropy was assumed for all variables except for surficial alluvium permeability category. The effect of assuming isotropy is that predictions form circular shapes instead of elliptical. There were some directional semivariograms that alluded to anisotropy (e.g., surficial alluvium thickness, Figure C-43, and 110-ft interbed elevation, Figure C-48) but was discounted. The main reason for discounting this was sample location; most locations fall along a NE-SW axis, leaving few sample pairs in the NW-SE directions as well as N-S and E-W directions. It is possible that directional semivariograms using many more azimuths would provide the necessary evidence of anisotropy, but this limits further the number of pairs for given directions. We base our decision on the advice that “An anisotropy that is not clearly apparent on experimental semivariograms nor backed by any qualitative information is better ignored” (Goovaerts 1997).

The predictions of vadose zone lithology depend on a data set that is interpreted from well logs and other reports. The following are issues of concern with the data: (1) In assessing the data, many layers are not connected, are labeled as separate, but seem to be connectable. (2) The labeling process and data set have had minimal review. In the process of flow and transport modeling, some of the material designations changed based on perched water data. (3) Many of the wells within the INTEC fence are shallow; no wells exist within the tank farm, the location of most interest; and there are large areas with no sample locations. Thus, large volumes are predicted without sample data close by to support them. If further wells, or deeper wells, are to be drilled, then minimizing the kriging variance would be an appropriate goal for the sample design. This can be done by using the estimated semivariogram parameters provided here and the method of McBratney, Webster, and Burgess (1981).

C-6. REFERENCES

- Anderson, 1989, *Stratigraphy of the Unsaturated Zone at the Radioactive Waste Management Complex, Idaho National Engineering Laboratory, Idaho*, U.S. Geological Survey Water-Resources Investigations Report 89-4065, Idaho Falls, Idaho.
- Anderson, 1991, *Stratigraphy of the Unsaturated Zone and Uppermost Part of the Snake River Plain Aquifer at the Idaho Chemical Processing Plant and Test Reactors Area, Idaho National Engineering Laboratory, Idaho*, U.S. Geological Survey Water-Resources Investigations Report 91-4010, Idaho Falls, Idaho.
- Bouma, J. and P. Finke, 1993, "Origin and nature of soil resource variability," in *Proceedings of the First Workshop: Soil Specific Crop Management, April 14 – 16, 1992, Minneapolis, MN*, eds, P. C. Robert, R. H. Rust, and W. E. Larson, American Society of Agronomy, Inc., Crop Science Society of America, Inc., Soil Science Society of America, Inc., Madison, Wisconsin.
- Deutsch, C.V. and A.G. Journel, 2000, *GSLIB: Geostatistical Software Library and User's Guide*, New York: Oxford University Press.
- DOE-ID, 1997, *Comprehensive RI/FS for the Idaho Chemical Processing Plant OU 3-13 at the INEEL—Part A, RI/BRA Report (Final)*, DOE/ID-10534, U.S. Department of Energy Idaho Operations Office, November 1997.
- DOE-ID, 2002, *Annual INTEC Groundwater Monitoring Report for Group 5 – Snake River Plain Aquifer (2001)*, DOE/ID-10930, Rev. 0, U.S. Department of Energy Idaho Operations Office, February 2002.
- Goovaerts, P., 1997, *Geostatistics for Natural Resources Evaluation*, New York: Oxford University Press.
- Leecaster, M. and L. Hull, 2004, *Spatial Distribution of Neptunium and Uranium Partition Coefficients (K_d) for Interbed Sediments at a Radioactive Waste Subsurface Disposal Area*, ICP/EXT-03-00088, Idaho Completion Project, Idaho National Engineering and Environmental Laboratory, February 2004.
- Leecaster, M., 2004, *Fiscal Year 2004 Geostatistical Modeling of Lithologic Characteristics in the Radioactive Waste Management Complex for OU 7-13/14*, ICP/EXT-04-00494, Idaho Completion Project, Idaho National Engineering and Environmental Laboratory, September 2004.
- Magnuson, S. O. and A. J. Sondrup, 1998, *Development, Calibration, and Predictive Results of a Simulator for Subsurface Pathway Fate and Transport of Aqueous- and Gaseous-Phase Contaminants in the Subsurface Disposal Area at the Idaho National Engineering and Environmental Laboratory*, INEEL/EXT-97-00609, Idaho National Engineering and Environmental Laboratory, July 1998.
- McBratney, A. B., R. Webster, and T. M. Burgess, 1981, "The design of optimal sampling schemes for local estimation and mapping of regionalized variables," *Computers and Geosciences*, 7, pp. 331-334.

- Welhan, J. A., T. M. Clemo, and E. L. G go, 2002, "Stochastic simulation of aquifer heterogeneity in a layered basalt aquifer system, eastern Snake River Plain, Idaho," Special Paper 353, *Geology, hydrology, and environmental remediation: Idaho National Engineering and Environmental Laboratory, eastern Snake River Plain, Idaho, Vol. 353*, pp. 225–247.
- Welhan, J. A., C. M. Johannesen, K. S. Reeves, T. M. Clemo, J. A. Glover, and K. W. Bosworth, 2002, "Morphology of inflated pahoehoe lavas and spatial architecture of their porous and permeable zones, eastern Snake River Plain, Idaho," Special Paper 353, *Geology, hydrology, and environmental remediation: Idaho National Engineering and Environmental Laboratory, eastern Snake River Plain, Idaho, Vol. 353*, pp. 135–150.
- Welhan, J. A. and M. F. Reed, 1997, "Geostatistical analysis of regional hydraulic conductivity variations in the Snake River Plain aquifer, eastern Idaho," *Geological Society of America Bulletin, Vol. 109*, pp. 855–868.

Appendix D

**Estimation of K_d Values
for INTEC Groundwater Model**

**D. Craig Cooper
George D. Redden
Laurence C. Hull**

CONTENTS

D-1. SUMMARY	D-7
D-2. PROCEDURE FOR K_D DATA ANALYSIS	D-9
D-2.1 General Considerations	D-9
D-2.1.1 Acidic Conditions.....	D-10
D-2.1.2 The Equilibrium Assumption	D-10
D-2.1.3 Effect of Sediment/Water Ratio on K_d Measured from Batch Experiments.....	D-10
D-2.1.4 Normalization to CEC as a Proxy for Sediment Surface Area.....	D-11
D-2.2 INTEC and SDA Sediment Geochemistry	D-13
D-2.3 INTEC and SDA Aqueous Geochemistry	D-15
D-2.4 Colloidal Transport.....	D-17
D-3. SELECTION OF K_d VALUES FOR INTEC CONTAMINANTS OF CONCERN	D-20
D-3.1 General Approach to K_d Presentation.....	D-20
D-3.2 Previous Compilations of K_d Values for Common Contaminants of Concern.....	D-20
D-3.3 ^{241}Am K_d Values for INTEC Alluvium, Sediment, and Basalt.....	D-22
D-3.4 Arsenic K_d Values Applicable to INTEC Alluvium, Sediment, and Basalt	D-24
D-3.5 ^{14}C K_d Values Applicable to INTEC Alluvium, Sediment, and Basalt	D-26
D-3.6 Cr K_d Values Applicable to INTEC Alluvium, Sediment, and Basalt	D-27
D-3.7 ^{137}Cs K_d Values Applicable to INTEC Alluvium, Sediment, and Basalt	D-29
D-3.8 ^{154}Eu K_d Values Applicable to INTEC Alluvium, Sediment, and Basalt	D-30
D-3.9 Hg K_d Values Applicable to INTEC Alluvium, Sediment, and Basalt.....	D-31
D-3.10 ^{129}I K_d Values Potentially Applicable to INTEC Alluvium, Sediment, and Basalt	D-32
D-3.11 NO_3^- and NO_2^- K_d Values Potentially Applicable to INTEC Alluvium, Sediment, and Basalt	D-34
D-3.12 ^{237}Np K_d Values Applicable to INTEC Alluvium, Sediment, and Basalt.....	D-35
D-3.13 $^{238/239/240}\text{Pu}$ K_d Values Applicable to INTEC Alluvium, Sediment, and Basalt	D-36
D-3.14 Potential for Formation of Colloidal $^{238/239/240}\text{Pu}$ in INTEC Alluvium, Sediment, and Basalt	D-38

D-3.15	^{90}Sr K_d Values Applicable to INTEC Alluvium, Sediment, and Basalt	D-39
D-3.16	^{99}Tc K_d Values Potentially Applicable to INTEC Alluvium, Sediment, and Basalt	D-40
D-3.17	$^{234/235/238}\text{U}$ K_d Values Applicable to INTEC Alluvium, Sediment, and Basalt.....	D-41
D-4.	REFERENCES	D-43

FIGURES

D-2-1.	Correlation between sediment surface area and CEC for SDA interbed sediments	D-11
D-2-2.	Correlation between surface area, porosity, and hydraulic conductivity for INL-SDA interbed sediments	D-12
D-2-3.	SEM micrographs of INL-SDA sediments with chemical data for selected spots	D-12
D-2-4.	Mössbauer spectrum for SDA surficial sediment	D-15
D-3-1.	K_d compilation, from Sheppard and Thibault (1990)	D-21
D-3-2.	Histogram of Am K_d for ISTD pit sediments at short (<24 hr) and long (>1 Mo) contact time.....	D-23
D-3-3.	Phase diagram for chromium speciation in INL-SDA groundwater	D-27
D-3-4.	Phase diagram for iodine speciation in INL-SDA groundwater	D-33
D-3-5.	Histogram of Pu K_d for ISTD pit sediments at short (< 24 hr) and long (>1 Mo) contact time.....	D-37
D-3-6.	Phase diagram for uranium speciation in INTEC groundwater (pH 8, 0.1 mM total U).....	D-42

TABLES

D-1-1.	Summary of estimated K_d values for INTEC alluvium, all isotopes	D-7
D-1-2.	Summary of estimated K_d values for INTEC interbed, all isotopes	D-8
D-1-3.	Summary of estimated K_d values for INTEC basalt, all isotopes	D-8
D-2-1.	Summary of sediment geochemical properties for INL INTEC and SDA	D-14
D-2-2.	Aqueous geochemical properties for INL INTEC and SDA	D-16
D-3-1.	Am K_d values for INTEC alluvium, basalt, and interbed sediments	D-23

D-3-2.	As K_d values for INTEC alluvium, basalt, and interbed sediments.....	D-25
D-3-3.	C K_d values for INTEC alluvium, basalt, and interbed sediments.....	D-26
D-3-4.	Cr K_d values for INTEC alluvium, basalt, and interbed sediments	D-28
D-3-5.	Cs K_d values for INTEC alluvium, basalt, and interbed sediments	D-30
D-3-6.	Eu K_d values for INTEC alluvium, basalt, and interbed sediments.....	D-31
D-3-7.	Hg K_d values for INTEC alluvium, basalt, and interbed sediments	D-32
D-3-8.	I K_d values for INTEC alluvium, basalt, and interbed sediments	D-34
D-3-9.	NO ₃ - and NO ₂ - (NO _x -) K_d values for INTEC alluvium, basalt, and interbed sediments	D-35
D-3-10.	Np K_d values for INTEC alluvium, basalt, and interbed sediments	D-36
D-3-11.	Pu K_d values for INTEC alluvium, basalt, and interbed sediments	D-38
D-3-12.	Sr K_d values for INTEC alluvium, basalt, and interbed sediments.....	D-40
D-3-13.	Tc K_d values for INTEC alluvium, basalt, and interbed sediments	D-41
D-3-14.	U K_d values for INTEC alluvium, basalt, and interbed sediments	D-43

Appendix D

Estimation of K_d Values for INTEC Groundwater Model

D-1. SUMMARY

Models currently used by the INTEC at the INL to estimate the rate of migration of contaminants to the aquifer require partition coefficients (K_d) to describe solute retardation along subsurface flow paths. This appendix outlines (1) a process for estimating K_d parameters from accessible reported data that acknowledges critical assumptions that are inherent in the K_d concept; (2) summarizes maximum and minimum K_d values for ^{241}Am , As, ^{14}C , Cr, ^{137}Cs , ^{154}Eu , Hg, ^{129}I , NO_3^- , ^{237}Np , $^{238/239/240}\text{Pu}$, ^{90}Sr , ^{99}Tc , and $^{234/235/238}\text{U}$ observed under experimental conditions assumed for the subsurface at INTEC; and (3) gives *recommended* K_d values as an aid for transport model simulations. Advantages and disadvantages associated with the K_d model approach are well known, and the more important issues relevant to this analysis are discussed. Significant variability and uncertainty in geochemical properties at INTEC limit the degree to which ancillary data can be used to estimate K_d values in new systems and prevent making single-value, high-confidence K_d predictions. However, current data do allow estimation of a range of potential and likely K_d values for a particular type of subsurface formation. A summary of K_d estimates is provided in Tables D-1-1 through D-1-3.

Table D-1-1. Summary of estimated K_d values for INTEC alluvium, all isotopes.

INTEC Alluvium	Estimated Minimum K_d (mL/g)	Estimated Maximum K_d (mL/g)	Recommended K_d (mL/g)
^{241}Am	100	10,000	400
As	0.7	190	40
^{14}C	0.5	2.8	1.6
Cr	0.08	12	2.4
^{137}Cs	10	160	50
^{154}Eu	15	19,600	400
Hg	118	1,912	118
^{129}I	0.04	8.7	1.5
NO_3^- , NO_2^-	0	0.5	0.1
^{237}Np	0.1	60	2
$^{238/239/240}\text{Pu}$	96	12,712	1,000
^{90}Sr	8	20	12
^{99}Tc	-0.1	1.4	0
$^{234/235/238}\text{U}$	0.12	12	1.6

Table D-1-2. Summary of estimated K_d values for INTEC interbed, all isotopes.

INTEC Interbed	Estimated Minimum K_d (mL/g)	Estimated Maximum K_d (mL/g)	Recommended K_d (mL/g)
²⁴¹ Am	100	10,000	400
As	0.5	230	45
¹⁴ C	0.5	2.8	1.6
Cr	9	685	90
¹³⁷ Cs	10	160	50
¹⁵⁴ Eu	15	19,600	400
Hg	72	673	156
¹²⁹ I	0.04	3	0.7
NO ₃ ⁻ , NO ₂ ⁻	0	0.5	0.1
²³⁷ Np	0.1	60	2
^{238/239/240} Pu	96	12,712	1,000
⁹⁰ Sr	25	84	50
⁹⁹ Tc	-0.1	0.1	0
^{234/235/238} U	0.12	12	1.6

Table D-1-3. Summary of estimated K_d values for INTEC basalt, all isotopes.

INTEC Basalt	Estimated Minimum K_d (mL/g)	Estimated Maximum K_d (mL/g)	Recommended K_d (mL/g)
²⁴¹ Am	0	140	0.85
As	0	10	2
¹⁴ C	0	2.8	0
Cr	0	50	1.5
¹³⁷ Cs	0	44	25
¹⁵⁴ Eu	0	140	0.85
Hg	0	88	0
¹²⁹ I	0	No data	0
NO ₃ ⁻ , NO ₂ ⁻	0	No data	0
²³⁷ Np	0	8	0
^{238/239/240} Pu	0	130	70
⁹⁰ Sr	0	15	0.5
⁹⁹ Tc	0	No data	0
^{234/235/238} U	0	1.4	0

D-2. PROCEDURE FOR K_d DATA ANALYSIS

D-2.1 General Considerations

The theoretical basis for K_d , experimental methods for determination, critical assumptions in application, and important limitations are well understood (Stumm and Morgan 1981). The K_d parameter (Equation 1) has units of L/kg and is an expression of how a substance, generally a solute, is distributed between the dissolved (mobile) and solid (immobile) states normalized to the mass of solid. As an experimentally measured parameter, K_d represents the sum of all physical, chemical, and biological conditions and processes that contribute to solute adsorption and desorption under the conditions of the measurement.

$$K_d = \text{solid concentration (mol/kg)} / \text{aqueous concentration (mol/L)} \quad (1)$$

If a K_d value is to be used in transport models, a number of assumptions must be satisfied. The system must be assumed to (1) be in equilibrium, (2) remain under constant conditions that are equivalent to the experiments used to measure K_d , and (3) adsorbed concentration must vary linearly with aqueous concentration.

In this analysis, the correspondence between field conditions at INTEC and the data used to estimate K_d values for each of the contaminants of interest was considered. In a few cases, direct data from INTEC are available and are given the highest priority. When direct INTEC data are not available, INL-SDA (SDA) data are judged to be most representative. These sediments have been studied more thoroughly than INTEC, originate from the same geologic source, and possess similar geochemical properties. The main difference between these two subsurface regions is in the grain size distribution, cation exchange capacity (CEC), and reactive surface area of the respective sediments. When SDA data are not available, data from the open literature on comparable sediments are used. In all cases, data from the open literature are used to help identify potentially spurious measurements that may reflect a large degree of experimental bias. The following procedure was used to estimate K_d values for INTEC:

1. The sediment and solution geochemistry of each INTEC subsurface zone is described. For this report, the following definitions are used:
 - a. *Alluvium sediments/water*: Sediments and water sampled from the subsurface region from 0 to 40 ft in wells and boreholes designated INTEC, ICPP, or CPP.
 - b. *Interbed sediments, perched water*: Sediments and water sampled from the subsurface region from 40 to 450 ft in wells and boreholes designated INTEC, ICPP, or CPP.
 - c. *Basalt*: Fractured basaltic rock sampled from the subsurface region from 40 to 450 ft in wells and boreholes designated INTEC, ICPP, or CPP.
 - d. *Groundwater*: Water from the Snake River Plain Aquifer (SRPA), as sampled from the subsurface region deeper than 450 ft in wells designated INTEC, ICPP, or CPP. Water associated with basalt is assumed to have the same chemistry as SRPA water.
2. If K_d measurements have been made for a contaminant on INTEC subsurface materials using experimental conditions that emulate *in situ* groundwater conditions, then these measurements are used to make K_d recommendations.

3. If no K_d measurements exist for INTEC subsurface materials, then measurements on analogous materials are used to establish a potential K_d range. SDA sediments are considered to be the most analogous, and K_d estimates based on SDA are scaled according to typical CEC of the respective sediments (INTEC/SDA = 1:5).
4. If SDA data are not available, K_d data collected from analogous systems described in the open literature are employed, using INTEC and SDA geochemistry as a guide.

The end result of this process will be three K_d values for each contaminant in each subsurface region (alluvium, interbed, basalt); minimum reported for assumed equivalent conditions, maximum reported for assumed equivalent conditions, and a recommended K_d value. Recommendations are based on knowledge of the geochemistry of each contaminant of concern (COC), available data on *in situ* geochemical conditions at INTEC, and reported K_d values from previous experiments conducted under the most analogous conditions. These *most analogous* experiments are chosen on the basis of sediment and solution geochemistry, with greater weight being given to results from experiments that best emulate field conditions. When available for directly analogous conditions, field lysimeter experiments are considered to provide the most accurate estimate of K_d . If such data are not available, then greater credence is given to column transport experiments over batch equilibration experiments. In practice, only limited batch experimental data are available for INTEC sediments and basalt on a few COC. Thus, the recommended K_d values reflect an estimate based on predominance of data when all factors are considered.

D-2.1.1 Acidic Conditions

A number of contaminant releases within INL INTEC have been accompanied by release of concentrated mineral acids (e.g., HCl, HF, HNO₃). In general, acidic conditions will increase metal solubility (reducing K_d). However, comprehensive analyses of solution geochemistry under acidic conditions are not available. Given this general behavior and the lack of specifically applicable data, it is also reasonable to designate a K_d of 0 mL/g for acid-impacted sediments. However, acid-impacted sediments will retain some adsorptive capacity, and this report recommends that the recommended minimum K_d be applied to acid-impacted sediments for as long as acidic conditions persist.

D-2.1.2 The Equilibrium Assumption

K_d based transport predictions assume that the fluid in contact with the environmental surface has reached a point of equilibrium equivalent to that reached in an experimental measurement. This point may be a true thermodynamic equilibrium, or simply a point of steady-state sorption kinetics. This is a reasonable assumption for many saturated and unsaturated groundwater systems where flow is slow. In fact, the long contact times in the field would favor higher K_d values, so experimentally determined values determined in shorter times would result in more conservative, lower values. However, fluid flow through basalt fractures is very different than for sediments. Rather than move slowly over the surfaces of many sediment grains, fluid flow through unsaturated basalt tends to proceed via a series of rapid pulses (Glass et al. 2002; Glass et al. 2003; Wood et al. 2002). This may not allow time for the fluid to fully equilibrate with the basalt surfaces encountered. To accommodate this difference, we estimate a minimum K_d of 0 mL/g for all contaminants transported through INTEC fractured basalt.

D-2.1.3 Effect of Sediment/Water Ratio on K_d Measured from Batch Experiments

In sorption studies conducted on INL surficial sediments, Hemming et al., (1997) demonstrated that Sr K_d decreased by approximately half when the sediment/water ratio was increased from 1:20 to 1:2. This phenomenon was observed only in experiments where sediment slurries were equilibrated on a

shaker table and not a rotary mixer. Similar observations have been reported by other researchers, but there is not a consensus as to what causes this effect or how to quantify this potential source of bias. This report will not apply a correction factor for sediment/water ratio, but we do give greater weight to results from column and field-lysimeter experiments that are conducted at sediment/water ratio(s) more closely representative of field conditions. When considering results from batch experiments, we desire to avoid uncertainty resulting from differences in sediment/water ratio. Therefore, this report only uses data from experiments with a 1:20 sediment/water ratio.

D-2.1.4 Normalization to CEC as a Proxy for Sediment Surface Area

Contaminant sorption to sediment surfaces is typically closely correlated to sediment surface area (Stumm and Morgan 1981). Previous studies of Sr sorption to INL sediments from both INTEC and SDA by Liszewski et al. (2000) report a strong correlation between Sr K_d and surface area, indicating that this trend also applies to the INL. These researchers also observed a strong inverse correlation between Sr K_d and the grain size fraction >4.5 mm in diameter. INTEC sediments are generally much coarser-grained than SDA sediments (Bartholomay 1990; Bartholomay and Knobel 1989; Bartholomay et al. 1989), but few surface area measurements are available. However, there are a number of measurements of CEC for both regions and unpublished data presented in Figure D-2-1^a demonstrate a clear relationship between surface area and CEC for SDA interbed sediments.

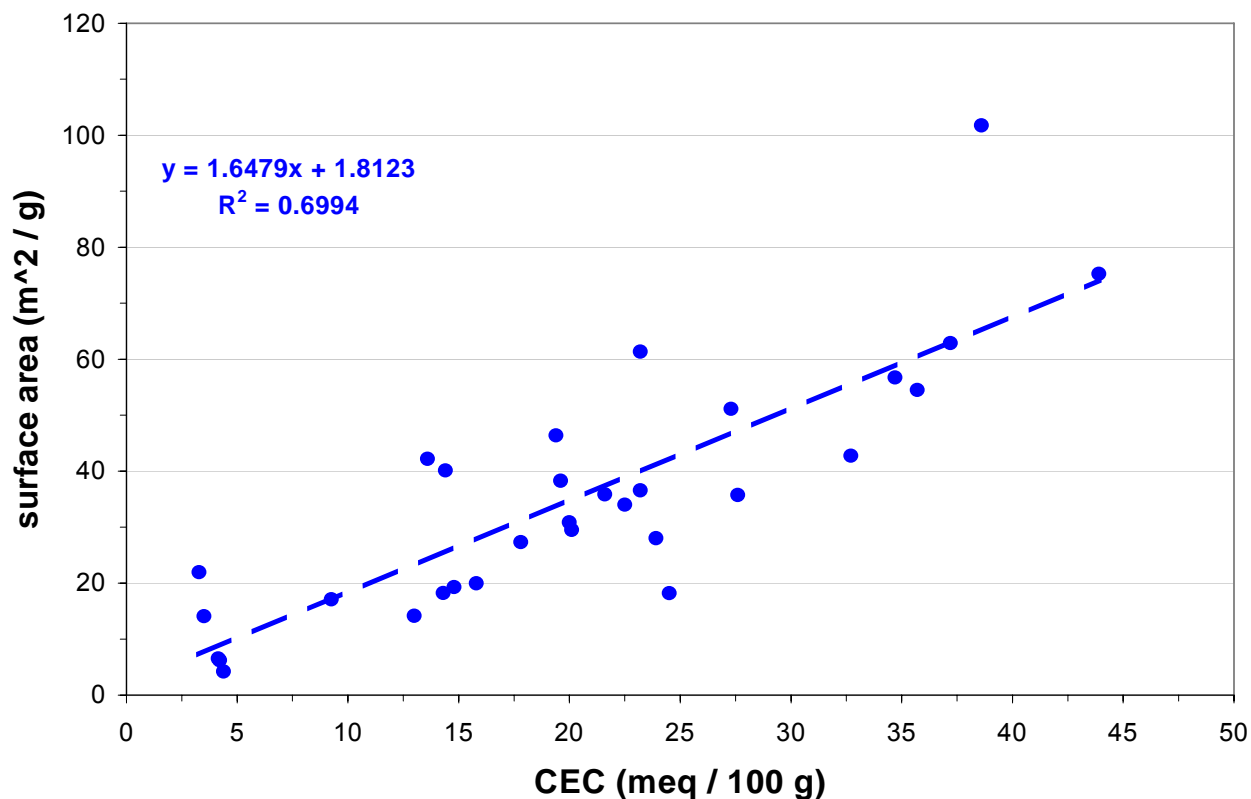


Figure D-2-1. Correlation between sediment surface area and CEC for SDA interbed sediments.

a. Hull L. C., 2002, Unpublished data on INL-SDA interbed sediments (ed. D. C. Cooper).

The surface area correlation cannot be easily extended to transport properties. Figure D-2-2 compares surface area, hydraulic conductivity, and porosity for the same sediments depicted in Figure D-2-1. These data show a weak correlation between surface area and porosity, but no correlation between surface area and saturated hydraulic conductivity. There is not a clear link between fluid transport and sediment chemistry; and thus hydrologic properties are not predictive of geochemical properties. Unpublished data presented in Figure D-2-3^b indicate that this discrepancy can be partially attributed to the presence of clay mineral coatings on larger sediment grains; which can give high-permeability sands some of the chemical properties of clays and blur the hydrological and geochemical differences between sandy and clayey sediments.

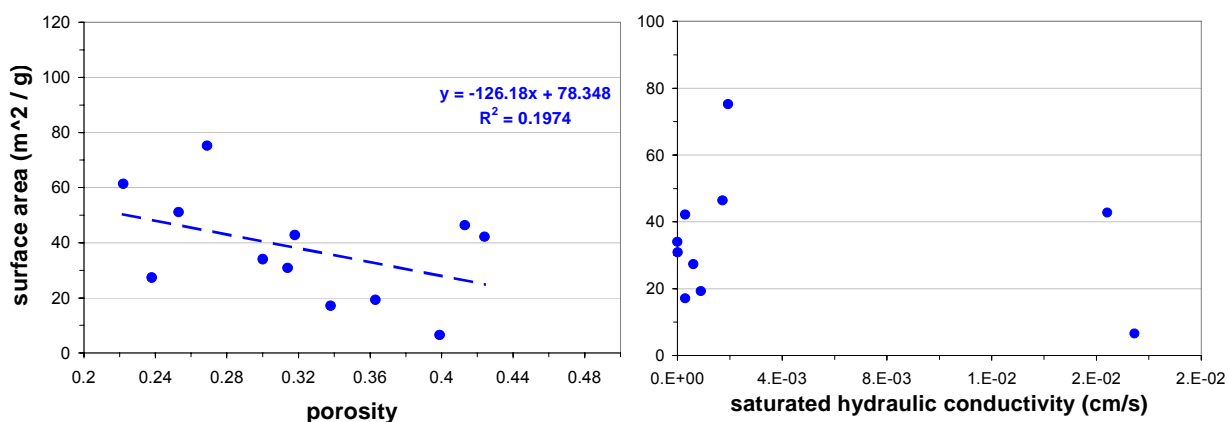


Figure D-2-2. Correlation between surface area, porosity, and hydraulic conductivity for INL-SDA interbed sediments^c.

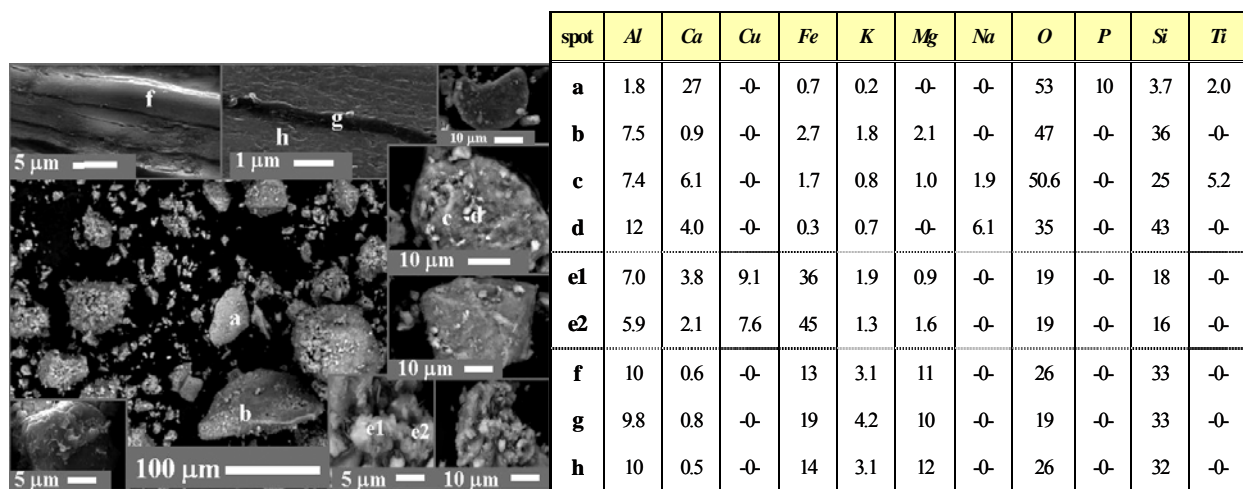


Figure D-2-3. SEM micrographs of INL-SDA sediments with chemical data for selected spots.

b. Cooper D. C., 2002, Unpublished data on INL-SDA ISV Pit Sediments (ed. D. C. Cooper, Battelle Energy Alliance. Idaho National Laboratory).

c. Hull L. C., 2002, Unpublished data on INL-SDA interbed sediments (ed. D. C. Cooper).

Taken together, these data indicate that geochemical properties should generally be scaled to surface area. If sufficient surface area data are not available, then CEC (measure of clay mineral reactivity) provides a reasonable proxy. Consequently, this report will use the ratio of typical INTEC CEC to typical SDA CEC to scale K_d recommendations based on SDA data to INTEC sediments. The CEC ratio for INTEC/SDA sediments is 1:5 (see following section). For a few select cases where organic carbon content is a more important parameter than surface area (e.g., Hg), then this parameter will be given greater weight. The basalt at INTEC is assumed to be equivalent to that at SDA, and results from SDA basalt studies are directly applied to INTEC.

D-2.2 INTEC and SDA Sediment Geochemistry

A summary of sediment geochemical data is presented in Table D-2-1. This summary provides the range, median, and average values for surface area, CEC, sediment mineral composition, and other sediment geochemical properties known to affect the sorption of the COCs discussed herein. Comparable data are also presented for INL SDA sediments, as the history of research at SDA can help guide the selection of appropriate K_d values for waste area group (WAG) 3. These data indicate that INTEC alluvium and interbeds consist of coarse-grained sediments with a low CEC and low organic carbon content. Weight percent CaCO_3 is highly variable in both INTEC alluvium and interbed sediments, but interbeds generally contain significantly more carbonates. INTEC sediments are predominantly quartz, with notable amounts of plagioclase and clay minerals. Minor phases include K-feldspar, olivine, pyroxene, and potentially some hematite. INTEC sediments are distinctly different from SDA sediments, which are fine-grained sediments that contain higher amounts of clay minerals and organic-carbon. It should also be noted that SDA interbeds contain less CaCO_3 than SDA surficial sediments, which is opposite from the trend seen at INTEC. Weight percent iron oxides (as FeO) are comparable in INTEC alluvium, INTEC interbed, and SDA surficial sediments. SDA interbeds have the lowest iron content.

Basalt has the highest iron content. The high iron content of basalt makes it difficult to interpret iron content data, as this measurement does not discriminate between iron associated with sedimentary iron oxide minerals and iron associated with basalt pebbles. Unpublished Mössbauer analyses of a fine-grained sediment from SDA preferentially selected for high iron content^d indicate that ~30% of the total iron is present as iron oxides, predominantly hematite (Figure D-2-4). The remainder is present as illite clay. A small amount of goethite (< ~1% of total) cannot be discounted. Oxalate extractions are also considered to provide a reasonable estimate of the total iron oxide mineral content, e.g., Kostka and Luther (1994). If the data presented in Table D-2-1 are compared on an equivalent basis (g Fe/g sediment), then 5 to 25% (average = 15%) of total iron in SDA sediments is present as iron oxides. Equivalent data are not available for INTEC sediments.

In summary, INTEC sediments are coarse grained with few chemically reactive surfaces. They are also low in organic carbon, and have high carbonate content. The ratio of INTEC CEC to SDA CEC is 1:5, so INTEC K_d values are assumed to be ~5× lower than those estimated for

d. Cooper D. C., 2002, unpublished data on INL-SDA ISV Pit Sediments (ed. D. C. Cooper, Battelle Energy Alliance. Idaho National Laboratory).

Table D-2-1. Summary of sediment geochemical properties for INL INTEC and SDA. Range and average values are given. If no range is given, only one data point is available. Basalt data are from crushed basalt.

	INTEC Alluvium	INTEC Interbed	INL Basalt	SDA Surficial	SDA Interbed
CEC (meq/100g)	1.8 – 4.5 (3) ¹	2.7 ¹	0.5 – 22.5 (3.2) ¹	6.6 – 30 (15) ¹	3.1 – 45 (15) ¹
Surface area (m ² /g)	---	---	0.3 – 2.5 (1.4) ²	33 ³	4.2 – 75 (34) ⁴
Organic-C (weight%)	0.03 – 0.9 (0.3) ⁵	3e-5 – 0.3 (0.02) ⁶	---	0.1 – 2.8 (0.7) ^{3,7}	---
CaCO ₃ (weight%)	0 – 15 (5.5) ^{8,10}	0 – 30 (12) ^{8,10}	---	0 – 41 (11) ¹	0 – 35 (4) ¹
Oxalate Fe (mg Fe/g)	---	---	---	2.4 – 3.4 (2.8) ³	---
Total FeO (weight%)	2.5 ⁸	3.7 ⁸	10 ⁸	2 – 5 (2.7) ³	0.5 – 1.5 (1) ³
Grain size (weight%)					
< 4 μm: range (avg)	0 – 20 (4) ¹	1 – 20 (6) ¹	---	1 – 55 (34) ¹	0 – 70 (20) ¹
4 – 63 μm: range (avg)	0 – 40 (7) ¹	2 – 40 (10) ¹	---	1 – 73 (46) ¹	0 – 75 (38) ¹
63 – 125 μm: range (avg)	1 – 10 (3) ¹	1 – 25 (5) ¹	---	1 – 22 (7) ¹	0 – 40 (8) ¹
125 – 250 μm: range (avg)	3 – 12 (6) ¹	1 – 25 (8) ¹	---	1 – 18 (5) ¹	1 – 65 (10) ¹
250 μm – 1 mm: range (avg)	7 – 15 (12) ¹	3 – 35 (10) ¹	---	0 – 42 (4) ¹	0 – 40 (10) ¹
1 – 4 mm: range (avg)	1 – 17 (13) ¹	0 – 20 (7) ¹	---	0 – 38 (3) ¹	0 – 40 (5) ¹
> 4 mm: range (avg)	12 – 70 (55) ¹	0 – 90 (54) ¹	---	0 – 12 (1) ¹	0 – 50 (9) ¹
Mineralogy (weight%)					
Quartz: range (avg)	30 – 53 (38) ^{8,10}	20 – 36 (28) ^{8,10}	---	15 – 45 (30) ¹	5 – 50 (25) ¹
Plagioclase: range (avg)	15 – 33 (23) ^{8,10}	10 – 28 (18) ^{8,10}	---	5 – 25 (15) ¹	5 – 50 (20) ¹
K-feldspar: range (avg)	0 – 13 (5) ^{8,10}	7 – 10 (8) ^{8,10}	---	0 – 5 (3) ¹	0 – 10 (6) ¹
Clay minerals: range (avg)	0 – 25 (15) ^{8,10}	0 – 30 (18) ^{8,10}	---	15 – 60 (30) ¹	0 – 70 (25) ¹
other phases: range (avg)	0 – 22 (13) ^{8,10}	0 – 40 (16) ^{8,10}	---	0 – 15 (11)	1 – 50 (20) ¹
1. (Bartholomay et al. 1989) 2. (Colello et al. 1998) 3. (Cooper 2002) ^a 4. (Hull 2002) ^b 5. EDW, CPP/ICPP/INTEC, 0-40 ft 6. EDW, CPP/ICPP/INTEC, > 40 ft 7. EDW, SDA area, 0-40 ft 8. (Del Debbio and Thomas 1989) 9. (Liszewski et al. 1997) 10. (Liszewski et al. 1998) EDW – Electronic Data Warehouse, a database maintained by the Idaho Completion Project (ICP). a. Cooper D. C., 2002, unpublished data on INL-SDA ISV Pit Sediments (ed. D. C. Cooper, Battelle Energy Alliance. Idaho National Laboratory). b. Hull L. C., 2002, unpublished data on INL-SDA interbed sediments (ed. D. C. Cooper).					

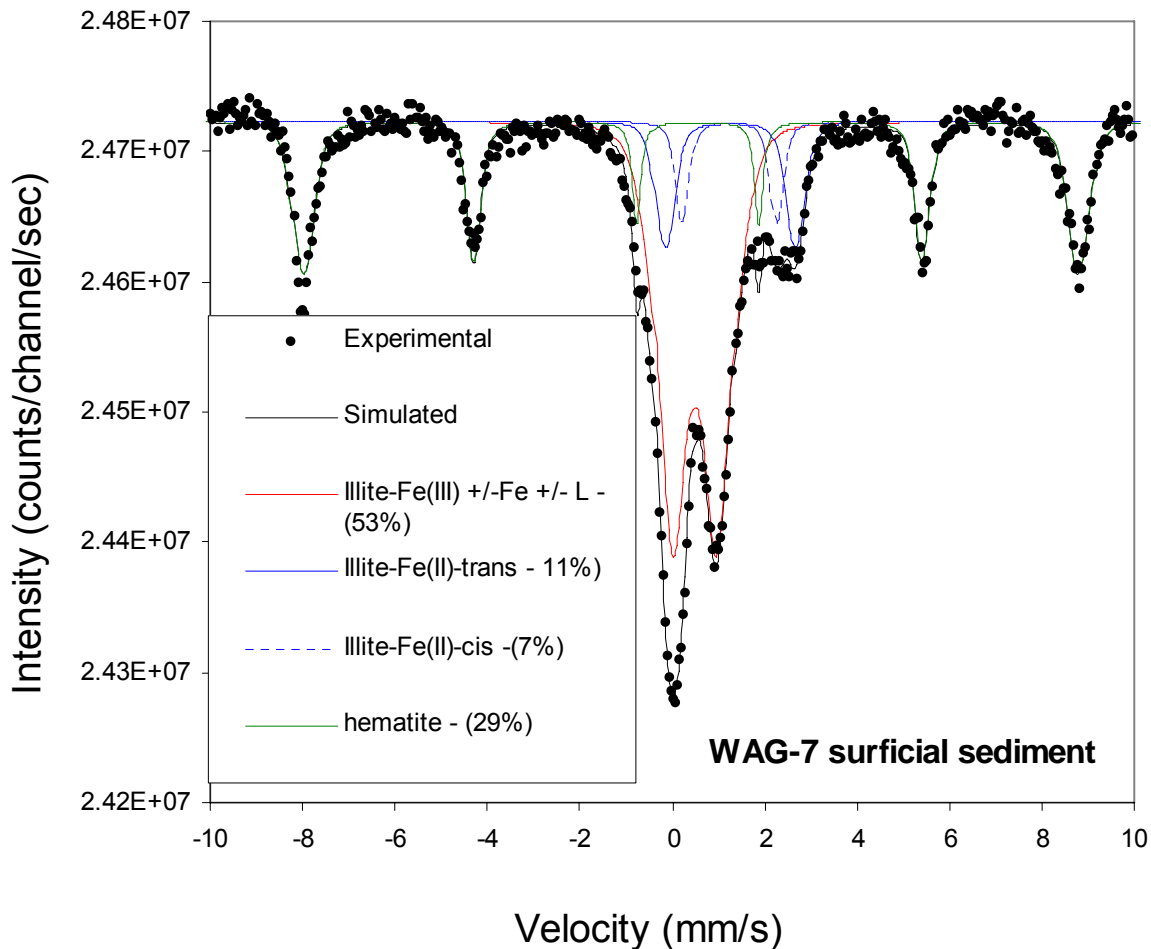


Figure D-2-4. Mössbauer spectrum for SDA surficial sediment.

SDA. When comparing with sediments from regions outside the INL, INTEC sediments will be most comparable to coarse-grained carbonate sands with low iron content and low levels of organic carbon.

D-2.3 INTEC and SDA Aqueous Geochemistry

Contaminant K_d values can vary with temperature, aqueous contaminant concentration, pH, alkalinity, dissolved organic carbon, system oxidation state, and the concentration of aqueous complexing agents (Stumm and Morgan 1981). Consequently, it is important to consider aqueous geochemistry when recommending K_d values. Summary data on the range, median, and average values of key aqueous chemical properties for INTEC and SDA alluvium water, perched and lysimeter water for interbed region, and aquifer/groundwater (assumed for basalt) are presented in Table D-2-2. Comparable data are also presented for SDA.

INTEC groundwater (alluvium, perched water, and aquifer water) is moderately alkaline, with a pH that ranges from approximately 7 – 9. Biological oxygen demand is generally low, and the groundwater is generally oxidizing, with dissolved oxygen concentrations typically exceeding 6 mg/L (DOE/NE-ID 2005). INTEC perched water also contains appreciable dissolved oxygen concentrations at most locations (DOE/ID 2006), but dissolved oxygen concentrations are mostly in the range of 3 to

Table D-2-2. Aqueous geochemical properties for INL INTEC and SDA. For simplicity, interbed region includes data from both lysimeters and perched water. Range and average values are given for all constituents. If no range is given, only one data point is available. Data are from the ICP-EDW unless otherwise noted.

	INTEC Alluvium¹	INTEC Interbed Region²	INTEC Aquifer³	SDA Surficial¹	SDA Interbed²
pH	8.1	7.2 – 8.7 (8.0)	6.4 – 11 (7.6)	7.6 – 8.8 (8.2) ⁷	
Eh (mV)	---	115 – 228 (160)	---	---	---
HCO₃⁻ Alk. (mM)	---	1 – 5 (3.2)	1 – 14 (2.8)	---	---
O₂ Demand (mM)	---	0.06 – 0.6 (0.2)	0 – 1.4 (0.2)	---	---
Dissolved O₂ (mg/L)	---	b.d.l. – 7.6 (6) ⁵	---	---	---
O₂-(g) (atm)	---	b.d.l. – 0.18 (0.12) ⁶	---	0.005 – 0.18 (0.08)	---
Ca²⁺ (mM)	0.1 – 6.2 (2) median = 1.1	0.2 – 14 (2) median = 1.7	0.01 – 2.1 (1.4) median = 1.4	0.4 – 50 (4.7) median = 1.6	0.05 – 235 (9) median = 2.2
Mg²⁺ (mM)	0.05 – 2.2 (0.8)	0.04 – 5.8 (0.9)	0.003 – 1.1 (0.65)	0.4 – 67 (5.2) median = 1.8	0.06 – 307 (8.3) median = 1.6
Na⁺ (mM)	0.3 – 26 (6.5) median = 4.1	0.3 – 65 (3.5) median = 1.9	0.01 – 4.3 (1.1) median = 0.7	0.4 – 258 (25) median = 15	1.8 – 186 (22) median = 11
K⁺ (mM)	0.03 – 0.3 (0.15)	0.05 – 1.2 (0.2)	0.001 – 0.2 (0.09)	0.05 – 20 (0.6) median = 0.15	0.08 – 68 (1.8) median = 0.3
NH₄⁺ (mM)	---	6e-4 – 9e-4 (7e-4)	6e-4 – 5.5e-3 (1.9e-3)	---	---
NO₃⁻ (mM)	0.06 – 7.8 (2.6)	0.01 – 50 (0.4)	0.01 – 1.1 (0.1)	0.002 – 14 (1.5) median = 0.7	b.d.l. – 15 (0.9) median = 0.2
NO₂⁻ (mM)	---	0.007 – 0.28 (0.08)	1e-4 – 0.007 (0.003)	b.d.l. – 0.38 (0.025)	b.d.l. – 0.06 (0.007)
SO₄²⁻ (mM)	0.6 – 14 (4.1)	0.1 – 16 (0.6)	0.2 – 15 (0.4)	0.2 – 76 (9.2) median = 1.7	– 91 (4.8) median = 2.6
Cl⁻ (mM)	0.2 – 4.5 (1.3) median = 0.8	0.1 – 89 (3.5) median = 1.8	0.04 – 7 (1.6) median = 0.7	– 310 (28) median = 3.2	– 150 (18.5) median = 3.95

b.d.l. = below detection limit (detection limit not reported for aqueous O₂).

1. Alluvium: 0-40 ft.

2. Interbed: 40 ft to Snake River Plain Aquifer (~400 ft).

3. Aquifer: depths greater than 400 ft.

4. Eh (mV) estimated from NO₃⁻/NO₂⁻ redox couple.

5. DOE-ID (2003).

6. Calculated from Henry's Law assuming equilibrium at STP (K_H = 1.3 e-3 M/atm).

7. No depth data available.

7 mg/L, which is somewhat lower than observed in the SRPA. At isolated locations, such as shallow perched well ICPP-2018, the presence of lower dissolved oxygen levels in perched water (<2 mg/L) may be attributable to the presence of fuel hydrocarbons in the vadose zone (Golder 1991). Redox potentials measured in INTEC perched water are mostly in the range of +125 to +200 mV, indicating generally oxidizing conditions. Lower redox potentials are observed at a few locations, such as well ICPP-2018 (DOE/ID 2006), where the perched water appears to have been impacted by past releases of fuel hydrocarbons. Considered together, these data indicate that oxidizing conditions prevail in INTEC alluvium and interbed sediments, but isolated zones characterized by geochemically reducing conditions may also exist.

With respect to cations and anions, INTEC alluvium water and interbed-region water contain higher concentrations than the SRPA or a number of surficial sources (e.g., irrigation water, percolation ponds). Thus, water addition results in dissolution of soluble salts (including calcite). Since calcite dissolution generally increases pH, the combination of pH and cation/anion data indicate that calcite is dissolving in INTEC alluvium. This process also likely occurs in SDA surficial sediments. It is difficult to characterize the transition from alluvium to interbed sediments, as there are insufficient data to draw a complete conclusion. The available data indicate that ionic strength is greater in INTEC interbeds than alluvium (higher ion concentration). The same trend holds for SDA, with a larger magnitude of increase.

INTEC interbeds have a higher weight percent CaCO_3 than the alluvium, suggesting that calcite may be precipitating in the interbeds. However, geochemical calculations using INTEC perched water quality data (EDF-5758), suggest that the perched water is close to saturation with respect to calcite, with calcite saturation index values ranging from -0.3 to +0.3^e. This suggests that the perched water is in chemical equilibrium with the calcite, and that calcite is neither dissolving nor precipitating at appreciable rates. The slow precipitation of calcite may be expected to immobilize some Sr-90 through co-precipitation. However, the partitioning coefficient for strontium into the calcite crystal lattice is only about 0.03, indicating that relatively little strontium would be co-precipitated in this manner under existing conditions (Tesoriero and Pankow, 1996). In any case, adsorption of strontium on clay minerals is of much greater importance than co-precipitation in controlling rates of subsurface Sr-90 transport. Adsorption onto interbed sediments is proportional to the CEC of the interbed material, with higher CEC values equating to higher strontium K_d values (greater adsorption). CEC of the interbed sediments has been shown to be among the most important parameters in predicting Sr-90 mobility (Appendix J).

D-2.4 Colloidal Transport

There is some evidence, or concern, that fractions of some contaminants at INTEC can migrate at rates that are greater than what is described by the range of K_d values used for the simple solute forms. Explanations include: (1) Transport during rapid flow events where sorption reactions cannot approach equilibrium, (2) formation of stable chemical complexes (e.g., with organic ligands) that do not react readily with mineral and organic surfaces, and (3) transport as colloidal particulates. The first case applies to the fractured basalt and has already been addressed elsewhere in the conceptual model where $K_d = 0$ is assumed. The second situation is possible, but more likely if significant concentrations of complexing agents were released with the wastes. Such complexes would have to be chemically stable and resistant to biological degradation for long periods of time. Without a steady re-supply of complexing agents, rapid contaminant transport via complexation is likely to be limited to a near-field phenomenon. Monitoring data from INTEC wells and interbeds do not indicate the presence of persistent organic compounds, and

e. Hull L.C. (2005) Unpublished PHREEQC geochemical modeling results for INTEC perched water.

thus complexation is not expected to be a transport vector. Contaminant transport in colloidal form remains a possibility.

Unstable flow through the gravelly alluvium is another phenomenon that could potentially result in more rapid downward contaminant transport than would otherwise be expected. Wetting front instability can result in downward flow along discrete “fingers” within the alluvium, as opposed to propagation of a uniform planar wetting front (Stephens, 1996). Such flow fingering has been observed in many types of sediments, both in the field and the laboratory. Fingering is especially likely below the contact between fine sediments overlying coarse sediments (Stephens, 1996). Laboratory studies have shown that water from successive infiltration events tends to repeatedly follow the same finger-like pathways (Glass et al., 1989). In coarse sediments, such as the gravelly alluvium at INTEC, the flow fingers tend to occupy a smaller portion of the total cross-sectional area, with drier zones occupying the regions between adjacent fingers (Yao and Hendrickx, 1994). In stratified sediments, distinct fingers may coalesce at depth as a result of lateral spreading at contacts between sediments of contrasting permeabilities. However, because the original structure of the alluvium underlying the tank farm has been destroyed by excavation and backfilling, less lateral spreading would be expected. Therefore, fingering of flow through the gravelly alluvium is plausible, if not probable. The presence of preferential flow pathways along fingers would generally result in more rapid downward contaminant transport than would be expected under uniform flow conditions.

Assignment of a K_d to colloid facilitated transport of contaminants must consider the nature of colloid migration in porous media, and how contaminants are associated with colloids. The following condensed analysis considers three possible scenarios:

Contaminants irreversibly attached to colloids, or present as colloids: In this case, contaminant migration is dictated by colloid migration alone. Colloid migration cannot be simulated accurately in natural environments, but the governing principles are reasonably well established. The analysis summarized here is given in more detail with references in Batcheller and Redden (Batcheller and Redden 2004), and is supported by field evidence cited in the reference. In the absence of chemical and physical perturbations, colloid interactions with other surfaces are described by DLVO (Derjaguin, Landau, Verwey, and Overbeek) theory (Derjaguin and Landau 1941), and migration is described by filtration theory. DLVO theory correlates surface charge, which is controlled by the concentrations and types of other solutes, to attachment strength. The important points of DLVO theory are: (1) colloid attachment to other surfaces is irreversible unless overcome by physical perturbations such as shear forces during fast or turbulent flow, and (2) lower ionic strength and higher surface charge decreases colloid attachment in porous media. DLVO theory only addresses a number of basic factors governing colloid stability and it is well recognized that there are numerous other factors affecting surface-surface interactions even if quantification is not yet possible. Filtration theories are used to model the capture efficiency of a media for particular material. This includes surface-surface interactions governed by DLVO forces, and multiple physical factors such as pore straining, flocculation, development of filter mats, etc. Filtration theories are successful for idealized experimental systems, and are applied semi-empirically for engineering and natural systems. According to filtration theory, in the absence of chemical and physical perturbations, particle capture is irreversible and colloid deposition approaches 100% depending on the distance of colloid travel. For these reasons, and because the parameterization or data needed to predict colloid transport do not exist, the K_d for a colloidal contaminant fraction must be set to zero for large aperture (fractured) systems that experience at least episodic fast flow. Colloids will be expected to be effectively trapped in fine-grained porous media with stable chemical and flow conditions. Migration of colloids does not follow a K_d model, but a high K_d value, at least equivalent to the highest value for associated contaminants, can be used in regions where criteria for colloid filtration can be met. Because the impact of chemical and physical perturbations cannot currently be quantified, rapid changes in ionic strength from <0.01 to >0.1 , flow perturbations, events that cause physical disturbances, and the

advancement of air-water interfaces (where colloids can accumulate) in unsaturated systems should be modeled with contaminant $K_d = 0$ during the period of the disturbance.

Contaminants reversibly attached to colloids: In this situation, contaminants are actively partitioning between the colloid, solution, and stationary phases. Therefore, colloids will accelerate contaminant migration partly because colloids are confined to faster flow paths (they do not diffuse into microporous zones) and because they represent another reservoir for contaminants in the mobile phase. However, unless there is clear evidence for significant and persistent concentrations of colloids in the INTEC groundwater, there is no justification for decreasing the effective K_d for any contaminant due to this transport mechanism. A “borescope” (Aquavision) has been used in some wells at the INL in an attempt to measure fluid flow by monitoring the movement of colloidal particles in well water. The presence of colloidal material should not be interpreted at this time as evidence for a persistent colloid concentration at INTEC because suspended matter can be generated as artifacts in wells and during deployment of the borescope. In some tests, no particles could be observed and is more likely to represent an undisturbed condition for groundwater.

In situ generation of contaminant bearing colloids: Some areas at INTEC were impacted by highly acidic wastes, and secondary precipitates could form as acidic solutions containing contaminants and dissolved minerals are neutralized. This is especially likely if the saturation index is well above unity, and the crystallites will often be much less than 1 micron in size. If such colloids are formed, they should be treated in the same way as described in the first scenario. However, particles smaller than 1 micron impact other surfaces at a higher rate and are more likely to be captured by surface-surface interactions even though they can be more readily transported through small pores.

Batcheller and Redden (2004) applied basic filtration theory to INL interbed sediments in the SDA in order to determine the likelihood of plutonium oxide colloids passing through interbed sediments. These calculations treat INL interbed sediments as packed-bed granular filters, and employ a semitheoretical model to calculate the distance of colloid travel within the interbeds. The model employs a filtration efficiency factor, α , that must be determined empirically. $\alpha = 1$ means collisions between colloids and sediment grains always result in attachment (i.e., highly favorable for filtration). A value of $\alpha = 0.001$ represents conditions that are unfavorable for filtration (i.e., 99.9% of colloid-grain collisions do not result in attachment) and smaller values are generally not observed in laboratory experiments. A more extreme value of 0.00001 is used here. Based on this previous work, calculations to determine the travel distance required to remove 99.999% of colloids under two different cases are described here.

1. *Case 1:* INTEC interbed conditions most favorable for colloid transport

- $\alpha = 0.00001$ (much more unfavorable for filtration than previous experiments)
- Colloid diameter = 0.001 mm (a size near the optimal range for transport)
- Colloid density = 11.4 gm/cm³
- Sediment porosity = 0.523 (highest reported value at INTEC)
- Flow = 40 cm/year
- Mean grain size = 1.0 mm (typical sand grain size, low efficiency for colloid capture).

2. *Case 2: Generic interbed conditions highly favorable for colloid filtration*

- Porosity = 0.064
- Grain size = .002 mm
- All other parameters the same.

In both cases, the temperature is 10°C. The calculated travel distances through a porous medium where 99.999% of colloids are removed ($CL/C_0 = 0.0001$) are:

- Case 1 = 47 cm
- Case 2 = 0.41 cm.

Therefore, with respect to colloid transport, if water is intercepted by sedimentary interbeds that are 1 m or greater, all colloids should be effectively removed. Again, the important assumption is that the chemical and physical conditions within the interbed are constant.

D-3. SELECTION OF K_d VALUES FOR INTEC CONTAMINANTS OF CONCERN

D-3.1 General Approach to K_d Presentation

Recommendation of K_d requires knowledge of the chemistry of the contaminant of concern, knowledge of how that chemistry applies to subsurface conditions, and knowledge of previous work to establish a K_d for that system or under analogous conditions. The following logical structure is adopted in this report: (1) the general chemistry of the contaminant is briefly described, (2) the important aspects of the general chemistry are described as they apply to INTEC, (3) previous measurements of K_d values under analogous conditions are summarized, (4) the chemistry of each element as it applies to INTEC is used to narrow the range of possible K_d down to a likely minimum K_d , likely maximum K_d and single best estimate, and (5) the recommended values are summarized and defended.

D-3.2 Previous Compilations of K_d Values for Common Contaminants of Concern

Dicke (1997) provides a summary of K_d values applicable to the SDA. The mineral composition of these sediments is comparable to that of INTEC, though INTEC sediments are coarser grained and contain a slightly lower proportion of clay minerals. Because SDA sediments are generally comparable to INTEC sediments and both experience similar hydrological cycles; these SDA recommendations will be considered when recommending K_d values for INTEC. Dicke (1997) used an earlier compilation prepared by Sheppard and Thibault (1990). This compilation is very useful, and deserves special mention here.

Figure D-3-1 presents a reproduction of Table 1 of Sheppard and Thibault (1990). This table lists “typical” K_d values for 48 different elements in 4 different soil types. Values in bold were compiled from measurements reported in the peer-review literature, and all other values were estimated from a phenomenological relationship between K_d and a known soil-to-plant concentration ratio. We generally treat these values as an independent source. These values are not directly incorporated into the K_d estimates discussed here, but have been used as a general guide. They are presented here to help the reader determine if the suggested K_d values for INTEC are reasonable. INTEC sediments are most closely comparable to sand.

Table 1. Summary of GM K_d values ($L\ kg^{-1}$) for each element by soil type.^{a,b}

Element	Sand	Loam	Clay	Organic
Ac	450 ^a	1 500	2 400	5 400
Ag	90 ^b	120	180	15 000
Am	1 900	9 600	8 400	112 000
Be	250	800	1 300	3 000
Bi	100	450	600	1 500
Br	15	50	75	180
C	5	20	1	70
Ca	5	30	50	90
Cd	80	40	560	800
Ce	500	8 100	20 000	3 300
Cm	4 000	18 000	6 000	6 000
Co	60	1 300	550	1 000
Cr	70	30	1 500	270
Cs	280	4 600	1 900	270
Fe	220	800	165	600
Hf	450	1 500	2 400	5 400
Ho	250	800	1 300	3 000
I	1	5	1	25
K	15	55	75	200
Mn	50	750	180	150
Mo	10	125	90	25
Nb	160	550	900	2 000
Ni	400	300	650	1 100
Np	5	25	55	1 200
P	5	25	35	90
Pa	550	1 800	2 700	6 600
Pb	270	16 000	550	22 000
Pd	55	180	270	670
Po	150	400	3 000	7 300
Pu	550	1 200	5 100	1 900
Ra	500	36 000	9 100	2 400
Rb	55	180	270	670
Re	10	40	60	150
Ru	55	1 000	800	66 000
Sb	45	150	250	550
Se	150	500	740	1 800
Si	35	110	180	400
Sm	245	800	1 300	3 000
Sn	130	450	670	1 600
Sr	15	20	110	150
Ta	220	900	1 200	3 300
Tc	0.1	0.1	1	1
Te	125	500	720	1 900
Th	3 200	3 300	5 800	89 000
U	35	15	1 600	410
Y	170	720	1 000	2 600
Zn	200	1 300	2 400	1 600
Zr	600	2 200	3 300	7 300

^a Values with regular numbering are default values predicted using CRs.^b Values with italic bold numbering come from the *literature*.Figure D-3-1. K_d compilation, from Sheppard and Thibault (1990).

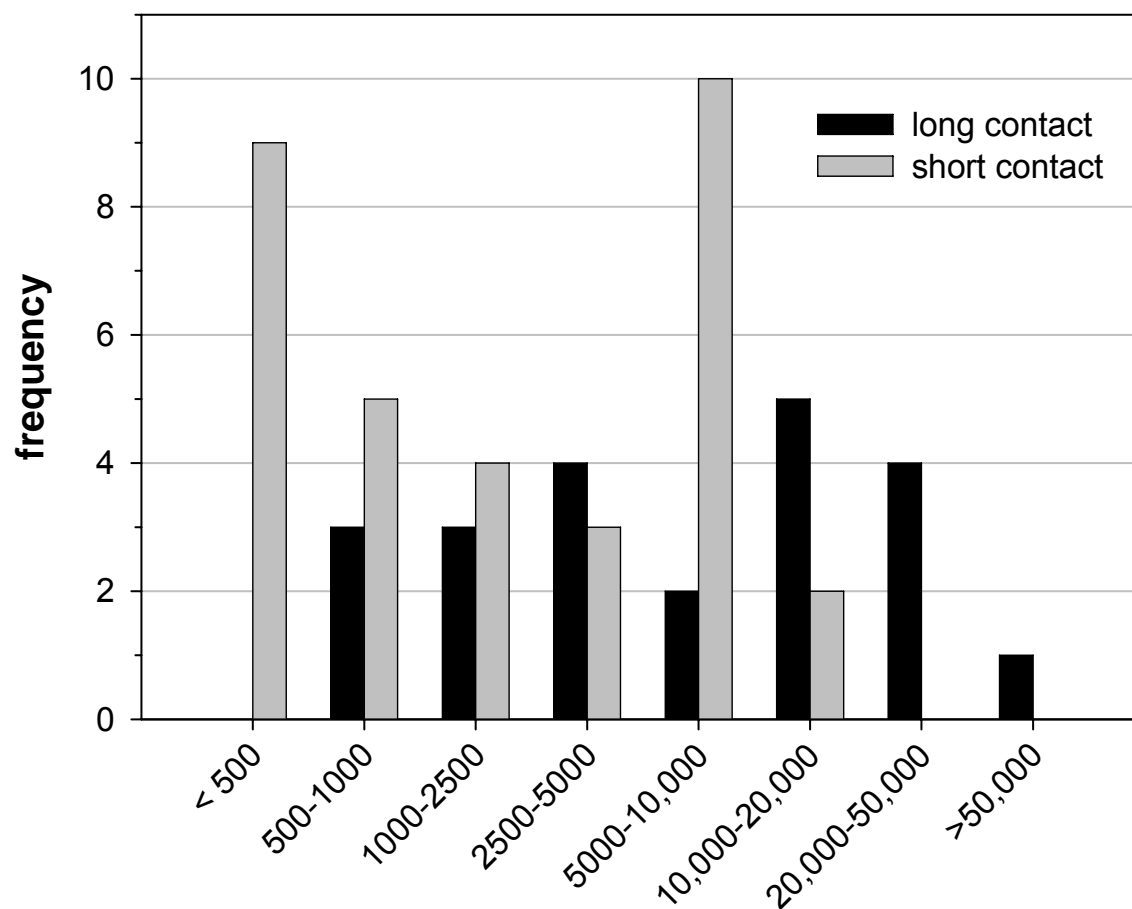
D-3.3 ²⁴¹Am K_d Values for INTEC Alluvium, Sediment, and Basalt

Am predominantly occurs as Am³⁺ in natural environments, and generally adsorbs strongly to iron oxide and clay minerals in soils and sediments (Lu et al. 1998; Ticknor et al. 1996). The specific isotope of interest at INTEC is ²⁴¹Am. High level of soil organic matter can enhance Am mobility (Artinger et al. 1998; Schuessler et al. 2000; Ticknor et al. 1996), however, both INTEC and SDA sediments have little organic matter and the impact of organic matter is assumed to be negligible. Clay minerals are expected to control Am sorption in both systems and K_d values are expected to correlate with CEC.

No site-specific K_d data are available for Am adsorption to INTEC subsurface media. However, some data are available for Am adsorption to SDA sediments. Newman et al. (1996) provides a summary of results from short term batch experiments measuring Am K_d for basalt and various SDA interbed sediments. The Am K_d ranged from 70 – 280 mL/g for basalt, and from 450 – 1100 mL/g for interbed sediments. Dicke (1997) uses these data to recommend an Am K_d of 450 mL/g for sediments and 70 mL/g for basalt. Unpublished data from Am sorption experiments conducted on sediments collected from 18-ft deep within the ISTD (*In situ* Thermal Desorption) test pit at the SDA are presented in Figure D-3-2^f. These sorption experiments used an artificial groundwater and the experimental techniques of Mincher et al. (2003). Total Am ranged from 0.003 – 0.03 μmol/L. The mineral composition and grain size distribution of these sediments is similar to that of SDA interbed sediments and to the materials used by Newman et al. (1996). These data agree with the lower end of the range of Newman et al. 1996 but extend the maximum K_d to ~10,000 mL/g at <24 hr equilibration. Longer-term sorption experiments conducted under the same conditions indicate a shift to higher K_d. In column tests conducted on basalt and interbed samples from the SDA area, Fjeld et al. (2001) report Am retardation factors (R) that range from 2.6 – 5.8 for basalt and 200 – 800 for interbed sediments. Under experimental conditions, these retention factors equate to a K_d of 0.5 – 1.2 mL/g for basalt and no less than 200 mL/g for interbeds. No Am breakthrough was observed for the interbed experiments, and the retention factors were estimated from γ-spectroscopy of the intact cores.

The batch experimental data for Newman et al. (1996) and the long-term contact data presented in Figure D-3-2 indicate that Am K_d should range from 500 – 50,000 mL/g in SDA sediments. The lower limit is similar to the minimum K_d estimate of 200 mL/g for SDA interbed sediments derived from column experiments by Fjeld et al. (2001). The mineral composition of alluvium and interbed sediments is not sufficiently different to merit separate Am K_d estimates, and the aqueous chemistry differences should not greatly affect Am sorption. Assuming that Am K_d values for INTEC can be estimated by scaling SDA values by CEC, then Am K_d for INTEC alluvium and interbeds should range from 100 to 10,000 mL/g. INTEC basalt is assumed to have the same chemical properties as SDA basalt, and the minimum estimate for basalt is 0 mL/g for all contaminants. The maximum estimate of 140 mL/g is equivalent to the highest value measured by Newman et al. (1996) for basalt, and corrected for sediment/water ratio. These maximum and minimum estimates are summarized in Table D-3-1, as are the recommended K_d values.

f. Cooper D. C., 2002, unpublished data on INL-SDA ISV Pit Sediments (ed. D. C. Cooper, Battelle Energy Alliance, Idaho National Laboratory).



^{241}Am K_D (mL/g)

Figure D-3-2. Histogram of Am K_d for ISTD pit sediments at short (<24 hr) and long (>1 Mo) contact time.

Table D-3-1. Am K_d values for INTEC alluvium, basalt, and interbed sediments. Values from batch experiments corrected for sediment/water ratio.

	Minimum Estimate Am K_d (mL/g)	Maximum Estimate Am K_d (mL/g)	Recommended Am K_d (mL/g)
Alluvium	100	10,000	400
Interbed	100	10,000	400
Basalt	0	140	0.85

Estimating the recommended Am K_d value from the range of values estimated for INTEC requires that data from other sites be used in concert with SDA measurements. In batch experiments conducted on sandy soils with a low organic carbon content, Artinger et al. (1998) report Am K_d values that range from 505 – 1090 (\pm 100) mL/g. In subsequent column experiments with the same sediments, Artinger et al. (2002) report Am K_d values that range from 1950 – 2150 (\pm 200) mL/g. The K_d difference arising from different experimental methodologies conducted on otherwise equivalent systems of sediment and simulated groundwater is thought to arise from the larger mass of iron encountered by a smaller volume of water in the column experiment (different sediment/water ratio). The range of batch K_d values reported by Artinger et al. (1998) corresponds closely with the range of 450 to 1,100 mL/g reported by Newman et al. (1996) for SDA sediments, and indicates that these sediments likely display comparable ^{241}Am sorption chemistry to SDA sediments. It is, therefore, reasonable to assume that the later column experiments of Artinger et al. (2002) are also comparable to SDA sediments and that the average K_d of 2000 mL/g is applicable to typical SDA sediments. Adjusting for the CEC-based scaling factor leads to a recommended Am K_d estimate of 400 mL/g for INTEC alluvium and interbeds. The recommended Am K_d for basalt is estimated to be the average K_d reported by Fjeld et al. (2001) for Am transport through basalt samples collected from the SDA.

D-3.4 Arsenic K_d Values Applicable to INTEC Alluvium, Sediment, and Basalt

Data used to estimate a K_d range for As should be derived from experiments that match the expected oxidation state for INTEC. Environmental arsenic exists either as As^{III} , predominantly $\text{H}_3\text{As}^{\text{III}}\text{O}_3^0$ for $\text{pH} < 9$, or As^{V} , as a mix of $\text{H}_2\text{As}^{\text{V}}\text{O}_4^-$ and $\text{HAS}^{\text{V}}\text{O}_4^{2-}$ at $\text{pH} 6 - 8$. As^{III} is generally more mobile than As^{V} . Thermodynamic calculations indicate that As^{V} should be the predominant form of arsenic in all but the most reducing environments, but a number of biotic and abiotic processes can cause kinetic disequilibria that enable As^{III} and As^{V} to co-exist in soil and groundwater environments (Smedley and Kinniburgh 2002). Both As^{III} and As^{V} adsorb strongly to clays and iron oxide minerals, and these minerals often control arsenic transport in subsurface systems (Smedley and Kinniburgh 2002). Organo-arsenic complexes have been observed, though these are usually limited to environments with high organic carbon content.

The oxic, organic-poor conditions in the INTEC subsurface are expected to favor As^{V} over As^{III} , and As^{V} is assumed to be the dominant arsenic form. Both INTEC and SDA sediments have little organic matter and organo-arsenic compounds can be assumed to be unimportant. The most important factor controlling arsenic transport is assumed to be As^{V} sorption to sedimentary iron oxide and clay minerals. The mineralogy of INTEC alluvium and interbeds is similar, and the aqueous chemistry is not sufficiently different to notably affect arsenic adsorption.

No site-specific K_d data are available for arsenic adsorption to INTEC or SDA subsurface media. Smedley and Kinniburgh (2002) present a summary of As^{III} and As^{V} K_d values for a number of common soil minerals that are also found in the INTEC subsurface. Assuming that arsenate (As^{V}) is the predominant form of arsenic in INTEC alluvium, basalt, and interbed sediments, whole sediment As K_d values can be calculated as a weighted sum from the As^{V} K_d data provided by Smedley and Kinniburgh (2002). Other data considered include Kuhlmeier (1997) who reports As K_d values ranging from 0.26 to 3.3 mL/g for As leaching from sandy soils mixed with various organic and inorganic arsenic contaminants, and De Brouwere et al. (2004) who performed batch studies of As sorption to a number of European grassland soils, and found K_d values that ranged from 14 – 4430 mL/g. These studies used materials that are not directly applicable to INTEC subsurface media.

The mineralogical data presented in Table D-2-1 gives values for quartz, feldspar, plagioclase, total clay minerals, calcite, iron content, and total “other” phases (e.g., olivine, pyroxene, dolomite). Smedley and Kinniburgh (2002) provide $As^V K_d$ values for a large number of soil minerals, with the most comparable to INTEC alluvium interbeds being quartz (~2 mL/g), kaolinite (~760 mL/g), goethite (~1800 mL/g), and hematite (25 mL/g). Because the only clay mineral data available for As^V are for kaolinite, we assume that all INTEC clay minerals behave as kaolinite. Second, we must make certain assumptions concerning the iron oxide content of INTEC sediment. If we assume that the same proportion of total weight percent iron is oxalate-extractable in both INTEC and SDA, we can then estimate that 5 – 25% (average 15%) of total iron (units of g Fe/g sediment) in INTEC sediments consists of iron oxide minerals (goethite + hematite). Limited data are available on the iron content of INTEC sediments (Table D-2-1), but the available data allow an estimate of the iron oxide content based on the single measurement of weight percent FeO (note: 1 wt% FeO = 0.78 wt% Fe, or 1.11 wt% Fe_2O_3). If we assume that SDA sediments emulate INTEC sediments with regard to sediment iron speciation and make the appropriate unit conversions, then hematite in INTEC alluvium ranges from 0.14 – 0.70 wt% Fe_2O_3 (average 0.42 wt% Fe_2O_3). Similarly, hematite in INTEC interbeds ranges from 0.20 – 1.03 wt% Fe_2O_3 (average 0.62 wt% Fe_2O_3). Goethite commonly exists in natural sediments, and its effect cannot be discounted. Mössbauer data indicate that goethite likely constitutes less than 1% of total iron. This report assumes that 0.5% of total iron is associated with goethite.

The $As^V K_d$ values calculated from sediment mineral composition are presented in Table D-3-2. The minimum and maximum estimated arsenic K_d values are based on the data of Smedley and Kinniburgh (2002), the clay mineral and iron oxide contents based on data in Table D-2-1, and the previously discussed assumptions about iron speciation in INTEC alluvium and interbeds. Values were calculated as in equation 2 (i = an idealized soil mineral).

$$K_D = \sum_i mass\ fraction_i * (K_D)_i \quad (2)$$

For these calculations, the entire clay mineral content is assumed to behave as kaolinite. The largest factor controlling $As^V K_d$ is the clay mineral content. When calculating the recommended K_d estimate, we have assumed the average clay mineral content and that only ~30% of the total clays are kaolinite and the rest of the clays are non-reactive towards As^V . This is a somewhat conservative estimate, as previous INL sediment data have indicated that kaolinite makes up slightly less than one-third of total clays (Bartholomay et al. 1989) and illite/smectite clays are reactive towards arsenic. No $As K_d$ data are available for basalt, and the estimated minimum is 0 mL/g. Basalt can have thin coatings of clay minerals, with the uncoated surfaces being approximately as reactive as silica. If we assume a thin coating of “typical INTEC clays” equivalent to ~0.1% of total basalt mass, then the

Table D-3-2. $As K_d$ values for INTEC alluvium, basalt, and interbed sediments. Values from batch experiments corrected for sediment/water ratio.

	Minimum Estimated $As K_d$ (mL/g)	Maximum Estimated $As K_d$ (mL/g)	Recommended $As K_d$ (mL/g)
Alluvium	0.7	190	40
Interbed	0.5	230	45
Basalt	0	10	2

maximum As K_d for basalt is estimated to be ~10 mL/g. The recommended estimate of ~2 mL/g is based on no appreciable clay effect, and assuming that basalt behaves as quartz (Smedley and Kinniburgh 2002).

D-3.5 ^{14}C K_d Values Applicable to INTEC Alluvium, Sediment, and Basalt

Process knowledge and monitoring data from the INTEC facility indicate that ^{14}C contamination is highly unlikely at this location. However, in order to be consistent with other WAGs, we provide estimates for ^{14}C K_d values for INTEC. Estimating ^{14}C K_d values requires knowledge of the multiple possible organic and inorganic forms of ^{14}C . The ^{14}C present in INL waste streams originates from nuclear fuel processing, and is predominantly inorganic in nature. Inorganic ^{14}C transport occurs via both (1) slow aqueous transport of $\text{H}^{14}\text{CO}_3^-$ ion, and (2) rapid transport of $^{14}\text{CO}_2$ gas. Most ^{14}C will be transported as CO_2 gas, even if most ^{14}C exists as the HCO_3^- (Plummer et al. 2004). Assessments of ^{14}C fate must consider gas-phase transport and quantification of the mass released to the atmosphere. Due to the rapid transport of ^{14}C as CO_2 gas, other organic and mineral forms (e.g., calcite) of ^{14}C are not considered.

No site-specific K_d data are available for ^{14}C adsorption to INTEC subsurface media, but some data are available for ^{14}C adsorption (as $\text{H}^{14}\text{CO}_3^-$) to SDA sediments. Dicke (Dicke 1997) suggests that ^{14}C -aq K_d (as $\text{H}^{14}\text{CO}_3^-$) can range from 2 – 20 mL/g (average 5 mL/g) for INL sediments, and recommends a K_d of 0 mL/g for basalt. Plummer et al. (2004) conducted a near-field scale unsaturated column study to quantify ^{14}C transport in SDA surficial soils collected from Spreading Area B at the INL-SDA. This work indicated that approximately 70% of total ^{14}C was released from the surface of the column as $^{14}\text{CO}_2$ (e.g., vented to atmosphere), 4% exited in the aqueous phase, 2% was lost to sampling, and 24% remained in the column at the end of the experiment (1% in soil gas, 3% in soil water, 20% adsorbed). When the ^{14}C data were fit to a multi-phase transport equation that accounted for minor variations in pH, ^{14}C K_d values of $\sim 0.5 \pm 0.1$ mL/g were calculated for the first 3 months following ^{14}C injection and ranged from 0.8 – 2.4 mL/g after 1 year of transport.

Recommendations for ^{14}C K_d are summarized in Table D-3-3. These values are not scaled to CEC, as pH has the greatest effect on C speciation and sorption and CEC is expected to have a secondary effect. Solution pH is similar for INTEC and SDA, so C-aq K_d values should be similar for these two systems. The pH is very similar for INTEC alluvium and basalt, and thus the C K_d values should be equivalent as well. The experiments of Plummer et al. (2004) most closely emulate the INTEC subsurface, and this reported range of values is recommended for INTEC alluvium and interbeds. The recommended ^{14}C K_d is estimated to be the median of the range of values reported for the 1-yr transport experiment (1.6 mL/g). No data are available for C partitioning to basalt, and a value of 0 mL/g is recommended.

Table D-3-3. C K_d values for INTEC alluvium, basalt, and interbed sediments. Values from batch experiments corrected for sediment/water ratio.

	Minimum Estimated C K_d (mL/g)	Maximum estimated C K_d (mL/g)	Recommended C K_d (mL/g)
Alluvium	0.5	2.8	1.6
Interbed	0.5	2.8	1.6
Basalt	0	2.8	0

D-3.6 Cr K_d Values Applicable to INTEC Alluvium, Sediment, and Basalt

Data used to estimate a K_d range for Cr should be derived from experiments that match the expected oxidation state for INTEC. Environmental chromium exists either as Cr^{III} , predominantly aqueous Cr^{3+} , or Cr^{VI} as CrO_4^{2-} . Cr^{III} is much less soluble than Cr^{VI} . Thermodynamic calculations presented in Figure D-3-3 indicate that Cr^{VI} should be the predominant form of chromium in highly oxidizing systems ($E_h > 600$ mV), and that Cr^{III} is stable under more reducing conditions typical of INTEC interbeds. $\text{Cr}^{\text{VI}}\text{O}_4^{2-}$ can adsorb weakly onto anion sorption sites and/or form CrO_4^{2-} minerals at high concentrations (e.g., Baron and Palmer 2002; Palmer and Wittbrodt 1991; Zachara et al. 1989), but significantly greater sorption occurs when Cr^{VI} is reduced to insoluble Cr^{III} by bacteria, organic matter, and soil minerals. A number of soil microorganisms can metabolically reduce Cr^{VI} , but most Cr^{VI} reduction occurs via abiotic reactions with Fe^{II} , S^{2-} , and organic matter (Fendorf et al. 2000). In systems where appreciable O_2 is present, Cr^{VI} reduction occurs predominantly via reaction with organic matter and Fe^{II} present in soil minerals such as biotite (Palmer and Puls 1994). Once formed, Cr^{III} is likely to remain reduced until exposed to oxidized $\text{Mn}^{\text{III,IV}}$ (e.g., Banerjee and Nesbitt 1999; Kozuh et al. 2000).

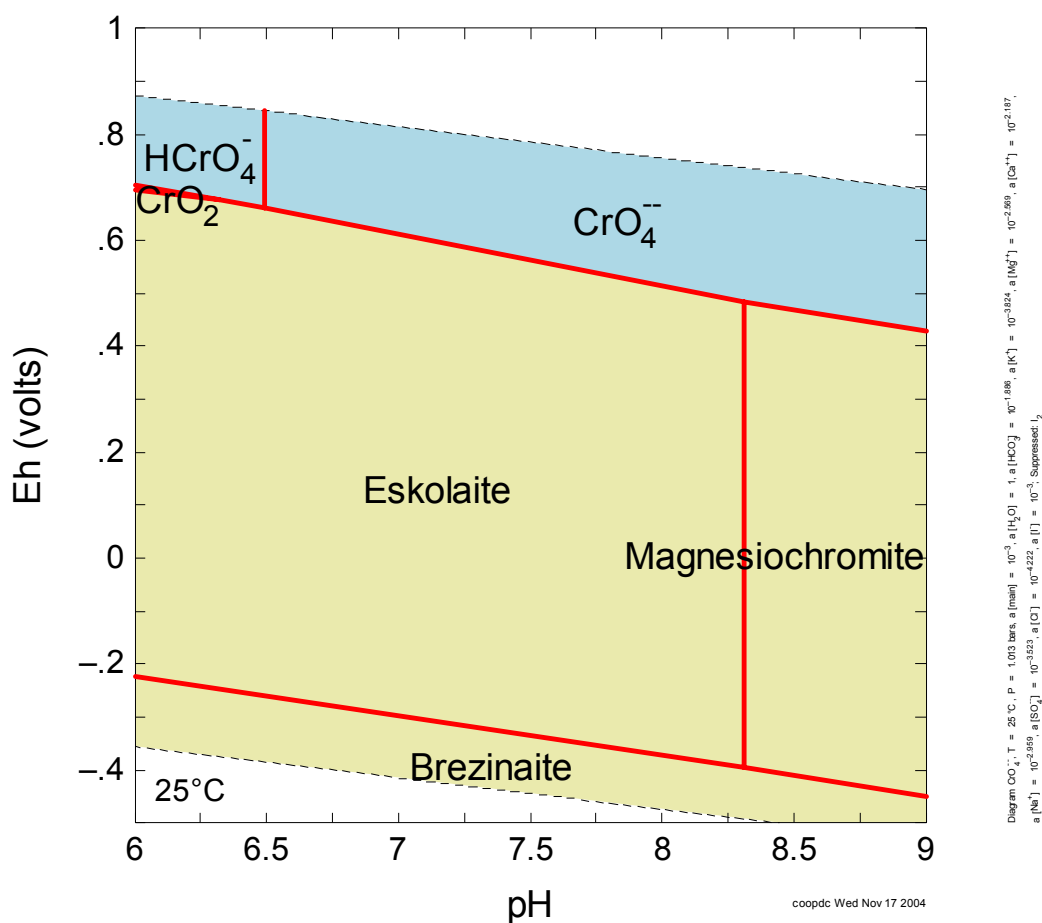


Figure D-3-3. Phase diagram for chromium speciation in INL-SDA groundwater.

INTEC basalt and soil minerals contain appreciable amounts of crystalline Fe^{II} that can chemically reduce adsorbed Cr^{VI} to Cr^{III} , and the speciation diagram given in Figure D-3-3 indicates that oxidation/reduction potential within INTEC sediments ($E_h \sim 100 - 300 \text{ mV}$) are sufficiently reducing to allow Cr^{VI} reduction. Thus, we assume that abiotic Cr^{VI} reduction controls Cr sorption in INTEC interbeds and basalt. A number of sedimentary minerals contain appreciable amounts of Fe^{II} that can reduce Cr^{VI} to Cr^{III} , and the CEC-based scaling cannot be applied to INTEC interbeds. Insufficient data exist to establish oxidation potential for INTEC alluvium, and we assume that Cr^{VI} reduction does not occur in these coarse grained, oxic sediments. Clay minerals are the primary adsorbent for Cr^{VI} , and thus Cr^{VI} K_d values can be scaled according to CEC.

No site-specific K_d data are available for Cr adsorption to INTEC subsurface media, but some data are available for Cr adsorption to SDA sediments. Grossman et al. (2001) reports K_d values that range from 0.11 – 392 mL/g for batch experiments with SDA interbed sediments. Of these measurements, >85% ranged from 0.4 – 60 mL/g. Dicke (1997) recommends total-Cr K_d values that range from 2.2 to 1000 mL/g for SDA sediments and from 0.11 – 50 mL/g for basalt. For Cr^{VI} only, Dicke (1997) recommends K_d values that range from 0.1 – 10 mL/g for SDA sediments and 0 mL/g for basalt. For these recommendations, the total-Cr values include both Cr^{III} and Cr^{VI} and account for the effects of Cr^{VI} reduction.

We assume that Cr^{VI} reduction does not occur in INTEC alluvium, and thus the CEC-based scaling factor can be applied here. Applying this scaling factor to the batch experiments of Grossman et al. (2001) yields a K_d range of 0.08 – 12 mL/g for INTEC alluvium (subset consisting of ~85% of all measurements). To recommend a single estimate within this range, we refer to column experiments conducted by Stollenwerk and Grove (1985) on coarse grained alluvial sediments analogous to INTEC (0.4 – 1400 μM Cr). Here, the conditions most comparable to INTEC (960 μM CrO_4^{2-} , flow rate of ~60 cm/d for 232 days) yielded an estimated Cr^{VI} K_d of 2.4 mL/g.

Because the CEC-based scaling cannot be applied to INTEC interbeds, data from the open literature must be used as a guide. Sheppard and Thibault (1991) conducted a 4 yr lysimeter study of Cr mobility across several sediment horizons roughly comparable to INTEC interbeds (< 0.5 wt% organic carbon) and report Cr K_d values that range from 9 – 160 mL/g at 1 yr aging (average ~90 mL/g), and 476 – 685 mL/g at 4 yr aging (average ~580 mL/g). The higher K_d at 4 yr was considered to arise from *in situ* Cr^{VI} reduction. Recommendations for the maximum and minimum Cr K_d for INTEC interbeds are based on this work. The recommended single estimate of 90 mL/g is the average of the 4 K_d values reported for the 1 yr lysimeter tests conducted by Sheppard and Thibault (1991). The minimum K_d for basalt is estimated to be 0 mL/g, and the maximum K_d for basalt is estimated to be equivalent to that previously suggested by Dicke (1997). For a single best estimate for basalt, we adopt Dicke's recommendation of 1.5 mL/g. These Cr K_d recommendations are summarized in Table D-3-4.

Table D-3-4. Cr K_d values for INTEC alluvium, basalt, and interbed sediments. Values from batch experiments corrected for sediment/water ratio.

	Minimum Estimated Cr K_d (mL/g)	Maximum Estimated Cr K_d (mL/g)	Recommended Cr K_d (mL/g)
Alluvium	0.08	12	2.4
Interbed	9	685	90
Basalt	0	50	1.5

D-3.7 ¹³⁷Cs K_d Values Applicable to INTEC Alluvium, Sediment, and Basalt

¹³⁷Cs is a hard cation that exists primarily in the +1 oxidation state and has chemistry similar to that of K⁺. Cs is not sensitive to a system's oxidation state, does not strongly adsorb onto iron oxide minerals, and is largely unaffected by organic matter. Cs⁺ primarily adsorbs via ion exchange reactions with sedimentary clay minerals, and Cs K_d should correlate with CEC. Variations in aqueous chemistry between INTEC alluvium and interbeds are not expected to be large enough to alter Cs K_d. Alluvium and interbeds also display similar sediment geochemistry with respect to parameters that affect Cs⁺ sorption, and thus Cs K_d should not vary significantly between INTEC alluvium and interbeds.

Hawkins and Short (1965) provide an equation to calculate Cs K_d for INTEC alluvium from CEC and aqueous Ca²⁺, NH₄⁺, K⁺, and Cs⁺ concentration. The equation is strongly dependent on [Cs⁺-aq]. If [Cs⁺-aq] < 1 mM and the maximum and minimum values for the listed geochemical parameters in INTEC alluvium is applied to this equation, then Cs K_d can be estimated to range from 10 – 160 mL/g under typical INTEC alluvium and interbed conditions. Cs K_d decreases with increasing [Cs⁺-aq], and this equation cannot predict K_d at [Cs⁺-aq] concentrations > ~1 mM. This conclusion also holds when the maximum and minimum values for the listed geochemical parameters in interbeds are used. Thus, the minimum and maximum recommended range for Cs K_d in INTEC alluvium and interbeds is 10 to 160 mL/g. The minimum Cs K_d for basalt is estimated to be 0 mL/g, and the maximum is as recommended by Dicke (1997).

The current INTEC model does not allow calculation of Cs⁺ K_d as a function of [Cs⁺-aq], and the strong dependence of the Hawkins and Short (1965) equation on [Cs⁺-aq] limits its usefulness in estimating an average K_d value for large subsurface regions. Thus, data from other experiments are necessary to bound the uncertainty in Cs K_d values for INTEC. In column tests conducted on basalt and sedimentary interbed samples from SDA, Fjeld et al. (2001) report Cs retention factors (R) that range from 70 – 90 for basalt and >200 to >800 for sedimentary interbed sediments. Under experimental conditions, these retention factors equate to a K_d of 20 – 26 mL/g for basalt and >50 to >200 mL/g for interbed sediments. Cs breakthrough was not observed in interbed sediments, and the reported estimates are based on γ-spectroscopic analyses of the intact cores. If these results from SDA sediments are scaled according to CEC, they would suggest Cs⁺ K_d values ranging from >10 to, >40 mL/g. In a field lysimeter study conducted under geochemical conditions somewhat analogous to INTEC, Sheppard and Thibault (1991) report Cs⁺ K_d values that ranged from 1.5 – 17.2 mL/g at 1 yr and from 0.2 – 51 mL/g at 4 yr contact. These systems had lower pH, higher major ion content, and slightly lower CEC than is typical for INTEC alluvium and interbeds; and should be considered to provide an approximate lower boundary.

A summary of recommended Cs K_d data is provided in Table D-3-5. The recommended Cs K_d for INTEC interbed and alluvium is based on the reasoning that Fjeld et al. (2001) observed a CEC-normalized Cs⁺ K_d of >40 mL/g for comparable sediments and Sheppard and Thibault (1991) observed a maximum K_d of ~50 mL/g during their lysimeter study under conditions generally comparable to INTEC alluvium and interbeds (but with lower CEC). The value of 50 mL/g is a reasonable median between these datasets, and falls within the range estimated from the equation of Hawkins and Short (1965). The recommended K_d values for basalt are based on the work of Fjeld et al. (2001).

Table D-3-5. Cs K_d values for INTEC alluvium, basalt, and interbed sediments. Values from batch experiments corrected for sediment/water ratio.

	Minimum Estimated Cs K_d (mL/g)	Maximum Estimated Cs K_d (mL/g)	Recommended Cs K_d (mL/g)
Alluvium	10	160	50
Interbed	10	160	50
Basalt	0	44	25

D-3.8 ^{154}Eu K_d Values Applicable to INTEC Alluvium, Sediment, and Basalt

^{157}Eu predominantly occurs as Eu^{3+} in natural environments, and is chemically similar to Am. Eu generally adsorbs strongly to iron oxide and clay minerals in soils and sediments, and undergoes electrostatic interactions with negatively charged surfaces (Benes et al. 2002; Dong et al. 2001). Eu mobility is strongly impacted by soil organic matter, with humic acids increasing Eu mobility by suppressing sorption, whereas fulvic acids enhance Eu sorption (Benes et al. 2002; Dong et al. 2001; Dong et al. 1999). In the absence of humic materials, Eu sorption onto soil minerals can be reasonably described by equilibrium expressions (Dong et al. 2001). INTEC sediments have little organic matter, and therefore organic matter effects can be assumed to be negligible. Similarly to Am, Eu sorption is likely to be controlled by clay minerals and K_d would be proportional to CEC. The differences in aqueous and sediment geochemistry between INTEC alluvium and interbeds are unlikely to notably alter Eu sorption, and K_d is assumed to be the same for alluvium and interbeds.

There are no data available that provides site-specific measures of Eu K_d for INTEC or SDA sediments; and it is necessary to find information on other comparable systems. Dong et al. performed batch sorption experiments with bentonite and iron/clay-rich red earth (24 – 36 hr equilibration, 0 to 55 μM Eu), and report that Eu K_d can range from 23 to 3500 mL/g at pH 4 – 6 (Dong et al. 2001). In Goreleben sand (~85% quartz, 10 – 15% feldspar, <5% clay minerals and <0.5 wt% organic carbon), similar batch experiments revealed 40 – 60% of 0.034 μM ^{157}Eu adsorbed to the sand at pH 6 – 8 and a 1:20 sediment/water ratio ($K_d \sim 15 - 30$ mL/g). McCarthy et al. (1998) report K_d values of 8900 mL/g for Am and 19,600 mL/g for Eu from batch studies (48 hr equilibration) with a clay-rich saprolite from Oak Ridge National Laboratory (ORNL). In a parallel field transport study, Eu moved as quickly as non-reactive Nd and Br⁻ tracers. The apparent discrepancy between the large Eu K_d measured in batch experiments and the small Eu K_d observed in a field tracer experiment was resolved by considering hydrologic history. Water transport at this experimental site occurred predominantly through brief periods of storm runoff moving through a fractured rock environment, rather than continuous flow through a porous medium. This stochastic flow (analogous to fractured basalt) overwhelmed geochemical effects.

A summary of recommended Eu K_d values is presented in Table D-3-6. The available Eu K_d data range from 15– 19,600 mL/g for sediments. These data are similar to the literature range reported for Am. Because these two elements share similar chemistry (same group on Periodic Table) and have similar ranges, Am recommendations are also adopted for Eu. This is reasonable, as available comparisons indicate that Eu adsorbs more strongly than Am (McCarthy et al. 1998).

Table D-3-6. Eu K_d values for INTEC alluvium, basalt, and interbed sediments. Values from batch experiments corrected for sediment/water ratio.

	Minimum Estimated Eu K_d (mL/g)	Maximum Estimated Eu K_d (mL/g)	Recommended Eu K_d (mL/g)
Alluvium	15	19,600	400
Interbed	15	19,600	400
Basalt	0	140	0.85

D-3.9 Hg K_d Values Applicable to INTEC Alluvium, Sediment, and Basalt

Mercury predominantly exists as Hg^{2+} in soil systems, adsorbs to a number of soil constituents, and can form organo-Hg compounds through microbial metabolic activity (Schuster 1991). One of the most important soil constituents affecting Hg^{2+} sorption is soil organic matter, which dominates Hg^{2+} sorption when present in appreciable quantities (Schuster 1991). In the absence of soil organic matter, Hg^{2+} can react with soil minerals to form inner-sphere surface complexes with silica and alumina sites on soil minerals or sorb via electrostatic interactions with charged surfaces (Sarkar et al. 1999; Schuster 1991). Hg^{2+} can also exist as gaseous Hg^0 in soils, and transformations from Hg^{2+} to Hg^0 are thought to control mercury emission from soils (Lindberg et al. 1999; Zhang and Lindberg 1999). Large changes in Hg^0 emission have been observed to be associated to occur in response to rainfall or irrigation in desert soils – with water addition increasing the rate of Hg emission and potentially impacting subsurface Hg transport (Lindberg et al. 1999).

Taken together, these data suggest that organic carbon content will control Hg^{2+} sorption and partitioning in INTEC alluvium and interbeds. Vapor phase transport of Hg^0 may also represent an important Hg transport vector, but cannot be easily quantified at this time. Hg K_d is only weakly affected by CEC, and any scaling should be done in relation to soil organic matter. The aqueous geochemical parameters expected to impact Hg sorption are similar for INTEC alluvium and interbeds, and K_d should not vary significantly between these different subsurface regions.

Del Debbio and others (del Debbio 1991; del Debbio and Thomas 1989) report Hg K_d values from column experiments that range from 236 – 1912 mL/g for INTEC alluvium, 72 – 673 mL/g for INTEC interbed and 9.2 – 87 mL/g for basalt. Dicke et al. (1997) use these data to suggest Hg K_d values that range from 72 – 1912 mL/g (recommend 176 mL/g) for SDA sediments and from 9.2 – 87 mL/g (recommend 9.2 mL/g) for basalt. As discussed previously, we extend the minimum K_d for basalt to 0 mL/g in order to account for the effects of stochastic fluid transport.

These reported ranges for Hg K_d in INTEC sediments are large, and estimation of recommended K_d values requires further guidance. Lee, Chang et al. (2001) provide conditional K_d values for Hg^{2+} adsorbing to soil organic matter, iron oxides, aluminum oxides, and manganese oxides. When combined in a weighted sum similar to that used to estimate As K_d , these data allow estimation of Hg^{2+} K_d from soil mineral data. The provided equations are most useful at pH < 6, but can provide a basis for estimating Hg K_d in INTEC alluvium and interbed sediments. Lee, Chang et al. (2001) provide four different equations for use when different soil constituents are known, and the best fits were obtained from a 4-parameter equation. However, the improvement of the 3- or 4-parameter equations over the 2-parameter equation was only marginal and we only have robust data for 2 parameters (wt% iron oxide, wt% organic

carbon). Thus, this report will use the 2-parameter equation to estimate Hg K_d in INTEC alluvium and interbed sediments ($Hg\ K_d = 44.76 * \text{weight\% organic matter} + 249.73 * \text{weight\% FeO}$). Employing the same set of assumptions regarding iron oxide content for the calculation of As K_d and the range of organic matter content reported in Table D-3-7 yields estimated Hg K_d values that range from 36 – 215 mL/g for INTEC alluvium and from 50 – 270 mL/g for INTEC interbeds. The predictions for interbeds agree well with the data from del Debbio and others (del Debbio 1991; del Debbio and Thomas 1989), but severely underpredict the reported range for INTEC alluvium. To accommodate this discrepancy, the minimum estimate for Hg K_d is extended to include these calculations.

A summary of recommended Hg K_d values is provided in Table D-3-7. The minimum and maximum Hg K_d values represent a combination of the ranges reported by del Debbio and others (del Debbio 1991; del Debbio and Thomas 1989) and the previously described calculations. Here, organic matter content is as reported in Table D-3-7 and iron oxide mineral content can range from 5 – 25% of total weight percent FeO on an equivalent basis. The recommended K_d values are based on calculations involving the average organic matter content and recommended iron oxide content. Limited data are available for Hg sorption to basalt, and thus we recommend a value of 0 mL/g.

Table D-3-7. Hg K_d values for INTEC alluvium, basalt, and interbed sediments. Values from batch experiments corrected for sediment/water ratio.

	Minimum Estimated Hg K_d (mL/g)	Maximum Estimated Hg K_d (mL/g)	Recommended Hg K_d (mL/g)
Alluvium	118	1,912	118
Interbed	72	673	156
Basalt	0	87	0

D-3.10 ¹²⁹I K_d Values Potentially Applicable to INTEC Alluvium, Sediment, and Basalt

¹²⁹I generally occurs as iodate (IO₃⁻), iodide (I⁻), or organic iodine in natural environments. As is demonstrated in Figure D-3-4, which was prepared using a commercially available geochemical modeling program (Geochemists' Workbench[®] v4) with solution conditions representative of INTEC alluvium and interbed water IO₃⁻ is the predominant species at Eh > ~750 mV. Under more reducing conditions, iodide (I⁻) is the predominant inorganic iodine species. Highly oxidizing environments may also generate I₂(g). Iodide (I⁻) will slowly react with O₂ and soil organic matter to form organic iodine species (Zengshou et al. 1996). One of the important forms of organic iodine is gaseous methyl iodide, which can control iodine transport in environments with appreciable levels of microbial activity. (Amachi et al. 2003; Amachi et al. 2000; Bostock et al. 2003; Muramatsu and Yoshida 1999).

INTEC subsurface materials are poor in organic carbon and are unlikely to generate appreciable amounts of methyl iodide. Thus, gaseous transport is not likely to affect iodine transport at INTEC. However, the small amount of available organic matter can adsorb appreciable amounts of I⁻ and organic matter is expected to be equally important to clay minerals. Both constituents need to be considered when estimating I K_d , and CEC cannot be used as a sole scaling factor. Another factor to consider is iodine speciation. Iodide (I⁻) is expected to be the dominant iodine species in most aquifer systems (Kaplan 2003), but iodate (IO₃⁻) can form by interaction of I⁻ with radiolysis products and can persist in solution (Ticknor and Cho 1990). The INTEC ¹²⁹I source is radioactive, and it is reasonable to expect

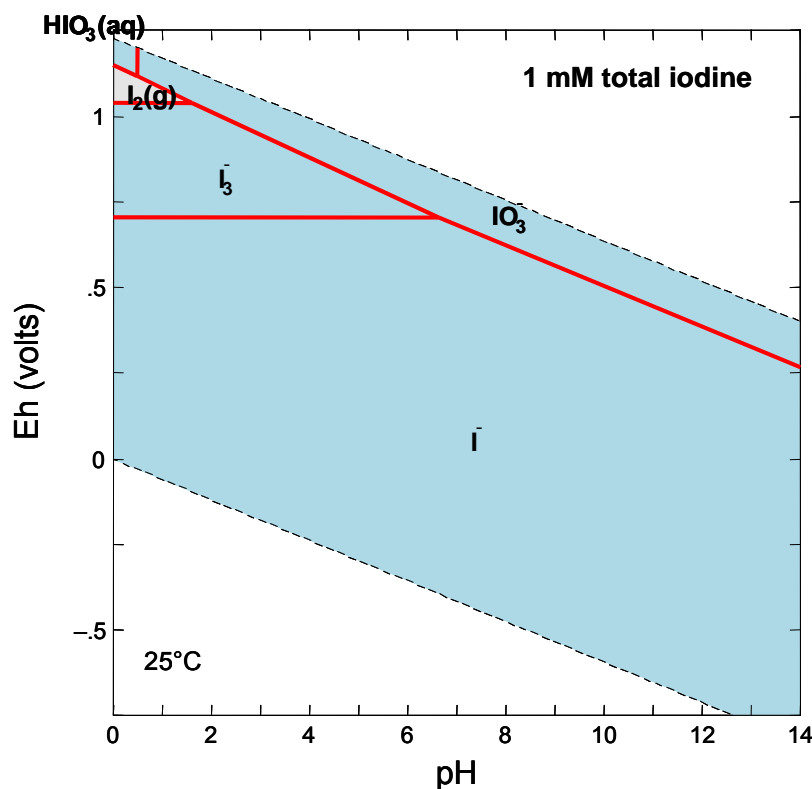


Figure D-3-4. Phase diagram for iodine speciation in INL-SDA groundwater.

that most ^{129}I may have originally existed as IO_3^- . However, a study of iodine speciation in INTEC reprocessing wastes indicated that 69% of the iodine was present as iodide (I^-), with the remainder believed to be present in more the highly-oxidized forms IO_3^- , HOI , and I_2 (McManus et al. 1982). Since iodide (I^-) is recommended as the predominant iodine species in the INTEC Tank Farm liquid wastes and most ^{129}I sorption studies use I^- , all $\text{I} K_d$ recommendations will be based on I^- . This is a reasonable and conservative approach, as IO_3^- generally sorbs more strongly to common soil minerals than I^- (Ticknor and Cho 1990).

There are no data available that provides site-specific measures of $\text{I} K_d$ for INTEC or SDA alluvium, interbed sediment, and basalt, and it is necessary to find information on other systems. Dicke (1997) has previously analyzed comparable systems and concluded that $\text{I} K_d$ in SDA sediments should range from 0.02 – 5 mL/g (best guess = 0.1 mL/g). Kaplan et al. (2003) report K_d values that range from ~0.6 – 2 mL/g ($\text{pH} > 4$) for batch experiments (14 d equilibration) with two different Savannah River Site (SRS) sediments that are comparable to INTEC sediments. The iodide (I^-) K_d for upland silty-sand (0.3 wt% Fe_2O_3 , < 0.02 wt% organic carbon) ranged from 0.6 – 0.8 mL/g, and the K_d for a wetland sediment (0.01 wt% Fe_2O_3 , 0.14 wt% organic carbon) ranged from 1 – 2 mL/g. Sheppard, Hawkins, and Smith (1996) provides I^- sorption isotherms for seven natural soils exposed to iodide for time periods that range from 1 – 153 days, and reports $\text{I}^- K_d$ values that range from 6.2 to 1800 mL/g. These K_d values correlated positively with Al-oxide content, organic matter content, and contact time. Sheppard (2003) measured $\text{I}^- K_d$ for 5 different soils at two different equilibration periods (~1 d, 14 d). $\text{I}^- K_d$ ranged from 0.1 to 68 mL/g at 1 d equilibration and from 0.82 – 140 mL/g for 14 d equilibration. Increasing contact time in a batch experiment increased $\text{I}^- K_d$, but Sheppard and Thibault (1991) found an inverse relationship between $\text{I}^- K_d$ and contact time in a long-term field lysimeter experiment conducted across several soil horizons that are somewhat comparable to the INTEC alluvium and interbeds. In the soil horizons most comparable to INL INTEC alluvium (0.2 – 0.3 wt% organic carbon), $\text{I}^- K_d$ ranged

from 0.1 to 8.7 mL/g at 1 yr of transport and ranged from 0.04 – 0.06 mL/g at 4 yr transport. In the soil horizons with high organic carbon (1 – 7 wt%), $I K_d$ ranged from 8.2 – 198 mL/g at 1 yr, and 0.1 – 1.9 mL/g at 4 years. The aging effect increases with increasing organic carbon content – suggesting that microbial transformation of I^- to adsorbed organic-I first increases K_d and then decreases K_d as organic-I is transformed to gaseous methyl-iodide. This is likely to be of lesser importance in the organic-poor INTEC sediments.

Recommendations for $I K_d$ in INTEC are presented in Table D-3-8. The maximum and minimum values for alluvium and interbed sediments are based on the maximum and minimum values reported for comparable sediments. The recommended estimates are based on the work of Kaplan et al. (2003), and assume that microbial I transformations are of negligible importance in the low organic carbon sediments typical of the INTEC subsurface. The upland sediment of Kaplan et al. roughly corresponds to INTEC interbeds, and displays an $I K_d$ of $\sim 0.7 \pm 0.1$ mL/g. The wetland sediment, roughly corresponds to INTEC alluvium sediments (higher organic carbon), and displays a K_d of $\sim 1.5 \pm 0.5$ mL/g. No data are available for basalt. The minimum K_d is assumed to be 0 mL/g, which is also considered to be the best estimate for $I K_d$ in basalt.

Table D-3-8. $I K_d$ values for INTEC alluvium, basalt, and interbed sediments. Values from batch experiments were corrected for sediment/water ratio.

	Minimum Estimated $I K_d$ (mL/g)	Maximum Estimated $I K_d$ (mL/g)	Recommended $I K_d$ (mL/g)
Alluvium	0.04	8.7	1.5
Interbed	0.04	3	0.7
Basalt	0	No data	0

D-3.11 NO_3^- and NO_2^- K_d Values Potentially Applicable to INTEC Alluvium, Sediment, and Basalt

NO_3^- and NO_2^- (NO_x^-) are negatively charged anions that typically sorb poorly to sediments and are highly mobile. They display similar sorption chemistry, and can be expected to have similar aqueous solubility in soil environments. Both NO_3^- and NO_2^- can be reduced chemically or microbiologically to $NO_2^-(aq)$, $N_2O(g)$, $N_2(g)$, and/or $NH_4^+(aq)$. These chemical transformations typically affect NO_x^- transport to a much greater degree than sorption processes.

There are no data available that provide site-specific measures of $NO_x^- K_d$ for INL alluvium, sediment, and basalt, and it is necessary to find information on other systems that are comparable to INL INTEC. Dicke (1997) suggests a $NO_3^- K_d$ of 0 mL/g for INL SDA sediments. Clay et al. (2004) measured NO_3^- transport in 24 soil columns collected from an agricultural corn/soybean field. All columns displayed minimal NO_3^- retention, with $NO_3^- K_d$ values of 0.15 ± 0.05 mL/g. Duwig et al. (2003) report NO_3^- retention factors that range from 1 – 2 ($K_d \sim 0 - 0.5$ mL/g) for column experiments in soils with a high aluminum oxide content. Sonon and Schwab (2004) report that Br^- and NO_3^- transport was comparable in columns of sandy loam soils, indicating minimal NO_3^- retention. No values for NO_3^- sorption onto basalt are available.

These soils are not directly comparable to INTEC alluvium and interbed sediments, but the broad agreement between these different studies suggests that $\text{NO}_3^- K_d$ values in INTEC range from 0 to 0.5 mL/g. The recommended $\text{NO}_3^- K_d$ values for INTEC alluvium and interbeds are estimated to be equal to the lower end of the range of data collected by Clay et al. (2004). The lower end is chosen over the median, because INTEC sediments are coarser-grained and have a lower surface area than most of the surficial sediments examined by Clay et al. Based on the work of Dicke (1997) and Sonon and Schwab (2004), the best conservative estimate is 0 mL/g. $\text{NO}_2^- K_d$ is considered to be equal to $\text{NO}_3^- K_d$. Summary data are presented in Table D-3-9.

Table D-3-9. NO_3^- and NO_2^- (NO_x^-) K_d values for INTEC alluvium, basalt, and interbed sediments. Values from batch experiments corrected for sediment/water ratio.

	Minimum Estimated $\text{NO}_x^- K_d$ (mL/g)	Maximum Estimated $\text{NO}_x^- K_d$ (mL/g)	Recommended $\text{NO}_x^- K_d$ (mL/g)
Alluvium	0	0.5	0.1
Interbed	0	0.5	0.1
Basalt	0	No data	0

D-3.12 ^{237}Np K_d Values Applicable to INTEC Alluvium, Sediment, and Basalt

^{237}Np predominantly exists as aqueous $\text{Np}^{\text{V}}\text{O}_2^-$ ion in soil systems, and adsorbs onto soil minerals via both site specific surface complexation reactions and non-specific ion exchange reactions (Andre et al. 1998). NpO_2^- is not sensitive to changes in an environmental system's bulk oxidation state, adsorbs most strongly to clay minerals and iron oxides, and only weakly adsorbs to quartz. Aqueous organic complexes can enhance Np solubility, but sedimentary organic matter is not known to notably affect Np sorption. NpO_2^- forms aqueous complexes with CO_3^{2-} , and solubility increases with increasing pH and alkalinity.

INTEC alluvium and interbed sediments are similar with respect to sediment geochemistry, and the small differences should not greatly affect Np mobility. The higher Ca^{2+} concentrations in INTEC interbeds may be accompanied by higher alkalinity and a greater extent of Np complexation with aqueous carbonate. However, it is impossible to quantify this difference in the absence of direct measurements and this report assumes that Np K_d is similar for INTEC alluvium and interbeds. For both systems, sorption is expected to occur predominantly through reactions with clay mineral surfaces and K_d should be proportional to CEC.

No site-specific K_d data are available for ^{237}Np adsorption to INTEC subsurface media, but some data are available for Np adsorption to SDA sediments. Dicke (1997) recommends Np K_d values that range from 1 – 80 mL/g for SDA sediments, and from 1.3 – 51 mL/g for basalt. A value of 8 mL/g is recommended for both sediment types. Mincher et al. (2004) used batch experiments to investigate the sorption behavior of Np onto fine-grained SDA surficial soils, and found K_d values that ranged from 40 to 500 mL/g ($[\text{Np-aq}]$ ranged from $1\text{e-}10$ – 6 mM). The data fit a Freundlich isotherm, indicating that variability in K_d was primarily due to variations in Np aqueous concentrations. Grossman et al. (2001) reports Np K_d values that range from 17 – 300 mL/g for batch experiments with SDA interbed sediments. Ayaz et al. (2003) measured Np K_d values ranging from 12 – 83 mL/g in experiments with a different set of SDA interbed sediments under parallel conditions. Leecaster and Hull (2004) integrated these interbed-specific K_d data with geographic records of sample location to create a 2-D grid of Np K_d in

SDA interbeds. When plotted as a histogram, these data indicated that >95% of K_d measurements fell within the range of 0.5 – 50 mL/g.

Taken together, these batch studies suggest that Np K_d values range from 0.5 – 300 mL/g. Scaling to CEC reduces this range to 0.1 – 60 mL/g for INTEC. These values provide reasonable bounds on the minimum and maximum K_d for Np. In estimating the recommended Np K_d for alluvium and interbeds, it is useful to seek guidance from studies conducted at other sites. André et al. (1998) report ^{237}Np K_d values ranging from 1.5 – 2.0 mL/g (pH ~8) for column experiments with sandy sediments containing fewer clay minerals than INTEC. In a field lysimeter study with a sandy sediment roughly comparable to INTEC alluvium and interbeds, Sheppard and Thibault (1991) report Np K_d values ranging from 0.5 – 1.6 mL/g at 1 yr aging, and 0.6 – 5 mL/g at 4 yr aging. The median value of these experiments conducted in comparable sediments is ~2 mL/g. This range of Np sorption data from the SDA and scaled by CEC to INTEC conditions brackets the 2 mL/g value, and thus this value is recommended for Np K_d in INTEC interbeds and alluvium. Lacking direct data, we assume that the K_d value of 8 mL/g recommended by Dicke (1997) for basalt provides a reasonable maximum value. The recommended Np K_d for basalt is assumed to be 0 mL/g. These recommendations are summarized in Table D-3-10.

Table D-3-10. Np K_d values for INTEC alluvium, basalt, and interbed sediments. Values from batch experiments corrected for sediment/water ratio.

	Minimum Estimated Np K_d (mL/g)	Maximum Estimated Np K_d (mL/g)	Recommended Np K_d (mL/g)
Alluvium	0.1	60	2
Interbed	0.1	60	2
Basalt	0	8	0

D-3.13 $^{238/239/240}\text{Pu}$ K_d Values Applicable to INTEC Alluvium, Sediment, and Basalt

Plutonium generally exists as a highly insoluble Pu^{IV} oxide mineral in natural systems, but can rapidly shift oxidation state to more soluble Pu^{III} , Pu^{V} , and Pu^{VI} species. These oxidation shifts typically impact plutonium mobility to a greater extent than does aqueous complexation of any single plutonium oxidation state with organic and inorganic ligands (Choppin and Morgenstern 2001). Fjeld et al. (2003) have described a conceptual model for plutonium transport through sediment columns where Pu transport is controlled by the net rate of reduction of adsorbed Pu^{V} to adsorbed Pu^{IV} . Field studies have supported this model in Savannah River Site vadose zone sediments (Kaplan et al. 2004). In this model, solid $\text{Pu}^{\text{IV}}\text{O}_2$ reacts with environmental oxidants to form a more oxidized surface coating that is more soluble than bulk $\text{Pu}^{\text{IV}}\text{O}_2$ (Haschke et al. 2000). This oxidized Pu can mobilize as Pu^{V} , and the Pu^{V} can re-adsorb onto iron bearing minerals and be slowly reduced to Pu^{IV} . In this way, kinetic control of Pu transport can allow a small fraction to move while the bulk of Pu is largely immobile.

Based on these studies, plutonium chemistry should be controlled by the kinetics of surface-mediated redox reactions that mediate electron cycling between Pu^{IV} , Pu^{V} , and sedimentary iron bearing minerals. This type of non-equilibrium behavior is difficult to capture with a K_d approach, but K_d can be used if the system is assumed to have reached steady-state with respect to Pu redox kinetics. The balance of forward and back reactions that create this assumed steady-state is likely to be impacted by both surface area and surface potential. CEC is also related to these two properties, and so the relative rates of Pu^{IV} and Pu^{V} redox transformations that contribute to a given steady-state condition used to estimate K_d should be correlated to CEC provided that iron mineral composition remains unchanged. The available

data indicate that iron mineralogy is analogous in INTEC and SDA, and thus K_d values can reasonably be scaled using CEC. Mineral composition is similar for INTEC alluvium and interbeds, and difference in aqueous chemistry should not greatly affect Pu redox kinetics. The same CEC-scaled Pu K_d is recommended for INTEC alluvium and interbeds.

Limited site-specific K_d data are available for Pu adsorption to INTEC subsurface media. Navratil (1997) reviewed historical studies of Pu sorption to INTEC and SDA interbed material, and recommended a Pu K_d between 300 – 3500 mL/g for INTEC interbed material. This recommendation was also supported by Falconer (1997). Miner et al. (1982) report Pu K_d values that range from 120 – 5000 mL/g for batch experiments with Snake River Plain soils. Mincher et al. (2003) report Pu K_d values from batch experiments with SDA surficial soils that range from 14 – 650 mL/g after short contact (<24 hr). Data from similar, unpublished studies on the same soils^g indicate that Pu K_d values can range from 475 – 63,560 mL/g after long-term exposure (1 – 6 months). Dicke (1997) recommends a Pu K_d range of 5100 – 22,000 mL/g for SDA sediments. This range is higher than the data provided by Miner et al. (1982) and Mincher et al. (2003), but is in agreement with the long-term contact data presented in Figure D-3-5. When these long-term contact data are scaled to CEC, these Pu K_d values range from 96 to 12,712 mL/g and provide a reasonable range for possible Pu K_d values in INTEC alluvium and interbeds. These data were gathered from the same experiment previously described for Am, and are summarized in Figure D-3-5.

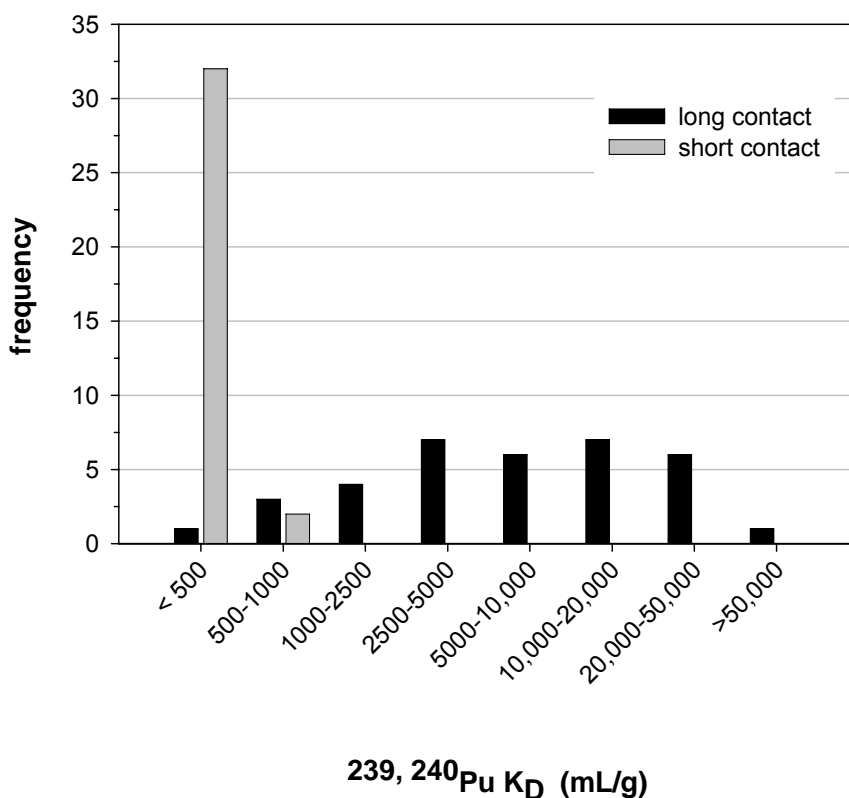


Figure D-3-5. Histogram of Pu K_d for ISTD pit sediments at short (< 24 hr) and long (>1 Mo) contact time.

g. Cooper D. C., 2002, unpublished data on INL-SDA ISV Pit Sediments (ed. D. C. Cooper, Battelle Energy Alliance. Idaho National Laboratory).

The available SDA data provide a wide range of likely Pu K_d values, and it is useful to refer to studies performed at other sites when recommending a Pu K_d for INTEC subsurface media. In column experiments with SDA interbed sediments, Fjeld et al. (2001) report retention factors of > 200 for noncolloidal ^{239}Pu ($K_d > 50 \text{ mL/g}$). In the lysimeter experiment described by Kaplan et al. (2004), the sediment was a sandy clay roughly comparable to INTEC alluvium and interbeds (CEC, organic content, iron content). These unsaturated Pu transport experiments reported a retention factor of ~3000 for Pu^{IV} , which equates to a K_d of ~1000 mL/g. This value falls within the range of CEC and sediment/water ratio normalized 1-Mo contact data for SDA sediments, and is estimated as recommended for INTEC sediments. For basalt, Dicke (1997) recommends a Pu K_d range of 70 – 130 mL/g with a suggested value of 100 mL/g. We extend this range to a minimum estimate of 0 mL/g. In column experiments with basalt, Fjeld et al. (2001) report retention factors of > 200 for non-colloidal Pu ($K_d > 50 \text{ mL/g}$). These results are in agreement with the recommendations of Dicke (1997). This work provides an estimate of the minimum probable Pu K_d for basalt, and indicates that the recommended Pu K_d for basalt is higher. We recommend a basalt Pu K_d of 70 mL/g, which is greater than the minimum reported by Fjeld et al. (2001) and equal to the minimum value suggested by Dicke (1997). Recommendations for Pu K_d in INTEC are presented in Table D-3-11.

Table D-3-11. Pu K_d values for INTEC alluvium, basalt, and interbed sediments. Values from batch experiments corrected for sediment/water ratio.

	Minimum Estimated Pu K_d (mL/g)	Maximum Estimated Pu K_d (mL/g)	Recommended Pu K_d (mL/g)
Alluvium	96	12,712	1000
Interbed	96	12,712	1000
Basalt	0	130	70

D-3.14 Potential for Formation of Colloidal $^{238/239/240}\text{Pu}$ in INTEC Alluvium, Sediment, and Basalt

Recent work in INL SDA has focused on the potential for a small fraction of total Pu to be rapidly transported by colloids. Due to this effort at another INL WAG-7 to quantify colloidal Pu, an estimate of the potential to form colloidal Pu at INTEC has been requested. Knopp, Neck et al. (1999) have reported that Pu^{IV} hydrolysis can generate colloidal particles of amorphous $\text{Pu}(\text{OH})_4\text{(s)}$, and plutonium can adsorb onto natural colloidal material (Lu et al. 2003). Thus, colloidal material may provide a vector for plutonium transport at INTEC.

Dai et al. (2002) have found that a small fraction (< 4%) of total mobile Pu in Savannah River Site sediments is associated with colloids, and Kersting, Efurud et al. (1999) report that colloidal material accounts for > 99% of total mobile $^{239,240}\text{Pu}$ at the Nevada Test Site. However, sampling methods employed at the Nevada Test Site may significantly increase the recovered colloidal fraction over the actual ambient conditions and the data provided by Dai et al. (2002) are considered to be more reliable. Litaor, Barth et al. (1998) used low-tension samplers to measure Pu transport through soil interstitial water at Rocky Flats, and report that from 1.5 – 15% of total mobile Pu was associated with colloids. Transport was not continuous, and most transport was associated with simulated rainfall events. A strong association between simulated rainfall events and colloidal Pu transport has also been reported by Ryan, Illangasekare et al. (1998). Fjeld and others (Fjeld et al. 2000; Fjeld et al. 2001) report that 1 - 2.5% of total added Pu was associated with a weakly retained fractions in column experiments with

INL SDA interbed sediments and 17 – 29% of added Pu was weakly retained in column experiments with INL basalt. All plutonium was added as aqueous Pu^{IV}, and we consider this to be equivalent to the mobile fraction entering a subsurface region. Colloids were not directly measured, but the transport properties of the weakly retained fraction are similar to what has been previously reported for colloids.

Taken together, the most reliable data on colloidal Pu transport indicate that between 1 – 15% of total mobile Pu (< 0.45 µm diameter) is potentially associated with colloids. Column studies conducted on SDA interbed sediments (Fjeld et al. 2000; Fjeld et al. 2001) and field studies conducted at Savannah River Site (Dai et al. 2002) suggest that the actual percentage is probably less than 4% of total mobile Pu. Based on the column work of Fjeld and others (Fjeld et al. 2000; Fjeld et al. 2001), we estimate that ~1.5% of total mobile Pu is associated with colloids. This fraction will rapidly reduce as the aqueous Pu decreases (and colloids are filtered out). Total mobile Pu is defined as the fraction that passes through a 0.45 µm filter and is not associated with larger particles.

D-3.15 ⁹⁰Sr K_d Values Applicable to INTEC Alluvium, Sediment, and Basalt

⁹⁰Sr is a hard cation that exists primarily in the +2 oxidation state, and displays sorption chemistry that is sensitive to both sediment mineral composition (e.g., Liszewski et al. 1997; Liszewski et al. 1998; Liszewski et al. 2000) and aqueous geochemistry (e.g., Bunde et al. 1998; Bunde et al. 1997). Sr²⁺ adsorbs to both clay minerals and carbonate minerals, and its K_d can be expected to reflect a balance between ion exchange with clay minerals and carbonate saturation state. It is difficult to quantify the effect of carbonate saturation state, and we assume that this effect is negligible in comparison to ion exchange reactions with clay minerals. This dominance of Sr interaction with clays indicates that CEC can be used as a scaling factor.

Several researchers have investigated Sr sorption onto INL sediments in INTEC, SDA, and other sites across the INL. In general, these studies indicate that Sr²⁺ sorption is strongly impacted by variability in both solution composition and sediment mineral content. Data from Liszewski and others (Liszewski et al. 1997; Liszewski et al. 1998; Liszewski et al. 2000) for INL surficial sediments indicate that Sr K_d values can range from 36 to 275 mL/g in aqueous solutions generally representative of INTEC percolation ponds. For interbed sediments, Liszewski et al. (1998) report Sr K_d values that range from 66 – 266 mL/g (average ~180 mL/g) in similar low ionic strength solutions. Sr K_d could be correlated to MnO content, surface area, and > 4.75 mm grain size fraction (Liszewski et al. 2000). CEC was not measured, but we have previously demonstrated that CEC and sediment surface area are correlated. Colello et al. (1998) have measured Sr K_d values on 22 different basalt samples collected from beneath the INL. Measured K_d for these samples ranged from 3.6 – 29 mL/g (average ~10 mL/g). No correlation was observed between Sr K_d and any physical properties of the basalt. Del Debbio and Thomas (1989) measured Sr K_d values ranging from 1.1 – 2.7 mL/g for basalt samples collected from beneath INTEC. All available measurements for basalt were done in batch mode with a 1:20 sediment/water ratio, and low ionic strength groundwater representative of INTEC percolation ponds. Bunde and others (Bunde et al. 1998; Bunde et al. 1997) report that elevated concentrations of major ions (e.g., Na⁺, K⁺, Ca²⁺, Mg²⁺) can greatly reduce Sr K_d values. High concentrations of these ions are often found in INTEC alluvium and interbed water, and this effect needs to be considered.

Strontium K_d values in alluvium and sedimentary interbeds at INTEC were estimated three ways. Strontium K_d values were measured on samples collected from sedimentary interbeds at INTEC (Liszewski et al. 1998). After review of the laboratory procedures used to collect these K_d values, we conclude that they are biased high because of the water chemistry used during the measurements. Therefore, the measured values may not be representative of the geochemical conditions in the interbeds.

Hawkins and Short (1965) developed an equation to predict the K_d value of strontium for INTEC alluvium after measuring the partitioning of strontium as a function of water chemistry. This equation includes a term for CEC (called saturation capacity). However, all Hawkins and Short measurements were made at one CEC value, and so the sensitivity of the calculated K_d to CEC was never validated. Entering water analyses for perched zone wells compiled by Roddy (2005), the Hawkins and Short equation can be used to calculate a strontium K_d for each water analysis. Finally, we use the PHREEQC geochemical code and selectivity coefficients for a cation exchange geochemical model to calculate strontium K_d values using the Roddy water analyses. While quite a few measurements of CEC of surficial alluvium at INTEC have been made, no CEC values have been measured on interbeds at INTEC. CEC measurements have been made on interbeds at the Subsurface Disposal Area (Barraclough and Jensen 1976; Rightmire 1984; Leecaster and Hull 2003). We use the summary statistics (range and average) of the SDA CEC data in the calculations for INTEC. A complete discussion of the development of K_d values for strontium is given in Appendix J. From these methods, we determine that the range of K_d for surficial alluvium is between 8 and 20 mL/g with a median value of 12 mL/g. For sedimentary interbeds, K_d values are expected to range between 25 and 84 mL/g with a median value near 50 mL/g.

Sr K_d recommendations are summarized in Table D-3-12. For basalt, K_d estimates are taken from Colello et al. (1998), with the recommended estimate equal to the minimum Sr K_d observed for basalt. For alluvium and interbeds the maximum and minimum values reflect the range of Sr K_d estimates made using the equation of Hawkins and Short (1965) and calculations with the PHREEQC geochemical code. The recommended Sr K_d values reflect the median of all estimates from *in situ* groundwater chemistry.

Table D-3-12. Sr K_d values for INTEC alluvium, basalt, and interbed sediments. Values from batch experiments corrected for sediment/water ratio and differences in divalent cation chemistry.

	Minimum Estimated Sr K_d (mL/g)	Maximum Estimated Sr K_d (mL/g)	Recommended Sr K_d (mL/g)
Alluvium	8	20	12
Interbed	25	84	50
Basalt	0	15	0.5

D-3.16 ^{99}Tc K_d Values Potentially Applicable to INTEC Alluvium, Sediment, and Basalt

^{99}Tc predominantly occurs as pertechnetate (TcO_4^-) in natural environments, generally sorbs poorly to sediments, and is typically highly mobile (e.g., Denys et al. 2003; Kaplan 2003; Mashkin and Shikov 2000). Current data indicate that (1) Tc binds weakly to carbonates, (2) Tc mobility increases with increasing pH (Denys et al. 2003), and (3) Tc mobility decreases under organic-rich, reducing conditions (Keith-Roach et al. 2003; Mashkin and Shikov 2000). The pH effect may arise from pH-dependent changes in surface charge, or may reflect the role of organic matter – which both provide anion sorption sites for TcO_4^- and reduce pH (Kaplan 2003). Sedimentary microorganisms are known to be able to mediate reduction of highly-soluble Tc^{VII} (TcO_4^-) to poorly-soluble Tc^{IV} (TcO_2) via either direct, enzymatic Tc^{VII} reduction (Lloyd et al. 2000), or through indirect creation of Fe^{III} reducing conditions (Fredrickson et al. 2004; Wildung et al. 2004). In general, microbial Fe^{III} reduction does not occur until all O_2 and NO_3^- have been consumed. Thus, while Tc reduction is possible in isolated pockets in the INTEC subsurface, soluble $\text{Tc}^{\text{VII}}\text{O}_4^-$ should be the dominant Tc species in the INTEC subsurface. Tc adsorption is primarily controlled by organic matter, and thus Tc should scale to wt% organic carbon rather than CEC.

Del Debbio and Thomas (1989) report TcO_4^- K_d values of ~ 0 mL/g for INTEC alluvium and interbeds. Dicke (1997) uses these data to recommend a Tc K_d of 0 mL/g for SDA sediments, and we recommend a Tc K_d value of 0 mL/g for INTEC alluvium and interbeds. To establish a range of maximum and minimum ^{99}Tc K_d estimates, it is necessary to examine Tc behavior in other systems. Kaplan (2003) reports Tc K_d values that range from $(-0.1) - 0.1$ mL/g for a silty-sand upland Savannah River Site (SRS) sediment (0.3 wt% Fe_2O_3 , < 0.02 wt% organic carbon) and from $0 - 0.3$ mL/g for a silty-sand wetland SRS sediment (0.01 wt% Fe_2O_3 , 0.14 wt% organic carbon) under similar experimental conditions. Sheppard and Thibault (1991) conducted a 4-yr study of Tc transport in surficial soils, and report Tc K_d values that range from $0.1 - 1.4$ mL/g (average 0.8 mL/g) for sediments with $0.2 - 0.3$ wt% organic carbon. No data are available for basalt. The SRS upland sediment is most similar to INTEC interbeds, while the SRS wetland sediment and lysimeter studies are most comparable to INTEC alluvium. The maximum and minimum Tc K_d values presented in Table D-3-13 correspond to the maximum and minimum values observed in these studies. Lacking direct measurements, the minimum and recommended Tc K_d for basalt is 0 mL/g.

Table D-3-13. Tc K_d values for INTEC alluvium, basalt, and interbed sediments. Values from batch experiments corrected for sediment/water ratio.

	Minimum Estimated Tc K_d (mL/g)	Maximum Estimated Tc K_d (mL/g)	Recommended Tc K_d (mL/g)
Alluvium	-0.1	1.4	0
Interbed	-0.1	0.1	0
Basalt	0	No data	0

D-3.17 $^{234/235/238}\text{U}$ K_d Values Applicable to INTEC Alluvium, Sediment, and Basalt

Uranium predominantly exists as either soluble $\text{U}^{\text{VI}}\text{O}_2^{2-}$ or an insoluble U^{IV} oxide in natural environments. Under oxidizing conditions that are typical for INTEC it is assumed that U^{VI} predominates and that insoluble U^{IV} species do not need to be considered in the K_d analysis. Even in reducing environments authigenic U^{IV} minerals can react with NO_3^- to form soluble U^{VI} and reduced nitrogen compounds (Finneran et al. 2002), and thus the absence of oxygen is not sufficient to maintain U^{VI} reducing conditions. Since INTEC groundwater contains high levels of NO_3^- , most uranium that leaches from the source term should be present as soluble U^{VI} . Aqueous complexation with calcium and carbonate ligands (e.g., Abdelouas et al. 1999; Burns and Finch 1999; Clark et al. 1995) can be significant and must be considered when evaluating data for K_d estimates. Recent studies have identified a ternary $\text{Ca}_2\text{UO}_2(\text{CO}_3)_3\text{-aq}$ ligand that is much more soluble than the previously identified uranyl carbonate ligands (Bernhard et al. 2001; Kalmykov and Choppin 2000), and helps explain previous observations of enhanced uranium solubility in Ca-carbonate rich environments (e.g., Brooks et al. 2003; Chen and Yiaccoumi 2002; Duff and Amrhein 1996; Elless and Lee 1998). INTEC alluvium water, interbed water, and groundwater are rich in both Ca^{2+} and carbonate species; and the effect of these complexes on U K_d needs to be considered.

Laboratory and modeling studies of U^{VI} sorption to SDA interbed sediments by Ayaz et al. (2003) indicate that greater than 95% of total uranium is adsorbed at $\text{pH} < \sim 7.5$. That percentage rapidly drops to a range of $\sim 10\% - 50\%$ of total uranium adsorbed from $\text{pH} 7.5 - 10.5$, and then increases again at $\text{pH} > 10.5$. Solution pH in INTEC groundwater is relatively constant, but that there are large variations in Ca^{2+} and carbonate alkalinity that can alter uranium speciation. The influence of Ca^{2+} and carbonate alkalinity

on uranium speciation at constant pH and constant pO_2 is shown in Figure D-3-6. When Ca^{2+} is greater than ~ 0.5 mM and carbonate alkalinity is greater than ~ 2.5 mM, $(Ca)_2(UO_2)(CO_3)_3$ -aq will be the dominant uranium species. Average *in situ* conditions in INTEC sediments are ~ 2 mM Ca^{2+} and ~ 3 mM total carbonate, indicating that $(Ca)_2(UO_2)(CO_3)_3$ -aq will be the dominant uranium species in the absence of sorbing surfaces. When Ca^{2+} and carbonate alkalinity drop below these levels, $CaUO_4$ or sodydyte can be expected to control uranium solubility. When quartz, clay, and iron oxide surfaces are present, uranium solubility will be controlled by a pH, Ca^{2+} , and CO_3^{2-} dependent balance between $(Ca)_2(UO_2)(CO_3)_3$ -aq, sodydyte solubility, and U^{VI} sorption to clays and soil minerals.

No site-specific K_d data are available for U adsorption to INTEC subsurface media, but some data are available for U adsorption to SDA sediments. These studies did not encompass the entire range of INTEC Ca^{2+} and carbonate concentrations, but did approximate the median value for these ions in INTEC alluvium and interbed water. Dicke (1997) recommends U K_d values that range from 3.4 to 9 mL/g for SDA sediments, and from 0.2 – 5.2 mL/g for basalt. More recently, a series of batch studies

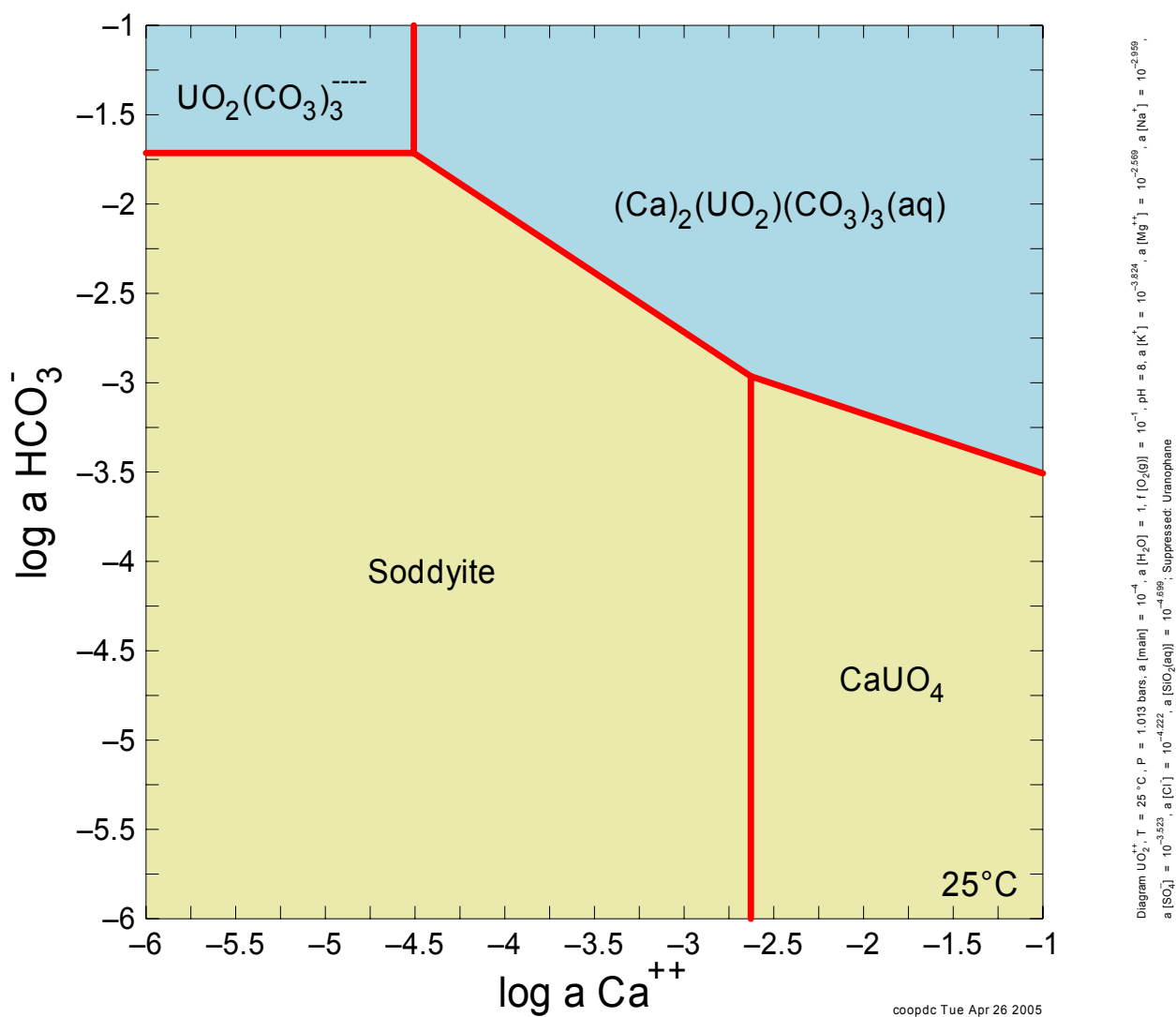


Figure D-3-6. Phase diagram for uranium speciation in INTEC groundwater (pH 8, 0.1 mM total U).

investigating uranium sorption to interbed sediments collected from SDA indicate that K_d can range from 0.6 – 58 mL/g under simulated groundwater conditions (Ayaz et al. 2003; Grossman et al. 2001; Leecaster and Hull 2004). Leecaster and Hull (2004) integrated these interbed-specific K_d data with geographic records of sample location to create a 2-D grid of U K_d in SDA interbeds. When plotted as a histogram, these data indicated that >95% of K_d measurements fell within the range of 0 – 35 mL/g (median ~18 mL/g). When compared to sediment properties, U K_d correlated most strongly with CEC – suggesting that surface reactions with clay minerals control uranium sorption chemistry in the INL subsurface. In a series of column studies, Fjeld et al. (Fjeld et al. 2001) report retention factors that range from 30 – 31 ($K_d \sim 7.8$ mL/g) for SDA interbed sediments and from 5.1 – 6.1 ($K_d \sim 1.4$ mL/g) for SDA basalt. A recent unpublished study of uranium transport through unsaturated sediments in a near field-scale column reactor packed with SDA surficial sediments (Cooper and Hull 2004)^h indicate that uranium K_d can range from 4 – 50 mL/g, with a value of 10 mL/g providing a reasonable conservative estimate for SDA surficial sediments.

A summary of U K_d recommendations is provided in Table D-3-14. The minimum and maximum values represent the range of K_d values reported from all batch and column experiments for SDA sediments, as scaled to CEC (as previously described). The recommended U K_d value for these sediments is estimated to be equal to the value reported by Fjeld et al. (2001) for column experiments with SDA interbed sediments and groundwater constituents analogous to INTEC conditions, as scaled to CEC. The U K_d values for basalt range from an estimated minimum of 0 mL/g to a likely maximum of 1.4 mL/g as measured for basalt based on the column studies of Fjeld et al. (2001). A value of 0 mL/g is estimated to be recommended for basalt. Speciation calculations suggest that the elevated Ca^{2+} levels in INTEC interbeds should decrease U K_d with respect to INTEC alluvium. However, lacking alkalinity data for alluvium water and interbed water, this reduction cannot be quantified and U K_d is assumed to be comparable in both systems.

Table D-3-14. U K_d values for INTEC alluvium, basalt, and interbed sediments. Values from batch experiments corrected for sediment/water ratio.

	Minimum Estimated U K_d (mL/g)	Maximum Estimated U K_d (mL/g)	Recommended U K_d (mL/g)
Alluvium	0.12	12	1.6
Interbed	0.12	12	1.6
Basalt	0	1.4	0

D-4. REFERENCES

- Abdelouas, A., W. Lutze, and E. Nuttall, 1999, "Uranium Contamination in the Subsurface: Characterization and Remediation," In *Uranium: Mineralogy, Geochemistry and the Environment*, Vol. 38 (ed. P. C. Burns and R. J. Finch), Mineralogical Society of America, pp. 433-468.
- Amachi, S., M. Kasahara, S. Hanada, Y. Kamagata, H. Shinoyama, T. Fujii, and Y. Muramatsu, 2003, "Microbial participation in iodine volatilization from soils," *Environmental Science & Technology*, 37(17), 3885-3890.

^h. Cooper, D. C. and L. C. Hull, 2004, unpublished results from near-field scale uranium transport study in unsaturated sediments, report pending (INL/EXT-04-02147) (ed. D. C. Cooper).

- Amachi, S., Y. Muramatsu, and Y. Kamagata, 2000, "Radioanalytical determination of biogenic volatile iodine emitted from aqueous environmental samples," *Journal of Radioanalytical and Nuclear Chemistry*, 246(2), 337-341.
- Andre, C., M. Sardin, P. Vitorge, and M. H. Faure, 1998, "Analysis of breakthrough curves of Np(V) in clayey sand packed column in terms of mass transfer kinetics," *Journal of Contaminant Hydrology*, 35(1-3), 161-173.
- Artinger, R., B. Kienzler, W. Schussler, J. and Kim, 1998, "Effects of humic substances on the Am-241 migration in a sandy aquifer: column experiments with Gorleben groundwater/sediment systems," *Journal of Contaminant Hydrology*, 35(1-3), 261-275.
- Artinger, R., W. Schuessler, F. Scherbaum, D. Schild, J. I. Kim, 2002, "Am-241 migration in a sandy aquifer studied by long-term column experiments," *Environmental Science & Technology*, 36, 4818-4823.
- Ayaz, B., J. T. Coates, A. W. Elzerman, R. A. Fjeld, H. E. Holder, J. L. Myers, and B. A. Powell, 2003, *Development of Adsorption Parameters to Assess the Migration Potential for Uranium and Neptunium in the Subsurface at the INEEL*, INEEL/EXT-03-00306, Rev. 0, U.S. Department of Energy, April 2003.
- Banerjee, D. and H. W. Nesbitt, 1999, "Oxidation of aqueous Cr(III) at birnessite surfaces: Constraints on reaction mechanism," *Geochimica Et Cosmochimica Acta*, 63(11-12), 1671-1687.
- Baron, D. and C. Palmer, 2002, "Solid-solution aqueous-solution reactions between jarosite (KFe₃(SO₄)(2)(OH)(6)) and its chromate analog," *Geochimica Et Cosmochimica Acta*, 66(16), 2841-2853.
- Barracough, J. T. and R. G. Jensen, 1976, *Hydrologic Data For The Idaho National Engineering Laboratory Site, Idaho 1971 To 1973*, IDO-22055, USGS Geological Survey Open File Report 75-318, January 1976.
- Bartholomay, R. C., 1990, *Mineralogical Correlation of Surficial Sediment from Area Drainages with Selected Sedimentary Interbeds at the Idaho National Engineering Laboratory, Idaho*, 90-147, U.S. Geological Survey.
- Bartholomay, R. C. and L. L. Knobel, 1989, *Mineralogy and Grain Size of Surficial Sediment from the Little Lost River and Birch Creek Drainages, Idaho National Engineering Laboratory, Idaho*, 890385, U.S. Geological Survey.
- Bartholomay, R. C., L. L. Knobel, L. C. and Davis, 1989, *Mineralogy and Grain Size of Surficial Sediment from the Big Lost River Drainage and Vicinity, with Chemical and Physical Characteristics of Geologic Materials from Selected Sites at the Idaho National Engineering Laboratory, Idaho*, 89-384, U.S. Geological Survey.
- Batcheller, T. A. and G. D. Redden, 2004, *Colloidal Plutonium at the OU 7-13/14 Subsurface Disposal Area: Estimate of Inventory and Transport Properties*, ICP/EXT-04-00253, Idaho Completion Project, Idaho National Engineering and Environmental Laboratory, May 2004.

- Benes, P., K. Stamberg, L. Siroky, J. and Mizera, 2002, "Radiotracer study of sorption of europium on Gorleben sand from aqueous solutions containing humic substances," *Journal of Radioanalytical and Nuclear Chemistry*, 254(2), 231-239.
- Bernhard, G., G. Geipel, T. Reich, V. Brendler, S. Amayri, and H. Nitsche, 2001. "Uranyl(VI) carbonate complex formation: Validation of the $\text{Ca}_2\text{UO}_2(\text{CO}_3)_3(\text{aq.})$ species," *Radiochimica Acta*, 89(8), 511-518.
- Bostock, A. C., G. Shaw, and J. N. B Bell, 2003, "The volatilisation and sorption of I-129 in coniferous forest, grassland and frozen soils," *Journal of Environmental Radioactivity*, 70(1-2), 29-42.
- Brooks, S. C., J. K. Fredrickson, S. L. Carroll, D. W. Kennedy, J. M. Zachara, A. E. Plymale, S. D. Kelly, K. M. Kemner, and S. Fendorf, 2003, "Inhibition of bacterial U(VI) reduction by calcium," *Environmental Science and Technology*, 37(9), 1850-1858.
- Bunde, R. L., J. J. Rosentreter, and M. J. Liszewski, 1998, "Rate of strontium sorption and the effects of variable aqueous concentrations of sodium and potassium on strontium distribution coefficients of a surficial sediment at the Idaho National Engineering Laboratory, Idaho," *Environmental Geology*, 34(2-3), 135-142.
- Bunde, R. L., J. J. Rosentreter, M. J. Liszewski, C. H. Hemming, and J. Welhan, 1997, "Effects of calcium and magnesium on strontium distribution coefficients," *Environmental Geology*, 32(3), 219-229.
- Burns, P. C. and R. J. Finch, 1999, "Uranium: Mineralogy, Geochemistry and the Environment," In *Reviews in Mineralogy*, Vol. 38 (ed. P. H. Ribbe), Mineralogical Society of America, pp. 680.
- Chen, J. P. and S. Yiaccoumi, 2002, "Modeling of depleted uranium transport in subsurface systems," *Water Air and Soil Pollution*, 140(1-4), 173-201.
- Choppin, G. R. and A. Morgenstern, 2001, "Distribution and Movement of Environmental Plutonium," *Plutonium in the Environment*, 92-105.
- Clark, D. L., D. E. Hobart, and M. P. Neu, 1995, "Actinide Carbonate Complexes and Their Importance in Actinide Environmental Chemistry," *Chemical Reviews*, 95(1), 25-48.
- Clay, D. E., Z. Zheng, Z. Liu, S. A. Clay, T. P. Trooien, 2004, "Bromide and nitrate movement through undisturbed soil columns," *Journal of Environmental Quality*, 33, 338-342.
- Colello, J. J., J. J. Rosentreter, R. C. Bartholomay, and M. J. Liszewski, 1998, *Strontium Distribution Coefficients of Basalt Core Samples from the Idaho National Engineering and Environmental Laboratory, Idaho*, DOE/ID-22153, U.S. Geological Survey.
- Dai, M., J. M. Kelley, and K. O. Buesseler, 2002, "Sources and migration of plutonium in groundwater at the Savannah River Site," *Environmental Science & Technology*, 36(17), 3690-3699.
- De Brouwere, K., E. Smolders, R. Merckx, 2004, "Soil properties affecting solid-liquid distribution of As(V) in soils," *European Journal of Soil Science*, 55, 165-173.
- del Debbio, J. A., 1991, "Sorption Of Strontium, Selenium, Cadmium, And Mercury In Soil," *Radiochimica Acta*, 52-3, 181-186.

- del Debbio, J. A. and T. R. Thomas, 1989, *Transport Properties of Radionuclides and Hazardous Chemical Species in Soils at the Idaho Chemical Processing Plant*, WINCO-1068, Westinghouse Idaho Nuclear Company.
- Denys, S., G. Echevarria, L. Florentin, E. Leclerc-Cessac, and J. L. Morel, 2003, "Availability of Tc-99 in undisturbed soil cores," *Journal of Environmental Radioactivity*, 70(1-2), 115-126.
- Derjaguin, B. V. and L. D. Landau, 1941, "Theory of the stability of strongly charged lyophobic sols and the adhesion of strongly charged particles in solutions of electrolytes," *Acta Physicochimica URSS*, 14: 633-662.
- Dicke, C. A., 1997, *Distribution Coefficients and Contaminant Solubilities for the Waste Area Group 7 Baseline Risk Assessment*, INEL/EXT-97-00201, Idaho National Engineering and Environmental Laboratory, May 1997.
- DOE-ID, 2003, *Phase I Monitoring Well and Tracer Study Report for Operable Unit 3-13, Group 4, Perched Water*, DOE-ID-10967, Rev. 2, U.S. Department of Energy Idaho Operations Office, March 2003. (Availability of Revision 2 is restricted. Revision 1 is publicly available.)
- DOE-ID, 2006, *Annual INTEC Water Monitoring Report for Group 4—Perched Water (2005)*, DOE-ID-11259, Rev. 0, U.S. Department of Energy Idaho Operations Office, January 2006.
- DOE-NE-ID, 2005, *Annual INTEC Groundwater Monitoring Report for Group 5—Snake River Plain Aquifer (2004)*, DOE/NE-ID-11222, Rev. 0, U.S. Department of Energy Idaho Operations Office, May 2005.
- Dong, W. M., X. K. Wang, X. Y. Bian, A. X. Wang, J. Z. Du, and Z. Y. Tao, 2001, "Comparative study on sorption/desorption of radioeuropium on alumina, bentonite and red earth: effects of pH, ionic strength, fulvic acid, and iron oxides in red earth," *Appl. Radiat. Isot.*, 54(4), 603-610.
- Dong, W. M., X. K. Wang, J. Z. Du, X. Y. Bian, F. Ma, and Z. Y. Tao, 1999, "Sorption and desorption characteristics of Eu(III) on red earth," *Journal of Radioanalytical and Nuclear Chemistry*, 242(3), 793-797.
- Duff, M. C. and C. Amrhein, 1996, "Uranium(VI) adsorption on goethite and soil in carbonate solutions," *Soil Science Society of America Journal*, 60(5), 1393-1400.
- Duwig, C., T. Becquer, L. Charlet, B. E. Clothier, 2003, "Estimation of nitrate retention in a Ferralsol by a transient-flow method," *European Journal of Soil Science*, 54, 505-515.
- Elless, M. P. and S. Y. Lee, 1998, "Uranium solubility of carbonate-rich uranium-contaminated soils," *Water Air and Soil Pollution*, 107(1-4), 147-162.
- Falconer, K. L., Idaho National Engineering and Environmental Laboratory, to K. E. Hain, Department of Energy Idaho Operations Office, September 30, 1997, "Transmittal of Plutonium & Strontium Kd Batch Study Results for ICPP," KLF-202-97.
- Fendorf, S., B. W. Wielinga, and C. M. Hansel, 2000, "Chromium transformations in natural environments: The role of biological and abiological processes in chromium(VI) reduction," *International Geology Review*, 42(8), 691-701.

- Finneran, K. T., M. E. Housewright, and D. R. Lovley, 2002, "Multiple influences of nitrate on uranium solubility during bioremediation of uranium-contaminated subsurface sediments," *Environmental Microbiology*, 4(9), 510-516.
- Fjeld, R. A., J. T. Coates, and A. W. Elzerman, 2000, Final Report *Column Tests to Study the Transport of Plutonium and Other Radionuclides in Sedimentary Interbed at INEEL*, INL/EXT-01-00763, Rev. 0, Idaho National Engineering and Environmental Laboratory, December 2000.
- Fjeld, R. A., T. A. DeVol, R. W. Goff, M. D. Blevins, D. D. Brown, S. M. Ince, and A. W. Elzerman, 2001, "Characterization of the mobilities of selected actinides and fission/activation products in laboratory columns containing subsurface material from the Snake River Plain," *Nuclear Technology*, 135(2), 92-108.
- Fjeld, R. A., S. M. Serkiz, P. L. McGinnis, A. Elci, D. I. Kaplan, 2003, "Evaluation of a conceptual model for the subsurface transport of plutonium involving surface mediated reduction of Pu(V) to Pu(IV)," *Journal of Contaminant Hydrology*, 67, 79-94.
- Fredrickson, J. K., J. M. Zachara, D. W. Kennedy, R. K. Kukkadapu, J. P. McKinley, S. M. Heald, C. X. Liu, and A. E. Plymale, 2004, "Reduction of TcO₄⁻ by sediment-associated biogenic Fe(II)," *Geochimica Et Cosmochimica Acta*, 68(15), 3171-3187.
- Geochemists Workbench, Version 4, Urbana, Illinois: University of Illinois, Hydrogeology Program, Department of Geology.
- Glass, R.J., T. S. Steenhuis, and J. V. Parlange, 1989, "Wetting front instability 2: Experimental determination of relationships between system parameters and two-dimensional unstable flow-field behavior in initially dry porous media," *Water Resources Research*, 25:1195-1207.
- Glass, R. J., M. J. Nicholl, S. E. Pringle, and T. R. Wood, 2002, "Unsaturated flow through a fracture-matrix network: Dynamic preferential pathways in mesoscale laboratory experiments," *Water Resources Research*, 38(12).
- Glass, R. J., M. J. Nicholl, H. Rajaram, and T. R. Wood, 2003, "Unsaturated flow through fracture networks: Evolution of liquid phase structure, dynamics, and the critical importance of fracture intersections," *Water Resources Research*, 39(12).
- Golder Associates, Inc., 1991, *Report for the Idaho Chemical Processing Plant Drilling and Sampling Program at Land Disposal Unit CPP-59*, Golder Report 893-1195-320, January 1991.
- Grossman, C. J., R. A. Fjeld, J. T. Coates, and A. W. Elzerman, 2001, *The Sorption of Selected Radionuclides in Sedimentary Interbed Soils from the Snake River Plain*, INEEL/EXT-01-01106, Rev. 0, Idaho National Engineering and Environmental Laboratory, June 2001.
- Haschke, J. M., T. H. Allen, and L. A. Morales, 2000, "Reaction of plutonium dioxide with water: Formation and properties of PuO₂+x," *Science*, 287(5451), 285-287.
- Hawkins, D. B. and H. L. Short, 1965, *Equations for the Sorption of Cesium and Strontium on Soil and Clinoptilolite*, IDO-12046, U. S. Atomic Energy Commission, November 1965.

- Hemming, C. H., R. L. Bunde, M. J. Liszewski, J. J. Rosentreter, J. Welhan, 1997, "Effect of experimental technique on the determination of strontium distribution coefficients of a surficial sediment from the Idaho National Engineering Laboratory, Idaho," *Water Res.*, 31, 1629-1636.
- EDF-5758, 2005, "Geochemical Study for Perched Water Source Identification at INTEC," Rev. 0, Idaho National Laboratory, Idaho Cleanup Project, May 2005.
- Kalmykov, S. N. and G. R. Choppin, 2000, "Mixed $\text{Ca}^{2+}/\text{UO}_2^{2+}/\text{CO}_3^{2-}$ complex formation at different ionic strengths," *Radiochimica Acta*, 88(9-11), 603-606.
- Kaplan, D. I., 2003, "Influence of surface charge of an Fe-oxide and an organic matter dominated soil on iodide and pertechnetate sorption," *Radiochimica Acta*, 91(3), 173-178.
- Kaplan, D. I., B. A. Powell, D. I. Demirkanli, R. A. Fjeld, F. J. Molz, S. M. Serkiz, and J. T. Coates, 2004, "Influence of oxidation states on plutonium mobility during long-term transport through an unsaturated subsurface environment," *Environmental Science & Technology*, 38(19), 5053-5058.
- Keith-Roach, M. J., K. Morris, and H. Dahlgaard, 2003, "An investigation into technetium binding in sediments," *Mar. Chem.*, 81(3-4), 149-162.
- Kersting, A. B., D. W. Efurud et al., 1999, "Migration of plutonium in ground water at the Nevada Test Site," *Nature*, 397(6714): 56-59.
- Knopp, R., V. Neck et al., 1999, "Solubility, hydrolysis and colloid formation of plutonium(IV)," *Radiochimica Acta*, 86(3-4): 101-108.
- Kostka, J. E. and G. W. Luther, 1994, "Partitioning and speciation of solid phase iron in saltmarsh sediments," *Mar. Chem.*, 81(3-4), 149-162.
- Kozuh, N., J. Stupar, and B. Gorenc, 2000, "Reduction and oxidation processes of chromium in soils," *Environmental Science & Technology*, 34(1), 112-119.
- Kuhlmeier, P. D., 1997, "Sorption and desorption of arsenic from sandy soils: Column studies," *Journal of Soil Contamination*, 6, 21-36.
- Lee, S. Z., L. Z. Chang et al., 2001, "The effect of hydration on adsorption and desorption of heavy metals in soils," *Journal of Environmental Science and Health Part a- Toxic/Hazardous Substances & Environmental Engineering*, 36(1): 63-74.
- Leecaster, M. K. and L. C. Hull, 2004, *Spatial Distribution of Neptunium and Uranium Partition Coefficients (K_d) for Interbed Sediments at a Radioactive Waste Subsurface Disposal Area*, ICP/EXT-03-00088, Rev. 0, Idaho Completion Project, Idaho National Engineering and Environmental Laboratory, February 2004.
- Lindberg, S. E., H. Zhang, M. Gustin, A. Vette, F. Marsik, J. Owens, A. Casimir, R. Ebinghaus, G. Edwards, C. Fitzgerald, J. Kemp, H. H. Kock, J. London, M. Majewski, L. Poissant, M. Pilote, P. Rasmussen, F. Schaedlich, D. Schneeberger, J. Sommar, R. Turner, D. Wallschlager, and Z. Xiao, 1999, "Increases in mercury emissions from desert soils in response to rainfall and irrigation," *J. Geophys. Res.-Atmos.*, 104(D17), 21879-21888.

- Liszewski, M. J., J. J. Rosentreter, and K. E. Miller, 1997, *Strontium Distribution Coefficients of Surficial Sediment Samples from the Idaho National Engineering Laboratory, Idaho*, 97-4044, U.S. Geological Survey.
- Liszewski, M. J., J. J. Rosentreter, K. E. Miller, and R. C. Bartholomay, 1998, *Strontium Distribution Coefficients of Surficial and Sedimentary Interbed Sediment Samples from the Idaho National Engineering Laboratory, Idaho*, 98-4073, U.S. Geological Survey.
- Liszewski, M. J., J. J. Rosentreter, K. E. Miller, and R. C. Bartholomay, 2000, "Chemical and physical properties affecting strontium distribution coefficients of surficial-sediment samples at the Idaho National Engineering and Environmental Laboratory, Idaho," *Environmental Geology*, 39(3-4), 411-426.
- Litaor, M. I., G. Barth et al., 1998, "The behavior of radionuclides in the soils of Rocky Flats, Colorado," *Journal of Environmental Radioactivity*, 38(1): 17-46.
- Lloyd, J. R., V. A. Sole, C. V. G. Van Praagh, and D. R. Lovley, 2000, "Direct and Fe(II)-mediated reduction of technetium by Fe(III)-reducing bacteria," *Applied Environmental Microbiology*, 66(9), 3743-3749.
- Lu, N., K. Kung, C. Mason, I. Triay, C. Cotter, A. Pappas, and M. Pappas, 1998, "Removal of plutonium-239 and americium-241 from rocky flats soil by leaching," *Environmental Science & Technology*, 32(3), 370-374.
- Lu, N. P., P. W. Reimus, G. R. Parker, J. L. Conca, and I. R. Triay, 2003, "Sorption kinetics and impact of temperature, ionic strength and colloid concentration on the adsorption of plutonium-239 by inorganic colloids," *Radiochimica Acta*, 91(12), 713-720.
- Mashkin, A. N. and S. L. Shikov, 2000, "Effect of natural and technogenic factors on technetium behavior in the environment," *Radiochemistry*, 42(2), 205-210.
- McCarthy, J. F., W. E. Sanford, and P. L. Stafford, 1998, "Lanthanide field tracers demonstrate enhanced transport of transuranic radionuclides by natural organic matter," *Environmental Science & Technology*, 32(24), 3901-3906.
- McManus, G. J., F. A. Duce., S. J. Fernandez, and L. P. Murphy, 1982, *A Model of Iodine-129 Process Distributions in a Nuclear Fuel Reprocessing Plant*, ENICO 1108, Exxon Nuclear Idaho Company, Inc.
- Mincher, Bruce J., Robert V. Fox, D. Craig Cooper, Gary S. Groenewold, 2003, "Neptunium and plutonium sorption to Snake River Plain, Idaho soil," *Radiochimica Acta*, Vol. 91, Issue: 7, pp. 397-402.
- Mincher, B. J., R. V. Fox, C. L. Riddle, D. C. Cooper, G. S. Groenewold, 2004, "Strontium and cesium sorption to snake river plain, Idaho soil," *Radiochimica Acta*, 92, 55-61.
- Miner, F. J., P. A. Evans, W. L. Polzer, 1982, *Plutonium behavior in the soil/water environment*, RFP-2480, Rockwell International, November 1982.
- Muramatsu, Y. and S. Yoshida, 1999, "Effects of microorganisms on the fate of iodine in the soil environment," *Geomicrobiology Journal* 16(1), 85-93.

- Navratil, James D., Lockheed Martin Idaho Technologies Company, to, R. Douglas Greenwell, Lockheed Martin Idaho Technologies Company, September 5, 1997, "Idaho Chemical Processing Plant (ICPP) Kd Studies," JDN-001-97.
- Newman, M. E., I. Porro, R. Scott, F. M. Dunnivant, 1996, *Evaluation of the Mobility of Am, Cs, Co, Pu, Sr, and U through INEL Basalt and Interbed Materials: Summary Report of the INEL/Clemson University Studies*, INEL-95/282, WAG 7-82, Idaho National Engineering Laboratory, November 1996.
- Palmer, C. D. and R. W. Puls, 1994, "Natural Attenuation of Hexavalent Chromium in Ground Water and Soils," EPA/540/S-94/505, U.S. Environmental Protection Agency, October 1994.
- Palmer, C. D. and P. R. Wittbrodt, 1991, "Processes affecting the remediation of chromium-contaminated sites," *Environmental Health Perspectives*, 92, 25-40.
- Plummer, M. A., L. C. Hull, and D. T. Fox, 2004, "Transport of Carbon-14 in a Large Unsaturated Soil Column," *Vadose Zone Journal* 3, 109-121.
- Rightmire, C. T., 1984, *Description and Hydrogeologic Implications of Cored Sedimentary Material from the 1975 Drilling Program at the Radioactive Waste Management Complex, Idaho*, Water-Resources Investigations Report 84-4071, DOE/ID-22067, U. S. Geological Survey, June 1984.
- Roddy, M., 2005, *Geochemical Study for Perched Water Source Identification at INTEC*, EDF-5758, Rev 0, Idaho Cleanup Project, Idaho National Laboratory, May 2005.
- Ryan, J. N., T. H. Illangasekare et al., 1998, "Particle and plutonium mobilization in macroporous soils during rainfall simulations," *Environmental Science & Technology*, 32(4): 476-482.
- Sarkar, D., M. E. Essington, and K. C. Misra, 1999, "Adsorption of mercury(II) by variable charge surfaces of quartz and gibbsite," *Soil Science Society of America Journal*, 63(6), 1626-1636.
- Schuessler, W., R. Artinger, B. Kienzler, and J. Kim, 2000, "Conceptual modeling of the humic colloid-borne americium(III) migration by a kinetic approach," *Environmental Science & Technology*, 34(12), 2608-2611.
- Schuster, E., 1991, "The Behavior Of Mercury In The Soil With Special Emphasis On Complexation and Adsorption Processes - A Review Of The Literature," *Water Air and Soil Pollution*, 56, 667-680.
- Sheppard, S. C., 2003, "Interpolation of solid/liquid partition coefficients, K-d, for iodine in soils," *Journal of Environmental Radioactivity*, 70, 21-27.
- Sheppard, M. I. and D. H. Thibault, 1990, "Default Soil Solid/Liquid Partition Coefficients, Kds, for Four Major Soil Types: A Compendium," *Health Physics*, Vol. 59 (4), 471-482.
- Sheppard, M. I. and D. H. Thibault, 1991, "A 4-Year Mobility Study Of Selected Trace-Elements And Heavy-Metals," *Journal of Environmental Quality*, 20, 101-114.
- Sheppard, M. I., J. L. Hawkins, and P. A. Smith, 1996, "Linearity of iodine sorption and sorption capacities for seven soils," *Journal of Environmental Quality*, 25, 1261-1267.

- Smedley, P. L. and D. G. Kinniburgh, 2002, "A review of the source, behaviour and distribution of arsenic in natural waters," *Applied Geochemistry*, 17(5), 517-568.
- Sonon, L. S. and A. P. Schwab, 2004, "Transport and persistence of nitrate, atrazine, and alachlor in large intact soil columns under two levels of moisture content," *Soil Science*, 169, 541-553.
- Stephens, D. B., 1996, *Vadose Zone Hydrology*, Boca Raton, Florida: CRC Press, pp. 92-93.
- Stollenwerk, K. and D. Grove, 1985, "Adsorption and Desorption of Hexavalent Chromium in an Alluvial Aquifer Near Telluride, Colorado," *Journal of Environmental Quality*, 14, 150-155.
- Stumm, W. and J. J. Morgan, 1981, *Aquatic Chemistry*, New York: John Wiley & Sons.
- Tesoriero, A. J. and J. F. Pankow, 1996, "Solid Solution Partitioning of Sr^{2+} , Ba^{2+} , and Cd^{2+} to Calcite," *Geochimica et Cosmochimica Acta*, Vol. 60 (6), 1053-1063.
- Ticknor, K., P. Vilks, and T. Vandergraaf, 1996, "The effect of fulvic acid on the sorption of actinides and fission products on granite and selected minerals," *Applied Geochemistry*, 11(4), 555-565.
- Ticknor, K. V. and Y. H. Cho, 1990, "Interaction of iodide and iodate with granitic fracture filling materials," *Journal of Radioanalytical and Nuclear Chemistry*, 140(1), 75-90.
- Wildung, R. E., S. W. Li, C. J. Murray, K. M. Krupka, Y. Xie, N. J. Hess, and E. E. Roden, 2004, "Technetium reduction in sediments of a shallow aquifer exhibiting dissimilatory iron reduction potential," *FEMS Microbiol. Ecol.*, 49(1), 151-162.
- Wood, T. R., M. J. Nicholl, and R. J. Glass, 2002, "Fracture intersections as integrators for unsaturated flow," *Geophys. Res. Lett.*, 29(24).
- Yao, T. M. and J. M. H. Hendrickx, 1994, "Stability of wetting fronts in dry homogeneous soil under low infiltration rates," *Soil Science Society of America Journal*.
- Zachara, J. M., C. C. Ainsworth, C. E. Cowan, and C. T. Resch, 1989, "Adsorption of Chromate by Subsurface Soil Horizons," *Soil Science Society of America Journal*, 53(2), 418-428.
- Zengshou, Y., J. A. Warner, R. A. Dahlgren, and W. H. Casey, 1996, "Reactivity of iodide in volcanic soils and noncrystalline soil constituents," *Geochimica et Cosmochimica Acta*, 60(24), 4945-4956.
- Zhang, H. and S. E. Lindberg, 1999, "Processes influencing the emission of mercury from soils: A conceptual model," *J. Geophys. Res.-Atmos.*, 104(D17), 21889-21896.

